Dispersed bubble and particle-laden turbulent flows in the two-way coupling regime

Phd fellow : **Francesco Motta** **francesco.motta@uniroma1.it**

Supervisor : **Paolo Gualtieri** **paolo.gualtieri@uniroma1.it**

Dipartimento di Ingegneria Meccanica e Aerospaziale

Theoretical and Applied Mechanics - XXXIV Cycle

SAPIENZA
UNIVERSITÀ DI ROMA

23th May 2022

Abstract

The momentum exchange of bubble and particle laden incompressible turbulent flows is investigated by means of Direct Numerical Simulations (DNS), employing the Eulerian-Lagrangian approach. The Exact Regularised Point Particle method (ERRP) is used to achieve the inter-phase momentum coupling between the two phases. The first part of the research deals with bubble-laden turbulent homogeneous shear flow. The aim of this study consists in addressing the modulation of shear turbulence and the bubble clustering geometry in presence of different inter-phase momentum coupling conditions. Suspensions with different combinations of void fraction and Kolmogorov-based Stokes number, in the dilute regime, are studied. Bubbles suppress the turbulent kinetic energy and turbulent dissipation as well. Turbulent modulation occurs via the direct change of the Reynolds shear stress. In fact, the bubble energy source is proved to be negligible in the scale-by-scale turbulent energy budget. The bubble clustering, in agreement with the literature, occurs in the form of thin elongated structures. The clusters are aligned with principal strain direction of the mean flow, as usual in shear flows. The bubble clustering and turbulent modification are strictly related: both increase with the Stokes number and are independent of the void fraction, in the range of parameters considered in our simulations. The data show that the turbulent modification is disadvantaged when the bubble distribution is homogeneous (i.e. small Stokes number). Finally, the small scale bubble clustering is slightly reduced by two-way coupling effects even though the clustering anisotropy still persists at small scales as it occurs for inertial particles. In the next stage of the research, the objective is to study multiphase wall-bounded turbulent flows. Under the same flow rate, the dispersed phase can either reduce, as in bubbly-flows, or increase, as in particles-laden flows, the viscous wall drag. However, it is well acknowledged that bubbles must be large, and deformable, in order to reduce the viscous resistance in wall turbulence. On the other hand it is known that small inertial particles lead to a wall drag increase. Since we are interested on important turbulence modifications, the second part of the research is devoted to particle-laden wall turbulence flows. In this new investigation, the turbulence modulation is addressed in an particle-laden annular pipe flow, via Direct Numerical Simulation (DNS). The alteration of the heat exchange induced by the different turbulent mixing is studied as well. The turbulence modulation induced by small particles is addressed for the first time in the annular geometry, in the context of Direct Numerical Simulations. A wall correction is included in ERPP in order to take into account wall effects in the particle disturbance. The research also focuses on the particle preferential concentration close to the wall, the so-called turbophoresis. The relation between the particle concentration and the friction wall drag and heat exchange modification is explored. The first and second moment statistics, the two-point correlation functions and the energy spectra are studied. The two-way coupled momentum exchange leads up to 30% wall drag increase. The phenomenon is controlled by the particle mass loading and the wall radius ratio R_i/R_o, where R_i is the internal wall radius and R_o the external one. The mechanism leading to the increase of resistance is attributed to the modified Reynolds shear stress. The heaviest suspensions show a drastic modification of the coherent structures by the external wall, although the flow is altered in the whole annular pipe. The TKE significantly increases close the external wall, while it is suppressed close the internal wall. The increase of the heat-exchange, induced by the different turbulent mixing, is small, below 5 %.

In the annular pipe the dispersed phase preferentially migrates toward the external wall. In fact, the internal peak of the particle concentration is up to 100 times lower than the external one. Moreover, the findings suggest that the particle concentration is largely overestimated in the central and internal regions, in the one-way coupling regime (i.e. no turbulence modification). In fact, the particle feedback promotes the turbophoresis of the external wall, while the particle accumulation close the internal side is attenuated.

Contents

Chapter 1

Introduction

Dispersed turbulent multiphase flows consist of a background continuous phase, i.e. a fluid, that transports a discrete phase in the form of small bubbles, droplets or solid particles. When tiny bubbles are immersed in a liquid, e.g. water, the suspension is referred as bubbly flow. On the contrary, when the dispersed phase is made of collections of droplets or solid particles the flow is said to be "particle-laden". The difference between the two classifications, when the suspension is dilute, is the inertia between the dispersed and the carrier phase. Particle-laden and bubbly flows are very common. Microbubble turbulent systems are easily encountered in many natural phenomena and technological applications. Bubbles of diameters of the order of hundreds of micrometers are observed in breaking waves [1, 2], in the wakes of seafaring vessels [3, 4] or after the collision of raindrops in liquid pool [5]. The generation of microbubbles is caused by interface phenomena [6] and can affect the turbulence dynamics [7, 8], the surface reflectance [9, 4] or the acoustic wave propagation [4, 10]. Particle-laden flows are present in many natural and technological fluid dynamical processes as well. In nature, sand and dust storms, rain formation, volcanic ash dispersion in the atmosphere and geological sedimentation processes involve particle-laden flows. In industry, the dispersion of tiny fuel droplets in combustion chambers is crucial for the efficiency of the chemical reactions [11, 12, 13]. Pollutant deposition and dispersion is also a currently popular issue. The prediction of particulate diffusion in the atmosphere can help to abate the effects of climate change and safeguard the public health in urban and industrial areas [14, 15, 16].

Bubbles can be used to reduce the energy dissipation in many hydraulic or maritime applications, due to depletion of viscous drag at the wall. The first evidence of drag reduction was found by McCormick and Bhattacharyya [17], on a fully submersed body of revolution. Later, drag reduction was found in several different configurations, such as flat-plates boundary layers [8, 18, 19], channel flows [20, 21], Taylor-Couette flows [22, 23], or mixing layers [24], see e.g. the review by Elghobashi [25]. The bubble deformation plays an important role in the drag reduction mechanisms [22, 26], when the size of the bubbles is substantially larger than the Kolmogorov length-scale η. In this regime, the gaseous phase alters the turbulent structures even at very small void fraction φ_v as discussed by Prakash et *al.* [7]. The dynamics of large bubbles can be addressed by Direct Numerical Simulations at the price of resolving the bubble interface in the simulation. Different interface-resolved methods, have been used to address the behaviour of deformable bubbles in complex flows see e.g. refs. [27, 28, 29, 30, 31, 32, 33].

The wall bounded turbulence modification due to particles was studied as well in channels [34, 35] [36], round pipes [37, 38, 39] and Taylor-Couette flows [40, 41], and flat plates [42]. In contrast to bubbles, recent works have shown that the effect of tiny heavy particles in wall-bounded turbulence is to increase the friction coefficient [38, 42, 43]. In addition to this, other works suggest that inertial particles increase the heat exchange [36, 44]. Whether the heat exchangers can or cannot benefit of inertial particles is still an open topic.

The present research is focused on the effects of small rigid bubbles and particles on incompressible turbulent flows, employing the Eulerian-Lagrangian approach. The adjective "small" means

that particle Reynolds number is small. Therefore the bubble/particle diameter is smaller, or at least comparable, than the characteristic smallest turbulent length-scale. The dispersed multiphase suspensions are studied in both homogeneous and non-homogeneous turbulence. The presented homogeneous turbulence is a free-space shear flow, which is characterised by large scales anisotropies in the velocity field. The modification of the non-homogeneous turbulence in annular pipes is investigated in the second stage of the research. The objective is to understand whether the dispersed phase and the background flow may influence each other. The mechanisms of the preferential accumulation of the dispersed phase in homogeneous (i.e. the inertial clusterisation) and non-homogeneous (i.e. the turbophoresis) turbulence, affected by the turbulent transport, are investigated as well.

In the present research, given their small size, the bubbles/particles are modelled as collections of points. The dispersed phase interacts with the fluid through a point-wise forcing localised at the current bubble/particle position. The dynamics of such system is strictly connected to the inter-phase momentum exchange between the carrier and the transported phase. The present study explores dilute suspensions (small void fraction φ_v), where the bubble/particle collisions, break up or coalescence have negligible importance [25].

In the past years, the dynamic of pointwise multiphase suspensions, in the one-way coupling regime, has been well understood. In the one-way coupling regime the dispersed phases are transported by the turbulent flow with no chance to modify the background turbulence. In homogeneous turbulence, many important aspects such as bubble/particle dispersion [45, 46], effects of lift force [47], Lagrangian statistics [48], or clustering [49, 50, 51] [52, 53, 54] have been understood. In a turbulent homogeneous flow, bubbles migrates into regions of high vorticity of the flow, and form thin elongated clusters. The bubble clusters are strictly correlated to the most intense coherent vortical structures, the Kolomogorov vortices. In contrast, particles use to escape from these intense vortical structures, concentrating into the high pressure flow regions. This preferential accumulation occurs when the bubble/particle time response τ_p is of the order of the Kolmogorov time-scale τ_η. This phenomenon is called inertial clustering since depends on the different inertia between the dispersed phase and the fluid [55].

In a numerical context, the one-way coupling regime oversimplifies the reality. In fact, the dispersed phase is able to modify the turbulence even at small void fraction [8, 7, 56, 38, 57]. In the so called two-way coupling regime, the bubble/particle back-reaction is taken into account by considering a bidirectional interphase momentum exchange. However, due to the small size of bubbles and particles, the dispersed phase back-reaction field is singular, i.e. is represented by a set of concentrated forces localised at the current bubble position. The Navier-Stokes equations for the carrier phase must be resolved on a computational grid to be amenable of numerical treatment. Many issues arise when a singular field must be resolved on a discrete Eulerian framework. Several methods have been proposed to tackle this issue. The Particle In Cell (PIC) method introduced by Crowe et *al.* [58], undoubtedly represents the easiest approach. However, it lacks of a physically rigorous derivation, and suffers of several shortcomings and numerical biases, as discussed by Boivin et *al.* [59] and Gualtieri et *al.* [60]. These shortcomings can be mitigated when the number of bubbles or particles N_p per computational cell N_c is large. On average, this means $N_p/N_c \gg 1$. This condition, however, limits the range of applicability of the approach. In dilute suspensions (small void fraction), the number of bubbles or particles is fixed by physical conditions and must be set independently on the number of computational cells, which are set by the Reynolds number of the simulation. Additionally, PIC introduces errors when the hydrodynamic force is computed. In fact, the evaluation of this force requires the computation of the unperturbed fields [61], i.e. the velocity and pressure fields in absence of the back-reaction due to the bubble/particle itself. These difficulties call for special numerical procedures for the calculation of the force on the bubble/particle in the two-way coupling regime, as proposed by Horwitz et *al.* [62, 63]. Recently, an alternative approach, namely the Exact Regularised Point-Particle method (ERPP) [64], has been proposed. The method, already employed for the calculation of particle-laden free shear, [57] and wall-bounded flows [38], provides a physically consistent treatment of the singular back-reaction field.In the ERPP approach

the inter-phase momentum coupling occurs via the viscous diffusion of the vorticity generated by the transported phase. This circumstance has a twofold advantage: the disturbance velocity field that each bubble or particle produces on the carrier phase is known in a closed analytical form; the calculation of the hydrodynamic force in the two-way coupling regime can be exploited taking into account the bubble/particle self-disturbance velocity field.

The modulation of homogeneous isotropic turbulence due to point-wise bubbles have been previously investigated via Direct Numerical Simulation with PIC approach by many authors, see e.g. Refs. [47, 65] and references therein. The authors found that bubbles reduce the turbulent dissipation rate by few percentage points. In particular, they found depletion of the turbulent dissipation spectra at large fluid dynamic scales and increase at small scales. Note however, that the relative small number of bubbles per computational cell N_p/N_c, is far below the unity. As previously mentioned, this might introduce artificial numerical effects on the scale of the grid size, leading to unphysical extra dissipation. These issues call for alternative studies for comparisons. Having this in mind, the first part of this research investigates the homogeneous turbulence modification due to small bubbles. Therefore, direct numerical simulations of the bubble transport and turbulence modulation in a two-way coupled homogeneous shear flow are carried out. The ERPP approach is employed, which is able to capture inter-phase momentum coupling effects in a numerically accurate and physically consistent manner. The latter feature sets the present work apart from the previous researches [47, 65]. Several bubble populations, characterised by different combinations of void fraction and Stokes number, are addressed in the range of parameters $\varphi_v \leq 2\%$ (dilute regime) and $St_\eta \leq 0.2$ (small bubbles).

To study of homogeneous turbulence is very useful since it greatly simplifies the understanding of turbulent flows. However, the homogeneity is an idealised condition, only partially achieved in some real cases, like in the centre of channels and pipes. Since the new ERPP approach was applied for the first time on bubbly flows, as first stage, the study of turbulence was devoted to homogeneous flows. Our results from the bubbly homogeneous shear flows are compared with the particle-laden shear flows. The latter was studied by Battista et al. [57] via DNS, using the same model for the inter-phase momentum coupling (i.e. ERPP). After acknowledging that microbubbles can indeed interfere with the homogeneous turbulence, we aim at studying a more realistic fluidynamics problem where important turbulence modification are observed. In the literature it is well-acknowledged that only large deformable bubbles produce drag reduction [66, 67, 68]. On the other hand dilute suspensions ($\varphi_v < 0.1\%$) made of small particles have concrete effects in wall turbulence. In fact recent works [38, 42, 43] show that inertial particles augment the viscous wall resistance. On the other hand, a wide range of works, employing the problematic Particle In Cell method, suggest that particles can lead to wall drag reduction [69, 70]. The over-mentioned issues of PIC cast doubts on the reliability of such investigations, which are in clear disagreement to the physically consistent ERPP [38]. Further studies are required to understand the fluid dynamic phenomena. Besides, a wide range of control parameters comes into play when addressing the wall-bounded turbulence modulation. These parameters are the void fraction, the particle nature, size and shape, the density ratio between the particle and the fluid and the turbulence topology. While, in some conditions, particles seem to lead to drag reduction, in other it occurs the opposite phenomenon. The reader is referred to the recent review of Brandtl & Coletti [71] for additional details.

The effects of tiny heavy particles are investigated in turbulent heated annular pipe flows. The periodic annular pipe is a model of the concentric tube heat exchanger. The system is made of the annulus between two concentric cylinders, through which the suspension flows. So far, the turbulent annular pipe has been studied only as a single phase flow [72, 73, 74, 75, 76] , and the role of an additional discrete phase has been never investigated. The opposite wall curvatures in the annular pipe might affect the turbophoresis. The turbopheresis is the preferential concentration phenomenon of the dispersed phase, which in wall-bounded flow tends to migrate toward the walls. The turbopheresis has a crucial impact to the wall drag modification, since the particles massively interact with the near wall coherent structures.

In contrast to round pipes, the flow field in the annular pipes is highly asymmetric. Therefore, the characteristic length-scale of the near-wall vortical structures varies between the convex and concave side. The asymmetry is function of the distance between the two walls, and reduces when the walls are closer [77, 78, 76, 73] . In particular, the peak of the turbulent kinetic energy in the buffer layer is smaller at the internal side, than the external onw [79, 73, 72]. Similarly, the viscous wall stress at the internal wall is larger than the external one. Moreover the peak of mean velocity, instead of being central, is into the inner half of the pipe.

In such complex turbulent flow, a heavy but dispersed phase is present. The two-way interphase coupling is enforced on the momentum exchange, while the particles are thermally inert. The influence of the dispersed phase on the heat exchange, due to the change in the turbulent mixing, is addressed. The modification of the viscous wall drag is studied as well. The role of the wall curvature is explored in four different annular pipes, with different size of the internal cylinder. The effects of the particle mass loading Φ_p of the suspension are investigated as well. The viscous time-scale based Stokes number is constant in the two-way coupling regime. The Stokes number is selected from the one-way coupled simulations, where there is the most intense turbophoresis. The analysis in the one-way coupling regime is conducted as comparison, and show analogies with the literature.

The thesis is organised as follows: chapter §2 verbosely reports the theoretical framework of the research. The Exact Regularised Point Particle (ERPP) method and the bubble/particle momentum equation are derived and discussed in details. Chapter §3 introduces and provides the results of the two-way coupled simulations of homogeneous turbulent bubble-laden shear flow by presenting single point Eulerian statistics, energy spectra and the bubble clustering discussed in terms of the Angular Distribution Function. Chapter §4 introduces and provides the results of the one-way and two-way coupled simulations of the turbulent particle-laden annular pipe. The first and second moement statistics, the two-point correlation functions and the turbulent spectra are presented and discussed. The flow rate and the heat exchange are reported as function of the internal wall radius R_i. The particle preferential concentration, mean velocities and velocity variances are reported as well, and related to the fluid statistic. Finally chapter §5 summarises the main results and provides the conclusions of the numerical experiments.

Chapter 2

Theoretical framework

2.1 The point-particle dispersed multiphase system

The multiphase system is made of a turbulent carrier flow laden with small dispersed particles. Here the word "particle" is generically adopted and may refer to either a small bubble or a inertial particle. The adjective "small" refers to a comparison with the fluid lengthscale. In other words, we are studying particles whose diameter d_p is smaller than the smallest fluid dynamic lengthscale.

The dilute suspension allows to discard the particle-to-particle interactions, since they rarely happen. However we want to remark that this does not mean that particles can't influence each other. In fact only direct interactions, such as collisions, coalescence or break up, are irrelevant for the dynamic of the multiphase system, but a single particle can still experience the fluid perturbation induced by other ones.

Due to their small size, the particles are modelled as rigid spheres. This might seem unrealistic for bubbles. However, the deformability of a small bubble is controlled by the viscous forces and the surface tension γ_t. While the viscous forces tend to deform the bubble, the surface tension tries to preserve the spherical shape. When the surface tension is enough stronger than the viscous forces, the bubble remains spherical. This effect is measured by the Capillary number $Ca = \frac{\mu|v-u|_{ref}}{\gamma_t}$, that indeed compares the viscous forces to the surface tension. In the present study we are going to study only suspensions whose Capillary number is very small. This allows to model even bubbles as rigid spheres. For more details see the discussion in section 3.

The particle Reynolds number is $Re_p = \frac{|v-u|_{ref} d_p}{\nu}$, where $|v-u|_{ref}$ is the reference relative velocity and ν is the kinematic viscosity. Re_p describes how the flow field behaves around the particle, and it has a crucial role to assess the hydrodynamic force acting on the particle. In the small particle regime Re_p is vanishing. Hence the flow field on the particle scale is governed by the Stokes equations. On the fluid scale, what we see is a collection of points that are transported through the turbulent field. The fluid in turn experiences a globally dispersed but locally concentrated forcing due to the particles. We will show in the next sections that the equivalent governing equations, where the particle boundary are replaced by a singular forcing, are derived in the low-Re_p regime. This avoids the extreme computational effort necessary to capture the fluid dynamic motions on the particle sub-scale, filtered away in the equivalent model. The price of this operation is to resolve a singular forcing over the computational grid. This procedure requires special care, in order to avoid numerical biases.

In the present research we employ the Exact-Regularised Point Particle (ERPP) method to achieve the momentum coupling between the fluid and the dispersed phases. In the forthcoming sections we will provide the physical description of the multiphase system. We will describe in details the regularisation procedure of ERPP, that is performed introducing the time-scale ϵ_R. We will discuss the physical interpretation of ϵ_R as the viscous time diffusion of the particle disturbance, in terms of vorticity. We will show that the point-wise particle indeed introduces a singular vorticity at present time, but the singularity is rapidly dissipated by viscosity. Only when the particle distur-

bance diffuses up to the smallest relevant scales of the fluid dynamics, after the time ϵ_R, this effect becomes important for the turbulence. Following a lengthy but rigorous mathematical procedure, we will show how an equivalent regularised governing equation can be consistently derived, when ϵ_R and Re_p are small.

The algorithm evolves the solution from time t to time $t + dt$. The history of the motion from a reference state $t = 0$ to the current time t is known. The observation time must be sufficiently large, such that we can define the regularising parameter in the range $0 < \epsilon_R < t_n$. This concept will be crucial when we exploit the additivity property to split a time integral representation through the time scale ϵ_R.

We will firstly address the mathematical procedures used to derive the momentum coupling model in the free-space domain $\mathcal{D} = \mathbb{R}^3$. In this first stage, we willl assume that the particles are sufficiently far from the walls. The possibility of including wall effects in the model will be discussed in a later section.

2.2 The Exact Regularised Point Particle method in the free-space

Let's consider the multiphase system made of a carrier fluid laden with the N_p set of rigid spherical particles. The dispersed phase occupies the domain $\Omega = \cup_p \Omega_p$, where Ω_p is the domain of the p-th particle and $\cup_p$ is the union operator between the N_p set of particles. The fluid domain is $\mathbb{R}^3/\Omega$, where $\mathbb{R}^3$ is the free-space domain and the notation A/B denotes the complement of A with respect to B.

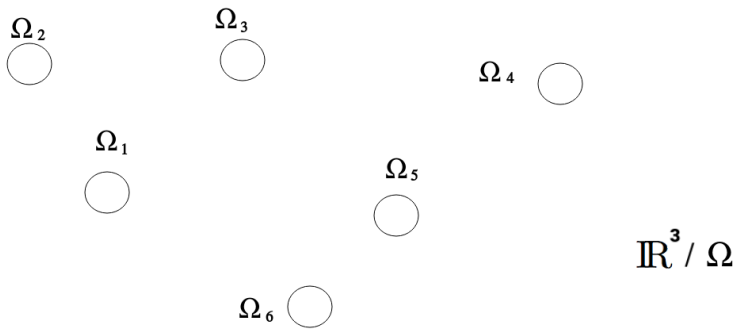

Figure 2.1: Sketch of the domain of the multiphase system. $\Omega = \cup_p \Omega_p$ is the domain of the overall dispersed phase , $\mathbb{R}^3/\Omega$ is the domain of the fluid.

The fluid dynamics is prescribed by the standard incompressible Navier-Stokes equations (2.1), embedded with the proper boundary and initial conditions.

$$\begin{cases} x \in \mathbb{R}^3 \backslash \Omega(t) \begin{cases} \rho_f \frac{Du}{Dt} = \rho_f g - \nabla p + \mu \nabla^2 u \\ \nabla \cdot u = 0 \end{cases} \\ \lim\limits_{|x| \to +\infty} u(x,t) = 0 \\ u(x,t)|_{\partial\Omega_p(t)} = V_p(x,t)|_{\partial\Omega_p(t)} \quad for \quad p = 1, 2, ..., N_p \\ u(x,0) = u_0(x) \end{cases} \tag{2.1}$$

The closure of the problem is provided by the momentum equation of the rigid particles, that must be coupled with the Navier-Stokes equations. The solution is evolved, from the initial condition

$u_0(x)$, in the free-space $\mathbb{R}^3$. The no-slip boundary conditions are enforced over the particle boundary. Hence, the fluid and particle velocity $u(x,t)|_{\partial\Omega_p(t)}$ and $V_p(x,t)|_{\partial\Omega_p(t)}$, where $\partial\Omega_p(t)$ is the particle boundary, are equal. The particle velocity obeys the kinematic law of the rigid bodies, $V_p(x,t) = V_p^C(t) + \omega(t) \times \mathbf{r_p}$. In the adopted notation, V_p^C is the velocity of the particle centroid $x_p(t)$, ω is its angular velocity and $\mathbf{r_p}$ is the distance between a particle surface element and $x_p(t)$.

The inter-phase momentum coupling occurs via the boundary conditions over the particle boundary. The velocity conditions on the particle surface locally deforms the flow field. In the attempt to restore the equilibrium, the fluid reacts with a stress field. Exerted on the particle surface, these stresses give rise to the hydrodynamic force.

The system (2.1) provides the complete description of the dynamic of the carrier phase. In principle we could solve the equations as they were presented, once resolving the particle boundary over the computational grid. However in the low-Re_p limit, the particle size is smaller than the smallest hydrodynamic lengthscale. In the context of homogeneous turbulence this means $d_p << \eta$, where η is the Kolmogorov lengthscale. Hence the grid should be finer than what the turbulence constraints, already computationally demanding, prescribe. Moreover, due to the small particle size, dilute suspensions can transport even millions of particles. Unfortunately, for the objectives of this research, the simulations would be unfeasible under the current computational resources. For this reason, a model of the inter-phase momentum coupling is required.

To this end, in the Exact-Regularised Point Particle approach the velocity field $u(x,t)$ is additively split into the fields $w(x,t)$ and $v(x,t)$. The field $w(x,t)$ can be explained as the background turbulent field, in the absence of the dispersed phase, and it will be referred to as the background or unperturbed field. The physical meaning of $v(x,t)$ is instead the fluid dyanmic disturbance induced by the dispersed phase, in a still fluid.

The field $w(x,t)$ obeys the equations

$$\begin{cases} \rho_f \left(\frac{\partial w}{\partial t} + F\right) = \rho_f g - \nabla p_w + \mu \nabla^2 w \\ \nabla \cdot w = 0 \qquad\qquad\qquad\qquad\qquad\qquad x \in \mathbb{R}^3 \\ \lim_{|x|\to+\infty} u(x,t) = 0 \\ w(x,0) = u_0(x) \end{cases} \tag{2.2}$$

The field $w(x,t)$ is prolonged into the particle volume, and is defined into the domain $\mathbb{R}^3$. The term F(x,t) contains all the non-linearity of the complete field $u(x,t)$, and must be interpreted as a forcing term for the field $w(x,t)$. $F(x,t)$ is prolonged using the particle velocity inside the particle domain, and its expression reads

$$F = \begin{cases} \rho_f u \cdot \nabla u \ , & for \ \ x \in D \backslash \Omega(t), \\ \rho_f V_p \cdot \nabla V_p \ , & for \ \ x \in \Omega(t). \end{cases} \tag{2.3}$$

We remark that any prolongation of $F(x,t)$ would be possible for the purpose of the algorithm, that is the solution $u(x,t)$. In fact, a different prolongation would affect the fields w and v, but not their sum, which would be unchanged. The initial condition of $w(x,t)$ is $u_0(x)$. This will be important since it leaves to $v(x,t)$ the homogeneous null initial condition. The free-space conditions remains the same.

Notice that the particle boundary conditions disappear from the field $w(x,t)$. Apart from the prolongation of $F(x,t)$, the dispersed phase in not present in $w(x,t)$. This is why $w(x,t)$ is referred to as the unperturbed or background turbulent field.

The inter-phase boundary are reintroduced into the equations of the perturbation field $v(x,t)$. The evolution of $v(x,t)$ is controlled by the linear Stokes equations over the domain $\mathbb{R}^3/\Omega(t)$, with initial homogeneous conditions.

$$\begin{cases} x \in \mathbb{R}^3 \backslash \Omega(t) \begin{cases} \nabla \cdot v = 0 \\ \rho_f \frac{\partial v}{\partial t} = -\nabla p_v + \mu \nabla^2 v \end{cases} \\ v(x,0) = 0 \\ v|_{\partial\Omega_p(t)} = V_p - w|_{\partial\Omega(t)} \quad for\ p = 1,2,...,N_p \end{cases} \tag{2.4}$$

The systems (2.4) and (2.2) cannot be independently advanced in time. In fact the two solutions w and v are strictly interconnected. The field w influences v through the particle boundary conditions. In turn v affects w due to the non-linear forcing term F. Since the field that is evolved by the algorithm is u, the interdependence between v and w won't be a problem. In fact, our purpose is to exploit the decomposition of the flow field to manipulate the equations of the particle disturbance. This procedure can be divided into two steps: first, to derive the point-particle model of the multiphase suspension, and second, to regularise the obtained singular system within a physically consistent framework. The Navier-Stokes equations of the complete field will be finally reassembled into this new regularised form, that will be solved by standard numerical codes.

In the present manipulation, the initial conditions with along the non-linear behaviour of $u(x,t)$ are assigned to the unperturbed field. This is a crucial point since allows to exploit the analytical solution of the corresponding unsteady Stokes equations. In fact, the solution of the particle disturbance, equation (2.5), is expressed in terms of the third order stress tensor $\mathbf{T}_{ikj}(x-\psi, t-\tau)$ and the unsteady Stokeslet $\mathbf{G}_{ij}(x-\psi, t-\tau)$, for the detailed calculation see F.5.

$$v_i(x,t) = \int_0^t d\tau \int_{\partial\Omega} t_j(\psi,\tau)\mathbf{G}_{ij}(x-\psi,t-\tau) - v_k(\psi,\tau)\mathbf{T}_{ikj}(x-\psi,t-\tau)n_j(\psi)dS_\psi \tag{2.5}$$

The second order tensor $\mathbf{G}_{ij}$ can be seen as the i-th fluid velocity component of the Stokes problem of known term the j-aligned impulse $\delta(t-\tau)\delta(x-\psi)$, centred at position ψ and time τ. The third order tensor $\mathbf{T}_{ikj}(x-\psi,t-\tau)n_j(\psi)n_k$ represents the stress tensor of the associated flow field. Further details are provided in F.3.

In equation (2.5) $t_j(\psi,\tau)$ is the fluid stress over the particle surface. t_j can be determined by solving the boundary integral equation, i.e. the system of the boundary integral equations (2.5) for the velocity $v(x,t)$ over each particle boundary. Then, the stress $t_j(\psi,\tau)$ can be integrated over the particle surface to obtain the hydrodynamic force, or added into the (2.5) to compute the velocity $v(x,t)$.

The resolution of the boundary integral representation is a lengthy and computationally demanding operation. However, in the small Re_p regime particles are smaller than the turbulent lengthscales. Therefore, it is easier to compute the solution (2.5) as the multipole expansion in the limit $|x_p - \psi| = d_p \to 0$. The equivalent expression of $v(x,t)$ can be readily derived, and reads

$$\begin{aligned} v_i(x,t) &= \int_0^t d\tau \int_{\partial\Omega} \left\{ t_j(\psi,\tau)[\mathbf{G}_{ij}(x-x_p,t-\tau) + o(|x_p-\psi|)] - \right. \\ &\left. [\hat{v}_p(t) + \omega_p \times (\psi - x_p)][\mathbf{T}_{ikj}(x-x_p,t-\tau) + o(|x_p-\psi|)n_j(\psi) \right\} dS_\psi = \\ &= \int_0^t d\tau \left\{ -\sum_p D_{j_p}(\tau)\mathbf{G}_{ij}(x-x_p,t-\tau) + o(|x_p-\psi|) \right\} = \\ &= -\sum_p \int_0^t D_{j_p}(\tau)\mathbf{G}_{ij}(x-x_p,t-\tau)d\tau + t\ o(|x_p-\psi|) \end{aligned} \tag{2.6}$$

where $D_{j_p}(\tau)$ is the hydrodynamic force, j-direction, to the p-th particle. Apart from the vanishing terms proportional to d_p, the particle disturbance is now only determined by the Stokeslet Tensor $\mathbf{G}$ and the hydrodynamic force D_p. Hence, in the limit $|x_p - \psi| = d_p \to 0$, the dispersed phase is modelled as the set of points where the concentrated forces D_p are applied to. Provided that we can somehow compute D^p, the relation (2.6) does not require any evaluation of the flow field in the vicinity of the particle surface. This intuition lets us think that the velocity

$v(x,t) = -\sum_p \int_0^t D_{j_p}(\tau)\mathbf{G}_{ij}(x-x_p, t-\tau)d\tau$ could be the solution of a Stokes equation over the simply connected domain $\mathbb{R}^3$. In fact, (2.6) is the exact solution of the following singular unsteady Stokes equation, whose extended calculation is provided in F.4,

$$\begin{cases} \rho_f \frac{\partial v}{\partial t} = -\nabla p_v + \mu\nabla^2 v - \sum_p D_p(t)\delta(x - x_p(t)) & x \in \mathbb{R}^3 \\ \nabla \cdot v = 0 \\ v(x,0) = 0. \end{cases} \tag{2.7}$$

In this new formulation the particle boundaries are replaced by a singular force, where δ is the Dirac delta function, centred at particle position $x_p(t)$ and of module $D_p(t)$. Once the equation (2.7) is reassembled to the (2.2), the resulting system provides the point-particle equivalent model of the multiphase system. Since the Dirac delta function is clearly unbounded, equations (2.7) still need additional treatments in order to be used by standard numerical codes.

Due to the linearity of the equations, hereafter we shall consider the forcing from a single particle. The final superimposition will return the solution of the whole system.

The particle disturbance can be represented in terms of the vorticity $\zeta = \nabla \times v$. The expression of $\zeta(x,t)$ can be extracted by either taking the curl of the (2.6) or by solving its singular evolution equation (2.8). In this discussion we favour the second path.

The equation of the vorticity $\zeta(x,t)$ induced by one particle is derived by taking the curl of equations (2.7), and reads

$$\begin{cases} \rho_f \frac{\partial \zeta}{\partial t} = \nu\nabla^2\zeta + D(t) \times \nabla\delta(x - x_p) \\ \zeta(x,0) = 0 \end{cases} \tag{2.8}$$

Due to the linearity, the solution is expressed as the time convolution of the hydrodynamic force and the Gaussian function $g(x - x_p, t - \tau)$ of variance $\sigma(t - \tau) = \sqrt{2\nu(t - \tau)}$, see section F.3 for additional details, namely

$$\zeta(x,t) = \frac{1}{\rho_f} \int_0^{t^+} D_p(\tau) \times \nabla g(x - x_p, t - \tau)d\tau \tag{2.9}$$

The gaussian function $g(x - x_p, t - \tau)$ is interpreted as the fundamental solution of the singularly scalar diffusion equation discussed in F.1.

t^+ denotes the right-sided limit of $\tau \to t$. Hence the integral passes through a singularity in the neighbourhood of $\tau = t$, where the gaussian tends to the Dirac delta function. We will explain in the next section how to remove the singularity, via a physical consistent procedure.

2.3 Regularisation procedure through the time-scale ϵ_R

The regularisation procedure used to extract the regular part from the vorticity ζ and the velocity v is now addressed. To this end, we define the regularisation parameter $\epsilon_R > 0$, whose dimension is time. Hence, we exploit the additive property of the integral to split $\zeta(x,t)$ into the singular $\zeta_S(x,t)$ and regular $\zeta_R(x,t)$ component, namely

$$\zeta_R(x,t) = \frac{1}{\rho_f} \int_0^{t-\epsilon_R} D_p(\tau) \times \nabla g(x - x_p(\tau), t - \tau)d\tau \tag{2.10}$$

$$\zeta_S(x,t) = \frac{1}{\rho_f} \int_{t-\epsilon_R}^{t^+} D_p(\tau) \times \nabla g(x - x_p(\tau), t - \tau)d\tau \tag{2.11}$$

The original field ζ is reconstructed simply as the sum of the two components,

$$\zeta(x,t) = \zeta_R(x,t,\epsilon_R) + \zeta_S(x,t,\epsilon_R) \tag{2.12}$$

The implicit assumption is that the observation time t is sufficiently large, such that $t - \epsilon_R$ is positive. This is always possible since the initial condition $t = 0$ is, at this step of the discussion, purely arbitrary. We just have to go back to the instant in the history of the motion that is earlier than $t - \epsilon_R$.

We observe that the function ζ_R is everywhere smooth, since the Gaussian function inside the convolution (2.10) has positive variance $\sigma(t-\tau) > \sigma_R = \sqrt{2\nu\epsilon_R}$. The singularity is entirely contained into ζ_S for any non-null ϵ_R. In fact, the neighbourhood of the point $\tau = t$ is included into the integral (2.11).

$$g(x - x_p, t - \tau^*) = \int_{\mathbb{R}^3} g(\psi - x_p, \hat{\tau} - \tau^*) g(x - \psi, t - \hat{\tau}) d^3\psi \tag{2.13}$$

From a physics point of view, the regularised vorticity can be interpreted as the free diffusion of the field $\zeta(x, t - \epsilon_R)$ from time $t - \epsilon_R$ to time t. This can be shown by exploiting the semi-group property (2.13), namely

$$\begin{aligned}
\zeta_R(x,t) &= \frac{1}{\rho_f} \int_0^{t-\epsilon_R} D_p(\tau^*) \times \nabla g(x - x_p, t - \tau^*) d\tau^* = \\
&= -\frac{1}{\rho_f} \int_0^{t-\epsilon_R} D_p(\tau^*) \times \nabla_{x_p} \int_{\mathbb{R}^3} g(\psi - x_p, t - \epsilon_R - \tau^*) g(x - \psi, \epsilon_R) d^3\psi d\tau^* = \\
&= \int_{\mathbb{R}^3} \left\{ \frac{1}{\rho_f} \int_0^{t-\epsilon_R} D_p(\tau^*) \times \nabla_\psi g(\psi - x_p, t - \epsilon_R - \tau^*) d\tau^* \right\} g(x - \psi, \epsilon_R) d^3\psi \\
&= \int_{\mathbb{R}^3} \zeta(\psi, t - \epsilon_R) g(x - \psi, \epsilon_R) d^3\psi
\end{aligned} \tag{2.14}$$

where ∇_{x_p} and ∇_ψ are the nabla operator with respect to the coordinates x_p and ψ. The result obatined in (2.14) is the exact solution of the free-diffusion problem, verbosely discussed in F.2, that is exactly what we wanted to prove.

The regularised vorticity field $\zeta_R(x,t)$, whose smallest scale is $\sigma_R = \sqrt{2\nu\epsilon_R}$, obeys the unsteady stokes equations where the Stokes drag is evaluated at the earlier time $t - \epsilon_R$.

$$\frac{\partial \zeta_R}{\partial t} = \nu \nabla^2 \zeta_R + \frac{1}{\rho_f} D_p(t - \epsilon_R) \times \nabla g(x - x_p(t - \epsilon_R), \epsilon_R) \ , \quad \zeta_R(x, 0) = 0 \quad x \in \mathbb{R}^3 \tag{2.15}$$

We can add the expression (2.10) into the equation (2.15) and verify that the operation returns the identity.

The solenoidal field $v_R(x,t)$ can be computed once known its vorticity, through decomposition

$$v_R(x,t) = v_{R_\zeta}(x,t) + \nabla \Phi_R(x,t) \tag{2.16}$$

where the expression of $v_{R_\zeta}(x,t)$ reads

$$v_{R_\zeta}(x,t) = -\frac{1}{\rho_f} \int_0^{t-\epsilon_R} D_p(\tau) g(x - x_p(\tau), t - \tau) d\tau \tag{2.17}$$

The field $v_{R_\zeta}(x,t)$, referred to as the pseudo-velocity, does not satisfy the incompressible continuity equation, but its curl returns the vorticity $\zeta_R(x,t)$. The zero-divergence constraint of $v_R(x,t)$ is provided thanks to the potential flow $\nabla\Phi_R(x,t)$, also referred to as the potential correction. The potential field Φ_R is computed by solving the free space Laplace problem $\nabla^2\Phi_R + \nabla \cdot v_{R_\zeta} = 0$.

In analogy with the solution of equation (2.15), the expression (2.17) is the solution of the partial differential equations

$$\frac{\partial v_{R_\zeta}}{\partial t} = \nu \nabla^2 v_{R_\zeta} - \frac{1}{\rho_f} D_p(t - \epsilon_R) g(x - x_p(t - \epsilon_R), \epsilon_R) \ , \quad v_{R_\zeta}(x, 0) = 0 \quad x \in \mathbb{R}^3 \tag{2.18}$$

By using the definition (2.16) into the previous equation (2.18) we compute the momentum equation corresponding to the regular velocity $v_R(x,t)$

$$\begin{cases} \frac{\partial v_R}{\partial t} = -\frac{1}{\rho_f}\nabla p_R + \nu\nabla^2 v_R - \frac{1}{\rho_f} D_p(t-\epsilon_R) g(x - x_p(t-\epsilon_R), \epsilon_R) & x \in \mathbb{R}^3 \\ \nabla \cdot v_R = 0 \\ v_R(x,0) = 0 \end{cases} \tag{2.19}$$

$$p_R(x,t) = -\frac{\partial \Phi_R}{\partial t}(x,t) + \nu\nabla^2\Phi_R(x,t)$$

The scalar p_R is function of the potential Φ_R, but the relationship is inessential while solving the system in bracket. In fact p_R is computed from the elliptic equation derived by taking the divergence of the momentum equation in (2.19). In this sense, p_R has the role of the regularised hydrodynamic pressure of the velocity field v_R. The singular forcing is replaced by the retarded Gaussian shaped term that appears in the right hand side of the momentum equation in the (2.19). The equation (2.19) can be solved in any numerical code, provided that the spatial scale σ_R of the regular forcing is resolved over the computational grid.

Under the present manipulation, the particle disturbance $v(x,t)$, whose expression is given by the (2.6), has been additively decomposed into the fields $v_R(x,t)$ (2.20) and $v_S(x,t)$ (2.21), that is $v(x,t) = v_R(x,t) + v_S(x,t)$.

$$v_R(x,t) = -\frac{1}{\rho_f}\int_0^{t-\epsilon_R} \mathbf{G}(x - x_p(\tau), t-\tau) \cdot D_p(\tau) d\tau \tag{2.20}$$

$$v_S(x,t) = -\frac{1}{\rho_f}\int_{t-\epsilon_R}^{t^+} \mathbf{G}(x - x_p(\tau), t-\tau) \cdot D_p(\tau) d\tau \tag{2.21}$$

Similar to the vorticity $\zeta_R(x,t)$, the velocity $v_R(x,t)$ (2.20) is the analytical solution of the equations (2.19), and it corresponds to the free-diffusion of the field $v(x, t-\epsilon_R)$ to time t.

In ERPP we will solve only the diffused field $v_R(x,t)$, by means of the equation (2.19), while the singular velocity $v_S(x,t)$ is discarded. The operation obviously results in a numerical error. In the next sections we will estimate the order of magnitude of such error. Then, we will show how, by properly choosing the time scale ϵ_R, the singular field can be safely removed from the computation.

2.4 Estimate of the singular part of the particle disturbance

In this section we report the estimate of the singular fields v_S ζ_S, in the vanishing limit of Re_p and ϵ_R. Due to the very high velocity gradients in the unbounded region, the dissipation is locally very strong. Thus, the singular perturbations introduced at time t will be rapidly regularised by viscosity after the vanishing time ϵ_R. This physical phenomenon is described by the additively decompositions, i.e. equation (2.12) for the vorticity. The separation scale between the vorticity ζ_R and ζ_S is the gaussian variance σ_R. If σ_R is the smallest scales for ζ_R, it is the largest for ζ_S. Hence we expect to prove that the singular fields, even if unbounded close to x_p, affect a restricted portion of space whose size is modulated by ϵ_R. For this purpose, we have to estimate the far-field component of the particle disturbance $v_S(x,t)$. Similar to what we have done in the former section, the field $v_S(x,t)$ can be decomposed into the potential flow $\nabla\Phi_S(x,t)$ and the pseudo-velocity $v_{S_\zeta}(x,t)$.

$$v_S(x,t) = v_{S_\zeta}(x,t) + \nabla\Phi_S(x,t) \tag{2.22}$$

The pseudo-velocity is $v_{S_\zeta}(x,t) = -\frac{1}{\rho_f}\int_{t-\epsilon_R}^{t^+} D_p(\tau) g(x - x_p(\tau), t-\tau) d\tau$, and is defined such that its curl returns the vorticity of the field singular field $v_s(x,t)$, namely $\zeta_S(x,t) = \nabla \times v_{S_\zeta}$. The divergence constraint, imposed by the continuity equation of $v_S(x,t)$, is satisfied by the potential correction. Before the projection of v_{S_ζ} over the solenoidal vector field, the potential Φ_S must be obtained by solving the following free-space Laplace problem

$$\nabla^2\Phi_S(x,t) = -\frac{1}{\rho_f}\int_{t-\epsilon_R}^{t^+} D_p(\tau)\cdot\nabla g(x-x_p(\tau),t-\tau)d\tau, \quad x\in\mathbb{R}^3 \tag{2.23}$$

In order to compute the far-field asymptotic estimate of v_S we need to evaluate the behaviour of both the pseudo-velocity v_{S_ζ} and the potential flow $\nabla\Phi_S$. While the pseudo-velocity is exponentially decaying in space, it is less evident how much fast $\nabla\Phi_S$ approaches the far-field.

The solution of this problem is provided by solving the Laplace problem (2.23). Due to the linearity, again, the solution is in the form $\Phi_S(x,t) = -\frac{1}{\rho_f}\int_{t-\epsilon_R}^{t^+} D_p(\tau)\cdot\nabla G(x-x_p(\tau),t-\tau)d\tau$, where $G(x-x_p(\tau),t-\tau)$ is the solution of the Laplace problem

$$\nabla^2 G(x-x_p(\tau),t-\tau) = g(x-x_p(\tau),t-\tau), \quad x\in\mathbb{R}^3 \tag{2.24}$$

$g(x-x_p(\tau),t-\tau)$ is the Gaussian function centred at position $x_p(\tau)$ of variance $\sigma=\sqrt{2\nu(t-\tau)}$. The solution of the Laplace problem (2.24) is easily computed, see the detailed calculation in F.4, and reads

$$G(r,t-\tau) = -\frac{1}{4\pi r}erf\left(\frac{r}{\sqrt{2}\sigma(t-\tau)}\right) \tag{2.25}$$

where $r=\sqrt{(x-x_p)\cdot(x-x_p)}$, and $erf(\eta)=\frac{2}{\sqrt{\pi}}\int_0^\eta e^{-t^2}dt$ is the Gauss error function. The function $G(r,t-\tau)$ is spatially isotropic, that is, it depends only on r. This is straightforward if we consider that G is derived by the free-space Laplace problem whose known term is the Gaussian function, indeed isotropic around its centre $x_p(\tau)$. The far-field contribution of the second order tensor $\nabla\otimes\nabla G(r,t-\tau)$ is computed from equation (2.25), and reads

$$\nabla\otimes\nabla G(r,t-\tau) \sim \ \mathrm{I}\frac{1}{4\pi r^3(\tau)} - \hat{r}(\tau)\otimes\hat{r}(\tau)\frac{3}{4\pi r^3(\tau)}\ , \quad r\to+\infty \tag{2.26}$$

With usual notation $\mathbf{I}$ is the identity matrix and the unit vector $\hat{r}=\frac{x-x_p(\tau)}{r}$. If we want to estimate the integral in (2.24), we have to remark that the distance r and the unit vector $\hat{r}$ are functions of time τ , since the particle is moving in the time interval $t-\epsilon_R\le\tau<t^+$. Thus, to evaluate the potential correction, we extract the upper bound of $|D_p(\tau)|$ and $1/r^3(\tau)$ over the considered temporal interval. If we then observe that $\sqrt{1+3\left(\frac{D_p(\tau)\cdot\hat{r}}{|D_p(\tau)|}\right)^2}\le 2$, we readily obtain

$$\begin{aligned}|\nabla\Phi_S| =& \frac{1}{\rho_f}\int_{t-\epsilon_R}^{t^+}\left|\frac{D_p(\tau)}{4\pi r^3} - D_p(\tau)\cdot\hat{r}\frac{3}{4\pi r^3}\hat{r}\right|d\tau = \\ =& \frac{1}{\rho_f}\int_{t-\epsilon_R}^{t^+}\frac{|D_p(\tau)|}{4\pi r^3}\sqrt{1+3\left(\frac{D_p(\tau)\cdot\hat{r}}{|D_p(\tau)|}\right)^2}d\tau \le \sup_{\beta\in[t-\epsilon_R,t^+)}\frac{\epsilon_R|D_p(\beta)|}{2\pi r^3(\beta)\rho_f}\end{aligned} \tag{2.27}$$

Equation 2.27 provides the far-field contribution of the singular projected velocity Φ_S. Since the singular-pseudo velocity is exponentially decaying, $\nabla\Phi_S$ is the dominant component far from the particle. It is convenient to write the expression (2.27) in the dimensionless form over the particle scale. The dimensional variables are measured with respect to the particle diameter d_p, the relative velocity $|u-v_p|_{ref}$, and the forces to $\rho_p d_p^2|u-v_p|^2$, where ρ_p is the particle density. We remind that the particle Reynolds number is $Re_p = d_p|u-v_p|_{ref}/\nu$, while $\epsilon_R=\frac{\sigma_R^2}{\nu}$. If the dimensionless variables are denoted with the tilde, the particle disturbance $\widetilde{\nabla\Phi}_S(x,t) = v_S(x,t)/|u-v_p|_{ref}$ is recast into the following equation

$$\widetilde{\nabla\Phi}_S(x,t) \le \frac{\rho_p}{\rho_f}\widetilde{\epsilon_R}Re_p\sup_{\beta\in[t-\epsilon_R,t^+)}\frac{|\widetilde{D}_p(\beta)|}{2\pi\widetilde{r}^3(\beta)} \tag{2.28}$$

The equation (2.28) provides the estimate of the algorithm error. Such error is vanishing when Re_p and $\widetilde{\epsilon_R}$ are small. Hence, far from the particle, that is for large $\widetilde{r}$, the disturbance $v_S(x,t)$ decays as $\widetilde{\epsilon_R} Re_p/\widetilde{r}^3$. The singular velocity v_S is clearly unbounded close to the particle. However, as far as the smallest resolved scale σ_R of the regular velocity v_R is larger than the smallest hydrodynamic lengthscale Δ, the singular near-field contribution will be unessential. Therefore the singular velocity $v_S(x,t)$ is neglected in the present algorithm, while advancing the solution of one time step. However the reader must notice that $v_S(x,t)$ is not entirely discarded. In fact its effect is reintroduced at a later time in the regular field v_R, as soon as v_S diffuses to the resolved scale σ_R. This is a crucial point since it avoids the accumulation of numerical errors while advancing the solution.

In the next section the original field $u(x,t)$ is reassembled under the present regularised form. The convective terms of the singular field will be proved to be negligible while observing the flow field from the relevant hydrodynamic lengthscale.

2.5 Reassemble of the original regularised field

In this section we reconstruct the complete regularised field $u_R(x,t)$, by reassembling the fluid decomposition $u_R(x,t) = w(x,t)+v_R(x,t)$. As reported in the previous section, the singular disturbance $v_S(x,t)$ is discarded when we observe the far-field hydrodynamic scales. This procedure leads to a regularised Navier-Stokes equations which are amenable to numerical treatment.

After reassembling the unperturbed field $w(x,t)$ with the regularised particle disturbance $v_R(x,t)$, the governing equations of $u_R(x,t)$ can be written as

$$\begin{cases} \frac{\partial u_R}{\partial t} + u_R \cdot \nabla u_R + \{v_S \cdot \nabla u_R + u_R \cdot \nabla v_S + v_s \cdot \nabla v_s\} = -\frac{1}{\rho_f}\nabla p + \nu \nabla^2 u_R + f(x,t) + g \\ f(x,t) = \frac{1}{\rho_f}\sum_p^{N_p} \left\{ m_f \left(\left.\frac{Du_{(0)}}{Dt}\right|_p (t-\epsilon_R) - g \right) - D_p(t-\epsilon_R) \right\} g[x - x_p(t-\epsilon_R), \epsilon_R] \\ \nabla \cdot u_R = 0 \\ \lim_{|x|\to+\infty} u_R(x,t) = 0 \qquad\qquad x \in \mathbb{R}^3 \\ u(x,0) = u_0(x) \end{cases} \tag{2.29}$$

The first important consideration is that the hydrodynamic force acting on the fluid, according to the system (2.29), is not opposite to the force acting on the particle. In fact, the fluid unperturbed acceleration $\left.\frac{Du_{(0)}}{Dt}\right|_p m_f$ and gravitational force $m_f g$ acting into the p-th particle volume is added into the back-reaction term, where the displaced fluid mass is $m_f = \frac{\pi d_p^3}{6}\rho_f$ [80, 81]. The unperturbed velocity field labelled by the subscript (0), corresponding to the p-th particle, is the fluid velocity evaluated in the absence of the p-th particle itself. The physical reason for adding these terms into the particle feedback, is that we are describing a system where the particle boundary is replaced by a concentrated force. In this equivalent model the inter-phase momentum exchanged, on the integral ground, must be conserved. However, since the volume of the particle is now filled with the fluid, the corresponding momentum and gravitational force from the unperturbed field must be removed, or equivalence is not achieved. Moreover, we stress that the fluid acceleration produced by the particle does not appear in the back-reaction term, since it is already included in the equivalence. In fact, the particle self-disturbances in the equivalent model and in the physical problem will be locally different, especially very close the particle. However, the overall momentum induced by the particle in the two problems will be the same. That is, the two particle self-disturbances will conserve the momentum, although being distributed differently across the space. In the point-particle limit, the concentrated force model is a good fit of the physical problem, since only the particle far-field is important for the dynamic of the fluid.

The second important aspect that we must consider is that the convective terms in curly bracket are clearly unbounded. These terms must be treated with particular care in the near-particle field,

since the domain of the resulting problem (2.29) is $\mathbb{R}^3$, which includes the particle volume itself. This is the equivalent problem discussed earlier, where the particle size is smaller than the hydrodynamic spatial scales and its boundary can be replaced by a concentrated force. If we filter the convective terms over the smallest hydrodynamic scale Δ, the operation will influence the singular fields, leaving the regular contributions unchanged. In fact, the dynamic of the fluid is well-described when all the relevant hydrodynamic scales are temporally advanced. However, in ERPP only the regular field is resolved over the computational grid and integrated. This means that the regularising parameter must satisfy the condition $\sigma_R \geq \Delta$. The equal sign provides the coarsest computational grid, and therefore requires the minimal computational effort, which properly reproduces the fluid motion. Therefore the regular field $u_R(x,t)$ includes all the relevant spatial scales of $u(x,t)$. The smaller hydrodynamic scales are unessential, due to the decaying of the turbulent energy spectrum. These sub-scale motions can be seen as the particle-induced disturbance which haven't reached the scale Δ yet. In this perspective, the regularising parameter ϵ_R can be seen as the time scale of the viscous diffusion of the singular perturbation, released by the particle along its trajectory $x_p(t)$, to reach the spatial scale Δ. In fact, the velocity $v_S(x,t)$ is naturally regularised by viscous diffusion. Only when the particle disturbance diffuses up to the scale Δ, it will become important for the fluid dynamics.

For these considerations, the filtering operation of the equations (2.29) over the scale Δ, that is denoted by the upper hat, acts only on the terms in curly brackets. The estimate of the filtering of the singular convective terms is reported below, for the detailed calculation the reader is referred to the paper of Gualtieri et al. [64].

$$\begin{aligned} \widehat{\widetilde{v}_S \cdot \nabla \widetilde{v}_S} &\sim Re_p \left(\frac{\sigma_R}{\Delta}\right)^3 \frac{\rho_p}{\rho_f} \widetilde{D}_p \widetilde{g}_{max} \\ \widehat{\widetilde{v}_S \cdot \nabla \widetilde{u}_R} \sim \widehat{\widetilde{u}_R \cdot \nabla \widetilde{v}_S} &\sim Re_p \left(\frac{\sigma_R}{\Delta}\right)^2 \frac{\rho_p}{\rho_f} \widetilde{D}_p \widetilde{g}_{max} \end{aligned} \tag{2.30}$$

For consistency,the expressions (2.30) are reported in dimensionless unit with respect to the particle scale motion, where the tilde denotes the dimensionless variables, as the expression (2.28) was. $\widetilde{g}_{max} = \frac{1}{(2\pi\sigma_R^2/d_p^2)^{3/2}}$ is the maximum of the gaussian function of variance σ_R/d_p. The expressions (2.30) are compared with the forcing term on the right hand side that reads

$$\widetilde{f}_p \sim \frac{\rho_p}{\rho_f} \widetilde{D}_p \widetilde{g}_{max} \tag{2.31}$$

Clearly the filtered convective terms are one Re_p order smaller than the forcing term, and they can be discarded.

We have finally obtained the regularised Navier-Stokes equation (2.32), where the effect of the dispersed phase is described by an extra forcing term. This forcing is expressed by the retarded Stokes drag $D(t-\epsilon_R)_p$, and the gaussian function $g(x - x_p(t-\epsilon_R), \epsilon_R)$ centred at the delayed position $x_p(t-\epsilon_R)$ and of variance $\sigma_R = \sqrt{2\nu\epsilon_R}$. The regularised forcing can be interpreted as the fundamental solution of the diffusion equation, where the original delta function of module $D_p(t)$ diffuses over the time interval ϵ_R.

Each particle influences the fluid over an area that is order σ_R close to the particle. Moreover, the particle perturbation is experienced by the fluid only at the delayed time ϵ_R. We observe that the ERPP equations are converging to the initial singular problem. This means that if we reduce the gaussian variance σ_R, that is we reduce the delaying time ϵ_R, the mollified forcing is recast back into the delta Dirac function. This operation progressively increases the resolution of the actual field $u_R(x,t)$ that we advance in time. The cost that we pay is the increased computational effort, required to represent the even more resolved field.

$$\begin{cases} \frac{\partial u_R}{\partial t} + u_R \cdot \nabla u_R = -\frac{2}{\rho_f}\nabla p + \nu \nabla^2 u_R + \frac{1}{\rho_f}\sum_p^{N_p} \left\{ m_f \left(\left.\frac{Du_{(0)}}{Dr}\right|_p - g \right) - D_p(t-\epsilon_R) \right\} g[x - x_p(t-\epsilon_R), \epsilon_R] + g \\ \nabla \cdot u_R = 0 \end{cases}$$

$$\begin{cases} \lim_{|x|\to+\infty} u_R(x,t) = 0 & x \in \mathbb{R}^3 \\ u(x,0) = u_0(x) \end{cases} \tag{2.32}$$

The regularised Navier-Stokes equations of the field $u_R(x,t)$, that is everywhere smooth, can be implemented in any numerical code. The only constraint is to resolve the mollified forcing over the computational grid. Additionally, the memories of the particle drag and position must be conserved over the time ϵ_R, before they are actually used.

As we have discussed, the scale parameter σ_R must be chosen according to the smallest hydrodynamic scale Δ. In the present research we deal with turbulent flows. In the homogeneous turbulence the Kolmogorov length-scale η will be the smallest resolved scale, i.e. $\sigma_R \approx \eta$. In wall-bounded turbulence σ_R will be similarly determined by the viscous length-scale ℓ^*.

The regularised field is obtained analysing the propagation of the singular disturbance produced by the particle, under a rigorous consistent framework. This is essential to prevent the deficiencies of other regularisation procedures, such as PIC or FCM. In particular, we stress that the particle forcing is grid-independent, in the sense that increasing the grid spacing (while the gaussian variance is constant) only increases the resolution of the feedback itself. Moreover the particle self-disturbance, required for the evaluation of the hydrodynamic force, can be computed in a analytical form. In fact, according to ERPP, the particle self-disturbance obeys the Stokes equations forced by the mollified forcing of the particle itself, with homogeneous initial condition.

2.6 The particle momentum equation

In section 2.2 we have discussed how the inter-phase momentum exchange occurs from the fluid perspective. While explaining ERPP, we have always assumed that the hydrodynamic force D_p was somehow known. The hydrodynamic force D_p has a crucial impact on the whole multiphase system, since it regulates the inter-phase mechanical energy transfer. In a real physical problem, the hydrodynamic force would be computed by integrating the fluid stresses over the particle surface. In the point-particle model this is impossible, since the near-particle field has been filtered out. In fact, the particle boundary conditions are replaced by a singular forcing in the Navier-Stokes equations. Therefore, the fluid velocity $u(x_p(t),t)$, evaluated at particle position $x_p(t)$, does not match the particle velocity $v_p(t)$. In fact, $u(x_p(t),t)$ is the velocity field observed from the relevant hydrodynamic scales. If we expanded the motion at the particle scale we would recover the inter-phase boundary, and we would see that $u(x_p(t),t)$ is indeed infinitely distant from the particle.

Clearly the hydrodynamic force must be somehow evaluated. In the hypothesis of vanishing Re_p, an equivalent model provides the expression of $D_p(t)$ when spherical rigid particles are considered. The model, known as the Maxey-Riley-Gatignol equation [61, 82], evaluates the hydrodynamic force as function of a far particle field. The detailed description of the physical and mathematical framework used to derive the particle momentum equation is reported in the Appendix G.

In this section the Maxey-Riley-Gatignol equation is provided. Let's consider a p-th particle of diameter d_p, positioned at $x_p(t)$, moving across a flow field whose velocity in the absence of the particle itself is $u_{(0)}(x,t)$. The unperturbed field $u_{(0)}(x,t)$ differs from the field $w(x,t)$ introduced in the (2.2). In fact, $u_{(0)}(x,t)$ takes into account not only the background flow w, but also the perturbation induced by all the remaining particles. That is, the velocity $u_{(0)}(x,t)$ is the actual fluid velocity $u(x,t)$ experienced by the particle, after its self-disturbance $u_{(1)}(x,t)$ is removed. Therefore, when the p-th particle is considered, the field $u(x,t)$, obeying the system (2.1), is additively decomposed into $u_{(0)}(x,t)$ and $u_{(1)}(x,t)$, namely

$$u(x,t) = u_{(0)}(x,t) + u_{(1)}(x,t) \tag{2.33}$$

The particle momentum, according to Maxey & Riley [61] and Gatignol [82], is driven by only the particle unperturbed field $u_{(0)}(x,t)$. Therefore, in the point-particle limit the particle momentum equation is written as

$$\begin{aligned}
&\rho_p V_p \frac{dv}{dt} = (\rho_p - \rho_f) g V_p + \rho_f V_p \frac{Du_{(0)}}{Dt}(x_p(t),t) + \frac{1}{2}\rho_f V_p \frac{d}{dt}\left\{u_{(0)}[x_p(t),t] - v_p(t) + \frac{1}{40} d_p^2 \nabla^2 u_{(0)}|_{x_p(t)}\right\} + \\
&+ 3\pi\mu d_p \left\{u_{(0)}[x_p(t),t] - v_p(t) + \frac{1}{24} d_p^2 \nabla^2 u_{(0)}|_{x_p(t)}\right\} + \\
&+ 3/2\pi\mu d_p^2 \int_0^t \left(\frac{d/d\tau(u_{(0)}[x_p(\tau),\tau] - v(\tau) + \frac{1}{24} d_p^2 \nabla^2 u_{(0)}|_{x_p(\tau)})}{[\pi\nu(t-\tau)]^{1/2}}\right) d\tau
\end{aligned} \tag{2.34}$$

The equation is better known as the Maxey Riley Gatignol equation, and describes the evolution of the momentum of a tiny rigid sphere in the presence of an unsteady background flow.

Between left to right, in equation (2.34), the terms that appear are the buoyancy force, the fluid inertia term, the added-mass force, the drag force and the history force. We will discuss more in details later about the physical interpretation of these forces, and their relevance in the context of bubbly ($\rho_p/\rho_f << 1$) or particle-laden ($\rho_p/\rho_f >>$) flows.

2.6.1 Drag force

$$3\pi\mu d_p (u_{(0)} - v_p + \frac{1}{24} d_p^2 \nabla^2 u_{(0)}) \tag{2.35}$$

The drag force is the action due to viscosity that tends to nullify the fluid-to-particle relative velocity. The force exhibits a Re_p dependency, that can be easily shown

$$C_D(Re_p)\frac{\pi d_p^2}{8}\rho_f |u - v_p|_{ref} (u_{(0)} - v_p + \frac{1}{24} d_p^2 \nabla^2 u_{(0)}) \tag{2.36}$$

$C_D(Re_p) = \frac{24}{Re_p}$ is the drag coefficient in the Stokes conditions, i.e. $Re_p << 1$. The Re_p dependency of the drag coefficient can substantially change from the hyperbole for higher Re_p, that are out of the solution (2.34). In intermediate ($1<Re_p<60$) or higher ($Re_p > 60$) regimes there exist corrective expressions of the drag coefficient C_D [83, 84]. In the present research however the drag force is expressed in the Maxey-Riley formulation, due to the negligible role of the particle Reynolds number. $\frac{1}{24} d_p^2 \nabla^2 u_{(0)}$ is the drag force Faxen correction. The correction takes somehow into account that the velocity field $u_{(0)}$ may be non-uniform in the particle surrounding. The role of the Faxen term grows in the intermediate regime, when the particle size is not far from the hydrodynamic scale Δ. In the other cases it can be discarded.

2.6.2 Added-mass force

$$\frac{1}{2} V_p \rho_f \frac{d}{dt}(u_{(0)} - v_p + \frac{1}{40} d_p^2 \nabla^2 u_{(0)}) \tag{2.37}$$

The added-mass force (2.37) describes the fluid inertia to overcome, in order to accelerate a spherical mass. In fact, due to continuity, there is always a portion of fluid that moves with along the particle, that must be accelerated as well. The added-mass force provides the energy required to produce such motion.

The effect of the added-mass force depends on the inertial difference between the two phases, i.e. by the density ratio ρ_p/ρ_f. When the fluid inertia is negligible with respect to the particle,

the contribution of the added-mass to the motion is irrelevant. This is the case of solid particles ($\rho_p/\rho_f \gg 1$), where the dynamics is controlled by only the drag force. Conversely in bubbly flow the fluid inertia prevails over the particle mass. The added-mass force has a crucial role in homogeneous turbulence and it is responsible for the bubble inertial clusterisation.

Similar to the drag force, a Faxen correction is present in the added-mass force. However, in the present research the added-mass Faxen term is discarded.

2.6.3 Basset force

$$\frac{3\pi\mu d_p^2}{2}\int_0^t d\tau\left(\frac{d/d\tau(u[x_p(\tau),\tau]-v(\tau)+\frac{1}{24}d_p^2\nabla^2 u|_{x_p(\tau)})}{[\pi\nu(t-\tau)]^{1/2}}\right) \tag{2.38}$$

The particle dynamics experiences somehow memory of the past configurations of the drag force. The phenomenon is described by the Basset force.

The history of the motion is recorded up to the reference, and purely arbitrary, time $t = 0$, where the particle self-disturbance is at rest. The integral is weighted by the temporal coefficient $\sqrt{\frac{\pi}{2}}\sigma(t-\tau)$, where $\sigma(t-\tau) = \sqrt{2\nu(t-\tau)}$ is the scale of the vorticity generated by the particle at time $t-\tau$ and diffused to current time t. The force is one order of d_p smaller than the drag force. For this reason it is neglected in the present research.

2.6.4 Buoyancy force

$$V_p(\rho_p-\rho_f)g \tag{2.39}$$

The buoyancy force is the resultant between the Archimede $-V_p\rho_f g$ and the gravity force $V_p\rho_p g$. Buoyancy is important to study the dynamics of rising bubbles or settling particles in turbulent flows. However, we assume that the particle acceleration due to the turbulent flow prevails over the gravity effects. In this case the buoyancy effects can be neglected.

2.7 The Maxey-Riley equation for bubbles and inertial particles

The particle momentum equation (2.34) refers to a rigid spherical object of mass $m_p = V_p\rho_p$. No assumptions are made on the state of matter, apart from the no-slip conditions on the particle surface. The spherical object, generically referred to as the "particle", can be either gaseous or solid. The general description of momentum does not change between the two cases. In other words the dynamics of both a bubble or a inertial particle is effectively dictated by the Maxey-Riley-Gatignol equation. However the dynamics of solid and gaseous phase dispersed in the turbulence is radically different. This effect is captured by the equation (2.34) through the particle-to-fluid density ratio ρ_p/ρ_f.

When we study bubbles, the relevant forces in the momentum equation (2.34) are the drag force, the added-mass force and the fluid-inertia term. Additionally, the lift force (2.40) of the Auton's model [85] is added to the equation. The influence of the local background vorticity $\zeta_{(0)} = \nabla\times u_{(0)}$ through the lift force recovers important bubble finite size effects.

$$F_L = \frac{1}{2}\rho_f V_p(u_{(0)}-v_p)\times\zeta_{(0)} \tag{2.40}$$

The particle inertia is expressed by the particle time response τ_p (2.42). τ_p is usually measured with respect to a turbulent background time-scale τ_Δ through the Stokes number $St_\Delta = \tau_p/\tau_\Delta$. The reference time-scale usually depends on the nature of the background flow. For the homogeneous turbulence τ_Δ is the time-scale of the smallest vortices, i.e. the Kolmogorov time-scale τ_η, and the Stokes number is $St_\eta = \tau_p/\tau_\eta$. In wall-bounded turbulence the Stokes number is referred to the viscous time-scale τ^*, that is $St^+ = \tau_p/\tau^*$.

$$\tau_p \frac{dv_p}{dt} = u_{(0)} - v_p + \frac{1}{24} d_p^2 \nabla^2 u_{(0)} + \frac{1}{2} \frac{\tau_p}{\rho_p/\rho_f + 1/2} \left(3 \frac{Du}{Dt}_{(0)} + (u_{(0)} - v_p) \times \zeta_{(0)} \right) \tag{2.41}$$

$$\tau_p = \frac{1}{18} \left(\frac{\rho_p}{\rho_f} + \frac{1}{2} \right) \frac{d_p^2}{\nu} \ , \quad St_\Delta = \frac{1}{18} \left(\frac{\rho_p}{\rho_f} + \frac{1}{2} \right) \frac{d_p^2}{\Delta^2} \tag{2.42}$$

In the case of inertial particles ($\rho_p/\rho_f >> 1$), the inertia of the fluid is negligible, and the added-mass and the lift forces are discarded. Hence the dominant term is the drag force.

$$\tau_p \frac{dv_p}{dt} = u_{(0)} - v_p + \frac{1}{24} d_p^2 \nabla^2 u_{(0)} \tag{2.43}$$

Clearly bubbles do not behave as light particles, in the sense that addition forces come into play. This explains how particles and bubbles exhibit motions so different when in the presence of turbulence. In fact, when in homogeneous turbulence bubbles tend to aggregate into the most intense vortical structures, while inertial particles are pushed away. The phenomenon is described by the equations (2.41) (2.43) through the balance between the drag and the added-mass force and can be addressed if we understand the structure of a vortex. In the vortex, the flow field consists in an increasing revolving velocity while moving inward, but into the very inner region where fluid returns still. The hydrodynamic pressure usually exhibits a decreasing monotonic behaviour, with the minimum in the central region of the vortex. The bubble motion approaching a vortex from the outer regions is dictated by the equation (2.41). Clearly the drag force increases the centrifugal force, since while moving inward the bubble experiences increasing revolving fluid velocity. If we do not consider any additional radial force, bubbles with initial small kinetic energy are simply pushed away and fail to reach the central region. Bubbles that own sufficient kinetic energy can overcome the drag force, and get to the center of the vortex. However, again in the absence of any radial force, the fluid accelerates the bubble along the azimuthal direction, and is expelled from the vortex. The radial force that opposes the drag force is the added-mass force. Such force provides two contributions to the bubble motion. These two effects are represented by the terms $1/2 m_f \frac{dv_p}{dt}$ and $1/2 m_f \frac{Du_{(0)}}{Dt}$, where $m_f = \rho_f V_p$ is the fluid displaced mass. The first term has a passive role: to increase the actual bubble inertia of the mass $1/2 m_f$. On the contrary the fluid momentum is an active forcing for the bubble, as described by the (2.41). Since in the vortex the fluid material derivative is dominated by the pressure gradient, the main effect is to produce an acceleration toward the central vortical region. Therefore the hydrodynamic pressure attracts the bubble inward the vortex, and such effect is proportional to the displaced mass. Bubbles, where the added-mass term is relevant, tend to be trapped into the smallest vortices, and inertial particles, where the displaced mass is small compared with the particle inertia, are simply pushed away.

In the 1-way coupling regime to compute the bubble/particle hydrodynamic force is trivial since the unperturbed field $u_{(0)}(x_p(t), t$ coincides with the resolved field $u(x_p(t), t)$. However the dispersed phase can significantly alter the background flow even at dilute regime. In this so called 2-way coupling regime, the background field $u_{(0)}(x_p(t), t)$ differs from $u(x_p(t), t)$, and the self-disturbance must be somehow evaluated. The operation can be achieved with ERPP, since the field $u_1(1)$, after the regularisation treatment, obeys the equation (2.19). For further details of the procedure, the reader is referred to the Appendix F.6.

2.8 The exact Regularised Point Particle method in wall-bounded flows

So far we have discussed how to model the inter-phase coupling of dilute suspensions in the free-space. In this section we will present the correction of the regularising method used in wall-bounded flow. The procedure is conceptually similar to the one provided in the free-space problem. The

disturbance of the dispersed phase is evaluated from a linear Stokes equation, where in this case the proper boundary conditions for the solid walls are considered. The formulation allows the manipulation of the analytic solution of the particle disturbance. Following considerations on how the particle disturbance diffuses, the singular part of the field is consistently removed. The time-scale regularising parameter is ϵ_R, that is, again, the diffusion time of the particle disturbance. In contrast to the free-space problem, a solid wall is introduced close to the particle. The new boundary condition of the particle disturbance is enforced by means of the method of images. A mirrored particle, with respect to the local tangent plane, provides the feedback that nullifies the velocity component normal to the wall.

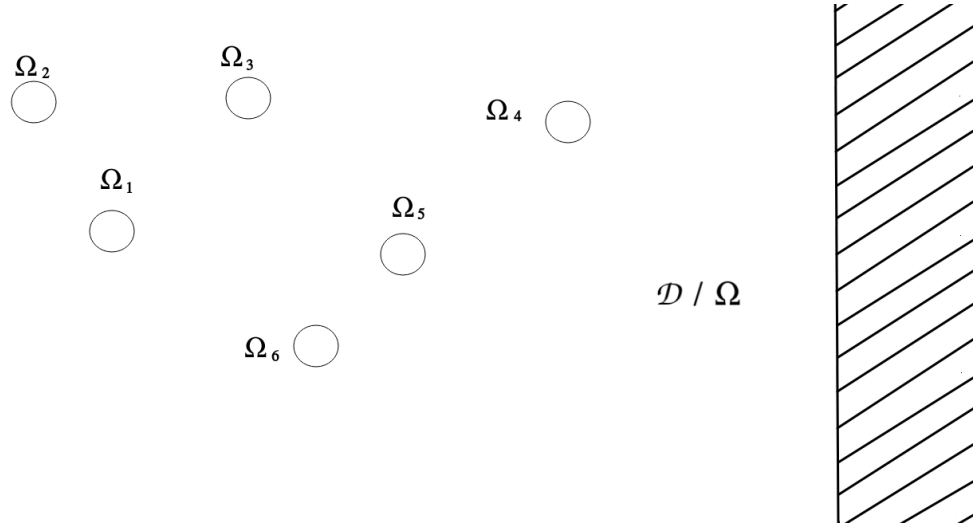

Figure 2.2: Sketch of the domain of the multiphase system. $\Omega = \cup_p \Omega_p$ is the domain of the overall dispersed phase , $\mathcal{D}/\Omega$ is the domain of the fluid.

The domain of the multiphase flow in this new configuration is $\mathcal{D}$. The boundary of $\mathcal{D}$ is the union of the plane $\partial\mathcal{D}$, i.e. the solid wall, and of the boundary at infinite $\partial\mathcal{D}_\infty$. The dispersed phase fills the domain $\Omega(t) = \cup_p \Omega_p(t)$, where $\Omega_p(t)$ is the p-th particle domain. The fluid obeys the standard incompressible Navier-Stokes equations with the no-slip condition at the solid boundaries

$$\begin{cases} x \in \mathcal{D}\backslash\Omega(t) \begin{cases} \rho_f \frac{Du}{Dt} = \rho_f g - \nabla p + \mu \nabla^2 u \\ \nabla \cdot u = 0 \end{cases} \\ u(x,t)^{(\pi)}|_{\partial\mathcal{D}} = 0 \\ u(x,t) \cdot n|_{\partial\mathcal{D}} = 0 \\ u(x,t)|_{\partial\Omega_p(t)} = v_p(x,t)|_{\partial\Omega_p(t)} \quad for \quad p = 1, 2, ..., N_p \\ u(x,0) = u_0(x) \end{cases} \tag{2.44}$$

The notation is the same of the one presented in the free-space problem. We only distinguish between the local tangent and normal velocity to the solid wall, respectively $u(x,t)^{(\pi)}|_{\partial\mathcal{D}}$ and $u(x,t) \cdot n|_{\partial\mathcal{D}}$. The field u is additively decomposed into the background field w and the particle disturbance v, namely $u = w + v$. The field w is described over the domain $\mathcal{D}$ by the equations

$$\begin{cases} \rho_f \left(\frac{\partial w}{\partial t} + F\right) = \rho_f g - \nabla p_w + \mu \nabla^2 w & \\ \nabla \cdot w = 0 & x \in \mathcal{D} \\ F = \begin{cases} \rho_f u \cdot \nabla u \ , & for \ \ x \in D \backslash \Omega(t) \\ \rho_f v_p \cdot \nabla v_p \ , & for \ \ x \in \Omega(t) \end{cases} & \\ w(x,t)^{(\pi)} = -v(x,t)^{(\pi)} & \\ w(x,t) \cdot n = -v(x,t) \cdot n = 0 & \\ w(x,0) = u_0(x) & \end{cases} \tag{2.45}$$

The forcing term F is, again, prolonged into the particle domain Ω_p, using the particle velocity v_p, and no boundary conditions are applied to the particle boundary. The particle disturbance v, defined over the domain $\mathcal{D}\backslash\Omega$, satisfies the unsteady Stokes equation with initial homogeneous condition

$$\begin{cases} x \in \mathcal{D}\backslash\Omega(t) \begin{cases} \nabla \cdot v = 0 \\ \rho_f \frac{\partial v}{\partial t} = -\nabla p_v + \mu \nabla^2 v \end{cases} & \\ v(x,t) \cdot n|_{\partial \mathcal{D}} = 0 & \\ \frac{\partial v}{\partial n}(x,t)\Big|_{\partial \mathcal{D}} = 0 & \\ v|_{\partial \Omega_p(t)} = V_p - w(x,t)|_{\partial \Omega(t)} \quad for \ p = 1,2,...,N_p & \\ v(x,0) = 0 & \end{cases} \tag{2.46}$$

The impermeability and free-slip conditions are enforced at the solid wall in v. We could object that they are not the proper boundary conditions for solid walls. However, the reader must notice that the resulting field u still satisfies the no-slip conditions, as it is meant to be.

The solution of the equation (2.46) can be found by means of the method of images. The wall is the solid plane π of unit normal $\hat{n}$. The mirrored particle is obtained as the reflection of the physical particle with the wall. Hence, the mirrored particle occupies the domain $\widetilde{\Omega_p}$, in the semi-space $\mathbb{R}^3/\mathcal{D}$, that is the mirror image of Ω_p with respect to the plane π. The motion of the mirrored particle is characterised by the velocity of its centroid $\widetilde{v}_p = -n \cdot v_p \hat{n} + v_p^{\pi}$ and the angular velocity $\widetilde{\omega}_p = -\omega_p$. Due to symmetric reasons, the linear combination of the fields induced by the mirrored and physical particle returns the boundary conditions over $\partial\mathcal{D}$ required by the particle disturbance. Therefore the solution of equation (2.46) is

$$\begin{aligned} v_i(x,t) = \int_0^t d\tau \Bigg(\int_{\partial\Omega} t_j(\psi,\tau) \mathbf{G}_{ij}(x-\psi, t-\tau) - v_k(\psi,\tau) \mathbf{T}_{ikj}(x-\psi, t-\tau) n_j(\psi) dS_\psi + \\ \int_{\partial\widetilde{\Omega}} \widetilde{t}_j(\widetilde{\psi},\tau) \mathbf{G}_{ij}(x-\widetilde{\psi}, t-\tau) - \widetilde{v}_k(\widetilde{\psi},\tau) \mathbf{T}_{ikj}(x-\psi, t-\tau) n_j(\widetilde{\psi}) \widetilde{dS}_\psi \Bigg) \end{aligned} \tag{2.47}$$

Physically, $\mathbf{G}_{ij}(x-\eta, t-\tau)$ is the i-th velocity component induced at position x and time t by the j-oriented impulse force located at position η acting at time τ. The stress tensor associated to such field is $\mathbf{T}_{ikj}(x-\eta, t-\tau) n_j(\eta)$. The reader must note that if the velocity v is computed over the domain $\mathcal{D}$, the tensors $\mathbf{G}$ and $\mathbf{F}$ fill the domain $\mathbb{R}^3$. Hence, due to the mirroring manipulation, the system is prolonged into the free-space domain where the velocity v is computed only over the semi-space $\mathcal{D}$. Therefore we can repeat all the considerations made in our original problem, where the wall was not present into the domain, to the price of including the additional particle image system. In the small-particle limit, the integral representation of the velocity is rapidly obtained into the following time convolution

$$v(x,t) = -\sum_p \int_0^t \left\{ D_p(\tau) \cdot \mathbf{G}(x - x_p, t-\tau) + \widetilde{D}_p(\tau) \cdot \mathbf{G}(x - \widetilde{x}_p, t-\tau) \right\} d\tau \tag{2.48}$$

For each p-th particle we consider the reflected one with respect to the local tangent plane of the solid wall, according to $\widetilde{x}_p^{\pi} = x_p^{\pi}$, $\widetilde{x}_p^{n} = -x_p^{n}$, $\widetilde{D}_p^{\pi} = D_p^{\pi}$, $\widetilde{D}_p^{n} = -D_p^{n}$. The expression (2.48) is the solution of the singular Navier-Stokes equation

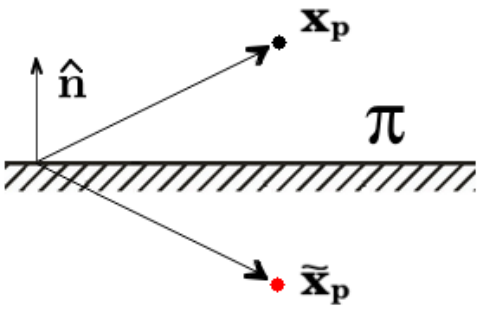

Figure 2.3: Sketch of the imaged system. The physical particle (black one) is labelled by the position x_p, while the mirrored particle (red one) by $\widetilde{x_p}$.

$$\begin{cases} \rho_f \frac{\partial v}{\partial t} = -\nabla p_v + \mu \nabla^2 v - \sum_p \{D_p(t)\delta(x - x_p(t)) + \widetilde{D}_p(t)\delta(x - \widetilde{x}_p(t))\} & x \in \mathcal{D} \\ \nabla \cdot v = 0 \\ v(x,0) = 0. \end{cases} \tag{2.49}$$

The equation must be somehow regularised to be amenable to numerical treatment. Exploiting the additivity property of the integral (2.48), the singularity can be removed from the particle disturbance.

$$v_R(x,t) = -\sum_p \int_0^{t-\epsilon_R} \left\{ D_p(\tau) \cdot \mathbf{G}(x - x_p, t-\tau) + \widetilde{D}_p(\tau) \cdot \mathbf{G}(x - \widetilde{x}_p, t-\tau) \right\} d\tau \tag{2.50}$$

$$v_S(x,t) = -\sum_p \int_{t-\epsilon_R}^{t} \left\{ D_p(\tau) \cdot \mathbf{G}(x - x_p, t-\tau) + \widetilde{D}_p(\tau) \cdot \mathbf{G}(x - \widetilde{x}_p, t-\tau) \right\} d\tau \tag{2.51}$$

The regularisation procedure is again performed through the parameter ϵ_R, that is the diffusion time-scale of the velocity induced by the dispersed phase and its image system. ϵ_R represents the time required by the singular initial velocity to diffuse up to the resolved scale $\sigma_R = \sqrt{2\nu\epsilon_R}$. The scale σ_R is chosen in order to resolve all the relevant hydrodynamic lengthscales of $v(x,t)$ up to the smallest one Δ. The remaining smallest scales are inside $v_S(x,t)$, that bears the singularities, and are inessential for the fluid dynamics. The far-field contribution of v_S rapidly decays in space, provided that ϵ_R and Re_p are small, and can be neglected.

The regularised velocity field $v_R(x,t)$ is described by the Stokes equation where the singularity $\delta(x - \eta_p(t))$ is replaced by the Gaussian function $g(x - \eta_p(t - \epsilon_R), \epsilon_R)$ of variance $\sigma_R = \sqrt{2\nu\epsilon_R}$ and the hydrodynamic force is evaluated at the anticipated time $t - \epsilon_R$. The notation η_p is generically referred to the position of either the physical x_p or the mirrored $\widetilde{x}_p$ particle.

$$\begin{cases} \frac{\partial v_R}{\partial t} = -\frac{1}{\rho_f}\nabla p_R + \nu\nabla^2 v_R - \frac{1}{\rho_f}\sum_p^{N_p}\{D_p(t-\epsilon_R)g(x-x_p(t-\epsilon_R),\epsilon_R) + \widetilde{D}_p(t-\epsilon_R)g(x-\widetilde{x}_p(t-\epsilon_R),\epsilon_R)\} \\ \nabla\cdot v_R = 0 \\ v_R(x,0) = 0 \qquad\qquad x\in\mathcal{D} \end{cases} \tag{2.52}$$

The final Navier-Stokes equations of the complete field $u(x,t)$ can be reassembled once filtering out the singularities in the convective terms. The effect of such terms will be again negligible, being one order of Re_p smaller than the forcing term in the right hand side.

$$\begin{cases} \frac{\partial u_R}{\partial t} + u_R\cdot\nabla u_R = -\frac{1}{\rho_f}\nabla p + \nu\nabla^2 u_R - \frac{1}{\rho_f}\sum_p^{N_p}\{F_p(t-\epsilon_R)g(x-x_p(t-\epsilon_R),\epsilon_R) + \widetilde{F}_p(t-\epsilon_R)g(x-\widetilde{x}_p(t-\epsilon_R),\epsilon_R)\} \\ \nabla\cdot u_R = 0 \\ F_p = D_p - m_f\left(\left.\frac{Du_{(0)}}{Dt}\right|_p - g\right) \\ \widetilde{F}_p^{\pi} = F_p^{\pi} \\ \widetilde{F}_p^{n} = -F_p^{n} \end{cases}$$
$$\begin{cases} u_R(x,t)|_{\partial\mathcal{D}} = 0 \qquad\qquad x\in\mathcal{D} \\ u(x,0) = u_0(x) \end{cases} \tag{2.53}$$

The system (2.53) provides the ERPP solution of the regularisation process required by the point-wise suspension. The concentrated force F_p equivalently replaces the p-th particle boundary, in the Navier-Stokes equation. The correction due to wall effects is accounted for through the image particle system, that provides the proper wall-boundary condition of the particle disturbance. The mirrored concentrated force $\widetilde{F}_p$ is reflected with respect to the local tanget plane π, of unit normal $\hat{n}$.

The regularising parameter σ_R, representing the smallest scale of the flow being resolved over the computational grid, is selected to reproduce the hydrodynamic up to the relevant scale Δ, namely $\sigma_R \leq \Delta$.

The procedure was derived when the wall is a solid plane. However we can expand the treatment to a generic wall, provided that the particle diameter is much smaller than the local curvature of the wall. In such condition we can approximate the wall to its local tangent plane, retaining the boundary conditions in the equation (2.46).

Chapter 3

The homogeneous turbulent bubbly shear flow

In present chapter we report the study of the homogeneous turbulent bubbly shear flow. Results and discussions refer to the paper of Motta et al. [86]. The layout is redited to adapt to the format of the present thesis.

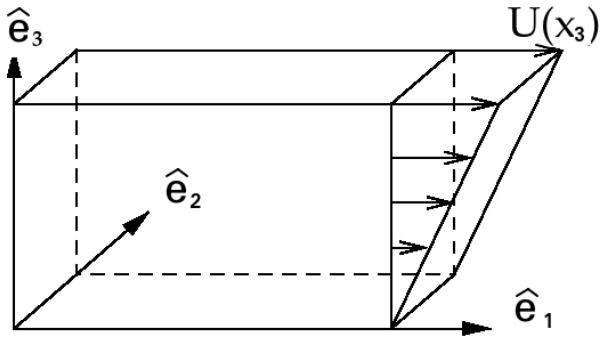

Figure 3.1: The domain of the shear flow $\mathcal{A}$.

3.1 Short overview on the homogeneous shear flow and simulation parameters

Given the orthonormal basis $(\hat{\mathbf{e}}_1, \hat{\mathbf{e}}_2, \hat{\mathbf{e}}_3)$ and the corresponding coordinates (x_1, x_2, x_3), in the homogeneous shear flow the mean velocity is imposed as $U(x_3) = Sx_3\hat{\mathbf{e}}_1$, with S the constant mean shear. The shear S is responsible of the energy transfer from the averaged field to the fluctuating field $\mathbf{u}$ via the Reynolds shear stress. This mechanism allows the system to reach a statistically steady state [87]. The production of turbulent kinetic energy at the largest scales is anisotropic, similar to what is observed in wall bounded flows like pipes, channels and boundary layers. The turbulence dynamics is characterised by two dimensionless parameters [88, 89]: the Taylor-Reynolds number Re_λ and the shear strength S^*. The Taylor-Reynolds number is defined as $Re_\lambda = u_{rms}\lambda/\nu$, being $u_{rms} = \sqrt{\langle v \cdot v \rangle/3}$ the root mean square value of the velocity fluctuations, λ is the Taylor scale and the angular brackets denote ensemble averaging, i.e. space and time average. When Re_λ is large enough, the scale separation allows for the process of small scales isotropy recovery via the energy cascade. In this case the turbulence energy production due to the shear $-S\langle u_1 u_3 \rangle$ and the turbulent energy dissipation ϵ fill two distinct regions of the spectral space. The shear strength is defined as $S^* = S\langle v \cdot v \rangle/\epsilon = (L_0/L_S)^{2/3}$ where L_0 is the integral length scale and $L_S = \sqrt{\epsilon/S^3}$ is the shear scale. The shear strength determines the range of scales where the fluctuations are driven by the anisotropic turbulent kinetic energy production due to mean velocity gradient [88, 90].

The Eulerian-Lagrangian approach is used to simulate the two-phase suspension. The Rogallo's algorithm [91] is employed to solve the Navier-Stokes equations in a reference frame advected by the mean flow. The instantaneous velocity $\mathbf{u}$ is decomposed into the mean $\mathbf{U}$ and fluctuating field υ, namely $\mathbf{u} = Sx_3\hat{\mathbf{e}}_\mathbf{1} + \upsilon$. The Navier-Stokes equations for the field υ are written in a coordinate system moving with the mean flow exploiting the variable transformation $\tilde{x}_1 = x_1 - S\tau x_3$; $\tilde{x}_2 = x_2$; $\tilde{x}_3 = x_3$; $\tau = t$. In order to allow long time integrations a remesh procedure is performed along the $\hat{\mathbf{e}}_\mathbf{1}$ direction at time $t_r = 2/S$, by exploiting the periodicity of the field υ. The advantage of this procedure is to make the field υ homogeneous. The non-homogeneous term $\mathbf{U} \cdot \nabla\upsilon$ is absorbed by the change of coordinates. Rogallo's technique allows the use of standard pseudo-spectral methods, with the solely cost of dealing with time-dependent wave-numbers $\mathbf{k} = (k_1, k_2, k_3 - S\tau k_1)$. The non-linear terms are dealiased by the standard 2/3 zero-padding rule. The pressure is evaluated in a closed analytical form in the Fourier space, by solving the associated Poisson problem. The Navier-Stokes equations for the Fourier coefficients are advanced in time through a four-stage, low-storage Runge-Kutta method. The same time integration scheme is also used for the bubble momentum equation (3.5). Further details are provided in sections A, B E.

The control parameters of the discrete phase are the ratio between bubble and fluid density ρ_p/ρ_f, the void fraction φ_v and the Stokes number $St_\eta = \tau_p/\tau_\eta$. The Stokes number is well known to control the bubble clustering dynamics in the one-way coupling regime. In the two-way coupling regime also the void fraction comes into play. The density ratio might be considered in its asymptotic regime $\rho_p/\rho_f \to 0$. Therefore the control parameters are $\{Re_\lambda, S^*, St_\eta, \varphi_v\}$ in conditions of small bubble Reynolds number Re_p and void fractions φ_v.

The simulation matrix shown in table 3.1 that reports the relevant parameters of each case study. The table is arranged into four sections. The cases labeled with A, B, C and D correspond to simulations with fixed St_η, and different void fractions φ_v. For each St_η, the corresponding one-way coupling simulation (no back-reaction) has been carried out. The parameters Re_λ, S^*, η, ϵ and Re_p are given for the uncoupled case, and must be read as reference values. Since the suspension is dilute, their actual values in the two-way coupling regime might, in principle, be slightly modified by two-way coupling effects. The range of St_η is selected in order to satisfy the condition of small bubble diameters when compared with the Kolmogorov scale. In fact, the bubble diameter is computed from the definition of St_η, namely $d_p/\eta \simeq \sqrt{36\,St_\eta}$. Since Re_p progressively increases with the response time, too large values of St_η make the local flow past the bubble move away from the Stokes solution. In the above conditions the bubbles can be also considered as non-deformable spheres. In a creeping flow the viscous force is the relevant one that tends to deform the bubble, while the surface tension acts to preserve its spherical shape. The relative importance of these effects are measured by the Capillary number Ca (i.e. the ratio between viscous force and surface tension), namely $Ca = \rho_f \nu \langle|\mathbf{u} - \mathbf{v}_p|\rangle/\gamma)$ where γ is the surface tension. The present shear flow, given the spatial homogeneity, might be considered as a portion of the logarithmic region of a wall bounded flow. This circumstance allows for an estimate of the Capillary number. The box height L_2 represents the log-layer thickness and the Reynolds shear stress $\langle u_1\, u_3\rangle$ the square of the friction velocity. Given the nominal Reynolds number $Re_0 = 500$ of the HSF simulation, the friction Reynolds number is $Re_* = 1100$. At this Reynolds number, in a channel of height $2h = 0.2\,cm$, and for an air-water suspension (kinematic viscosity $\nu = 10^{-6} m^2/s$, density $\rho_f = 1000 kg/m^3$ surface tension $\gamma = 0.072 N/m$), the bubble population at $St_\eta = 0.2$, corresponding to largest bubbles, have an (average) Reynolds number $Re_p \simeq 1.65$. The capillary number follows at once $Ca \simeq 10^{-3}$. This value turns out to be much smaller than the threshold value of $Ca = 0.05$ below which bubbles retain their spherical shape [92].

3.2 Momentum coupling model

This section shortly reports about the Exact Regularised Point Particle (ERPP) method, that is used to achieve the inter-phase momentum coupling between the carrier fluid and the dispersed

Case	N_p	φ_v	St_η	d_p/η	Re_p
A_1	4284006	0.02	0.025	0.95	0.09
A_2	2142003	0.01	0.025	0.95	0.09
B_1	1514496	0.02	0.05	1.34	0.23
B_2	757248	0.01	0.05	1.34	0.23
C_1	532072	0.02	0.1	1.9	0.61
C_2	266036	0.01	0.1	1.9	0.61
C_3	133018	0.005	0.1	1.9	0.61
C_4	66509	0.0025	0.1	1.9	0.61
D_1	189232	0.02	0.2	2.68	1.65
D_2	94616	0.01	0.2	2.68	1.65
D_3	47308	0.005	0.2	2.68	1.65
D_4	23654	0.0025	0.2	2.68	1.65

Table 3.1: Simulation matrix. The Navier-Stokes equations are integrated in a $4\pi \times 2\pi \times 2\pi$ periodic box with a resolution of $384 \times 192 \times 384$ Fourier modes corresponding to $576 \times 288 \times 576$ points in physical space. For each case the Taylor-Reynolds number is $Re_\lambda = u_{rms}\lambda/\nu = 100$, the shear parameter is $S^* = S\langle \mathbf{u} \cdot \mathbf{u} \rangle / \epsilon = 5$. The parameters Re_λ, S^* refer to the one-way coupling case, and must be read as reference values. The regularisation length-scale of the ERPP approach is set to $\sigma_R/\Delta x = 1.5$, being $\Delta x/\eta = 1.28$ the grid spacing which correspond to $k_{max}\eta = 4$. The bubble-to-fluid density ratio is $\rho_p/\rho_f = 0.001$. N_p denote the number of bubbles, φ_v the void fraction and $St_\eta = \tau_p/\tau_\eta$, where τ_p and τ_η are the bubble and the Kolmogorov time-scale. The averaged bubble Reynolds number is $Re_p = \langle |\mathbf{u}_p - \mathbf{v}_p| \rangle d_p/\nu$, being d_p the bubble diameter. For each value of St_η a corresponding one-way coupling simulation (no back-reaction on the fluid) has been carried out.

phase. The reader can refer to the original paper [64] for a detailed discussion of the methodology.

The carrier flow is laden with small bubbles such that bubble Reynolds number $Re_p = \langle |\mathbf{u}_p - \mathbf{v}_p| \rangle d_p/\nu$ is small, being $\langle |\mathbf{u}_p - \mathbf{v}_p| \rangle$ the bubble-to-fluid average relative velocity, d_p the bubble diameter and ν the kinematic viscosity of the fluid. Hereafter small bubbles will be considered. In a turbulent flow, this means that the bubble diameter is of order of the Kolmogorov length-scale η. Under these assumptions the set of N_p bubbles is modelled as a collection of points where concentrated forces are applied. The suspension is also assumed to be diluted, such that four-way coupling effects, e.g. collisions and bubble-bubble interactions, are negligible. In these conditions, the effects of the bubbles on the carrier phase is accounted by an additional forcing term in the incompressible Navier-Stokes equations, namely

$$\begin{cases} \nabla \cdot \mathbf{u} = 0 \\ \\ \rho_f \dfrac{D\mathbf{u}}{Dt} = -\nabla p + \mu \nabla^2 \mathbf{u} + \mathbf{f}_p \end{cases} \tag{3.1}$$

where

$$\mathbf{f}_p(\mathbf{x}, t) = -\sum_{p=1}^{N_p} \left\{ \mathbf{D}_p(t) - m_f \left. \frac{D\mathbf{u}_{(0)}}{Dt} \right|_p (t) \right\} \delta[\mathbf{x} - \mathbf{x}_p(t)] \tag{3.2}$$

is the singular forcing that each bubble exerts on the fluid, according to [81]. With usual notation, ρ_f denotes the density of the fluid, μ the dynamic viscosity, $\mathbf{D}_p(t)$ is the hydrodynamic force on the bubble, m_f is the displaced fluid mass, $\left. \frac{D\mathbf{u}_{(0)}}{Dt} \right|_p$ the unperturbed fluid acceleration, and $\delta(\mathbf{x} - \mathbf{x}_p)$ is the Dirac delta function that localises the bubble concentrated force on the fluid at the bubble instantaneous position $\mathbf{x}_p(t)$. In equations (3.1) the inter-phase forcing term needs to be regularised.

In the Particle-In-Cell (PIC) approach the regularisation occurs by averaging the feedback term on the computational cell. However, this treatment gives rise to several numerical and physical

drawbacks [59, 60], i.e. the numerical feedback becomes grid dependent. These shortcomings are overcome by the Exact Regularised Point-Particle approach. In ERPP method the singular feedback is regularised within a consistent physical framework. The disturbance of each bubble on the fluid is evaluated in a closed analytical form exploiting the solution of a unsteady Stokes equation that can be proved to describe the dispersed phase perturbation of the background carrier flow. The effect can be illustrated in terms of the vorticity that each point-wise bubble produces along its trajectory $\mathbf{x}_p(t)$ subjected to the force $\mathbf{D}_p(t)$. In fact, the vorticity is naturally regularised by viscous diffusion. Therefore it is possible to introduce a regularisation time-scale ϵ_R which correspond to the viscous diffusion time-scale of the vorticity on the length-scale $\sigma_R = \sqrt{2\nu\epsilon_R}$, where $\nu = \mu/\rho_f$ is the kinematic viscosity. The regularisation scale σ_R must be understood as the smallest hydrodynamical scale of the problem, i.e. the Kolmogorov length-scale η in a turbulent flow. Following this kind of reasoning, though a lengthy but rigorous path [64], the bubble back-reaction is recast into its regularised form,

$$\mathbf{f}_p(\mathbf{x},t) = -\sum_{p=1}^{N_p} \left\{ \mathbf{D}_p(t-\epsilon_R) - m_f \left.\frac{D\mathbf{u}_{(0)}}{Dt}\right|_p (t-\epsilon_R) \right\} g[\mathbf{x}-\mathbf{x}_p(t-\epsilon_R),\epsilon_R]. \tag{3.3}$$

In equation (3.3) $g[\mathbf{x}-\mathbf{x}_p(t-\epsilon_R),\epsilon_R]$ is the Gaussian function centred at the retarded bubble position $\mathbf{x}_p(t-\epsilon_R)$ with variance $\sigma_R = \sqrt{2\nu\epsilon_R}$ that accounts for the delay process associated to the diffusion of the disturbance vorticity up to the length-scale σ_R. Similarly, $\mathbf{D}_p(t-\epsilon_R)$ is the delayed hydrodynamic force.

3.3 The dispersed phase

The dispersed phase consists of small rigid spherical bubbles of diameter d_p order of the Kolmogorov scale. Bubbles can be considered as material points of mass m_p and their evolution is described by the standard Newton's law

$$\frac{d\mathbf{x}_p}{dt} = \mathbf{v}_p(t), \quad m_p\frac{d\mathbf{v}_p}{dt} = \mathbf{D}_p(t) \tag{3.4}$$

where $\mathbf{D}_p(t)$ is the hydrodynamic force due to fluid stresses. The expression for $\mathbf{D}_p(t)$ was derived independently by Maxey & Riley [61] and Gatignol [82], namely

$$\begin{aligned}\mathbf{D}_p = 3\pi\mu d_p\left(\mathbf{u}_{(0)}|_p - \mathbf{v}_p + \frac{d_p^2}{24}\nabla^2\mathbf{u}_{(0)}|_p\right) + m_f\left.\frac{D\mathbf{u}_{(0)}}{Dt}\right|_p + \frac{1}{2}m_f\frac{d}{dt}\left(\mathbf{u}_{(0)}|_p - \mathbf{v}_p\right) + \\ + \frac{1}{2}m_f\left(\mathbf{u}_{(0)}|_p - \mathbf{v}_p\right)\times\boldsymbol{\zeta}_{(0)}|_p.\end{aligned} \tag{3.5}$$

In the expression of the force, m_f is the mass of the fluid displaced by the bubble and the subscript $|_p$ means the Eulerian fields evaluated at the bubble position. The fields labeled with a "0" subscript, namely $\mathbf{u}_{(0)}$ and $\boldsymbol{\zeta}_{(0)} = \nabla\times\mathbf{u}_{(0)}$, are the unperturbed fluid velocity and vorticity respectively, i.e. the fields in *absence* of the $p-th$ particle. These undisturbed fields can be evaluated by subtracting the bubble self-disturbance generated by the $p-th$ bubble itself that, in the ERPP approach, is known in a closed analytical form [64]. This feature allows the correct evaluation of the hydrodynamical force within the ERPP approach.

The terms on the right hand side of equation (3.5) are the drag force with the Faxen correction, the fluid acceleration, the added mass force and the lift force, respectively. The buoyancy can be neglected whenever $St_\eta/Fr_\eta \ll 1$ where $Fr_\eta = a_\eta/g$ and $St_\eta = \tau_p/\tau_\eta$ are the Froude number and the Stokes number in Kolmogorov units [93]. Apart from the lift force, the equations (3.5) and (3.4) are the Gatignol-Maxey-Riley equation in the case of small particle-to-fluid density ratio. In fact, the lift force is not considered in the original derivation by Maxey-Riley's and Gatignol. However, this effect is included given its relevance for bubbles with $d_p/\eta \sim 1$ as discussed by many authors [47, 49, 65]. The lift force is written in the form of Auton's model [85], while the Basset force is discarded as discussed by many authors [47, 50, 49, 51, 94]. The bubble response time,

$\tau_p = 1/(18\nu)(\rho_p/\rho_f + 1/2)d_p^2$, where ρ_p/ρ_f is the ratio of the bubble to fluid density, can be and expressed in dimensionless form with respect to the Kolmogorov time scale τ_η to form the Stokes number, namely $St_\eta = \tau_p/\tau_\eta$. St_η measures the bubble response to the small scale turbulent fluctuations. Two limit regimes exist: the passive tracer and the ballistic regime. When $St_\eta \gg 1$ bubbles are insensitive to turbulent fluctuations and persist in their trajectory without any change in their state of motion. Conversely if $St_\eta \ll 1$ the bubble response is enough high that the dispersed phase faithfully follows the fluid. The phenomenon of preferential concentration occurs in some intermediate regime. Note however, that the point-particle approach poses obvious constraints in bubble size, which in terms of bubble time response translates into $St_\eta < 0.2$. Therefore the ballistic regime is out of feasibility, since bubbles would be too large and deformability effects would occur. The bubbles tend to be trapped into the most intense vortical structures of the turbulent flow because of the fluid inertia terms, i.e. the pressure gradient term. Conversely, the drag force tends to push away bubbles from inner regions of the vortices. Therefore the balancing between the fluid inertia and drag forces, that is parametrised by St_η, regulates the bubble preferential concentration [25]. In the two-way coupling regime, the cluster geometry might impact on how the fluid experiences the dispersed phase feedback. It follows that the Stokes number St_η eventually controls the turbulence modulation via its indirect effect on small scale bubble clustering. The second parameter that controls turbulence modulation is the void fraction $\varphi_v = V_G/V_L$, i.e. the ratio between the volume of the gas phase (V_G) and the volume of the carrier phase (V_L), i.e. the liquid. The reader might note that the void fraction plays a role only in the two-way coupling regime. Four-way coupling interactions are discarded in the limit of a dilute suspension of small bubbles. For this reason φ_v is limited to few percentage points in the present research.

3.4 Results and Discussion

The following sections discuss the turbulence modification due to different bubble populations in the homogeneous shear flow (HSF).

3.4.1 The turbulent kinetic energy and dissipation rate

In this section the modification of the turbulent kinetic energy (t.k.e.) $K = 1/2\,\langle \upsilon \cdot \upsilon \rangle$ and of the energy dissipation rate $\epsilon = 2\nu\langle \nabla\upsilon : \nabla\upsilon \rangle$ are discussed. Henceforth, angular brackets must be understood as time and spatial average which, given the statistically time steadiness and spatial homogeneity, are equivalent to ensemble average. K and ϵ describe the global statistical behaviour of the largest and smallest hydrodynamical scales, respectively.

In figure 3.2 the turbulent kinetic energy K is plotted versus the void fraction φ_v for different St_η. The asymptotic standard error of K is shown with error-bars computed as $\delta_\epsilon = 2\sigma/\sqrt{N_s}$, where σ is the standard deviation of the single measurement of K and N_s the number of samples. The values of K are normalised by the corresponding value of the unladen case K_0 (no back-reaction on the fluid). When the bubble feedback is active an attenuation of the t.k.e. of order 10% is measured within error-bars accuracy. The modification is controlled by St_η and φ_v. The effect is progressively more pronounced for increasing St_η. The largest modification occurs for $St_\eta = 0.1$ and $St_\eta = 0.2$, where the bubble clustering is more intense as it will be discussed in later sections. Therefore, the effect of the dispersed phase on the largest scales of turbulence is more effective when the feedback follows from the bubble clusters, rather than evenly dispersed bubbles.

The reduction of K is equally divided among its three cartesian contributions. The stream-wise $\langle \upsilon_1^2 \rangle$, span-wise $\langle \upsilon_2^2 \rangle$, and vertical (direction of the mean shear) $\langle \upsilon_3^2 \rangle$ velocity variances are shown in figure 3.3, figure 3.4 and figure 3.5, respectively. Data are normalised by root mean square values of the unladen case, namely $\langle \upsilon_1^2 \rangle_0$, $\langle \upsilon_2^2 \rangle_0$ and $\langle \upsilon_3^2 \rangle_0$. This behaviour is quite different from what is observed in two-way coupled simulations of inertial particles in the homogeneous shear flow [57], and wall bounded flows [38] where a preferential modulation of turbulence occurs being the stream-wise

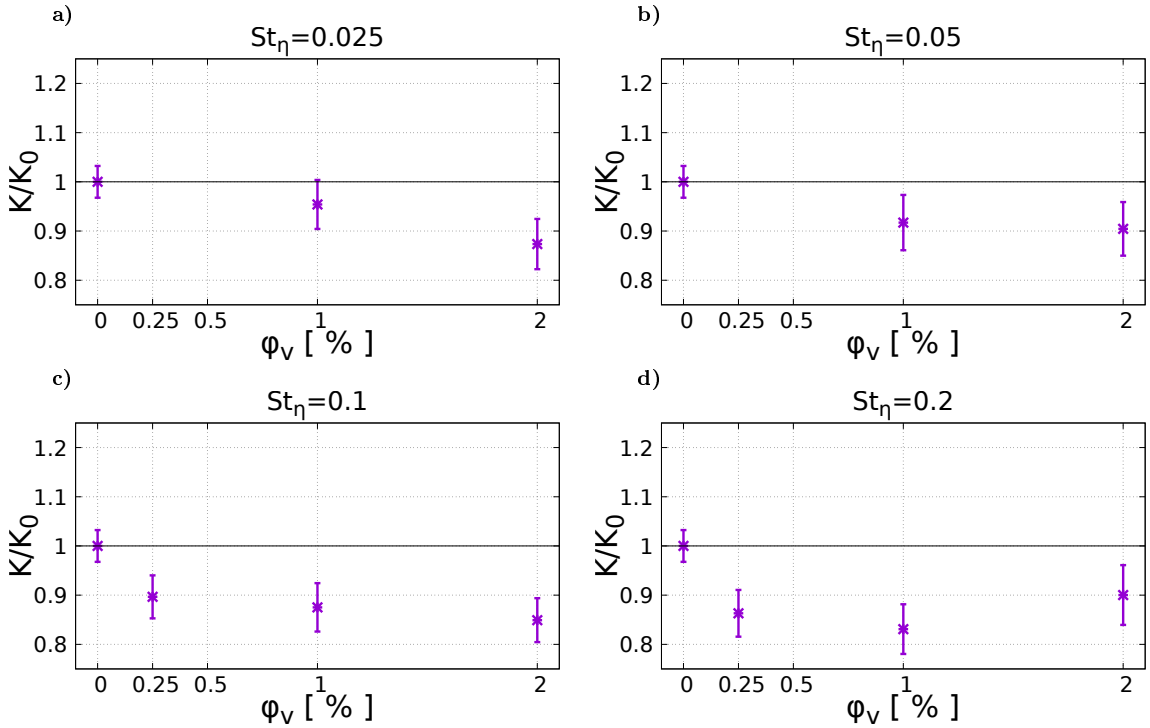

Figure 3.2: Turbulent kinetic energy K, normalised by the value of the unladen case K_0 (no back-reaction on the fluid), plotted versus the percentage void fraction. Panel **a)** $St_\eta = 0.025$; panel **b)** $St_\eta = 0.05$; panel **c)** $St_\eta = 0.1$; panel **d)** $St_\eta = 0.2$.

velocity variance attenuated more than the stream-wise and vertical component as the mass loading is increased.

The attenuation of the energy content K is accompanied by the reduction of the energy dissipation rate ϵ, reported in figure 3.6. As for the turbulent kinetic energy, the energy dissipation ϵ, along with its asymptotic standard error, is normalised by the value of the unladen case ϵ_0. The trend found for the t.k.e., is also found for this small scale observable. The modification increases with St_η. Likewise the turbulent kinetic energy, the reduction of ϵ is accentuated for $St_\eta = 0.1$ and $St_\eta = 0.2$. The behaviour is monotonic in the void fraction in all the cases apart from the bubble populations at the largest Stokes number . In fact, for $St_\eta = 0.2$ we observe, within the error bars accuracy, a minimum in the dissipation rate at $\varphi_v = 1\%$.

3.4.2 The turbulent kinetic energy and dissipation spectra

This section addresses the turbulent kinetic energy and dissipation spectra. The $3D$ spectrum is defined as the Fourier transform of the autocorrelation function, namely $\hat{E}(\mathbf{k}) = \mathcal{F}[\langle v(\mathbf{x},t) \cdot v(\mathbf{x}+\mathbf{r},t)\rangle]$. Due to the anisotropy of turbulence in the shear flow, $\hat{E}(\mathbf{k})$ depends on the direction of the wave-vector $\mathbf{k}$. The one-dimensional spectrum is extracted by averaging over the sphere of radius $|\mathbf{k}| = k$, namely $E(k) = \oint_{|\mathbf{k}|=k} \hat{E}(\mathbf{k})\, k^2\, d\Omega$, where $d\Omega$ is the solid angle. $E(k)$ represent the contribution to the turbulent kinetic energy given by the scales whose wave number is between k and $k + dk$. When integrated over the whole range of wave numbers $E(k)$ returns the turbulent kinetic energy content K, namely $K = \int_0^\infty E(k)\, dk$. The spectrum of the dissipation is computed from $E(k)$ as $D(k) = 2\nu k^2 E(k)$.

The energy balance in spectral space follows the equation,

$$\frac{\partial E(k)}{\partial t} + V(k) = P(k) - D(k) + \Phi(k)\,. \tag{3.6}$$

Equation (3.6) is the generalisation of the Kolmogorov-Onsager-von Weizsacker-Heisenberg equa-

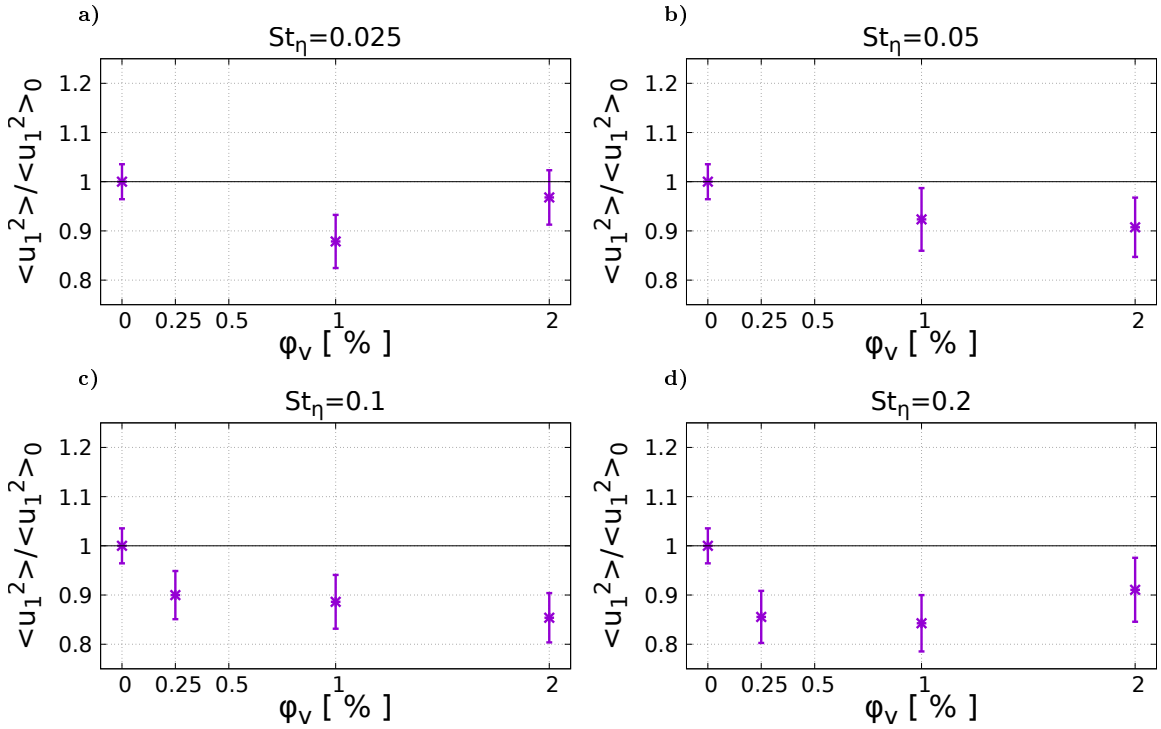

Figure 3.3: Stream-wise velocity variance $\langle v_1^2 \rangle$, normalised by the the value of the unladen case $\langle v_1^2 \rangle_0$ (no back-reaction on the fluid), plotted versus the percentage void fraction. Panel **a)** $St_\eta = 0.025$; panel **b)** $St_\eta = 0.05$; panel **c)** $St_\eta = 0.1$; panel **d)** $St_\eta = 0.2$.

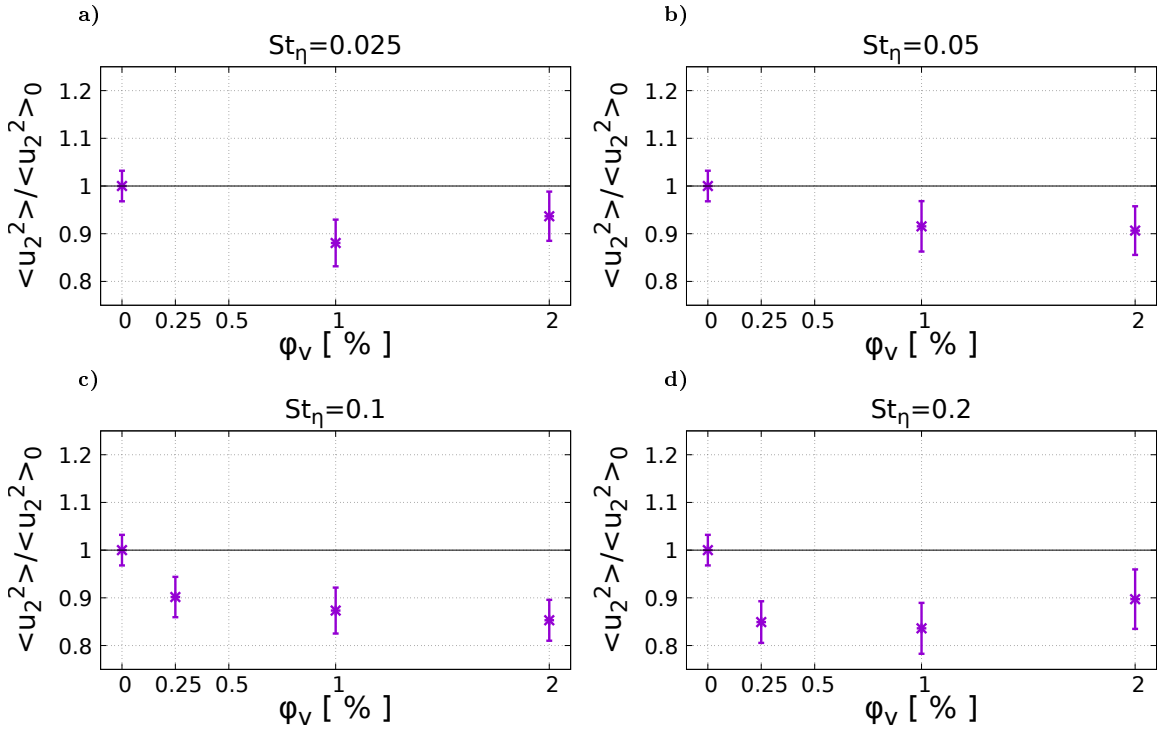

Figure 3.4: Span-wise velocity variance $\langle v_2^2 \rangle$, normalised by the value of the unladen case $\langle v_2^2 \rangle_0$ (no back-reaction on the fluid), plotted versus the percentage void fraction. Panel **a)** $St_\eta = 0.025$; panel **b)** $St_\eta = 0.05$; panel **c)** $St_\eta = 0.1$; panel **d)** $St_\eta = 0.2$.

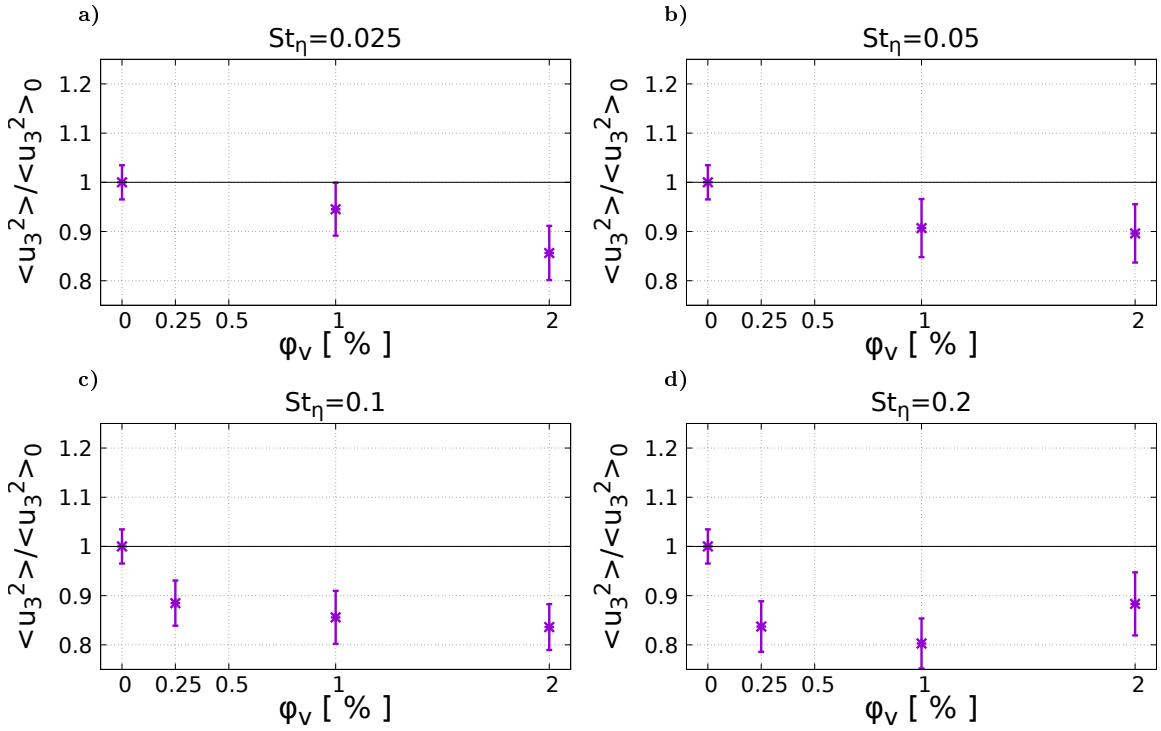

Figure 3.5: Vertical velocity variance $\langle v_3^2 \rangle$, normalised by the value of the unladen case $\langle v_3^2 \rangle_0$ (no back-reaction on the fluid), plotted versus the percentage void fraction. Panel **a)** $St_\eta = 0.025$; panel **b)** $St_\eta = 0.05$; panel **c)** $St_\eta = 0.1$; panel **d)** $St_\eta = 0.2$.

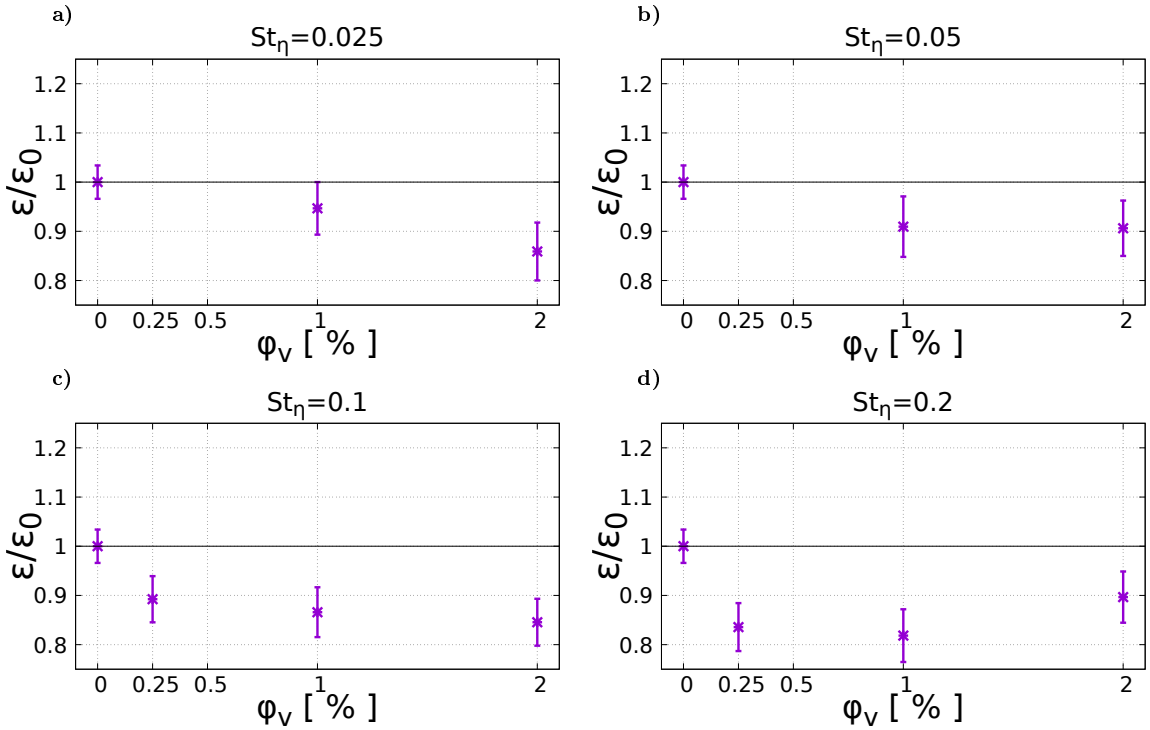

Figure 3.6: Energy dissipation rate ϵ, normalised with the value of the unladen case ϵ_0 (no back-reaction on the fluid), plotted versus the percentage void fraction. Panel **a)** $St_\eta = 0.025$; panel **b)** $St_\eta = 0.05$; panel **c)** $St_\eta = 0.1$; panel **d)** $St_\eta = 0.2$.

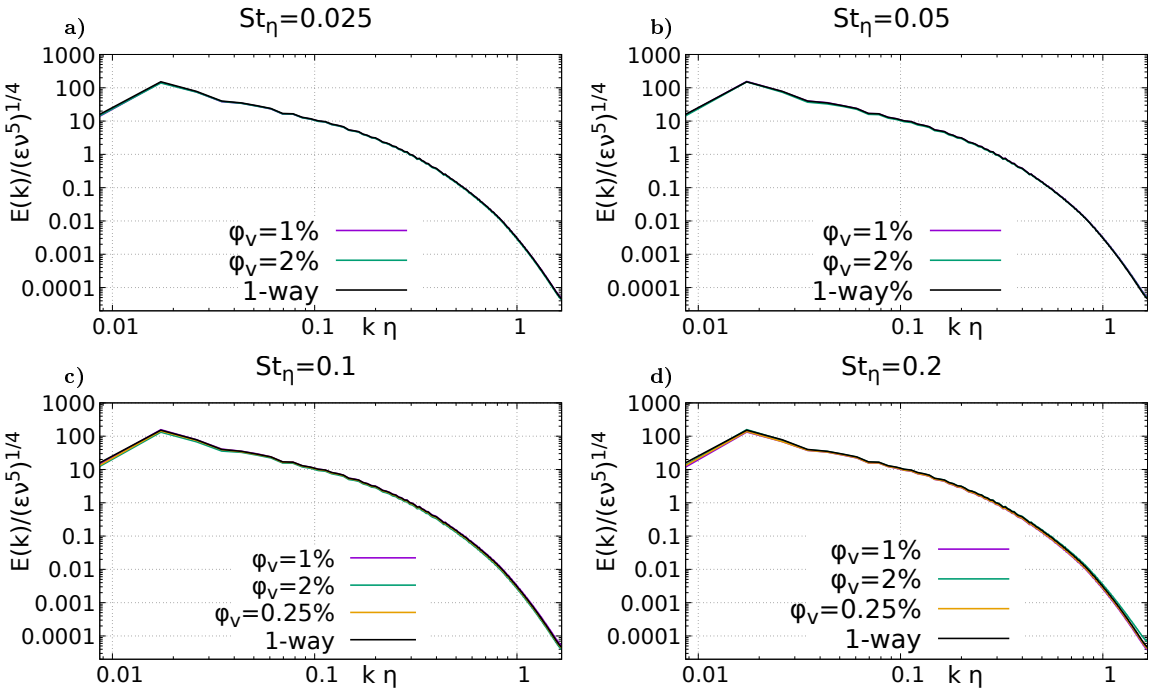

Figure 3.7: 1D energy spectrum $E(k)$ versus wave number. Data are normalised in Kolmogorov units of the unladen case. Panel **a)** $St_\eta = 0.025$; panel **b)** $St_\eta = 0.05$; panel **c)** $St_\eta = 0.1$; panel **d)** $St_\eta = 0.2$. In each panel the available data at different void fractions are reported and compared with the unladen case.

tion [95, 96], for bubble-laden flow where the coupling term Φ arising from the dispersed phase feedback on the fluid has been retained, namely $\Phi(k) = \int_\Omega \Psi_{ii}(\mathbf{k})\, k^2 d\Omega$, where $\Phi_{ij}(\mathbf{k}) = \mathcal{F}\langle f_i(\mathbf{x})\, v_j(\mathbf{x}+\mathbf{r})\rangle$. The spectrum of the non linear term is $V(k)$, and in homogeneous conditions $\int_0^\infty V(k)dk = 0$. The term $P(k) = -SE_{13}(k)$ is the production term where E_{13} is the Reynolds shear stress co-specrtum and $D(k)$ is the dissipation spectrum.

Figures 3.7 and 3.8 show the 1D energy $E(k)$ and dissipation $D(k)$ spectra, respectively. In each panel, data are plotted for bubble populations at fixed St_η and different void fractions. Data are normalised in the unladen Kolmogorov units, i.e. occurring in the one-way coupled simulations. In particular the wavenumber k is normalised by the Kolmogorov length-scale η while the energy and dissipation spectra by $(\epsilon\nu^5)^{1/4}$ and $(\epsilon\nu)^{3/4}$, respectively. For each bubble population, the corresponding data of the unladen case are also shown.

The reduction, of the order of 10%, found in the t.k.e. K and dissipation ϵ involves the first modes of the spectra. Such thin alteration is not observable in the present logarithmic representation, which can represent only large modification. In fact, the logarithmic scale is suitable for describing the behaviour of the intermediate and small scales, where significant alterations are not observed. In particular, no change in the spectral slope found in Ref. [47] can be inferred. In Ref. [47] the PIC approach is used to investigate homogeneous isotropic turbulence laden with point-like bubbles via DNS at $St_\eta = 0.1$ and $\varphi_v = 1.6\%$, where the effect of gravity is also considered. The authors find a depletion of the energy content at the dissipative scales, and augmentation at large scales. This leads to an overall depletion of the dissipation rate. Although the present simulations bear similarity to Mazzitelli et al. [47] for the turbulent kinetic energy, they are in disagreement for how it is distributed across the spatial scales. It is not clear if the different behaviour of the spectra depends on the shortcomings of the PIC approach or on the presence of gravity, which in the our simulations is not considered. In fact, the effects of the buoyancy on the multiphase system have been neglected, since the Stokes and Froud numbers are considered as $St_\eta/Fr_\eta \ll 1$. Since the presence of gravity introduces a further element of anisotropy, it could be relevant to study its effect on the back reaction

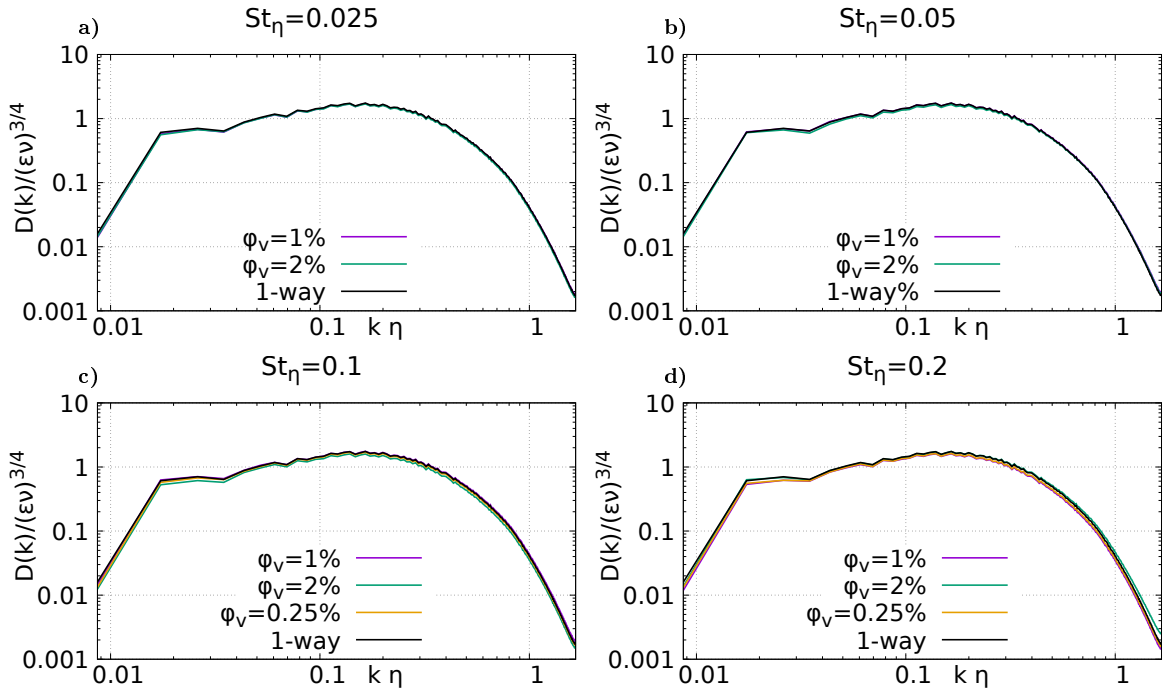

Figure 3.8: 1D dissipation spectrum $D(k)$ versus wave number. Data normalised in Kolmogorov units of the unladen case. Panel **a)** $St_\eta = 0.025$; panel **b)** $St_\eta = 0.05$; panel **c)** $St_\eta = 0.1$; panel **d)** $St_\eta = 0.2$. In each panel the available data at different void fractions are reported and compared with the unladen case.

term. On the other hands, the PIC approach suffers shortcomings when the feedback of an uneven bubble population is represented on the Eulerian grid, where the carrier phase equations are solved [59]. Due to biases in the feedback regularisation, PIC introduces an unphysical forcing, which acts on grid scale. To avoid this numerical error, the number of bubbles N_p per computational cell N_c should be large. However, this condition is not fulfilled in Ref. [47] since $N_p/N_c \simeq 0.05$. Therefore, the relatively high energy content at small scales found by the Authors might also be a side effect introduced by the PIC approach. In contrast, the ERPP approach can account, on a more solid physical ground, for the effects of uneven distributed population of bubbles. This is the case for the relatively diluted suspension considered here. The effect of the bubble feedback on the smallest dissipative scales seem to be less relevant than what observed in previous studies based on the PIC approach, where however gravity was present. Further investigations are required to understand the role of buoyancy and PIC shortcomings, on the spectra in Ref. [47], and results are not conclusive.

The spectral energy budget, equation (3.6), is shown in figure 3.9 for two reference cases, namely $St_\eta = 0.025, \varphi_v = 1\%$ and $St_\eta = 0.2, \varphi_v = 1\%$ which represent two limiting cases in terms of the Stokes number. In both cases, the relevant result is that the spectral energy flux $\Phi(k)$ is always negligible and the dominant terms are $D(k)$, $P(k)$ and $V(k)$ even though small fluctuations in $D(k)$, $P(k)$ and $V(k)$, of the order of few percent are observed. Therefore, rigid (and small) bubbles are unable to directly affect the turbulent energy budget through the coupling term $\Phi(k)$. In fact, turbulence modulation occurs only via a direct changes of the turbulence production term $P(k)$, due to modification of the Reynolds shear stress co-spectrum. It is also clear that the dissipation rate depletion observed in figure 3.6 must necessarily be accompanied by the reduction in the turbulent production $\mathcal{P} = -S\langle v_1 v_3 \rangle$, since the global amount of energy intercepted by the bubbles $\Phi_p = \int_0^\infty \Phi(k)\, dk$ is vanishing.

We want to stress the differences between the mechanisms of interphase energy transfer in the shear flows due to microbubbles and tiny heavy-particles by considering the particle-laden shear flows discussed in Ref. [97, 57], where the ERPP approach was used for the inertial particles. The

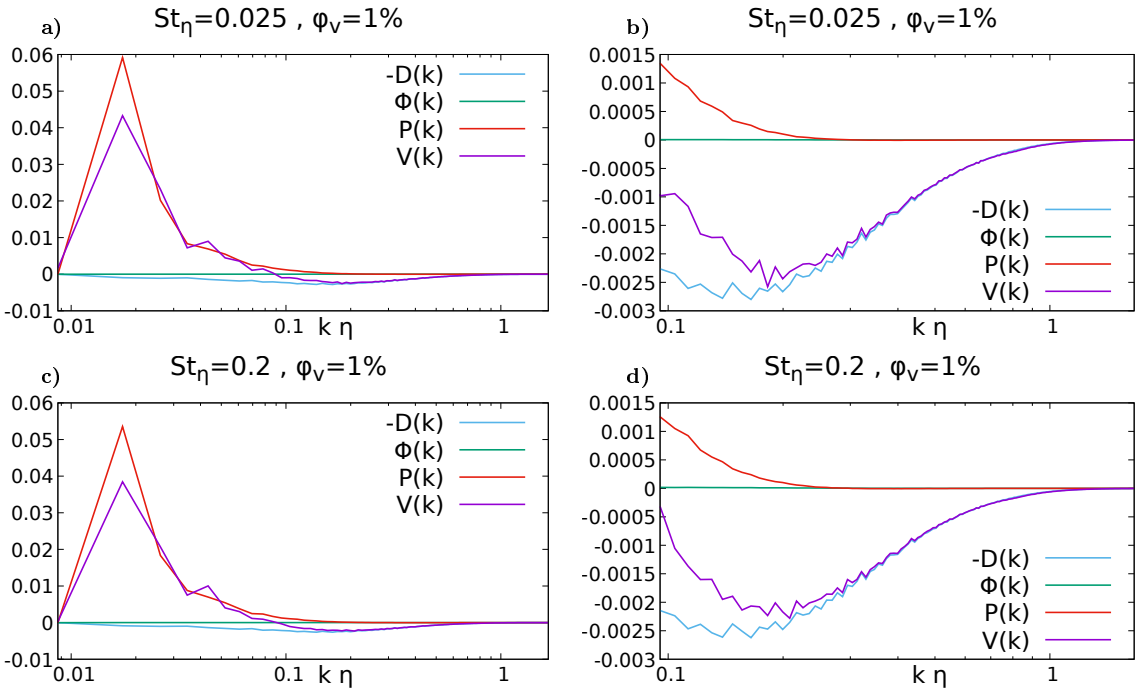

Figure 3.9: Spectral energy budget. $P(k)$ turbulent kinetic energy production; $D(k)$ energy dissipation; $V(k)$ non linear energy transfer; $\Phi(k)$ inter-phase momentum coupling due to the bubble back-reaction. Panel **a)** $St_\eta = 0.025\,\varphi_v = 1\%$; panel **c)** $St_\eta = 0.2\,\varphi_v = 1\%$. Panels **b)** and **d)** show a close up view of the smallest dissipative scales for the two cases respectively.

Authors show how inertial particles suppress the turbulent kinetic energy up to 40%, much more than what is observed here for microbubbles. Moreover, the stream-wise velocity component is less affected by the particle back-reaction, in contrast to what shown in this work, where the bubble large-scale modulation is almost isotropic. However, the most important difference is the particle inter-phase momentum flux $\Phi(k)$, and its global amount $\Phi_p = \int_0^\infty \Phi(k)\,dk$ that appears in the global t.k.e. budget $0 = \mathcal{P} - \epsilon + \Phi_p$, that is not negligible. In particle-laden shear flow the modification of the turbulence dynamics mainly occurs due to the energy intercepted by the dispersed phase. This mechanism is quite different from what happens for bubbles. In fact, the bubble-induced turbulence modification is solely due to the change in the production of turbulent kinetic energy, i.e. the Reynolds shear stress co-spectrum, and therefore in the viscous dissipation, being the inter-phase momentum flux $\Phi(k)$ always negligible. The differences in turbulence modification might be due to two aspects. Firstly the presence of the added-mass force in the bubble momentum equation drastically changes the bubble dynamics. Bubbles and particles selectively concentrate in different regions of the turbulent flow, i.e. the former accumulate in the low-pressure regions (high vorticity) and the latter form clusters in the strain regions (low vorticity). Secondly, the density ratio, and therefore the mass loading, is three order of magnitude smaller in the case of bubbles. This considerably reduces the ability of the gaseous phase to exchange momentum with the fluid, suggesting that the volume fraction could be used to provide a more fair comparison.

3.4.3 The bubble clustering in the two-way coupling regime

Figure 3.10 provides a snapshots of the instantaneous bubble configuration for increasing Stokes number at fixed void fraction. Two thin slices in the cross-flow $(y-z)$ and stream-wise $(x-z)$ plane are shown in the two columns of the figure. The typical bubble clustering, with bubbles that aggregate into thin elongated structures, is progressively more visible for increasing St_η. The clusters are correlated with high fluid enstrophy levels, corresponding to the more intense turbulent coherent vortical structures. The passive tracer limit, where bubbles faithfully follow the fluid,

seems close to the case $St_\eta = 0.025$. The ballistic limit, where bubbles are not influenced by fluid, is far to be achieved in the range of the Stokes number considered in this study.

In the homogeneous shear flow, the mean flow orients the largest vortical structure preferentially in the direction of the mean strain, that is the bottom-left/top-right direction in the $(x-z)$ plane. When the flow is laden by heavy particles, this anisotropy is proved to be transferred to the small scale clusters [98, 99]. A similar trend is found also for the bubbles. This behaviour is quite difficult to be observed by visual inspection, even though bubble filaments appear in panels **f)** and **h)** of figure 3.10. The bubble clustering can be more quantitatively measured following a more rigorous statistical approach based on the Angular Distribution Function (ADF) [99]. The ADF is the measure of the probability to find a bubble pair at distance r and oriented along the unit vector $\hat{\mathbf{r}}$. The ADF is defined as

$$g(r,\hat{\mathbf{r}}) = \frac{1}{r^2}\frac{d\nu_r}{dr}\frac{1}{n_0}, \tag{3.7}$$

where $n_0 = 0.5N_p(N_p-1)/V_D$ is the volume density of bubble pairs in the volume V_D, $\nu_r(r,\hat{\mathbf{r}})d\Omega$ is the numbers of bubble pairs contained in the spherical cone of radius r with axis along the direction $\hat{\mathbf{r}}$ and amplitude $d\Omega$. Therefore, the ADF contains information about the shape of the clusters and the distance between the bubble pairs. The spherical average of the ADF is so the called the Radial Distribution Function (RDF), namely $g_{00}(r) = 1/(4\pi)\int_\Omega g(r,\hat{\mathbf{r}})d\Omega$. The RDF has been already used to characterise clustering in isotropic conditions [100].

Figures 3.11, 3.12, 3.13 and 3.14 provide the ADF at the scale separation $r = d_p$, i.e. at collision scale, for the bubble populations at progressively increasing Stokes number. In the panels of each figure two void fraction, $\varphi_v = 1\%$ and$\varphi_v = 2\%$ are considered, and results are compared with the uncoupled case. At the smallest Stokes number $St_\eta = 0.025$, figure 3.11, the bubble clusters at collision distance are uniformly distributed on the unit sphere and the distribution does not differ from what is observed in the one-way coupling regime for both void fractions. Therefore, it is possible to conclude that no preferential orientation of the clusters occurs in these conditions. Note that the overall concentration is close to the homogeneous value n_0. However, when the Stokes number is progressively increased, see figures 3.12, 3.13 and 3.14, two new features appear. The first feature is that the bubble clusters present a preferential orientation, i.e. the peaks of the ADF are located in a direction corresponding to the bottom-right/top-left direction of the stream-wise $(x-z)$ plane addressed in figure 3.10, meaning that the clusters actually show a measurable anisotropy. The second feature consists in the fact that two-way coupling effects, here parametrised in terms of the void fraction φ_v, have a measurable effect on the intensity of the clustering when compared with the reference one-way data. This behaviour can be associated to the preferential alignment of the large scale turbulent structures induced by the mean shear. The bubble clusters preserve memory of the large scale directionality due to the coherent vortical structures. This occurs despite the fluid partially recovers isotropy at small scales. Finally, we observe that there is no substantial change in the clusters alignment when two-way coupling effects are present. The two-way coupling effects, however, modify the intensity of the clustering process. The ADF has been also measured for all the bubble populations and all the void fraction at a scale separation of the order of the integral scale (data not shown). At this separation, in all cases, the ADF does not show any anisotropy of the clusters. In fact, for increasing separation, distant bubble pairs are considered which mostly belongs to distinct clusters.

The ADF is a powerful tool to asses the bubble distribution at fixed separation r. However, providing the contour plots for several $r-$separations would be overly verbose, and somehow even confusing in understanding the results. difficulty can be overcome by using a mathematical tool able to capture the behaviour at each scale separation r, namely the $SO(3)$ expansion [101] of $g(r,\hat{\mathbf{r}})$. The method consists in the expansion of the function into the projections on the orthogonal subspaces generated by the spherical harmonics $Y_{jm}(\hat{\mathbf{r}})$,

$$g(r,\hat{\mathbf{r}}) = \sum_{j=0}^{\infty}\sum_{m=-j}^{j} g_{jm}(r)Y_{jm}(\hat{\mathbf{r}}). \tag{3.8}$$

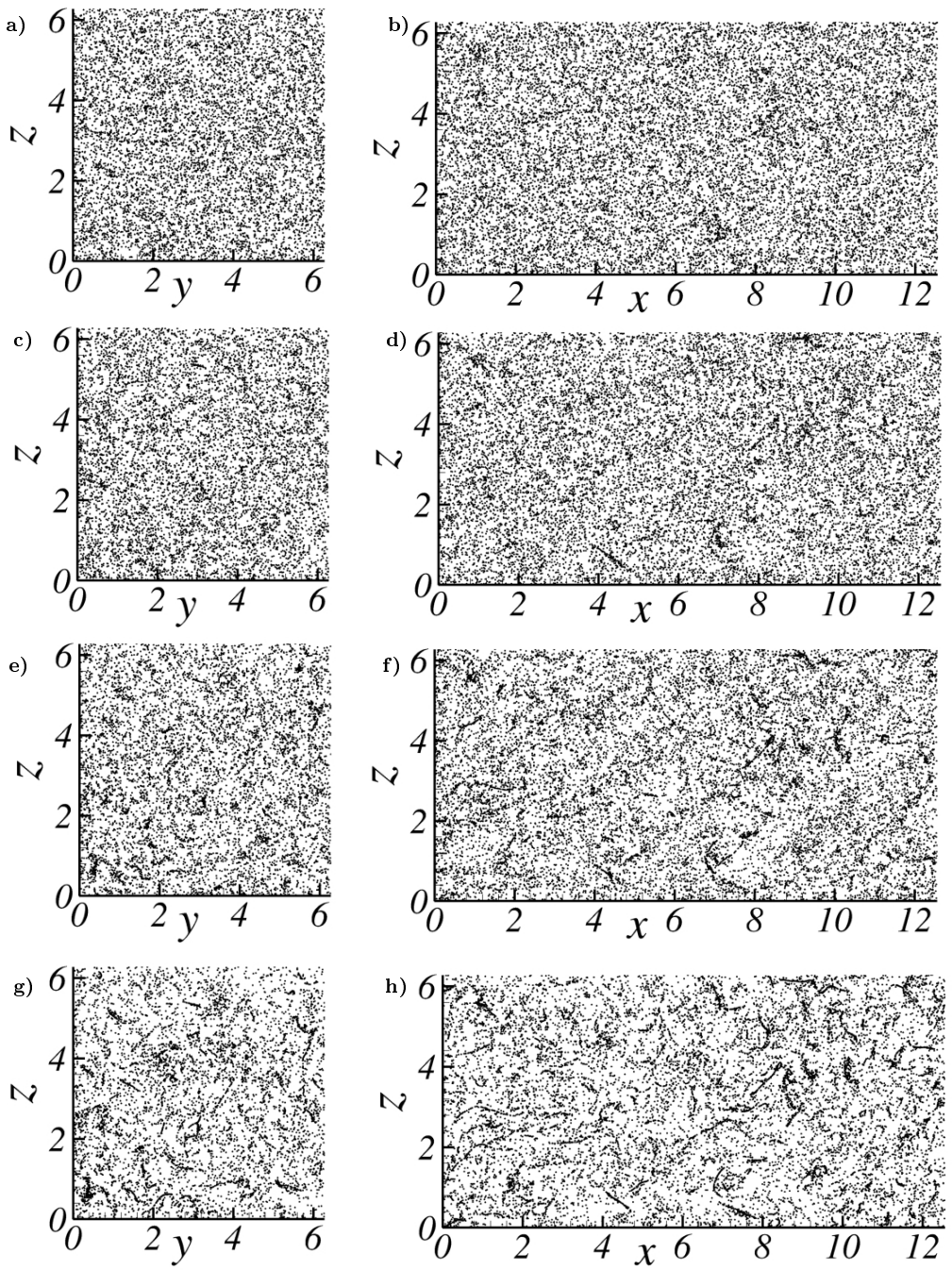

Figure 3.10: Snapshots of the instantaneous bubble position in a thin slice of thickness of the order of few Kolmogorov scales. Left column: the slice is in the cross-flow plane $(y-z)$. Right column: slice is in the stream-wise plane $(x-z)$. The Stokes number increases from top to bottom. Panels **a)**, **b)** $St_\eta = 0.025$; Panels **c)**, **d)** $St_\eta = 0.05$; Panels **e)**, **f)** $St_\eta = 0.1$; Panels **g)**, **h)** $St_\eta = 0.1$; In all cases the volume fraction is $\varphi_v = 1\%$.

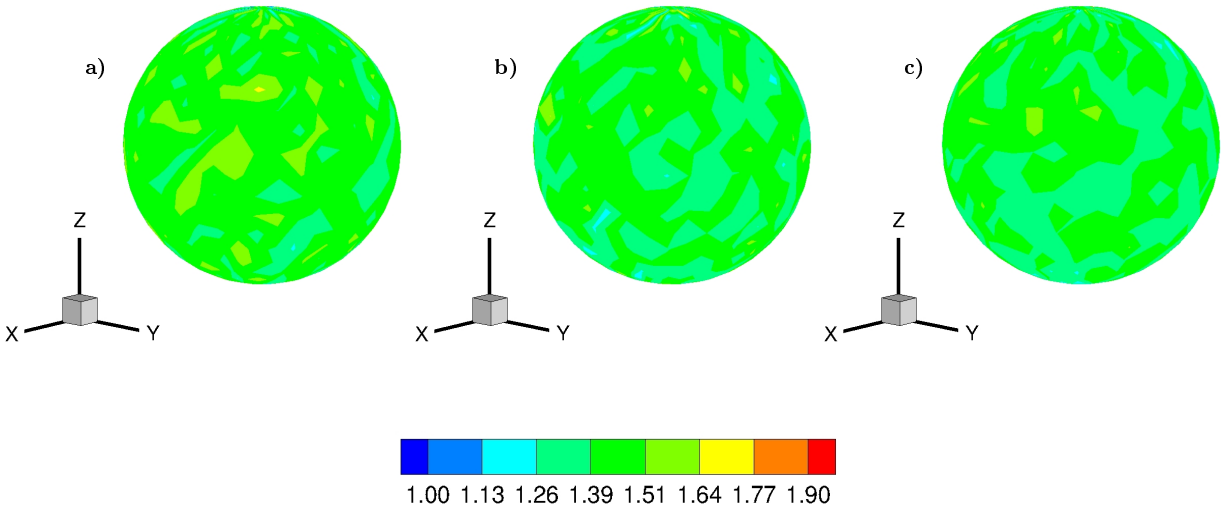

Figure 3.11: The ADF represented on the unit sphere at the collision distance $r = d_p$, for the bubble population $St_\eta = 0.025$. Panel **a)** one-way coupling; panel **b)** $\varphi_v = 1\%$; panel **c)** $\varphi_v = 2\%$

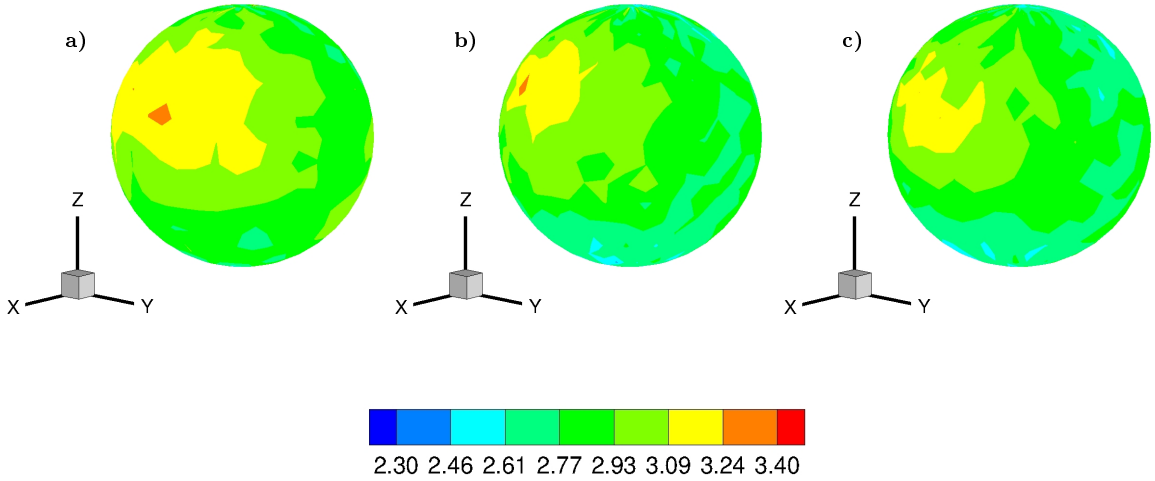

Figure 3.12: The ADF represented on the unit sphere at the collision distance $r = d_p$ for the bubble population $St_\eta = 0.05$. Panel **a)** one-way coupling; panel **b)** $\varphi_v = 1\%$; panel **c)** $\varphi_v = 2\%$

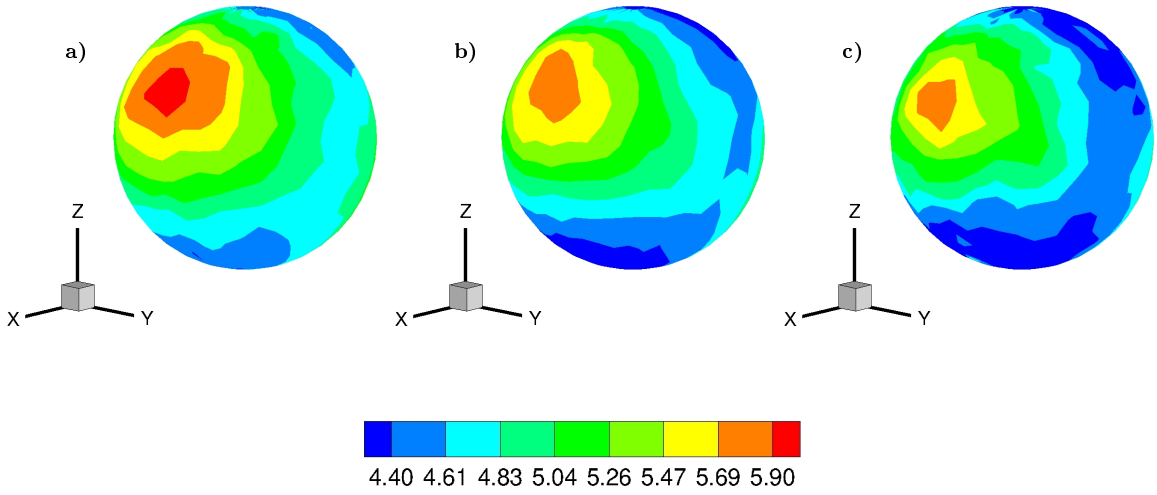

Figure 3.13: The ADF represented on the unit sphere at the collision distance $r = d_p$ for the bubble population $St_\eta = 0.1$. Panel **a)** one-way coupling; panel **b)** $\varphi_v = 1\%$; panel **c)** $\varphi_v = 2\%$

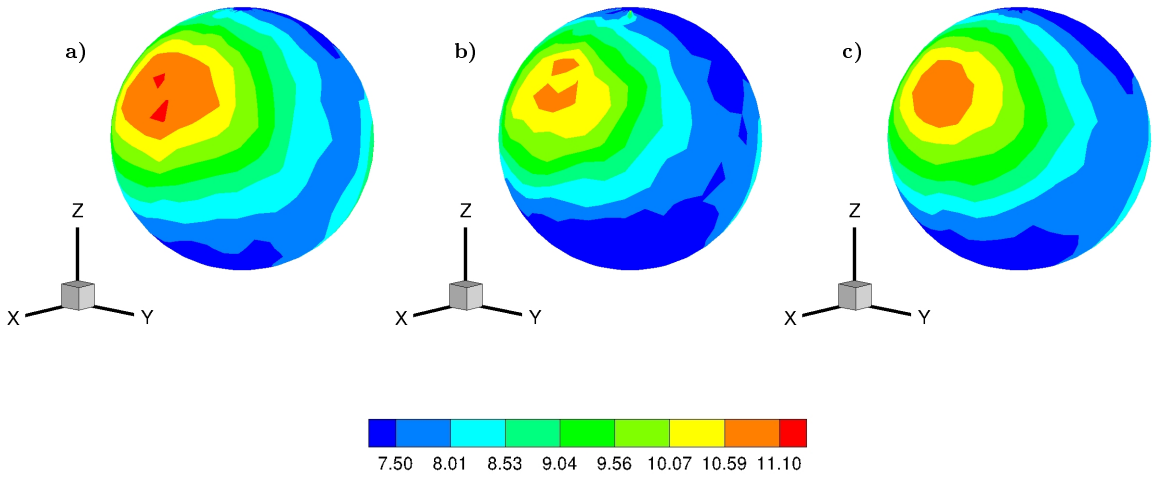

Figure 3.14: The ADF represented on the unit sphere at the collision distance $r = d_p$ for the bubble population $St_\eta = 0.2$. Panel **a)** one-way coupling; panel **b)** $\varphi_v = 1\%$; panel **c)** $\varphi_v = 2\%$

Each sub-space is labelled by the index j, that is spanned by $2j + 1$ base elements Y_{jm}. For instance, the basis of the sub-space $j = 1$ is the set of the spherical harmonics Y_{1-1}, Y_{10} and Y_{11}. The orthogonality condition of the base elements Y_{jm}, $\oint_\Omega Y_{jm} Y^*_{pq} d\Omega = 4\pi\delta_{jp}\delta_{mq}$, and the uniform convergence of the series for the regular function $g(r, \hat{\mathbf{r}})$, provide the expression of the modes $g_{jm}(r)$,

$$g_{jm}(r) = \frac{1}{4\pi} \oint_\Omega g(r, \hat{\mathbf{r}}) Y^*_{jm} d\Omega \tag{3.9}$$

where the superscript * denotes the complex conjugate. In this notation the isotropic component of $g(r, \hat{\mathbf{r}})$, i.e. the Radial Distribution Function (RDF), is represented by the sector $j = 0$, i.e. $g_{00}(r) = \frac{1}{4\pi} \int_\Omega g(r, \hat{\mathbf{r}}) d\Omega$. The sectors with $j \geq 1$, in ordered way, label specific spatial directions, therefore measuring specific anisotropies of the ADF.

Figure 3.15 provides the Radial Distribution Function $g_{00}(r)$ for the available bubble populations. The separation r is normalised by the Kolmogorov length-scale η. Data are plotted from largest scales up to the collision separation $r = d_p$. In each panel, the effect of the back-reaction can be appreciated by comparing the data with the respective unladen case (black line). The power law behaviour of the RDF at small separations proves that bubbles indeed show small scale clustering. The clustering intensity is progressively stronger for increasing Stokes number. At $St_\eta = 0.2$, the local bubble concentration at collision distance is about 10 times the overall homogeneous concentration. Note that the RDF approach to constant value $g_{00}(r) \sim 1$ above a critical scale ℓ_c. This means that the large scale clustering, above scale ℓ_c, recovers the behaviour of the homogeneous distribution. The data show that the general trend of the RDF is only slightly changed when the back-reaction is active, as already discussed when commenting the ADF.

A more detailed analysis of two-way coupling effects on the small scale clustering is provided in figure 3.16, where the RDF $g_{00}(r)$ is normalised by its respective unladen case $g_{00_{1-way}}(r)$ counterpart. The data show a small, though measurable, depletion of small scale clustering that ranges from 5% to order of 10% when the Stokes number is progressively increased form $St_\eta = 0.0025$ to $St_\eta = 0.2$ while the void fraction seems to play a minor role.

The scale-by-scale anisotropic behaviour of the ADF is addressed in figure 3.17 where some significant projections of the ADF $g_{jm}(r)$, up to subspace $j = 6$, are shown for the reference case $St_\eta = 0.1$, $\varphi_v = 2\%$. Due to the symmetry of the flow, many other modes are negligible and the figure provides only projections with significant amplitudes. The signal $g_{jm}(r)$ rapidly decreases with the order of the sector j indicating that the anisotropy in the ADF $g(r, \hat{\mathbf{r}})$ is dominated by the sectors $j \leq 2$. The mode with higher intensity is the $g_{21}(r)$ projection which corresponds to the spherical harmonic Y_{21}. Given the reference frame adopted, this specific harmonic selects the

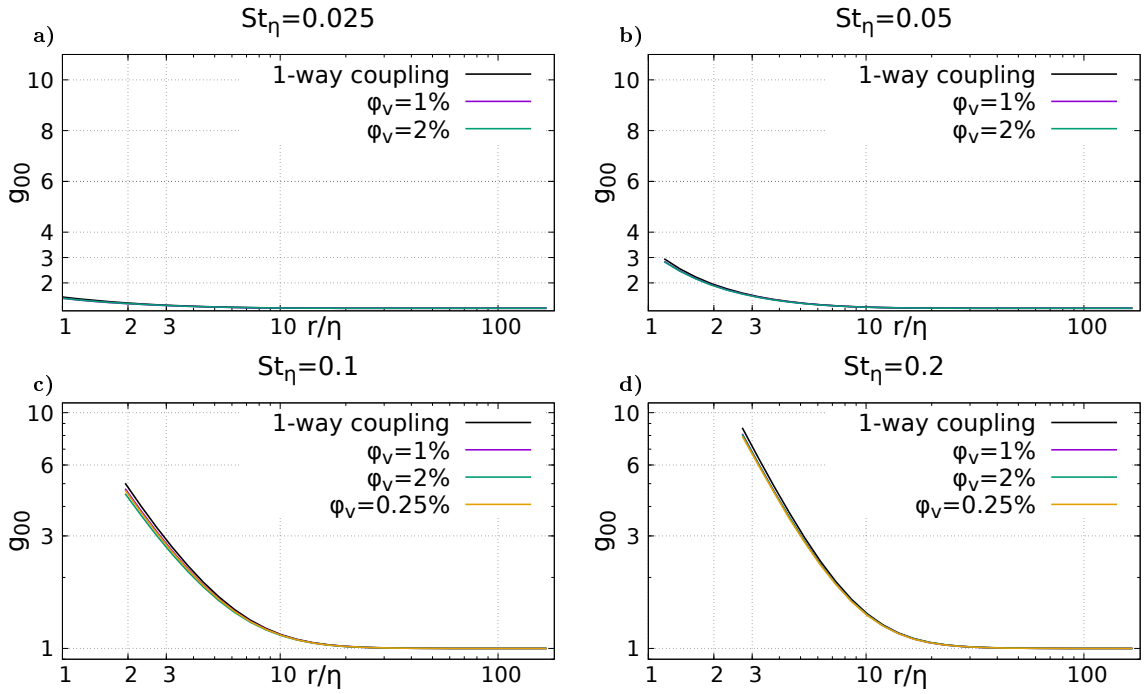

Figure 3.15: Isotropic projection g_{00} of the ADF versus separation r. The sector $g_{00}(r)$ is the average of $g(r, \hat{\mathbf{r}})$ over the solid angle and is proportional to the probability to find two bubbles at separation r. Panel **a)** $St_\eta = 0.0025$; panel **b)** $St_\eta = 0.05$; panel **c)** $St_\eta = 0.1$; panel **d)** $St_\eta = 0.2$. In each panel the available data for different void fractions φ_v are compared against the reference one-way coupling data (black line).

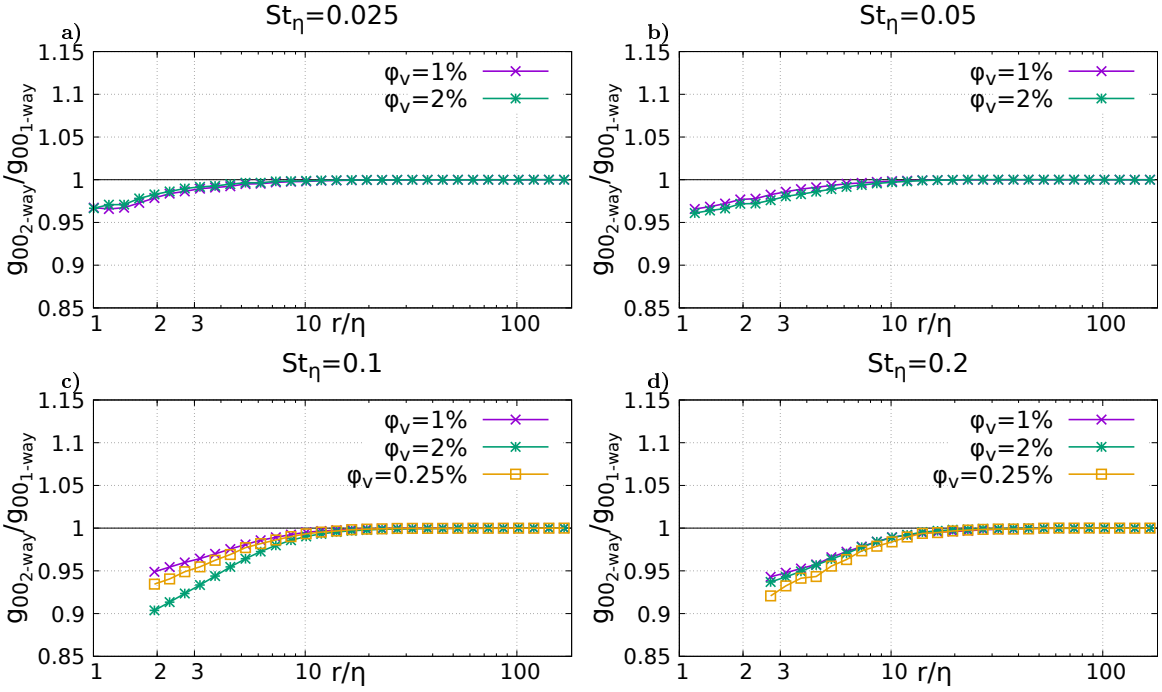

Figure 3.16: Ratio between the RDF in the two-way coupling regime $g_{00_{2-way}}(r)$ and its counterpart in the one-way coupling regime $g_{00_{1-way}}(r)$. Panel **a)** $St_\eta = 0.0025$; panel **b)** $St_\eta = 0.05$; panel **c)** $St_\eta = 0.1$; panel **d)** $St_\eta = 0.2$. In each panel the available data for different void fractions φ_v are plotted for each bubble population.

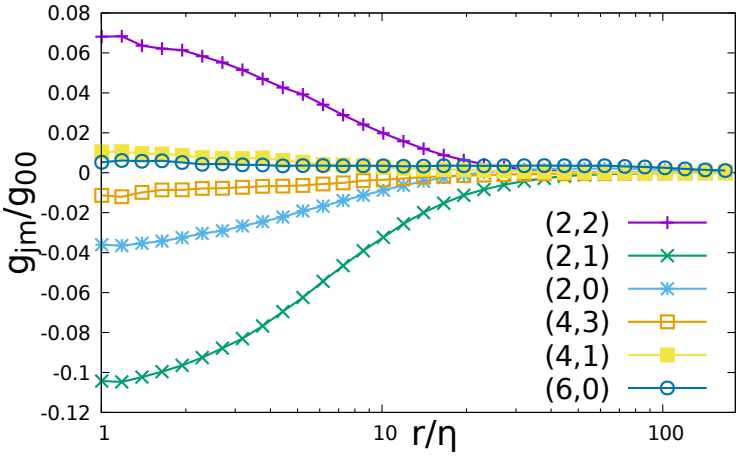

Figure 3.17: Anisotropic projections of the ADF $g_{jm}(r)$ normalised by the isotropic component $g_{00}(r)$ up to the sector $j = 6$. Only the higher signal sectors are shown for the reference case $St_\eta = 0.1$ $\varphi_v = 2\%$. The mode $(2,1)$ captures the bubble pair alignment along the bisector of the $(x-z)$ plane containing the mean flow. The mode $(2,2)$ selects the bubble pair alignment along the stream-wise direction.

principal strain directions of the mean flow. Therefore the $g_{21}(r)$ projection measures bubble pairs aligned along the bisector of the first and third quadrant of the $(x-z)$ plane that contains the mean flow. This data corroborate the more qualitative description of the clusters grasped from the visual inspection of the instantaneous bubble positions. The negative sign of $g_{21}(r)$ is due to the sign assumed by $Y_{21}(\hat{\mathbf{r}})$ when the unit vector $\hat{\mathbf{r}}$ spans the directions of space. The signal of the mode $(2,2)$ is also significant. Indeed, the spherical harmonic $Y_{22}(\hat{\mathbf{r}})$ captures, with positive sign, the bubble preferential alignment roughly in the steam-wise direction. Therefore $g_{22}(r)$ partially recovers the anisotropy peaks in $g(r,\hat{\mathbf{r}})$, that however are best captured by $g_{21}(r)$.

The data in figure 3.17 suggest $g_{21}(r)$ as the best representative mode among the anisotropic components of the ADF to be further analysed as one for all. The anisotropy content of the ADF measured by the ratio g_{21}/g_{00}, is reported in figure 3.18 for the available bubble populations. Each panel correspond to a specific Stokes number and compares the ratio g_{21}/g_{00} against the data in the one-way coupling regime (black line) when the void fraction is changed. The anisotropy content of the ADF increases at small scale denoting that the directionality of the clusters becomes more and more defined as bubble pairs approach each other. In other words, as the bubbles accumulate at small scales, the more are orientated with large scale turbulent vortices. A final comment concerns two-way coupling effects, that seems to be almost irrelevant. In fact, the ratio g_{21}/g_{00} is quite close to its one-way coupling regime counterpart, at least for the Stokes numbers and void fractions considered here.

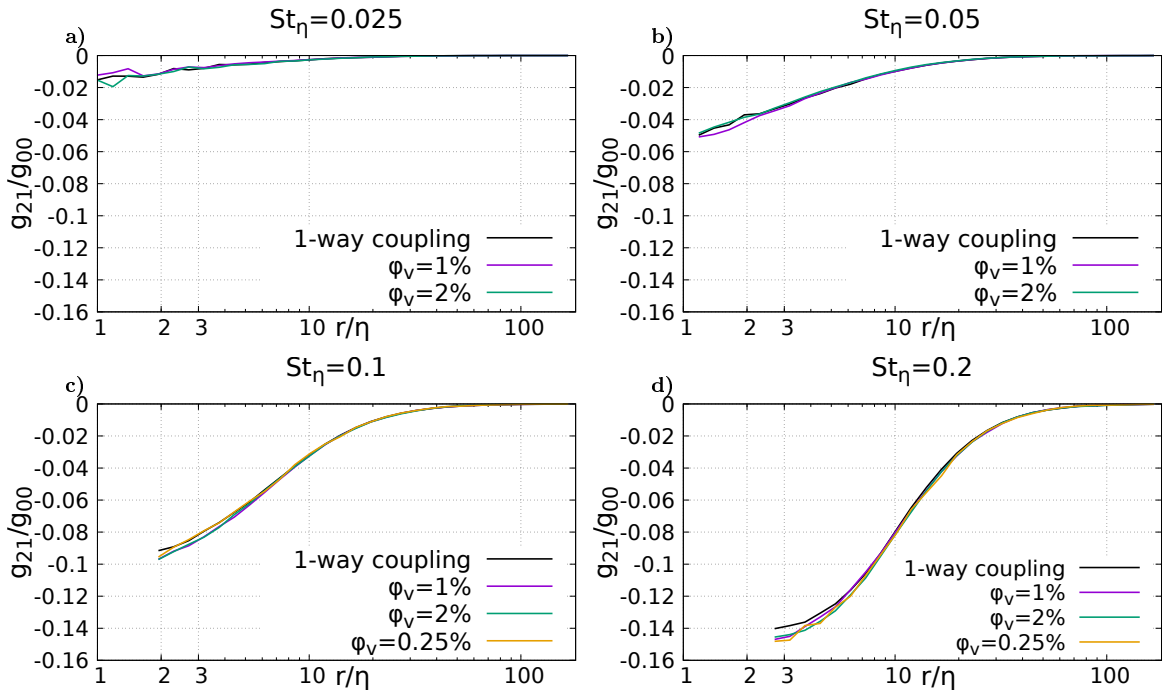

Figure 3.18: Anisotropic projection $g_{21}(r)$ of the $SO(3)$ decomposition of the ADF normalised by the isotropic sector $g_{00}(r)$. Panel **a)** St_η = 0.0025; panel **b)** St_η = 0.05; panel **c)** St_η = 0.1; panel **d)** St_η = 0.2. In each panel the available data for different void fractions are shown and compared against one-way coupling reference case (black line). The $g_{21}(r)$ mode captures bubble pairs orientated with the principal strain direction of the mean flow, i.e. the bisector of the first quadrant of the $(x-z)$ plane.

Chapter 4

The turbulent annular pipe flow

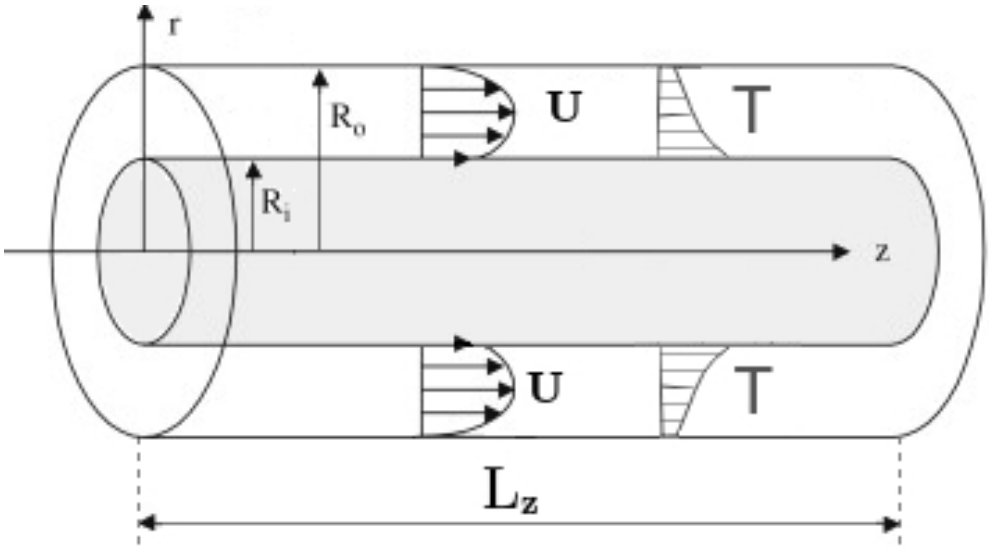

Figure 4.1: Sketch of the annular pipe. R_i and R_o are the inner and outer wall radius. The fluid flows in the gap between the cylinders.

The first part of this thesis has dealt with the inter-phase momentum exchange between small bubbles and homogeneous turbulence. Homogeneous turbulence is an idealised condition, that occurs when the statistical properties are invariant under arbitrary translation. Real turbulence tends to be homogeneous far from the walls, like in the centre of channels and pipes, or in atmospheric flows. Although the homogeneous property is never fully achieved, homogeneous turbulence has large interest since it greatly simplifies the understanding of turbulent flows. Due to the innovation of the research, our first study of bubbly flows has been conducted in the homogeneous turbulence. The complexity introduced by an non-homogeneous background flow is investigated in the later stage. We would aim at analysing bubbly flows in a more realistic fluid dynamic problem: a wall-bounded configuration. The presence of the wall introduces a non-homogeneous spatial direction , perpendicular to the wall. This inhomogeneity is transmitted to the injected discrete phase. The result is that the concentration of the discrete phase exhibits a peak close to the wall regions. The phenomenon is known as turbophoresis [102], and depends on the inertia of the transported phase, i.e. by τ_p. The turbopheresis is of crucial importance to determine the effect of the dispersed phase to the turbulent field. In fact, the massive particle or bubble clusters interact with the vortical structures in the buffer layer, affecting the average viscous stresses in the vicinity of the wall. Under constant flow rate, the result is the modification of the viscous wall drag. The nature of such modification depends on the phase of the dispersed phase. If bubbles tend to reduce the resistance, inertial particles increase it. After studying the depletion of homogeneous turbulence due to a

gaseous phase, we should expand the investigation to a wall-bounded configuration. However the momentum coupling model that we have adopted, i.e. ERPP, is restricted to the point-particle regime. As discussed in chapter 3, the small size of a bubble considerably reduces its aptitude of being deformed. The bubble deformation plays a crucial role in the drag reduction . As long as the bubble is rigid, the energy exchange can occur only through the momentum transfer. However this effect is small due to the very low density ratio ρ_p/ρ_f . In a wall-bounded domain the bulk modification of the flow is deemed to be negligible. In fact, only when bubbles are large and deformable [66, 67, 68], the near-wall vortical structures are altered, through interphase and wake effects, and they lead to the well-known reduction of dissipation. The main objective, in the second stage of the present research, is to understand when the wall drag can be affected by a dispersed phase. Therefore, the second part of the research is devoted to addressing wall-turbulence laden with inertial particles. In this case the well-acknowledged effect on the turbulent field, due to the dispersed phase, is the increase of the viscous wall resistance, occurring in the point-particle regime. Moreover, we know that the drag augmentation is sometimes accompanied by the increase of the heat exchange [36]. This phenomenon can be exploited to improve the heat exchanger efficiency, and still must be well understood. In the research that we are going to introduce, the effect of tiny particles on concentric tube heat exchangers will be investigated via Direct Numerical Simulations. Between the many optional configurations, we have chosen the concentric tube heat exchanger, that is the simplest one. It has two tubes, one inside the other. One tube carries hot fluid, the other carries cold fluid. With such purpose we propose a specific topology: the annular pipe. This system is made of the annulus between two concentric cylinders, through which the suspension flows. The flow is periodic in the stream-wise direction, while heat flux is provided from the walls. In particular, the external surface is cold, while the internal one is hot. The sketch of the domain is presented in figure 4.1.

4.1 Short overview of the numerical techniques

In this section we shortly report about the numerical techniques employed to carry out the DNSs of the annular pipe flows. The numerical scheme is verbosely discussed in the Appendix, section C. The Exact Regularised Point Particle (ERPP) method, that is used to achieve the inter-phase momentum exchange between the carrier and the dispersed phase, is briefly discussed as well. The detailed discussion of the momentum coupling model is provided in section 2 and refers to the original paper [38].

The carrier flow is laden with small inertial particles of vanishing particle Reynolds number $Re_p = \langle \mathbf{u}|_\mathbf{p} - \mathbf{v_p} \rangle d_p/\nu$. In a wall-bounded flow this means that the particle diameter d_p is smaller than the viscous length-scale ℓ^*. Under this assumption, the dispersed phased is modelled as a collection of points, to which concentrated forces are applied. The fluid on the other hands experiences the dispersed phases as a system of singular forcing. The singular forcing is regularised by mean ERRP, where a wall correction is included in the particle disturbance.

The regularised standard incompressible Navier-Stokes equations of the annular pipe are reported below

$$
\begin{cases}
\nabla \cdot \mathbf{u} = 0 \\
\rho_f \left(\dfrac{\partial \mathbf{u}}{\partial t} + \mathbf{u} \cdot \nabla \mathbf{u} \right) = -\nabla p - \dfrac{dP}{dz} \hat{e}_3 + \mu \nabla^2 \mathbf{u} + \mathbf{f}_p \\
\rho_f c_p \left(\dfrac{\partial T}{\partial t} + \mathbf{u} \cdot \nabla T \right) = \kappa \nabla^2 T \\
\mathbf{u}(\mathbf{x}, t)|_{\mathcal{W}_{R_i}} = 0 \\
\mathbf{u}(\mathbf{x}, t)|_{\mathcal{W}_{R_o}} = 0 \\
T(\mathbf{x}, t)|_{\mathcal{W}_{R_i}} = T_i \\
T(\mathbf{x}, t)|_{\mathcal{W}_{R_o}} = T_o
\end{cases}
\tag{4.1}
$$

$\frac{dP}{dz}$ is the averaged pressure gradient in the stream-wise direction $\hat{e}_3$. The pressure gradient sustains the turbulence, since it is responsible of the energy inlet. The temperature is evolved as a passive scalar by the Fourier equation, where κ is the thermal diffusivity and c_p heat capacity at constant pressure. The velocity $\mathbf{u}(\mathbf{x}, t)$ and temperature field $T(\mathbf{x}, t)$ are periodic along the stream-wise and azimuthal directions. Therefore periodic boundary conditions are enforced at the inlet and outlet surface. The no-slip condition is applied at the cylindrical walls, where also two different uniform temperatures are enforced.

The momentum-exchange occurs via the extra singular forcing term $\mathbf{f_p}(\mathbf{x}, t)$, which following the treatment of ERPP reads:

$$
\mathbf{f}_p(\mathbf{x}, t) = -\sum_{p=1}^{N_p} \{ \mathbf{D}_p(t - \epsilon_R) g[\mathbf{x} - \mathbf{x}_p(t - \epsilon_R), \epsilon_R] + \widetilde{\mathbf{D}}_p(t - \epsilon_R) g[\mathbf{x} - \widetilde{\mathbf{x}}_p(t - \epsilon_R), \epsilon_R] \}
\tag{4.2}
$$

The method of images is employed to recover near-wall effects, with $\widetilde{D}_p$ and $\widetilde{x}_p$ denoting the hydrodynamic force and position of the mirrored particle with respect to the local tangent plane. The approach is valid when the wall curvature is smaller than the length-scale σ_R, that is the smallest resolved length-scale of the particle disturbance. The regularising length-scale is chosen as $\sigma_R = 3/2\Delta z$, where Δz is the stream-wise grid spacing. The time-scale ϵ_R is calculated through the relation $\sigma_R = \sqrt{2\nu\epsilon_R}$, where ν is the fluid kinematic viscosity.

The system of partial differential equations (4.1) is solved, via direct numerical simulation, in cylindrical coordinates, exploiting a second order finite difference scheme on a staggered grid [103]. The classical Chorin's projection method [104], is employed to enforce the divergence-free constraint imposed by the mass balance. The pressure field is evaluated through a Laplace problem, after being expanded in the Fourier series in the azimuthal and streamwise directions. A Total Variation Diminishing (TVD) scheme is employed to treat the convection term of the Fourier equation. The integration in time is explicitly performed using a third-order low-storage Runge-Kutta algorithm.

4.1.1 The dispersed phase

The dispersed phase is made of small spherical solid-particles of diameter d_p smaller than the viscous length-scale ℓ^*. The particles are modelled as material point of mass m_p, whose evolution is prescribed by the standard Newton's law

$$
\frac{d\mathbf{x}_p}{dt} = \mathbf{v}_p(t), \quad m_p \frac{d\mathbf{v}_p}{dt} = \mathbf{D}_p(t)
\tag{4.3}
$$

where $\mathbf{D}_p(t)$ is the hydrodynamic force due to fluid stresses. The analytic expression of $\mathbf{D}_p(t)$ was derived independently by Maxey & Riley [61] and Gatignol [82]. In the case of particle-laden flows, i.e. high density ratio, the equation reads

$$
\mathbf{D}_p = 3\pi\mu d_p(\mathbf{u}_{(0)}|_p - \mathbf{v}_p)
\tag{4.4}
$$

In the equation μ is the dynamic fluid viscosity and $\mathbf{v}_p$ the velocity of the particle. $\mathbf{u}_{(0)}|_p$ is the unperturbed fluid velocity field, where the subscript "p" denotes that it is evaluated at particle position $\mathbf{x}_p(t)$. The unperturbed velocity is the velocity field $\mathbf{u}|_p$ in the absence of the p-th particle. This undisturbed field can be evaluated, thanks to ERPP, by subtracting the particle self-disturbance of the p-th particle $\mathbf{u}_{(1)}|_p$, from the complete field $\mathbf{u}|_p$.

The Faxen correction of the Stokes force is discarded due to the small particle diameter d_p. The fluid inertia, the added-mass and the Basset force are neglected as well, due to the high density ratio ρ_p/ρ_f. The buoyancy can be neglected in the present case, since the acceleration due to gravitational forces is negligible as compared with the contribution from the Stokes force. In other words $St^+/Fr^+ << 1$, where $Fr = a^+/g$ and $St^+ = \tau_p/\tau^*$ are the Froud and Stokes numbers based on the viscous length and time scale.

The particle time response $\tau_p = \frac{1}{18\nu}\frac{\rho_p}{\rho_f}d_p^2$ is represented, with respect to the viscous time-scale τ^*, by the Stokes number $St^+ = \tau_p/\tau^*$. Similar to bubbles, see the discussion in 3, the Stokes coefficient influences the particle transport across the turbulent field. The tracer and ballistic regimes occur when the particle time response is much smaller or larger than the viscous-time scale, namely $St^+ << 1$ and $St^+ >> 1$ respectively. The turbophoresis occurs at the intermediate regime $St^+ \sim 1$. Owing to the crucial role of turbophoresis in the drag modification, the Stokes number eventually controls the turbulence modification in the two-way coupling regime. The second important parameter is the particle mass loading $\Phi_p = m_D/m_F$, i.e. the ratio between the mass of the dispersed phase $m_D = N_p m_p$ and of the fluid m_F. Although the flow that we will consider has large particle mass loading, the suspension is dilute. In fact, owing to the large particle to fluid density ratio $\rho_p/\rho_f = 180$, the void fraction is $\varphi_p \approx 0.1\%$. Therefore the inter-particle collisions rarely occur and the four-way coupling interactions are discarded.

4.1.2 The objectives of the research

We will answer three important questions concerning the dynamic of the multiphase system:

- How does turbulence affect the particle transport?
- Are the turbulent coherent structures and the wall drag affected by the inter-phase momentum coupling?
- Is the heat exchange influenced by the modified turbulent mixing?

The particle transport is subjected to the asymmetric annular flow, owing to the different wall curvature. The influence of this non-homogeneous turbulence on a dispersed phase must be addressed. The turbophoresis can be in principle different when observed at the internal or external side. This phenomenon is crucial since the near-wall turbulent coherent structures, which can be modulated by the massive particle clusters, are responsible of the production of the turbulent kinetic energy in the whole channel. The modification of the turbulent kinetic energy, due to the high particle mass loading, is expected. We will understand if such alteration could produce the increase (or decrease) of the viscous resistance.

Which could be the effect on the temperature field is an other important question. The heat exchange is provided through the temperature difference at the walls, and it is regulated by the thermal resistance of the system. The thermal resistance depends on the conductivity the fluid and, in large part, on the turbulent mixing. The particles are thermally inert. Therefore the inter-phase heat-exchange is negligible. In fact, the inter-phase coupling is enforced only on the momentum equations. The modification of the thermal field can still occurs, but only due to the change of the thermal fluid convection. Therefore, we want to understand if the inter-phase momentum exchange can affect the turbulent mixing and the heat transfer as well, in the annular pipe.

4.2 Results and discussion

The following sections report the analysis of the particle-laden annular pipe flow. The turbulence is studied by means of the first and second moment statistic, two-point correlation functions and energy spectra. The analysis is conducted in both the one-way and two-way coupling regime. In the latter, of particular interest is the modulation of the turbulence. The investigation is carried out in terms of the mechanical and thermal modification of the fluid observables. The particle transport of the dispersed phase is studied as well. The turbophoresis and the statistic of the particle velocity are addressed, and their role to turbulence modulation explored.

4.2.1 Short overview of the annular pipe flow and simulation setup

Given the cylindrical coordinate system (r, θ, z) of basis $(\hat{r}, \hat{\theta}, \hat{e}_3)$ the domain consists of the annulus between two concentric cylinders, through which a particle-laden suspension flows. In the annular pipe the pressure gradient in the stream-wise direction provides the energy transfer to the turbulent field. The mechanism allows that the system reaches a stochastic steady state. The generated incompressible turbulence is homogeneous in the stream-wise and azimuthal directions, in both the thermal and velocity field. The heat fluxes is provided by two uniform temperature at the internal and external wall.

The flow in the annular pipe is more complex than in simple connected topologies, such as round pipe or channel flows. In fact, due to the opposite curvature of the inner and outer wall, the spatial and temporal scales changes substantially close the near wall regions. The asymmetry is observed in the velocity and temperature profiles, and in the turbulence intensities as well.

The dynamic of the system is described by six dimensionless parameters $\{ Re^*, Pr, St^+, \Phi_p, \rho_p/\rho_f, R_i/R_o \}$. The friction Reynolds number is $Re^* = (R_o - R_i)/\ell^*$, where R_o and R_i are the external and internal wall radius, respectively, ℓ^* is the viscous length-scale. The viscous length-scale ℓ^* is defined by the friction velocity u^* and the fluid kinematic viscosity ν, namely $\ell^* = \nu/u^*$. The friction velocity is $u^* = \sqrt{\tau_w/\rho_f}$, where τ_w is the mean viscous wall stress and ρ_f the fluid density. The Prandtl number $Pr = \nu/\alpha$ is the ratio between the momentum (ν) and the thermal (α) diffusivity . The particle time response τ_p, that is a measure of the particle inertia, is expressed through the Stokes number $St^+ = \tau_p u^*/\ell^*$. The Stokes number deeply influences the particle transport, since it determines how the discrete phase experiences the turbulent fluctuations [55]. The particle mass loading Φ_p is the ratio between the mass of dispersed phase and of the fluid, while ρ_p/ρ_f is the particle to fluid density ratio. Both Φ_p and ρ_p/ρ_f are very important in the 2-way coupling regime. In fact, Φ_p affects the global momentum exchange between the dispersed phase and the turbulence [57, 38]. The density ratio ρ_p/ρ_f, on the other hand, influences the local contribution of the momentum exchange with the single particle. In addition to this, the density ratio influences the dynamic of the particle, as dictated by the Maxey-Riley-Gatignol equation (2.34) [61, 82]. The equation is in general very complex, and describes the evolution of the particle momentum. However when the density ratio is high, the momentum equation is recast into a simple formulation (reported in chapter 2 by the equation (2.43)), where the control parameter is only the Stokes number St^+.

Finally the radial aspect ratio R_i/R_o, where R_i and R_o are the inner and outer wall radius, is very important to determine the flow asymmetry [77, 105, 78]. In fact, the peak of the turbulence intensities in the buffer layer is stronger close to the external wall than to the internal one [79, 73, 72]. The phenomenon entails the increase of the viscous stress at the internal wall, and the corresponding reduction to the outer wall. This asymmetry depends on wall radius ratio, and decreases while R_i/R_o is close to 1.

The set of control parameters is presented in the table 4.1. In the cylindrical coordinate system the domain is the annulus of size $h \times 2\pi \times L_z$, with resolution $N_r \times N_\theta \times N_z$. The height of the annulus is $h = R_o - R_i$, while the length in the stream-wise direction is $L_z = 2\pi$. The Reynolds friction and Prandtl number $Re^* = 180$ and $Pr = 0.79$ are fixed in the whole simulation setup.

Case	$N_r \times N_\theta \times N_z$	N_p	Φ_p	R_i/R_o	ℓ^*	τ^*	Re_N
A_0	$148 \times 512 \times 512$	300000	1-way	0.125	0.0048	0.0700	3010
A_1	$148 \times 512 \times 512$	368004	0.2	0.125	0.0048	0.0700	3010
A_2	$148 \times 592 \times 592$	552006	0.3	0.125	0.0048	0.0700	3010
B_0	$128 \times 512 \times 512$	800000	1-way	0.25	0.0041	0.0603	3510
B_1	$128 \times 512 \times 512$	556542	0.2	0.25	0.0041	0.0603	3510
B_2	$148 \times 592 \times 592$	834813	0.3	0.25	0.0041	0.0603	3510
C_0	$128 \times 512 \times 512$	800000	1-way	0.5	0.0028	0.0404	5300
C_1	$128 \times 512 \times 512$	1502689	0.2	0.5	0.0028	0.0404	5300
C_2	$148 \times 592 \times 592$	2254034	0.3	0.5	0.0028	0.0404	5300
D_0	$112 \times 512 \times 512$	150000	1-way	0.75	0.0014	0.0209	10960
D_1	$112 \times 512 \times 512$	7012560	0.2	0.75	0.0014	0.0209	10960
D_2	$112 \times 512 \times 512$	10518840	0.3	0.75	0.0014	0.0209	10960

Table 4.1: Simulation matrix. Given the cylindrical coordinate system (r, θ, z), the Navier-Stokes equations are integrated in the $h \times 2\pi \times 2\pi$ annular pipe with a resolution of $N_r \times N_\theta \times N_z$. For each case the friction Reynolds number is $Re^* = u_\tau h/\nu = 180$, the Prantl number is $Pr = \alpha/\nu = 0.79$. The nominal Reynolds number Re_N is different in the four geometry in order to have the same bulk velocity in the one-way coupling regime. The regularisation length-scale of the ERPP approach is set to $\sigma_R/\Delta z = 1.5$, being $\Delta z = L_z/N_z = 0.0123$ the stream-wise grid spacing. The particle-to-fluid density ratio is $\rho_p/\rho_f = 180$. N_p denote the number of particles, Φ_p the mass fraction. $St^+ = \tau_p/\tau^* = 10$, where τ_p and τ^+ are the particle and the viscous time-scale. The particle diameter measured in comparison to the viscous length-scale is $d_p/\ell^* = 1$. The nominal Reynolds number is $Re_N = u_{ref}\, l_{ref}/\nu$, being u_{ref} and l_{ref} the reference velocity and length-scale. The one-way coupled simulations (no back-reaction on the fluid) have been carried out for comparison.

The nominal Reynolds number Re_N is changed with the ratio R_i/R_o to maintain the unitary bulk velocity $u_b = 1$ in the one way coupling regime. The bulk velocity is defined by the flow rate Q crossing the surface $S = \pi(R_o^2 - R_i^2)$, i.e $u_b = Q/S$. Following a dimensional analysis, the bulk velocity depends on the wall stress τ_w, the height of the channel h and the nominal Reyolds number Re_N. Hence, while conducting a preliminary only-fluid simulation which guarantee the prescribed bulk velocity, by means of a first guess value of Re_N it is determined the wall stress that provides the required Reynolds friction number Re^*. The rationale behind this choice is that we want to exclude the influence of the geometry to the flow rate. The friction Stokes number is $St+ = \frac{1}{18}\frac{\rho_p}{\rho_f}\left(\frac{d_p}{\ell^*}\right)^2 = 10$ and the density ratio $\rho_p/\rho_f = 180$. The particle diameter d_p correspondingly equals the viscous length scale. In the two-way coupling regime the selected mass ratio Φ_p are 0.2 and 0.3. The resolution is increased when the mass ratio is $\Phi_p = 0.3$, due the extra particle-induced turbulence. The simulations with larger mass ratios ($\Phi_p > 0.3$) are unstable due to a lack of resolution of the grid. The increased computational cost cannot be afford with the current numerical techniques and HPC resources. We postpone the analysis of heavier suspension to successive works.

In figures 4.2, 4.3 and 4.4 we provide the contours of the instantaneous near-wall turbulent axial velocity fluctuations, for the annular pipe of wall radii $R_i/R_o = 0.25$. The contours report the axial velocity streaks (blue color) in the plane (θ, z), where θ is the azimuth and z the axial coordinate in the cylindrical coordinate system. The plane corresponds, in Cartesian coordinates, to the lateral surface of a cylinder concentric with the walls. The radius of the selected cylinders is $r/R_o = 0.3$ (internal side, left panels in figures) and $r/R_o = 0.93$ (external side, right panels in figures). The lateral surfaces of the two cylinders are distant $y^+ \approx 12$ from the internal wall and $y^+ \approx 17$ from the external wall. From top to bottom, the contours correspond to the one-way coupled (case B_0, figure 4.2) , two-way coupled $\Phi_p = 0.2$ (case B_1, figure 4.3) and $\Phi_p = 0.3$ (case B_2, figure 4.4). simulations. Snapshots of particles in the vicinity of the velocity streaks are overlapped over the contours.

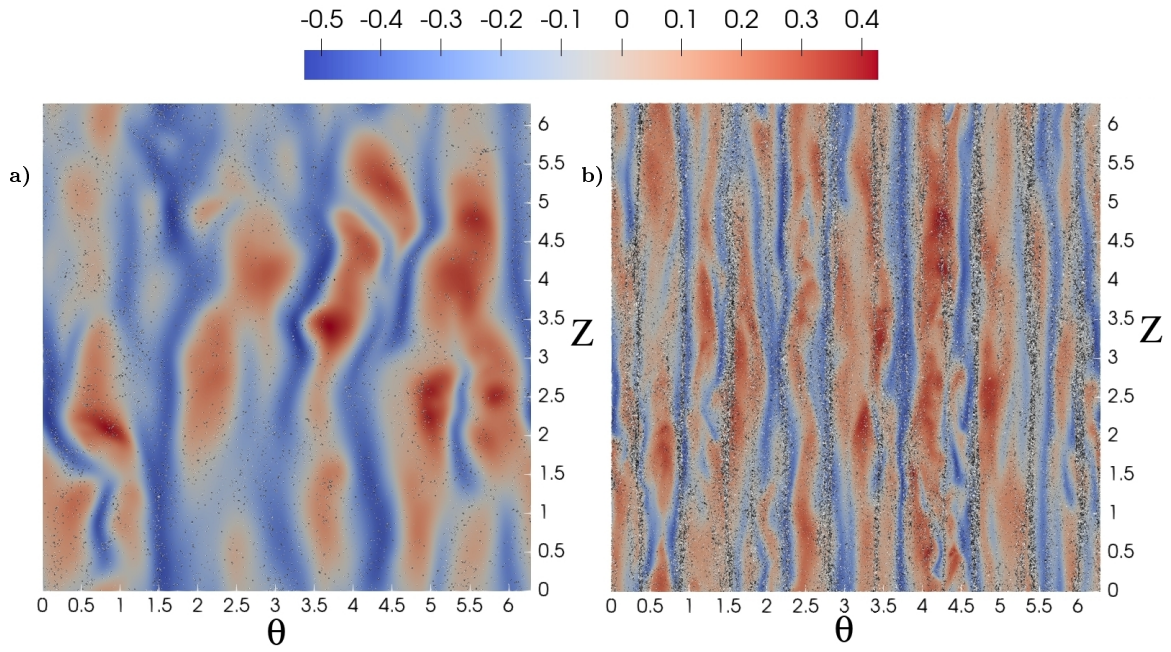

Figure 4.2: Contours of the axial fluid velocity fluctuations in the planes (θ, z) located at distance $y^+ \approx 12$ (internal) and $y^+ \approx 17$ (external) from the walls. Particles in the vicinity of the planes are depicted in white colour. The contours refer to the annular pipe of radial wall radii $R_i/R_o = 0.25$. The contours correspond to the one-way coupled simulation. The left panel depict the internal near-wall streaks (panels 'a'), while the right panel the external near-wall streaks (panels 'b').

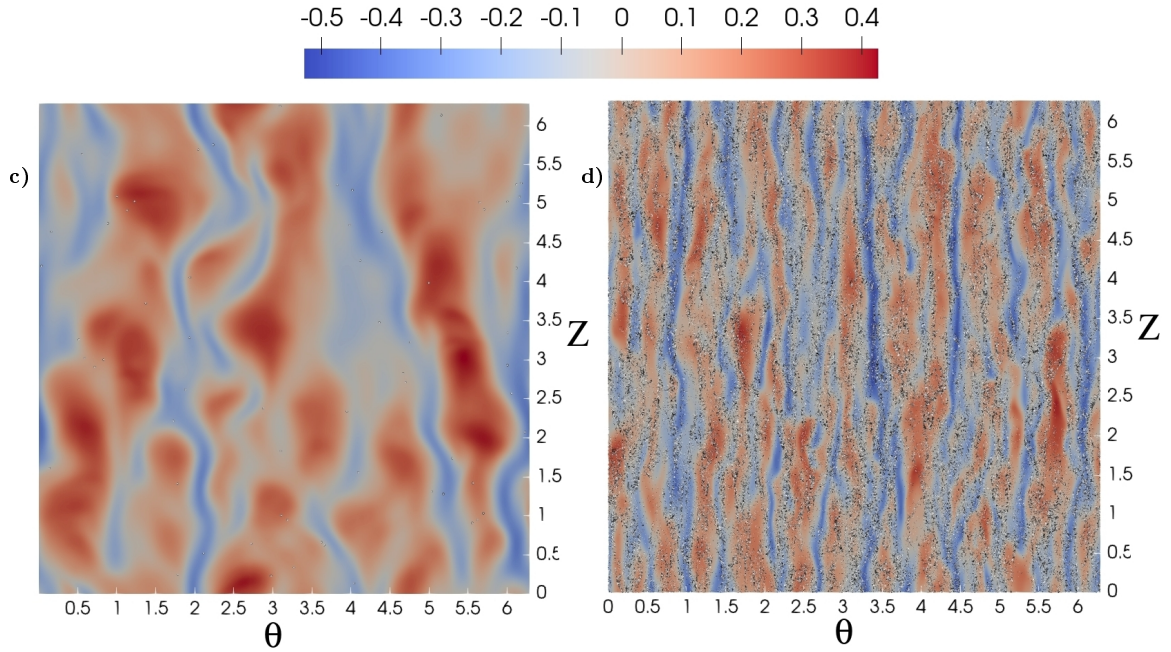

Figure 4.3: Contours of the axial fluid velocity fluctuations in the planes (θ, z) located at distance $y^+ \approx 12$ (internal) and $y^+ \approx 17$ (external) from the walls. Particles in the vicinity of the planes are depicted in white colour. The contours refer to the annular pipe of radial wall radii $R_i/R_o = 0.25$. The contours correspond to the two-way coupled simulation, with particle mass loading $\Phi_p = 0.2$ The left panel depict the internal near-wall streaks (panels 'a'), while the right panel the external near-wall streaks (panels 'b').

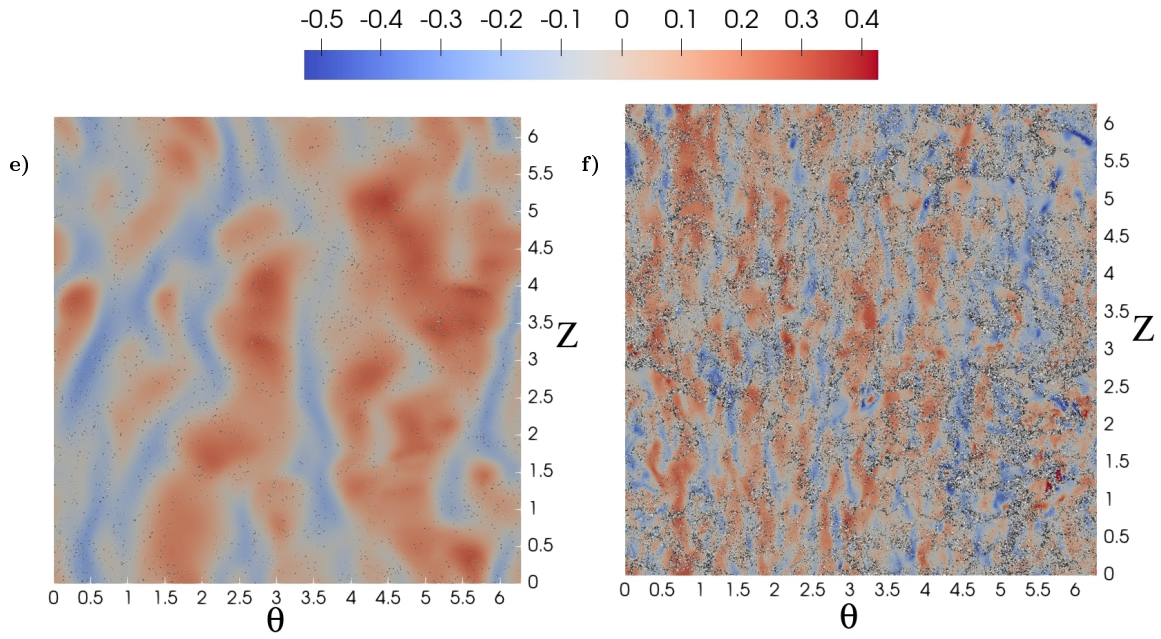

Figure 4.4: Contours of the axial fluid velocity fluctuations in the planes (θ, z) located at distance $y^+ \approx 12$ (internal) and $y^+ \approx 17$ (external) from the walls. Particles in the vicinity of the planes are depicted in white colour. The contours refer to the annular pipe of radial wall radii $R_i/R_o = 0.25$. The contours correspond to the two-way coupled simulation, with particle mass loading $\Phi_p = 0.3$ The left panel depict the internal near-wall streaks (panels 'a'), while the right panel the external near-wall streaks (panels 'b').

The modulation of the near wall streaks is evident. The effect is to disrupt the stream-wise coherent structures close the external wall, in particular for the case B_2. The streaks contribute to the production of the turbulence energy and ultimately to the wall drag [106, 107]. Therefore their modification is very important to assess how the wall resistance is modulated. The streaks near the internal wall are not modified as well. The reason is probably the low number of particles located at the internal side. In fact, the dispersed phase massively accumulates close the external wall. In this region, particles form elongated column-like clusters, that seem being correlated to the fluid streaks. In fact the clusters are noticeable in the uncoupled (panel 'b') and two-way coupled low particle loaded ($\Phi_p = 0.2$, panel 'd') suspensions, where the streaks are clearly present. On the other hand when the particle mass loading is $\Phi_p = 0.3$ (panel 'f'), the stream-wise fluid coherent structures are disrupted by the particles, which in turn lose their ordered structure.

In the forthcoming section the turbulence modification and the particle transport will be quantitatively measured following a rigorous statistical approach. The dynamics in the one-way coupling regime will be firstly addressed. The study in the two-way coupling regime will follow next.

4.2.2 The Reynolds stresses and the mean velocity in the one-way coupling regime

Owing to the non trivial behaviour of the turbulence structures in the annular pipe, we firstly report the study conducted in the one-way coupling regime. The standard notation of the Reynolds decomposition is employed. The instantaneous velocity field is $\mathbf{u}$. The ensemble average of the velocity is denoted with capital letter, $\mathbf{U} = \langle \mathbf{u} \rangle$. The single quote mark labels the turbulent fluctuation $\mathbf{u}' = \mathbf{u} - \mathbf{U}$.

In this section we report the turbulent Reynolds stress $\langle u_r' u_z' \rangle$ and the averaged velocity U_z in the one-way coupling regime. The Reynolds stress is expressed in wall unit, while the velocity U_z in computational unit. The dimensionless radial position is $\xi = (r - R_i)/(R_o - R_i)$.

The mean velocity and Reynolds stress profiles for the four geometries are shown in figure 4.5. The maximum of the velocity U_z is moved toward the inner side, compared with round pipes or channels. The slope $\frac{dU_z}{d\xi}$ is consequently higher at the internal side than the external one. This asymmetry is reduced when the distance between the walls decreases. Similarly, the zero of the Reynolds stress is moved toward the internal wall, in comparison to channels and round pipes. The external peak is in absolute value higher than the internal one, and besides, it is closer to the wall. As the mean velocity profile, the symmetry is recovered when wall distance is reduced. The results are in agreement with the literature [74, 73, 79, 76].

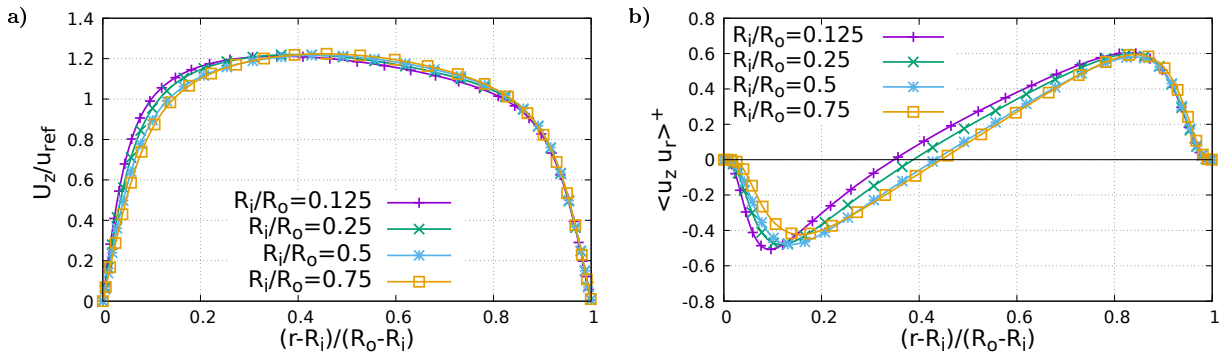

Figure 4.5: The axial averaged velocity $U_z = \langle u_z \rangle$ (figure 'a') and Reynolds turbulent stress $\langle u'_z u'_r \rangle$ (figure 'b'). The mean velocity is expressed in computational unit, with respect to the reference velocity u_{ref}. The Reynolds stress is in wall unit. The peak of the mean axial velocity is closer the internal wall, in contrast to round pipes and channels. The wall stress is higher on the internal side than on the external one. Similarly, the Reynolds stress exhibits an asymmetric behaviour, where the external peak is higher than the internal one. However the position of the external maxima is independent on the ratio R_i/R_o. Conversely the minimum, as well as the zero, of the Reynolds stress is moved to the left, while its value is increased, when the annular pipe is larger. The asymmetry of the annular pipe grows with the distance between the two walls.

The literature, in particular, agrees that the maximum of the mean axial velocity U_z occurs where Reynolds stress $\langle u'_r u'_z \rangle$ is zero. In figure 4.6 we show that this feature properly captured by our simulations. The mean viscous stress $\tau^+_\mu = \frac{1}{Re^*}\frac{dU^+_z}{d\xi}$ and the Reynolds stress $\langle u'_r u'_z \rangle^+$ are reported in wall unit versus the radial position $\xi = (r - R_i)/(R_o - R_i)$. The zero of τ^+_μ locates the maximum of U_z. Clearly the zero of $\langle u'_r u'_z \rangle^+$ and τ^+_μ are at same position, in all the four geometries. Moreover the more the ratio R_i/R_o is small the more the viscous wall stress is larger at the internal side, as compared with the external one. The largest difference occurs when $R_i/R_o = 0.125$, where $\left|\frac{\tau^+_\mu(\xi=0)}{\tau^+_\mu(\xi=1)}\right| \cong 1.5$. Owing to the area difference, the overall wall drag is applied for the most part on the external wall, namely $\left|\frac{\tau^+_\mu(\xi=0)}{\tau^+_\mu(\xi=1)}\right| \frac{R_i}{R_o} \cong 0.19$. The asymmetry is substantially reduced when the distance between the walls decreases. In particular, when $R_i/R_o = 0.75$ the viscous wall stress and drag ratios are $\left|\frac{\tau^+_\mu(\xi=0)}{\tau^+_\mu(\xi=1)}\right| \cong 1$ and $\left|\frac{\tau^+_\mu(\xi=0)}{\tau^+_\mu(\xi=1)}\right| \frac{R_i}{R_o} \cong 0.75$, respectively. The skewness of the stress profiles is additionally reported by the shape of the total stress $\tau^+_T = \tau^+_\mu - \langle u'_r u'_z \rangle^+$, which is quasi-linear when $R_i/R_o = 0.75$.

4.2.3 The velocity variance in the one-way coupling regime

This section reports the stream-wise $\langle u'^2_z \rangle$, radial $\langle u'^2_r \rangle$ and azimuthal $\langle u'^2_\theta \rangle$ velocity variances, shown in figure 4.7. Data are plotted in wall unit, labelled by the symbol '+', with respect to the friction velocity $u^2_\tau = \tau_W/\rho_f$. The radial position is expressed in dimensionless unit as $\xi = (r - R_i)/(R_o - R_i)$.

The flow is more turbulent at the external side than the internal one, in all the cases. In fact, the velocity variances have two local maxima close to the two walls. However, the peak at the external

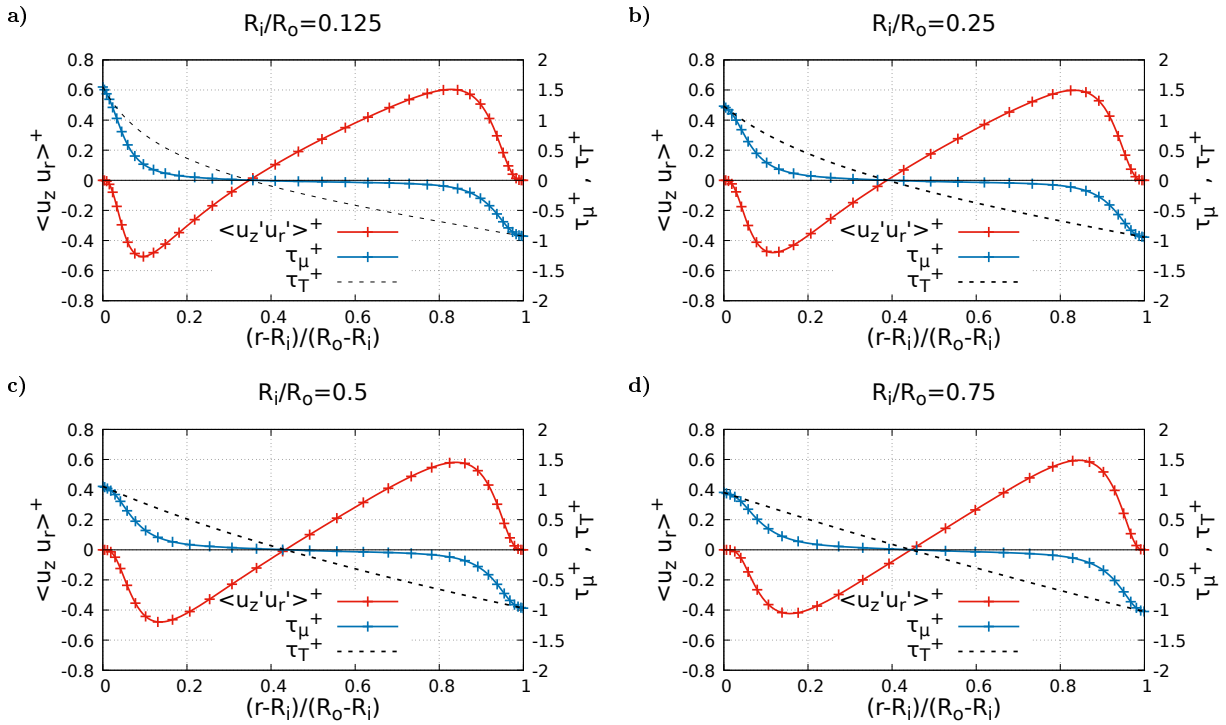

Figure 4.6: The Reynolds $\langle u_r' u_z' \rangle^+$, viscous $\tau_\mu^+ = \frac{1}{Re^*}\frac{dU_z^+}{d\xi}$ and total $\tau_T^+ = \tau_\mu^+ - \langle u_r' u_z' \rangle^+$ stresses in wall unit, where $\xi = (r - R_i)/(R_o - R_i)$. The plots refer to the four geometries $R_i/R_o = 0.125$ (case A_0, panel 'a'), $R_i/R_o = 0.25$ (case B_0, panel 'b'), $R_i/R_o = 0.5$ (case C_0, panel 'c') and $R_i/R_o = 0.75$ (case D_0, panel 'd'). The zero of the viscous and Reynolds stress are at same position. Hence, the maximum of the velocity U_z and the zero of Reynolds stress share the same location. The viscous wall stress is larger at the internal side than at the external one. The difference is reduced when the height of the annular pipe is smaller.

side is always higher than at the internal one. The turbulent kinetic energy $\mathbf{K} = \frac{\langle u_z'^2 \rangle + \langle u_r'^2 \rangle + \langle u_\theta'^2 \rangle}{2}$ is dominated by the stream-wise fluctuation. In fact, the stream-wise velocity variance is about 10 times higher than the other components. This is common is wall-bounded turbulence . The turbulent energy inlet is indeed provided to the stream-wise velocity fluctuation, by means of the transferring term $\langle u_r' u_z' \rangle \frac{dU}{dr}$. The energy is later redistributed by the turbulent pressure to the transverse components.

All the root mean square velocity fluctuations $\langle u_z'^2 \rangle$, $\langle u_r'^2 \rangle$ and $\langle u_\theta'^2 \rangle$ are asymmetric with respect to the centre of the annular pipe. However, the more the distance between the walls $h = R_o - R_i$ decreases, the more the asymmetry reduces. In fact, in the limit of vanishing h the annular pipe becomes a channel of width $2\pi R_o + R_i 2$. The results are in analogy with the literature [74, 73, 79, 76].

4.2.4 The thermal field and the Reynolds density heat flux in the one-way coupling regime

The present section reports the statistics of the thermal field of the annular pipe in the one-way coupling regime. The instantaneous temperature T follows the Reynolds decomposition $T = \mathcal{T} + T'$, where $\mathcal{T} = \langle T \rangle$ is the averaged temperature and T' is the turbulent fluctuation. The temperature can be expressed in wall unit, with standard notation, as $T^+ = \frac{T - T_i}{T_o - T_i}$, where T_o and T_i are the temperature at the internal and external wall, respectively. The instantaneous temperature is bounded between the two wall values, $T_o^+ = 0$ and $T_i^+ = 1$, since there are no source or sink of heat. In figure 4.8 the averaged temperature $\mathcal{T}^+$ and the variance $\langle T'^2 \rangle^+$ are reported for the four geometries of the annular pipe (i.e. four value of R_i/R_o). The radial position is expressed in dimensionless unit as $\xi = \frac{r - R_i}{R_o - R_i}$.

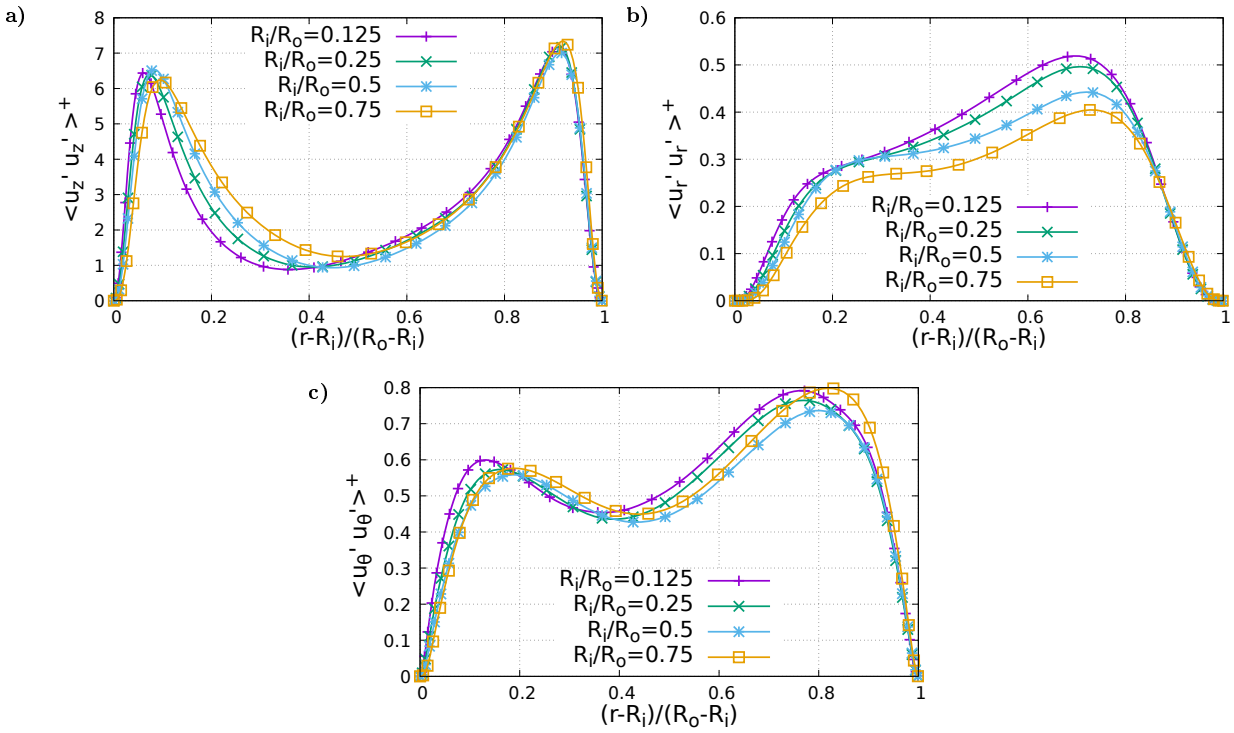

Figure 4.7: The root mean square of the stream-wise (figure 'a'), radial (figure 'b') and azimuthal (figure 'c') turbulent fluctuation, in wall unit. All the curves refer to a one-way coupling simulation. Among the three components, the dominant intensity is the stream-wise turbulent fluctuation. The asymmetry of the annular pipe is evident. The internal peaks of the turbulence intensities are smaller than the external ones. The asymmetry is reduced when the height of the annular pipe decreases.

The larger pipes are progressively colder than the smaller ones. The curves $\mathcal{T}^+$ are steeper close to the external wall, for hotter pipes, and conversely is less steep to the internal side. The ratio between the two slopes is exactly R_o/R_i, from the definition (4.6). The higher values of the temperature variance at the internal side suggest that here the instantaneous temperature is subjected to wide oscillations around its average $\mathcal{T}^+$. The highest peak of the variance is achieved by the case A_0, at $\xi \cong 0.1$. The reason could be the large radial gradient of the mean temperature close the internal wall. In fact the slope is so steep that the mean temperature at $\xi = 0.1$ is $\mathcal{T}^+(\xi = 0.1) \cong 0.5$, far from the threshold values imposed by the Dirichlet boundary conditions. On the other hand, close the external wall, at $\xi = 0.9$ the mean temperature is $\mathcal{T}^+(\xi = 0.9) \cong 0.1$, very close to the low threshold value $T_o^+ = 0$. Owing to the physical constraint, the temperature can never fall below 0. Therefore the temperature fluctuations can oscillate less freely.

In similarity with what seen for the velocity profiles, the symmetry is recovered when the walls are nearer, where the temperature profiles of the annular pipe resemble the channel's ones.

Imposing two different temperatures at the walls gives rise to the heat exchange q_W. The averaged heat flux, per unit of stream-wise length, at steady state is defined, in dimensional unit, as

$$Q_W = -2\pi R_i \kappa \left.\frac{d\mathcal{T}}{dr}\right|_{R_i} = -2\pi R_o \kappa \left.\frac{d\mathcal{T}}{dr}\right|_{R_o} \tag{4.5}$$

The heat flux is expressed in wall unit, with respect to the dimensional quantity $\rho_f c_p T_{ref} u_\tau h$, where u_τ is the friction velocity, namely

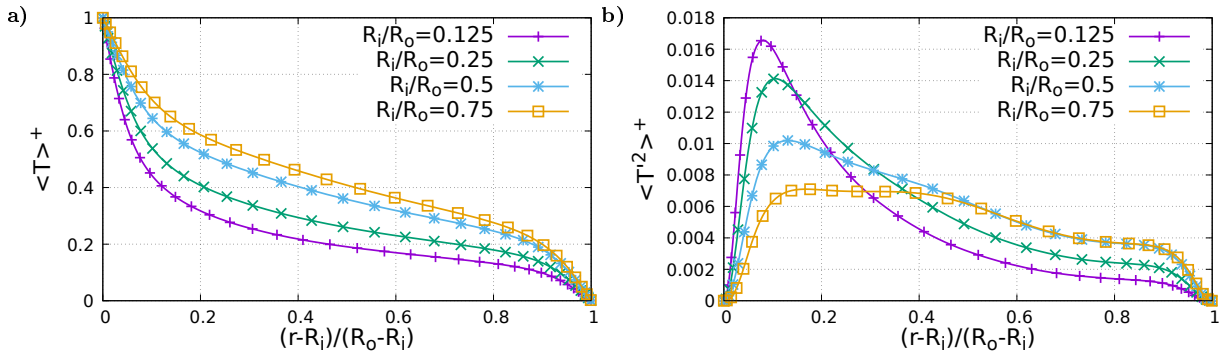

Figure 4.8: The average temperature $\langle T \rangle^+$ (figure 'a') and the variance $\langle T'^2 \rangle^+$ (figure 'b') in wall unit.

R_i/R_o	Q_W^+	δ_ϵ^+
0.125	0.0615	$+/-0,0007(1,13\%)$
0.25	0.0980	$+/-0.0009(0.97\%)$
0.5	0.2025	$+/-0.0012(0.58\%)$
0.75	0.4526	$+/-0.0014(0.30\%)$

Table 4.2: The heat flux Q_W^+ and the asymptotic standard error δ_ϵ^+ in the one-way coupling regime.

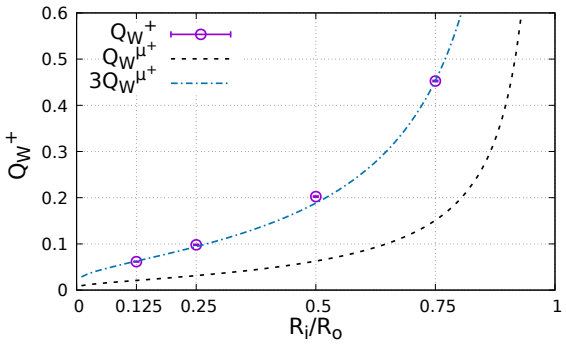

Figure 4.9: The heat flux Q_W^+ (points) and the thermal diffusion contribution $Q_W^{\mu+}$ (dashed line) in wall unit. The heat flux follows a logarithmic law, and is always 3 times the laminar heat $Q_W^{\mu+}$. The errorbar ϵ_ϵ^+ is included for Q_W^+ but is negligible under the present scale. $Q_W^{\mu+} = -\frac{2\pi}{Re^* Pr} \frac{\Delta T^+}{ln(R_o/R_i)}$ is the heat exchange occurring at laminar condition under the present setup. The turbulence enhances the heat fluxes proportionally to the ratio R_i/R_o.

$$Q_W^+ = -\frac{2\pi R_i/h}{PrRe^*} \left.\frac{d\mathcal{T}^+}{d\xi}\right|_{R_i} = -\frac{2\pi R_o/h}{PrRe^*} \left.\frac{d\mathcal{T}^+}{d\xi}\right|_{R_o} \tag{4.6}$$

The heat exchange Q_W^+ is reported in figure 4.9 and table 4.2.4. The asymptotic standard error is shown with error bars, in figure 4.2.4 below the observable scale, computed as $\delta_\epsilon^+ = 3\sigma^+/\sqrt{N_s}$, where σ^+ is the standard deviation of the single measurement, and N_s the number of samples. The error bar δ_ϵ^+ is close or below 1%, and it is negligible with respect to the difference of the results.

The heat exchange is inversely proportional to the height of the channel. In particular, the heat exchange in the smaller configuration, when $R_i/R_o = 0.75$, is eight times higher than in the larger configuration, when $R_i/R_o = 0.125$. Therefore, since the temperature difference between the walls is fixed, namely $\Delta T^+ = T_o^+ - T_i^+ = -1$, reducing the thermal resistance increases the heat exchange. A better understanding can be provided by the analysis of the heat equation of the annular pipe. In fact, the exact equation of the heat Q_W^+ can be derived from the Reynolds averaged Fourier equation,

whose detailed calculation is provided in section D.2. The equation relates the heat exchange to the temperature difference at the walls $\Delta\mathcal{T}^+ = -1$, the radial aspect ratio R_i/R_o and the turbulent convection $\langle u_r'T'\rangle^+$, namely

$$Q_W^+ = -\frac{2\pi}{Re^*Pr}\frac{\Delta\mathcal{T}^+}{ln(R_o/R_i)} + \frac{2\pi}{ln(R_o/R_i)}\int_0^1 \langle T'u_r'\rangle^+ d\xi, \quad \xi = (r-R_i)/(R_o-R_i) \tag{4.7}$$

The heat exchange in a turbulent annular pipe is caused by a thermal diffusion $Q_W^{\mu+} = -\frac{2\pi}{Re^*Pr}\frac{\Delta\mathcal{T}^+}{ln(R_o/R_i)}$ and a turbulent convection $Q_W^{R+} = \frac{2\pi}{ln(R_o/R_i)}\int_0^1 \langle T'u_r'\rangle^+ d\xi$ contribution. In a laminar annular pipe flow the heat exchange is $Q_W^{\mu+}$. In a wall bounded turbulent flow the heat exchange is usually higher than in the laminar condition with identical setup. The increase is due to the Reynolds heat flux $< u_rT' >^+$, which measures the turbulent mixing of the fluid, and it is represented by the term Q_W^{R+}. In figure 4.9 the turbulent contribution of the heat is represented by the vertical distance between the points (the heat Q_W^+) and the black dashed line (the laminar contribution $Q_W^{\mu+}$) . The increase of efficiency due to the turbulent mixing grows similar to the black dashed curve, proportional to $1/ln(R_o/R_i)$. In fact, the heat exchange is roughly 3 times the laminar contribution $Q_W^{\mu+}$ (blue dashed line), in all the four configurations. This suggests that the heat $Q_W{}^+$, with along the thermal diffusion and turbulent contributions, follow a $1/ln(R_o/R_i)$ scaling law. Therefore, the integral of the Reynolds flux $\langle u_r'T'\rangle$ is approximately constant, as shown in figure 4.10. In fact, the area under the curves $\langle u_r'T'\rangle$ represents the integral. The area appears to be roughly constant, by visual inspection. The Reynolds heat flux $\langle u_r'T'\rangle^+$ has a maximum close to the internal wall, that is more pronounced for the largest annular pipe. When the height of the pipe decreases, the reduction of the peak at the internal side is compensated by the increase of the curve at external side. The increase of heat therefore follows the scaling law $ln(R_o/R_i)$.

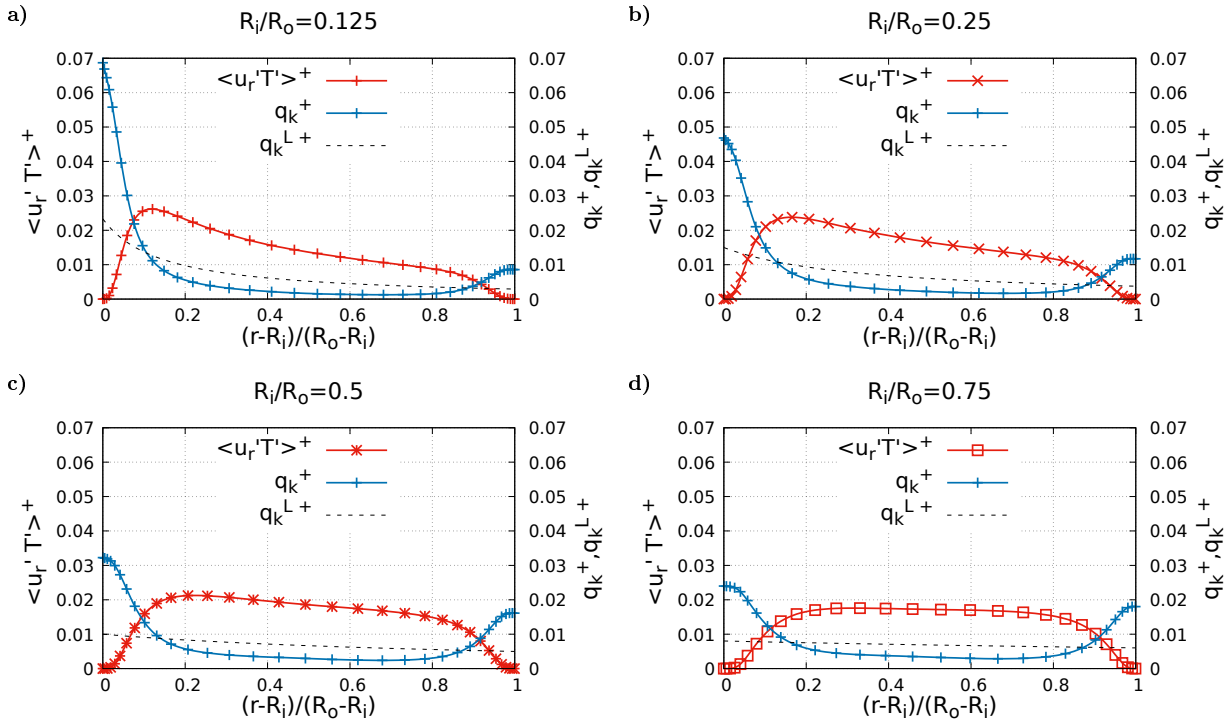

Figure 4.10: The Reynolds $\langle u_r'T'\rangle^+$ and radial $q_k^+ = -\frac{1}{PrRe^*}\frac{dT^+}{d\xi}$ heat density in wall unit, where $\xi = (r-R_i)/(R_o-R_i)$. The radial heat density in a laminar equivalent annular pipe $q_k^{L+} = -\frac{1}{Re^*Pr}\frac{dT_L^+}{d\xi}$ is also plotted (black dashed line) , where T_L is temperature profile if the flow was laminar. The plots refer to the four geometries $R_i/R_o = 0.125$ (figure 'a'), $R_i/R_o = 0.25$ (figure 'b'), $R_i/R_o = 0.5$ (figure 'c') and $R_i/R_o = 0.75$ (figure 'd').

The radial heat flux $q_k^+ = -\frac{1}{Re^* Pr}\frac{d\mathcal{T}^+}{d\xi}$, per unit of surface, is shown in figure 4.10 versus the radial distance $\xi = (r - R_i)/(R_o - R_i)$. When evaluated at the internal and external wall, q_k^+ is the heat exchange but the wall circumference $2\pi R_i/h$ and $2\pi R_o/h$, respectively. Owing to the different size of the walls, the heat density q_k^+ is higher at the internal side than the external one. The radial heat density $q_k^{L+} = -\frac{1}{Re^* Pr}\frac{dT_L^+}{d\xi}$ in the laminar equivalent annular pipe is also reported, where T_L^+ is the temperature if the flow was laminar. The wall radial heat density in the laminar condition is smaller than when the flow is turbulent, i.e. $q_k^{L+}|_W < q_k^+|_W$. This is because of the increased heat exchange due to the turbulent mixing, as previously discussed. The thermal diffusion, i.e. q_k^+, is therefore higher close to the walls, where the turbulent convection $\langle u_r' T' \rangle$ is negligible, than in the laminar flow. At the centre of the pipe however the thermal diffusion is more pronounced in the laminar flow, because in this region the heat in the turbulent flow is mainly due to the turbulent convection $\langle u_r' T' \rangle$.

4.2.5 The two-point correlations in the one-way coupling regime

In this section we report the two-point correlation of the velocity $\mathbf{u}$ and thermal field T in the one-way coupling regime. The two-point correlations are defined as

$$
\begin{aligned}
R_{zz}(r,z) &= \frac{\langle u_z'(r,\theta,\eta) u_z'(r,\theta,\eta+z)\rangle}{\langle u_z'(r,\theta,\eta) u_z'(r,\theta,\eta)\rangle} \\
R_{rr}(r,z) &= \frac{\langle u_r'(r,\theta,\eta) u_r'(r,\theta,\eta+z)\rangle}{\langle u_r'(r,\theta,\eta) u_r'(r,\theta,\eta)\rangle} \\
R_{\theta\theta}(r,z) &= \frac{\langle u_\theta'(r,\theta,\eta) u_\theta'(r,\theta,\eta+z)\rangle}{\langle u_\theta'(r,\theta,\eta) u_\theta'(r,\theta,\eta)\rangle} \\
R_{TT}(r,z) &= \frac{\langle T'(r,\theta,\eta) T'(r,\theta,\eta+z)\rangle}{\langle T'(r,\theta,\eta) T'(r,\theta,\eta)\rangle}
\end{aligned}
\tag{4.8}
$$

for the axial, radial and azimuthal velocity component and thermal field respectively.

The two point correlation functions $R(r,z)$ provide informations on the optimal size of the domain and on the characteristic length-scales of the coherent structures. The figures 4.11, 4.12, 4.13 and 4.14 provide the two-point correlation of the axial, radial, azimuthal velocity component and the temperature, respectively. The abscissa is the stream-wise separation coordinate z that spans between 0 and the semi-length $L_z/2 = \pi$ of the domain. The functions are computed at the local maximum/minimum of the Reynolds stresses $\langle u_r' u_z' \rangle >^+$. The figures 4.6 and 4.5 show the position ξ of such peaks. All the correlations are below 0.2, in absolute value, of the related turbulent intensity. Among the three velocity components, the coherent structures labelled by R_{zz} are the most correlated. In particular the cases A_0 and B_0 show $R_{zz} \cong 0.18$ at the external side. The case C_0 also reports non perfect convergence to zero of the internal axial velocity structures (panel 'a', $R_{zz} \cong -0.15$), as well as the internal temperature correlation, which fails to go below 0.1. All the remaining functions properly converge to zero at the separation scale $L_z/2$.

The results suggest that the stream-wise size of the domain L_z should be increased to to fully represent the near-wall coherent structures of the cases A_0, B_0 and C_0. In spite of that, the fist and second moment statistic of the flow are in good agreement with the literature. In addition to this we have to consider that the objective of this study is the turbulence modulation by the dispersed phase, i.e. the study of the two-way coupling regime. As we have previously mentioned, when the particle forcing is enabled, the elongated near-wall vortical structures are disrupted. Therefore in the two-way coupling regime, the correlations converge must faster to zero. In consideration of the available computational resources, this will be enough to justify the use of periodic boundary conditions.

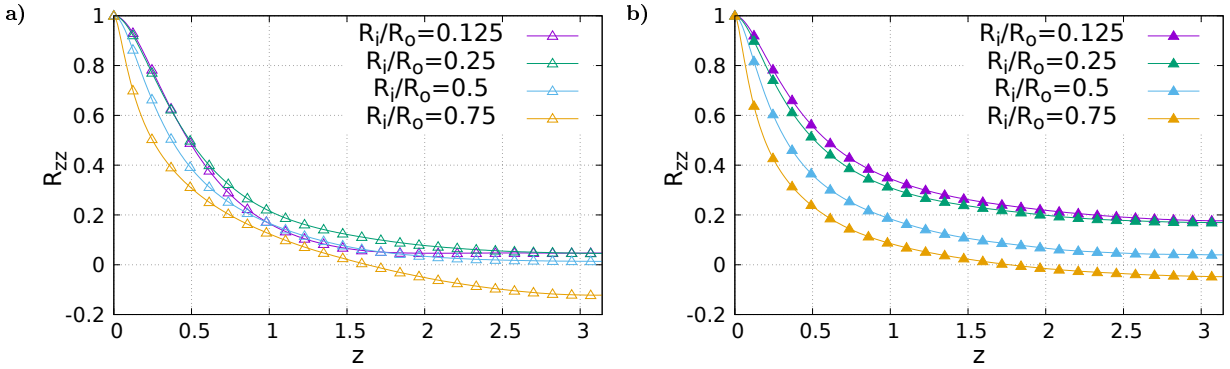

Figure 4.11: The two-point correlation of the axial velocity fluctuation, internal side (panel 'a'), external side (panel 'b'). The correlations are computed where the peaks of the Reynolds stress occur.

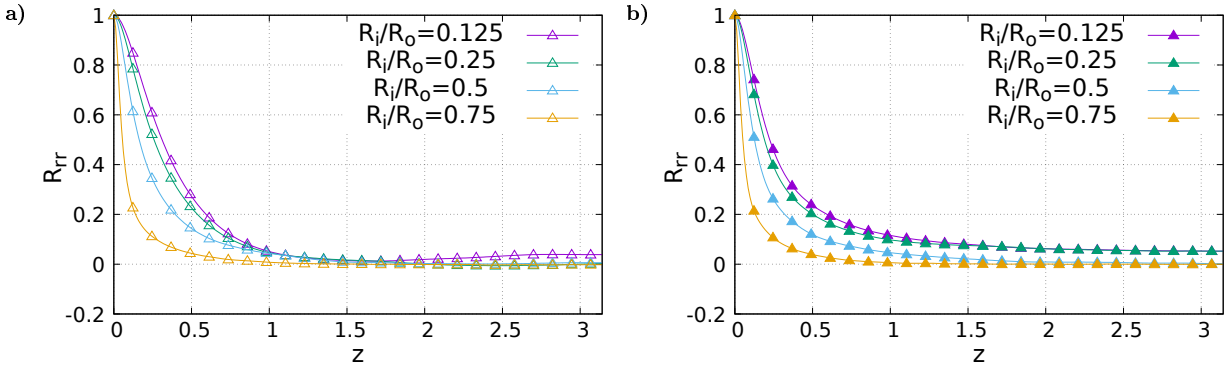

Figure 4.12: The two-point correlation of the radial velocity fluctuation , internal side (panel 'a'), external side (panel 'b'). The correlations are computed where the peaks of the Reynolds stress occur.

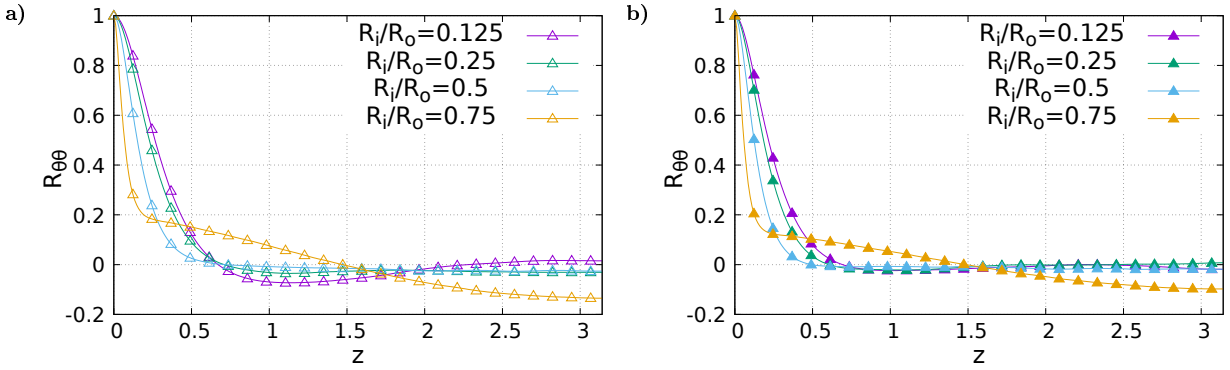

Figure 4.13: The two-point correlation of the azimuthal velocity fluctuation, internal side (panel 'a'), external side (panel 'b'). The correlations are computed where the peaks of the Reynolds stress occur.

4.2.6 Spectral analysis of the turbulence intensities in the one-way coupling regime

The energy spectra are another usuful tool to examine the turbulence coherent structures. The spectra describe how the energy of different turbulent signals distributes among the spatial length-scale, or wavenumbers. The spectrum over the homogeneous directions of the signal $\phi(r,\theta,x,t)$, expressed in cylindrical coordinates, is defined as the Fourier transform of the autocorrelation function, namely $\hat{\mathbf{E}}^{\phi}_{2D}(r,\mathbf{k}_\theta,\mathbf{k}_z) = \mathcal{F}[\langle\phi(r,\gamma,x,t)\phi(r,\gamma+\theta,x+z,t)\rangle]$. $\mathbf{k}_z$ and $\mathbf{k}_\theta$ are the wavenumbers

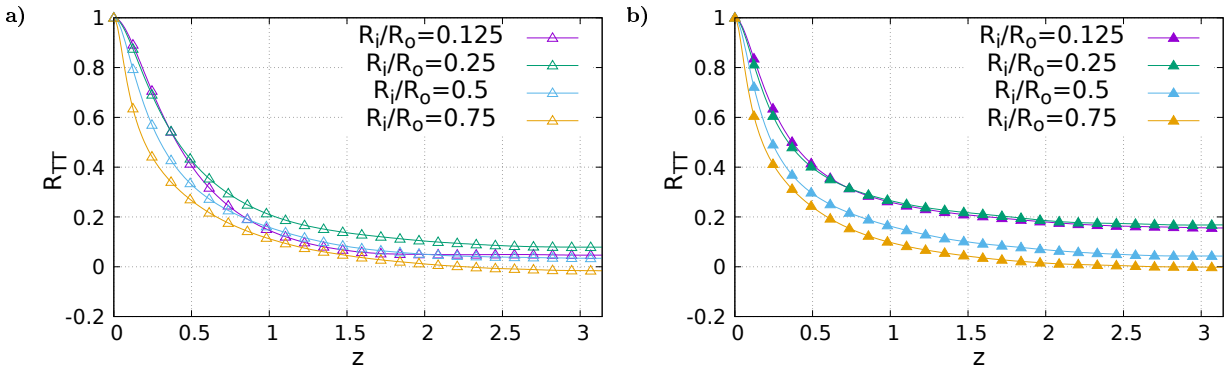

Figure 4.14: The two-point correlation of the thermal fluctuation $T' = T - \langle T \rangle$, internal side (panel 'a'), external side (panel 'b'). The correlations are computed where the peaks of the Reynolds stress occur.

in the axial and azimuthal periodic directions. Due to the anisotropy of wall-bounded turbulence, the 2-D spectrum is not invariant under rotations on the plane $(\mathbf{k}_z,\mathbf{k}_\theta)$. Since we aim at studying the axial elongation of the streaks, we are interested in extracting the modes of the 2-D spectrum denoting the energy content of the fluctuations in the axial direction. The modes of such 1-D spectrum are in the spectral plane of equation $\mathbf{k}_\theta = 0$. In order words the 1-D spectrum is computed as $\hat{E}^\phi(r,\mathbf{k}_z) = \hat{\mathbf{E}}_{2D}(r,\mathbf{k}_\theta = 0,\mathbf{k}_z)$. The axial wavenumber belongs to the real line, namely $\mathbf{k}_z \in \mathbb{R}$, and in general is both positive and negative. However when the function $\phi(r,\theta,x,t)$ is real, the spectrum $\hat{E}^\phi(r,\mathbf{k}_z)$ is symmetric around the mode $\mathbf{k}_z = 0$, and can be represented with respect to the absolute wavenumber $k = |\mathbf{k}_z|$. The relative one-dimensional spectrum, with respect to k, is therefore computed as

$$E^\phi_{1D}(k) = \begin{cases} \hat{E}^\phi(-k) + \hat{E}^\phi(k) & , k \neq 0 \\ \hat{E}^\phi(k) & , k = 0 \end{cases} \tag{4.9}$$

To be consistent with the literature, we will study the axial coherent structures by means of the premultiplied 1D energy spectrum $kE^\phi_{1D}(k)$. The premultiplied energy spectrum denotes the spectral energy content in the logarithmic scale of the signal ϕ, and is defined as $\langle \phi'^2 \rangle = \int_{-\infty}^{\infty} E^\phi_{1D} k dln(k)$, where $ln(k)$ is the natural logarithm of k.

The figures 4.15 and 4.16 report the premultiplied axial spectrum of the stream-wise velocity $k^+E^{u_z+}_{1D}(r,k^+)$ and of the temperature $k^+E^{T+}_{1D}(r,k^+)$ fluctuations. The contour is represented over the plane (ξ,k^+), where as usual $\xi = (r - R_i)/(R_o - R_i)$ while $k^+ = k\ell^+$. The premultiplied spectra are nondimensionalised by the friction velocity $k^+E^{u_z+}_{1D}(r,k^+) = \frac{kE^{u_z}_{1D}(r,k^+)}{u_\tau^2}$ and by the reference temperature $k^+E^{T+}_{1D}(r,k^+) = \frac{kE^{T}_{1D}(r,k^+)}{T^2_{ref}}$,

In figure 4.15 we report the premultiplied spectrum of the axial velocity component for the cases $R_i/R_o = 0.125$ and $R_i/R_o = 0.75$. In the larger configuration there is a clear asymmetry in the near wall peaks of the spectrum. The amplitude of the internal peak is higher than the external one, and is placed at a smaller lengthscale. Hence the stream-wise characteristic lengthscale is smaller for the internal coherent structures than the external ones. This was also confirmed by the two-point correlation function in figure 4.11, where for the geometry $R_i/R_o = 0.125$ the curves tend to zero faster at the internal side than at the external one. However, the radial extension of the peaks is wider at the external side than the internal one. The reader must note that the physical signal $\langle u'_z u'_z \rangle$ is in fact higher close to the external wall. Therefore, the spectrum of the stream-wise fluctuation, although being higher at the internal wall, decays faster at large wavenumber. The results are consistent to the spectra of Bagheri [73]. The more narrow configuration $R_i/R_o = 0.75$ recovers a partial symmetry. The intensity and position of the peaks are closer to each other. A zone of minimum values appears roughly at the centre of the pipe, at wavenumber $k^+ = 10^{-2.5}$.

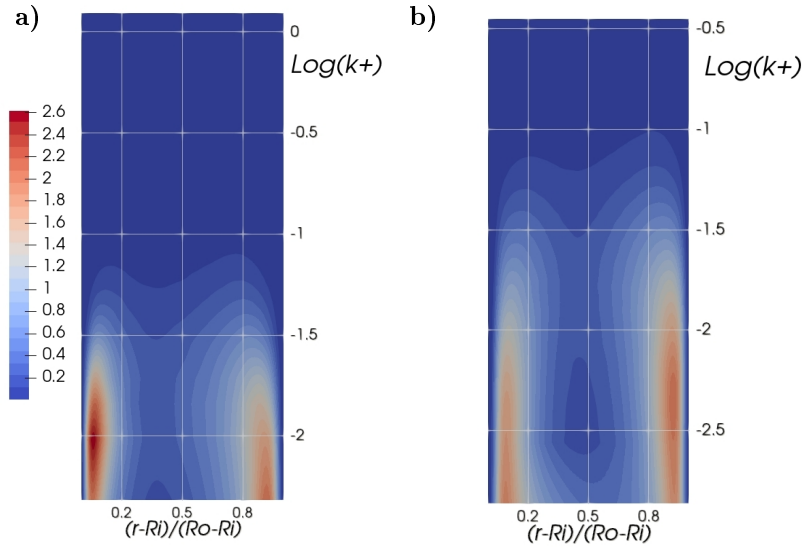

Figure 4.15: The one dimensional pre-multiplied (z-direction) spectrum of the streamwise fluctuation $k^+E_{1D}^{u_z+} = \frac{kE_{1D}^{u_z}}{U_\tau^2}$ versus the radial position $\xi = \frac{r-R_i}{R_o-R_i}$ and the axial wavenumber $k^+ = \frac{2\pi i}{N_z \ell^*}$, where $i = [0, N_z/2+1]$ and ℓ^* is the viscous length-scale. Data refer to the cases A_0 (panel 'a') and D_0 (panel 'b'). The vertical axis is $Log(k^+) = log_{10}(k^+)$, that is the logarithm in base 10 of k^+. The spectrum is defined as $\langle u_z' u_z' \rangle(\xi) = \int_{-\infty}^{\infty} k^+ E_{1D}^{u_z}(\xi, k^+) dln(k^+)$

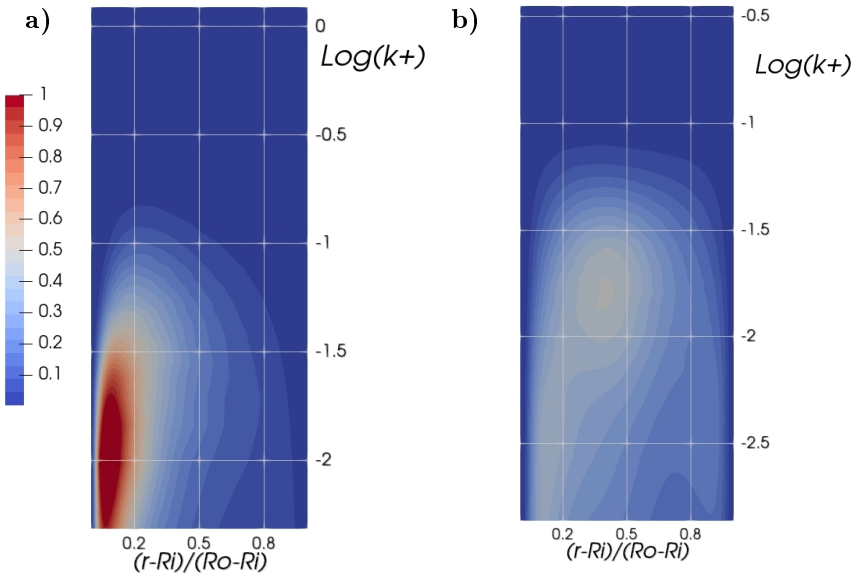

Figure 4.16: The one dimensional pre-multiplied (z-direction) spectrum of the temperature fluctuations $k^+E_{1D}^{T+} = \frac{kE_{1D}^{T}}{T_{ref}^2}$ versus the radial position $\xi = \frac{r-R_i}{R_o-R_i}$ and the axial wavenumber $k^+ = \frac{2\pi i}{N_z \ell^*}$, where $i = [0, N_z/2+1]$ and ℓ^* is the viscous length-scale. Data refer to the cases A_0 (panel 'a') and D_0 (panel 'b'). The vertical axis is $Log(k^+) = log_{10}(k^+)$, that is the logarithm in base 10 of k^+. The spectra are defined as $\langle T'^2 \rangle(\xi) = \int_{-\infty}^{\infty} k^+ E_{1D}^{T}(\xi, k^+) dln(k^+)$.

In figure 4.16 we report the premultiplied spectrum of the temperature of the cases A_0 and D_0. The configuration A_0, the largest one, exhibits a clear asymmetric spectrum with respect to ξ. A peak occurs in the internal side, while the spectrum is monotonically decreasing in the central and external regions.

The spectrum is consistent to the informations provided by the energy $\langle T'^2 \rangle$ in figure 4.8 (right panel). In fact, the energy peak of $\langle T'^2 \rangle$, when the wall radius ratio is $R_i/R_o = 0.125$, occurs close to the internal wall. On the right side of the peak, the energy decreases monotonically till the zero boundary condition. In other words, when the energy, i.e. the integral of the spectrum $k^+E_{1D}^{T+}$ in $ln(k)$, is larger, the energy containing modes of the spectrum are larger as well.

The smallest annular pipe, of wall radius ratio $R_i/R_o = 0.75$, is also shown in the same figure (right panel). The shape of the spectrum is very different as compared with the larger pipe. The peak reduces its amplitude and is moved toward the centre of the annular pipe, at higher wavenumber ($k^+ = 10^{-2}$, $R_i/R_o = 0.125$, to $k^+ = 10^{-1.75}$, $R_i/R_o = 0.75$). The symmetry of the spectrum is partially recovered in this narrow configuration.

The trend of the spectrum is consistent to the variance of the temperature depicted in figure 4.8, whose related maxima are in the region $\xi \in [0.2, 0.4]$.

The results are not comparable with the spectra of the temperature of of Bagheri [72]. In fact, Bagheri et al. impose the heat flux rather than the temperature. This leads to a very different evolution of the temperature fluctuations in the annular pipe, whose energy content is qualitatively similar to the axial velocity fluctuation's one.

4.2.7 The particle concentration and velocity in the one-way coupling regime

In this section we report the analysis of the turbophoresis in the one-way coupling regime of the annular pipe. The turbophoresis consists in the preferential accumulation of the particles in the low-velocity regions of the flow, i.e. close the walls. Before to report the results, we wish to describe the complex fluid dynamic mechanisms leading to the turbuphoresis. In a flow with Cartesian topology, such as a channel flow, the migration of the dispersed phase is dictated by the normal to the wall velocity component of the fluid. When a particle is in the logarithmic and buffer layer, it experiences high levels of turbulent velocity fluctuations. On the other hand, close to the wall the turbulent intensity vanishes, due to the no-slip boundary conditions. Hence, the probability that the particle is thrust toward the wall could be higher than to be later pushed away. This mechanism is regulated by the inertia of the particle, that is measured the time response τ_p. When the inertia is the right one, the normal velocity gained by the particle in the external regions is neither too high or too small. In fact, If the velocity is too high the particle appraching the wall would bounce away. If it is is too small the particle would fail to reach the wall. Once the particle enters the sub-viscous layer, due to its finite mass, it is very difficult that escapes. In fact the quasi-laminar flow is insufficient to push a finite-mass particle away from the wall. Therefore the intensity of the turbophoresis is modulated by the particle time response τ_p. τ_p is expressed by the viscous time-scale based Stokes number $St^+ = \tau_p/\tau^*$, where τ^* viscous time-scale.

In a channel flow the transverse fluctuations have no influence on the turbophoresis. On the other hand in the annular pipe this may be very different. In fact in the presence of concave curve walls, the turbophoresis is emphasised by the azimuthal turbulent fluctuations. The azimuthal fluid velocity, either positive or negative, accelerates the particle in the direction of the wall, since increases the particle centrifugal force. Conversely if the wall is convex the azimuthal turbulent fluctuations accelerates the particle away from the wall. The phenomenon is controlled by the Stokes coefficients St^+, and by the curvatures of the wall, that is by R_i/R_o. Owing to the opposite curvatures of the walls it is expected that the turbophoresis does not occurs symmetrically in the annular pipe.

In order to explore the effect of wall curvature and of the particle mass, in the one-way coupling regime a population of particles, characterised by eleven different Stokes number St^+, is transported by the fluid. The Stokes number in wall unit is defined as $St^+ = \frac{1}{18}\frac{\rho_p}{\rho_f}\left(\frac{d_p}{\ell^*}\right)^2$. With usual notation ρ_p/ρ_f is the particle to fluid density ratio and ℓ^* is the viscous length-scale. The aim is to find the particle inertia, labelled by St^+, leading to the most intense turbophoresis. The particle data set is shown in table 4.3.

$R_i/R_o = 0.125$		$R_i/R_o = 0.25$		$R_i/R_o = 0.5$		$R_i/R_o = 0.75$	
St^+	d_p/R_o	St^+	d_p/R_o	St^+	d_p/R_o	St^+	d_p/R_o
2	0.021	2	0.018	2	0.012	2	0.006
5	0.034	5	0.029	5	0.02	5	0.01
10	0.048	10	0.041	10	0.028	10	0.014
20	0.068	20	0.058	20	0.040	20	0.02
40	0.096	40	0.082	40	0.056	40	0.028
80	0.136	80	0.116	80	0.079	80	0.0396
160	0.192	160	0.164	160	0.112	160	0.056
320	0.271	320	0.232	320	0.158	320	0.079

Table 4.3: The particle data set in the one-way coupling regime.

The concentration of the dispersed phase $C(r)$ is defined as

$$C(r) = \frac{d\langle n_p(r,\theta,z,t)\rangle}{dV}/C_0 \tag{4.10}$$

where $n_p(r,\theta,z,t)$ is the number of particles inside the cell located by the cylindrical coordinate system, of volume $dV = rd\theta dzdr$ and at time t. The concentration is normalised by the averaged particle concentration $C_0 = N_p/V_D$, where the domain volume is $V_D = \pi L_z(R_o^2 - R_i^2)$.

In figure 4.17 the concentration $C(\xi)$ is reported with respect to the dimensionless radial position $\xi = (r - R_i)/(R_o - R_i)$. The plot shows how the particle inertia, labelled bu St^+, influences the turbophoresis for the geometry $R_i/R_o = 0.5$, when particle-to-fluid feedback is disabled. The near wall particle concentration is higher when $St^+ = 10/20$. In the other cases the inertia is either too high or too small, and the concentration is more uniform. At the centre of the annular pipe the curves are flat, far below the averaged concentration (i.e. below 1). This is the sign that particles have migrated to the near-wall regions. In fact, the more the concentration peaks are high, the fewer particles are found at the central region.

In contrast to the channel where the concentration is symmetric, in the annular pipe the peak close the concave side is about ten times higher than it is at the convex side. The opposite curvature of the two walls is the origin of this phenomenon. In fact, at the external side the azimuthal fluctuations always push the particle closer to the wall, while at the internal side it is the opposite.

The strong turbophoresis of the particles with $St^+ = 10$ or $St^+ = 20$, suggests that these populations could lead to the most significant turbulence modification. For the simulations in the two-way coupling regime, between the two choices, we selected the particles with $St^+ = 10$, owing to the restriction on the particle size of the point-particle approach.

Although the results are omitted, the analysis of the turbophoresis in the other three geometries of the annular pipe (i.e. cases A_0, B_0 and C_0) is carried out as well. The conclusions are the same just reported. The turbophoresis, in the uncoupled simulations, is strongest in an interval of the Stokes number $St^+ = 10$.

The particle concentration $C(\xi)$ of the population $St^+ = 10$ is shown in figure 4.18 for the four geometries of the annular pipe (panel 'a') . The radial position is $\xi = (r - R_i)/(R_o - R_i)$. In the central and external regions the concentration is more or less the same in the four geometries. In particular the turbophoresis on the concave side is not affected by the internal wall curvature. On the other hand, the internal peak grows when the internal wall curvature is increased. In the largest and smallest configurations of the annular pipe the difference is very clear. When the wall radius ratio is $R_i/R_o = 0.75$ the internal maximum of the concentration is 5 times higher that it is when $R_i/R_o = 0.125$.

The symmetrisation process of the flow field, observed to the fluid, also occurs to the discrete phase. However, although the difference between the intensity of the internal and external tur-

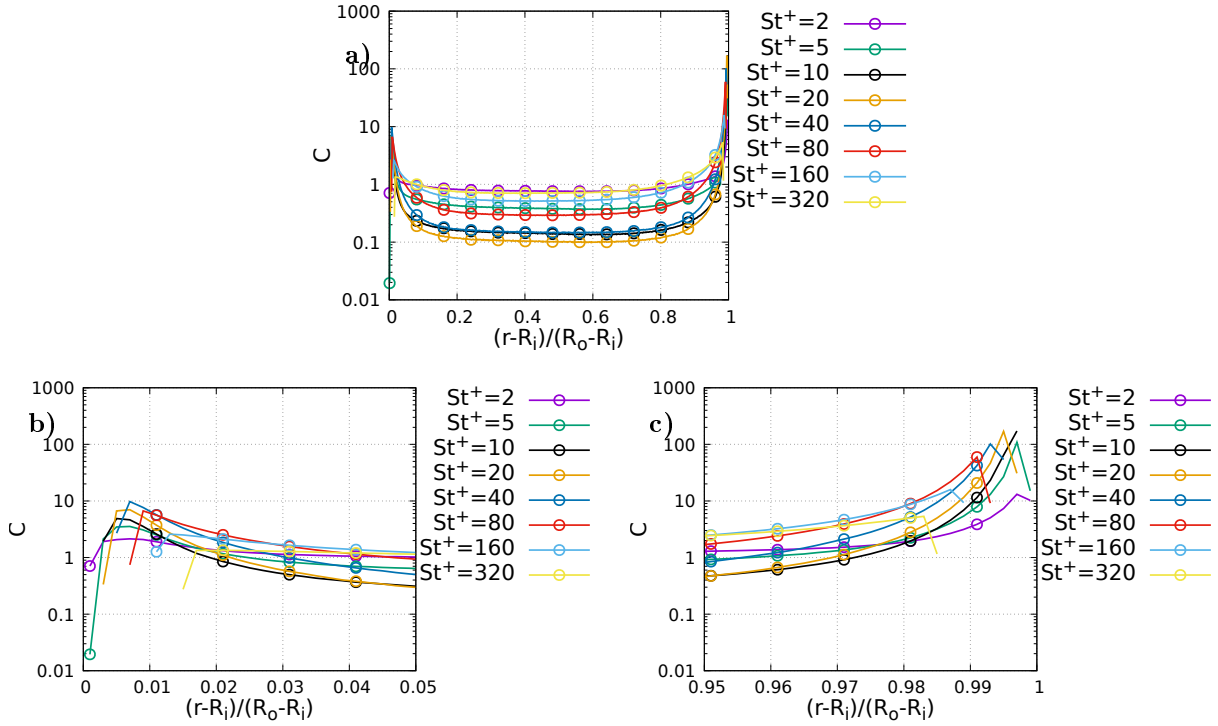

Figure 4.17: The concentration of dispersed phase $C(\xi)$ versus the radial position $\xi = \frac{r-R_i}{R_o-R_i}$ in the one-way coupling regime for the case $R_i/R_o = 0.5$ (panel 'a'). The particle data set includes $St^+ = 2/5/10/20/40/80/160/320$. Enlargements of the plot at the internal (panel 'b') and external (panel 'c') side are reported. Two peaks of the concentration are reported close to the walls. At the concave side the concentration is ten times higher than it is at the convex side. The turbophoresis is more pronounced when $St^+ = 10$.

bophoresis is reduced, it is still large when $R_i/R_o = 0.75$.

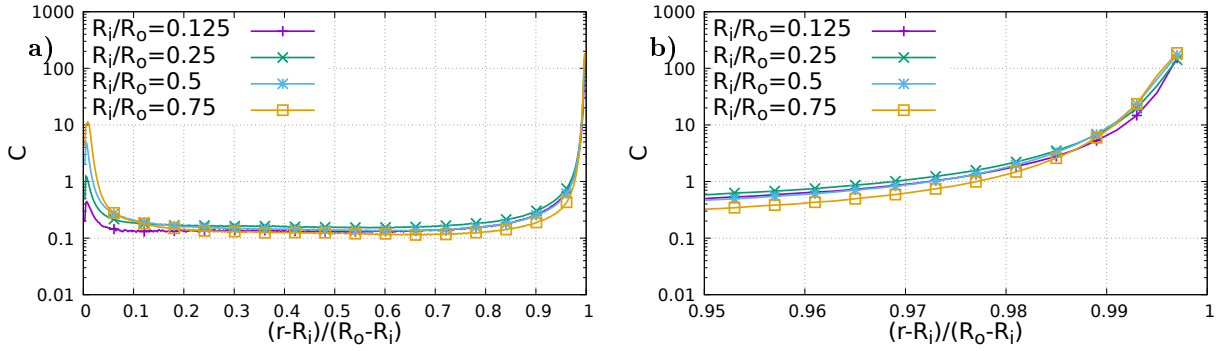

Figure 4.18: The concentration of dispersed phase $C(\xi)$ versus the radial position $\xi = \frac{r-R_i}{R_o-R_i}$ in the one-way coupling regime for the four geometries: $R_i/R_o = 0.125$ (pink line), $R_i/R_o = 0.25$ (green line), $R_i/R_o = 0.5$ (blue line), $R_i/R_o = 0.75$ (orange line). Enlargement of the plot at the external (panel 'b') side is provided. Two peaks of the concentration are reported close to the walls. At the concave side the concentration is between 10 to 100 times higher it is at the convex side.

In figure 4.19 the particle V_p^+ , fluid U^+ and fluid particle-conditioned U_p^+ averaged velocities are provided for the four configurations, when $St^+ = 10$. All the averaged velocities are aligned to the axial direction, and only this component is reported. The radial distance is $\xi = (r - R_i)/(R_o - R_i)$ while the velocity is in wall unit. The averaged velocity U_p^+ is the unperturbed fluid velocity eval-

uated at bubble position $x_p(t)$. This velocity field is necessary to evaluate the particle momentum equation, as the Maxey-Riley-Gatignol equation dictates. In the one-way coupling regime the unperturbed field, that was denoted by the subscript "(0)" in section 2.6, coincides with the actual velocity field. For this reason, the subscript "(0)" is safely removed in the present discussion. The reader must notice that this will be very different when the particle feedback is activated.

The field U_p^+ is asymmetric as well as U^+. However, the conditioned fluid velocity U_p^+ differs from the fluid velocity U^+ at the concave side. In this region the particles sample lower than average fluid velocity values. In contrast, in the other flow regions U^+ and U_p^+ are roughly the same. The discrepancy reduces when the distance between the walls decreases.

The averaged particle velocity V_p^+ and field U_p^+ are equal. In fact, at the stochastic steady state, the averaged particle drag force is zero, namely

$$\langle D_p \rangle^+ = \frac{3\pi}{Re^*} \frac{d_p}{h} (U_p^+ - V_p^+) = 0 \tag{4.11}$$

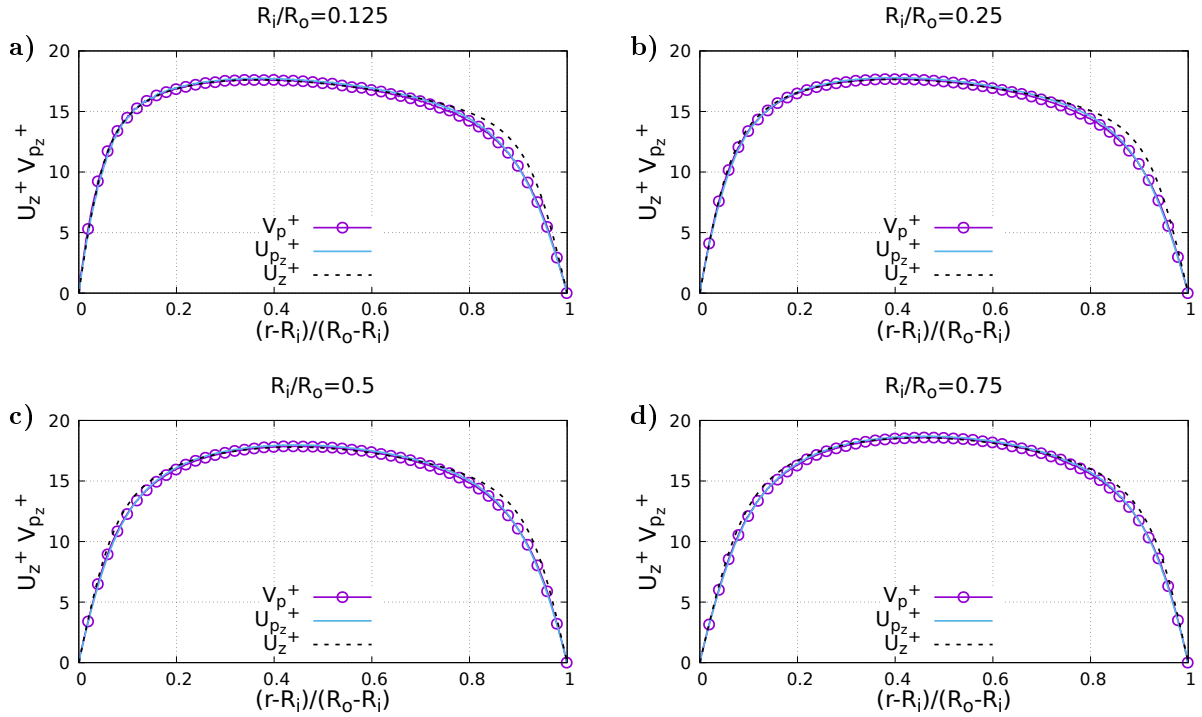

Figure 4.19: The averaged particle velocity V_p^+, the fluid velocity U^+ and the fluid velocity experienced by the particle U_p^+, in wall unit. The radial position is $\xi = \frac{r-R_i}{R_o-R_i}$. The plots refer to $St^+ = 10$ and to the the four configurations of the annular pipe (uncoupled-cases) : $R_i/R_o = 0.125$ (panel 'a'), $R_i/R_o = 0.25$ (panel 'b'), $R_i/R_o = 0.5$ (panel 'c'), $R_i/R_o = 0.75$ (panel 'd').

The mean is a useful tool that provides the central tendency of the distribution. In order to understand how the observables oscillate around the expected value, it is necessary to evaluate the second moment of the distribution. In figure 4.20 we report the velocity variances $\langle v_{p_z}'^2 \rangle^+$, $\langle v_{p_r}'^2 \rangle^+$, $\langle u_r'^2 \rangle^+$ of the dispersed phase and of the fluid $\langle u_z'^2 \rangle^+$, $\langle u_r'^2 \rangle^+$, $\langle u_\theta'^2 \rangle^+$, in wall unit. The curves refer to $St^+ = 10$. In the one-way coupling regime, the particle velocity variance of the stream-wise component increases, while the radial and azimuthal components reduce, independently on the distance between the walls. Although the intensity of the particle velocity fluctuations is differently modulated in the three physical directions, the asymmetry of the fluid energy profiles is reproduced by the particles as well.

The interpretation of the observations is as follows. Owing to the damping effect of the particle Stokes force, the amplitude of the homogeneous velocity components (i.e. the radial and azimuthal

components) is attenuated. On the other hand, while the particle moves radially, its finite inertia conserves its stream-wise velocity for a longer time than a fluid particle does. Hence, while entering or leaving the near-wall regions, the particles move with a wider (with respect to the average) stream-wise velocity distribution.

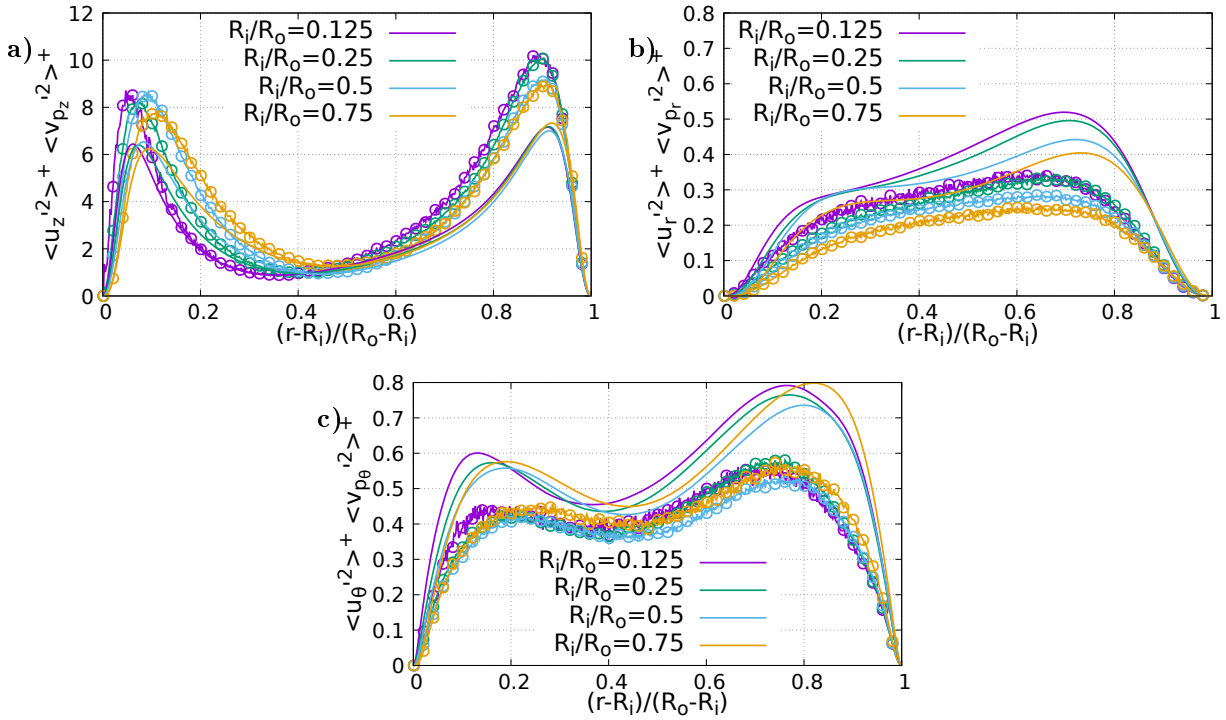

Figure 4.20: The velocity variance of the dispersed phase (solid lines with points) $\langle v'^2_{p_z}\rangle^+$ (panel 'a'), $\langle v'^2_{p_r}\rangle^+$ (panel 'b'), $\langle v'^2_{p_\theta}\rangle^+$ (panel 'c') and of the fluid (solid lines) $\langle u'^2_z\rangle^+$, $\langle u'^2_r\rangle^+$, $\langle u'^2_\theta\rangle^+$, in wall unit. The radial position is $\xi = \frac{r-R_i}{R_o-R_i}$ and the curves refer to $St^+ = 10$, and the the four configurations of the annular pipe (uncoupled-cases) : $R_i/R_o = 0.125$ (pink line), $R_i/R_o = 0.25$ (green line), $R_i/R_o = 0.5$ (blue line), $R_i/R_o = 0.75$ (orange line).

4.2.8 The velocity variance in the two-way coupling regime

We will now present the turbulence modulation induced by the dispersed phase. The particle feedback is considered for the present simulations, under the ERPP methodology.

Simulations are carried out under constant Reynolds friction $Re^* = \frac{hu_\tau}{\nu}$. The kinematic viscosity (the nominal Reynolds number in computational unit Re_N) and the height of the pipe $h = R_o - R_i$ are obviously unchanged when the particle feedback is activated. Consequently the friction velocity $u_\tau = \sqrt{\tau_w/\rho_f}$, and the viscous length-scale ℓ^*, of the one-way and two-way coupled cases are the same. In other words, each configuration of the annular pipe, labelled by the ratio R_i/R_o, is studied under constant mean viscous stress τ_w (or constant pressure gradient $\frac{dP}{dz}$).

Owing to the large particle mass loading Φ_p, we can expect both local and bulk modifications of the flow field. When the flow rate is constant, the expected bulk modification is the increase of the mean viscous stress τ_w. However, owing to the overmentioned simulation setup, the increased wall resistance will be measured with the flow rate reduction. An increased flow rate will be interpreted as a resistance reduction, and vice versa. We remark that to observe the modification of the wall drag (instead of the flow rate), it would be sufficient to rewrite the velocity field in a new dimensionless form, with respect to its bulk velocity $u_b = \frac{Q}{\pi(R_o^2-R_i^2)}$. However, in this research this passage is omitted.

Before to present how the particles globally affect the background flow, we will focus on the local modification of the flow field. In this section we report the velocity variances of the stream-wise $\langle u'_z u'_z \rangle^+$, azimuthal $\langle u'_\theta u'_\theta \rangle^+$ and radial $\langle u'_r u'_r \rangle^+$ components, expressed in wall unit in figures 4.21 4.22 4.23. The one-way coupled related quantity is reported as well (pink lines). The alteration of the turbulent kinetic energy (TKE) is finally provided.

In the two-way coupling regime, two particle mass loading ratios are considered: $\Phi_p = 0.2$ (green lines) and $\Phi_p = 0.3$ (blue lines). When $\Phi_p = 0.2$ there is a small, though observable, effect on the root mean squares of the velocity. The stream wise turbulent velocity fluctuations $\langle u'_z u'_z \rangle^+$ are attenuated by the particle back reaction. The most relevant effects are observed when $R_i/R_o = 0.25$ and $R_i/R_o = 0.5$. In these two configurations, both the internal and external peaks are attenuated, even if, as we will see later, particles mainly concentrate on the external wall. When $R_i/R_o = 0.125$ there is no modification at the internal side. In fact, the reduction is concentrated at the external side. When $R_i/R_o = 0.75$ the stream-wise turbulent fluctuation is preserved in the near-wall regions structure, even if there is a small reduction at the centre of the annular pipe. The radial $\langle u'_r u'_r \rangle^+$ and azimuthal $\langle u'_\theta u'_\theta \rangle^+$ velocity variances are slightly modified, as compared with the axial contribution, when $\Phi_p = 0.2$. The near-wall energy peaks are subjected to very small increase, barely noticeable under the present scale.

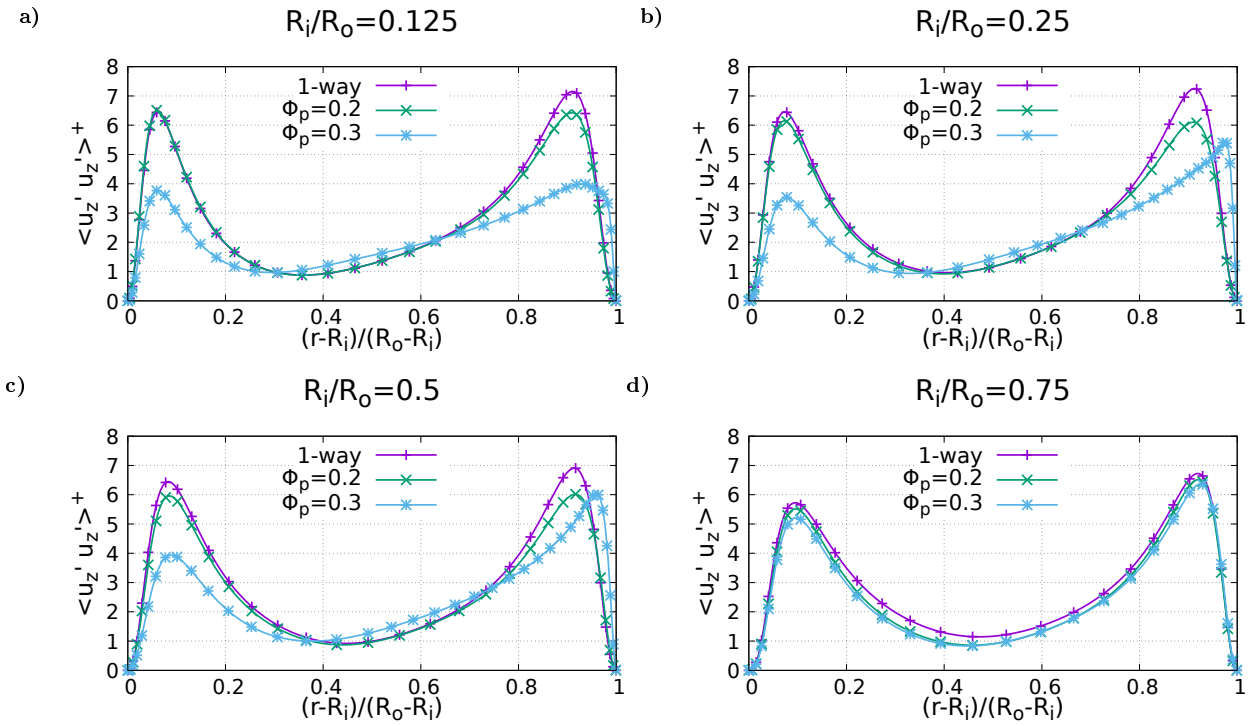

Figure 4.21: The root mean square of the stream-wise turbulent fluctuation $\langle u'_z u'_z \rangle$, in wall unit. The green and blue curves refer to the two-way coupled simulation. The pink curve refers to the uncoupled simulation.

Very important modifications of the turbulence intensities occur when the particle mass loading is $\Phi_p = 0.3$. The stream-wise velocity variances report very large attenuations of the peaks, in particular for the case $R_i/R_o = 0.125$. The external peaks are shifted outward, closer the near wall massive particle clusters. Moreover, in the centre of the annular pipes, small increments of the stream-wise energy content are detected. The radial and, in particular, the azimuthal velocity variances report drastic modifications as well. A very large peak appears in the radial energy component $\langle u'_r u'_r \rangle^+$, close the external wall. At the internal side, in contrast, the energy profiles are only slightly attenuated. The azimuthal velocity variances $\langle u'_\theta u'_\theta \rangle^+$ show even higher peaks, close the external wall. The external peaks are about 10 times higher than they are in the uncoupled

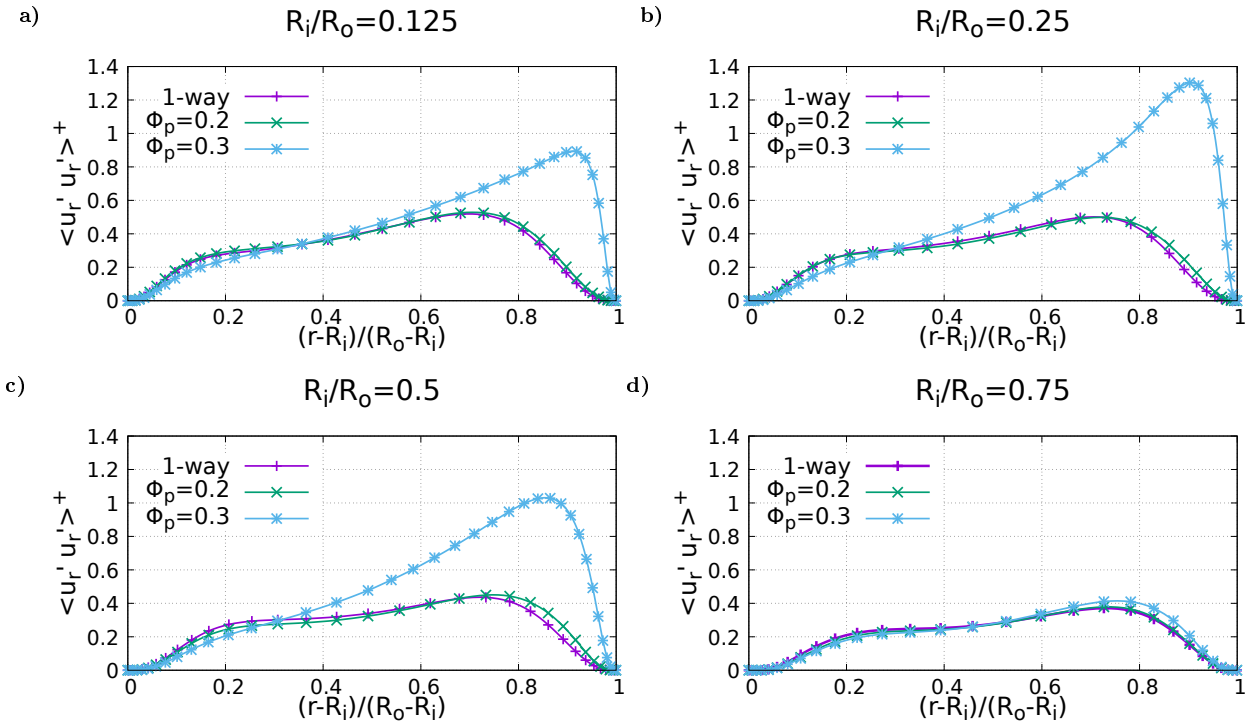

Figure 4.22: The root mean square of the radial turbulent fluctuation $\langle u_r' u_r' \rangle$, in wall unit. The green and blue curves refer to the two-way coupled simulation. The pink curve refers to the uncoupled simulation.

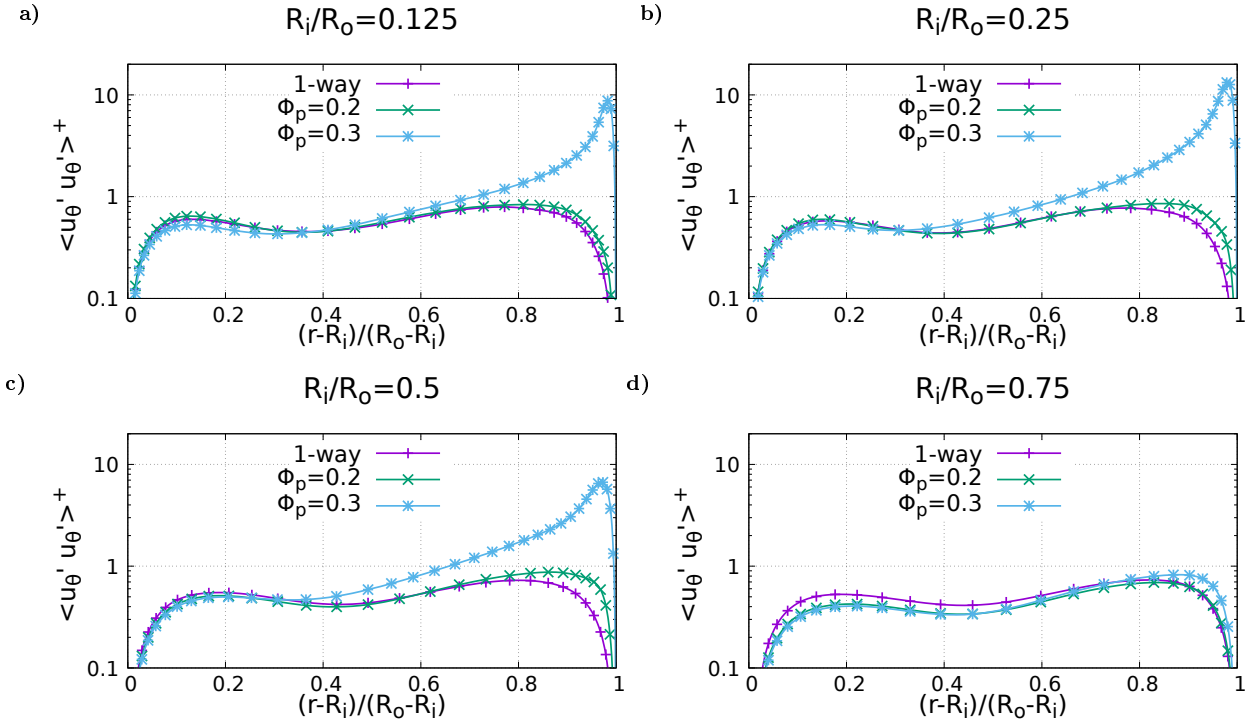

Figure 4.23: The root mean square of the azimuthal turbulent fluctuation $\langle u_\theta' u_\theta' \rangle$, in wall unit. The green and blue curves refer to the two-way coupled simulation. The pink curve refers to the uncoupled simulation.

case. They modification is so large, that the azimuthal and axial velocity variances are comparable in the external region. However, as the radial velocity fluctuations, the azimuthal profiles are only

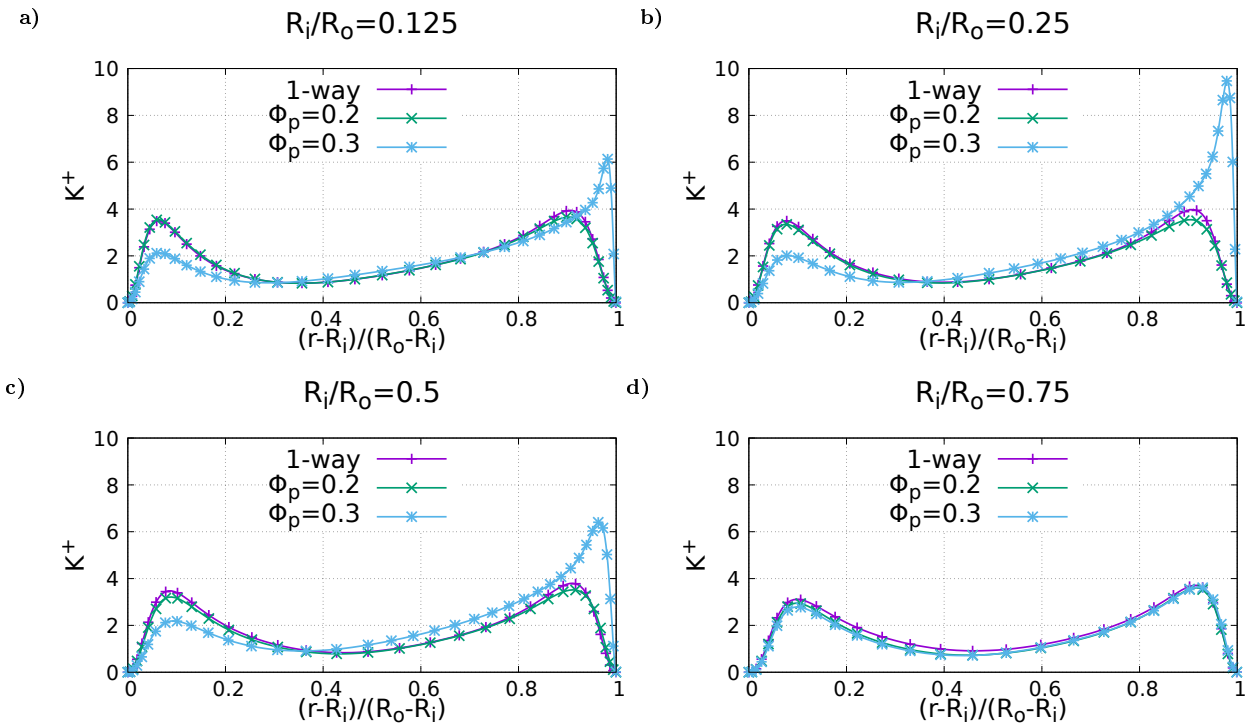

Figure 4.24: The turbulent kinetic energy $2K^+ = \langle \mathbf{u}' \cdot \mathbf{u}' \rangle^+$, in wall unit. The dashed lines refer to the one-way coupled simulations. The full lines with points refer to the two-way coupled simulations.

slightly reduced at the internal side.

The annular pipe with radial aspect ratio $R_i/R_o = 0.75$ is the only of the present configurations where the overmentioned radical change of the turbulence intensities are not observed. In fact, owing the strong fluid confinement, the turbulent intensities, when $\Phi_p = 0.3$, retain the shape of the lighter suspensions (i.e. $\Phi_p = 0.2$).

The reported results suggest that the near wall coherent structured are drastically modified when $\Phi_p = 0.3$, except when the flow confinement is too large (i.e. when $R_i/R_o = 0.75$). In particular, the strongest modification occurs at the external side, where the massive particle clusters are located. In this region, the reduction of the stream-wise turbulence intensities is partially compensated by the increase in the transverse components. In contrast, at the internal side, where the turbophoresis occurs with minor intensity, the effect on the fluid is considerably reduced.

The turbulent kinetic energy (TKE) $\mathbf{K}$ is the mean energy, per unit of mass, associated to the turbulent signal $\mathbf{u}'$. The TKE describes the energy of the turbulent eddies, and it is computed as the half sum of the variances of the three velocity components (axial, radial and azimuthal), namely $\mathbf{K}^+ = \frac{\langle u_z' u_z' \rangle^+ + \langle u_r' u_r' \rangle^+ + \langle u_\theta' u_\theta' \rangle^+}{2}$. In figure 4.24 the turbulent kinetic energy K^+ is reported, in wall unit, versus the radial position $\xi = (r - R_i)/(R_o - R_i)$.

As previously discussed, in the smallest annular pipe, i.e. when $R_i/R_o = 0.75$, there is only a very small attenuation of turbulent energy content. No influence of the particle mass loading Φ_p is found for this case. The results, of course, are in analogy with the negligible effects observed in the velocity variances.

In the other three geometries (the cases A, B and C) the energy of the turbulent velocity fluctuation is considerably increased at the external side, while attenuated at the internal one, when $\Phi_p = 0.3$. The largest modification occurs when the internal wall radius is $R_i/R_o = 0.25$. On the other hand, when $\Phi_p = 0.2$, the particle influence on the KTE is small, barely noticeable, as suggested by the analysis of the velocity variances.

The results show that there is a threshold value of the particle mass loading Φ_p beyond which a radical alteration of the coherent structures is somehow activated. The strong modification mainly

occurs at the external side of the annular pipe, close to the massive particle clusters. Although to a lesser extent, the particle effects are observable in the other regions of the flow field, in both the velocity variances and the TKE. The threshold value is between 0.2 and 0.3 in the geometries $R_i/R_o = 0.125$ $R_i/R_o = 0.25$ and $R_i/R_o = 0.5$, but it is beyond 0.3 when $R_i/R_o = 0.75$. This suggests that increasing the confinement of the fluid, the particle-induced turbulence is somehow reduced.

4.2.9 The viscous, Reynolds and extra stress in the two-way coupling regime

The Reynolds averaged momentum equation in the streamwise component describes how the stresses, the pressure and the volume forces are related each other. The presence of the dispersed phase calls for an additional stress in the momentum equation, called extra-stress τ_e. The extra-stress is expressed by the integral $\tau_e = \frac{1}{r}\int_{R_i}^{r} \eta F_{p_z} d\eta$, where $F_{p_z} = \langle f_{p_z} \rangle$ is the averaged particle back reaction in the axial direction. The sum of the extra-stress τ_e, the Reynolds shear stress $\tau_R = -\rho_f \langle u_r' u_z' \rangle$ and the viscous stress $\tau_\mu = \mu \frac{dU_z}{dr}$ is the total stress $\tau_T = \tau_e + \tau_R + \tau_\mu$. Following the proof provided by Fukagata [108], applied to the annular pipe, the equation of the total stress, that is equation (4.12), is derived. Additional details are provided in the appendix, in section D.1.

$$\frac{1}{r}\int_{R_i}^{R_o} \tau_e + \tau_R dr - \frac{1}{r}\left(\frac{R_o^2 - R_i^2}{4ln(R_o/R_i)} - \frac{r^2}{2}\right)\frac{dP}{dz} = \mu\frac{dU_z}{dr} + \tau_e + \tau_R \tag{4.12}$$

The Reynolds shear stress is $\tau_R = -\rho_f \langle u_r' u_z' \rangle$, $U_z = \langle u_z \rangle$ is the streamwise averaged velocity component and $ln(R_o/R_i)$ is the natural logarithm of R_o/R_i. In contrast to channel and round pipes [38, 108], the total stress is a non linear function with respect to r. In fact, τ_T is the sum of a straight line and a hyperbole. However, when the internal and external wall radii are very close the equation (4.12) equivalently reproduces the dynamic of a channel of width $2\pi\frac{R_i+R_o}{2}$. In the limit $R_o/R_i \to 1$, the extra-stress and Reynolds stress become odd functions in r with respect the centre of annular pipe, that is $\frac{R_i+R_o}{2}$. Therefore, the integral in the left-hand side is zero. Moreover, the multiplier factor of the pressure gradient can be expanded into a linear function in the neighbourhood of the mean radius $\frac{R_o+R_i}{2}$. Therefore, when the distance between the walls decreases, the total stress approximates a linear odd function. The feature was shown and discussed for the one-way coupled simulations, in figure 4.6. The same aspect will be now addressed when the particle-back reaction is active, and the additional extra-stress is taken into account.

In figure 4.25 we report the Reynolds stress (with negative sign) $\langle u_r' u_z' \rangle^+$, the viscous stress $\tau_\mu^+ = \frac{1}{Re^*}\frac{dU_z^+}{d\xi}$, the extra stress $\tau_e^+ = \frac{1}{\rho_f u_\tau^2}\frac{1}{r}\int_{R_i}^{R_o} \eta F_{p_z} d\eta$ and the total stress $\tau_T^+ = \tau_e^+ + \tau_\mu^+ - \langle u_r' u_z' \rangle^+$ in wall unit. The radial position is expressed in dimensionless unit by $\xi = (r - R_i)/(R_o - R_i)$. The two-way coupled simulations (lines with points) are compared with the unladen case (dashed line). From top to bottom, the figures show the effect of the radial aspect ratio R_i/R_o, in ascending order. The left panels report the findings when the particle mass loading is $\Phi_p = 0.2$, while the right panels are referred to suspensions with $\Phi_p = 0.3$

The first important result is that the extra-stress τ_e^+ is always negligible as compared with the other stresses, in particular to the Reynolds stress $\langle u_r' u_z' \rangle$. The total stress is therefore solely determined by the resultant of the Reynolds shear and viscous stress, as in the unladen case. The results are not in total agreement to the particle-laden round-pipe two-way coupled DNSs conducted by Battista et al. [38]. In fact, they found that close to the wall the extra-stress is up to 10% of the total stress, for particle density ratio $\rho_p/\rho_f = 180$ and Stokes number $St^+ = 10$. Although the discrepancy could be motivated by the different topology of the domain, we highlight that their findings refer to a particle mass loading $\Phi_p = 0.4$, which is higher than in the present research. In our annular pipes, suspensions with particle mass loading $\Phi_p = 0.4$ were unsuccessfully simulated, owing to numerical instabilities. Since the instabilities were caused by locally very high particle feedback, we can't exclude that similar effects, of those observed by Battista et al, could be present in the annular pipes, when heavier suspensions are considered.

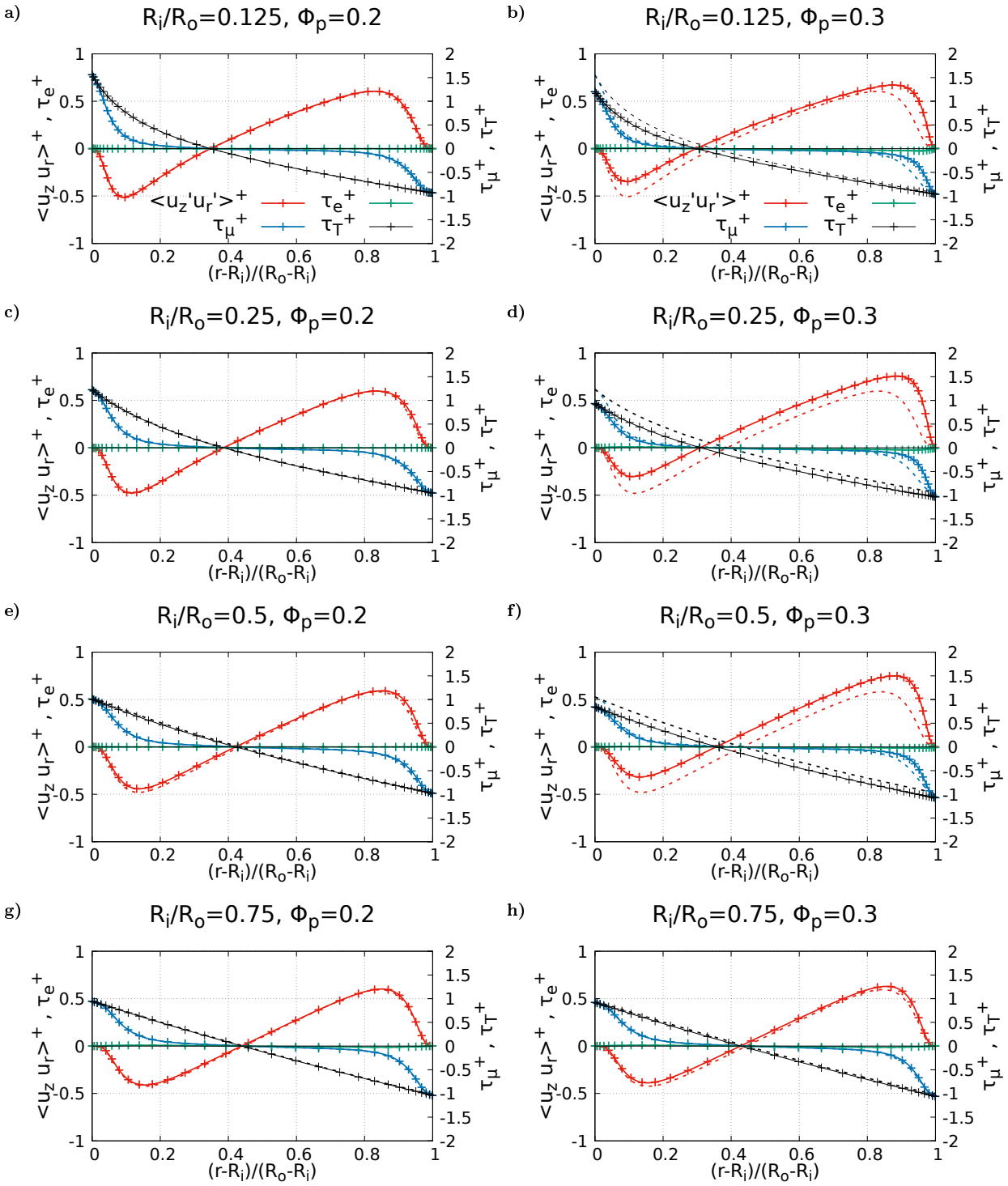

Figure 4.25: The turbulent shear convection $\langle u_r' r_z' \rangle^+$ (red lines), viscous stress $\tau_\mu^+ = \frac{1}{Re^*} \frac{dU_z^+}{d\xi}$ (blue lines), extra stress $\tau_e^+ = \frac{1}{u_\tau^2 r} \int_{R_i}^{R_o} \eta F_{p_z} d\eta$ (green lines) and total stress $\tau_T^+ = \tau_\mu^+ - \langle u_r' r_z' \rangle^+ + \tau_e^+$ (black lines) in wall unit, versus the radial distance $\xi = (r - R_i)/(R_o - R_i)$. Lines with points are referred to the two-way coupled simulations. The dashed lines report the results of respective unladen cases. In the left axis the scale of the extra-stress and of the turbulent shear convection is provided. The right axis reports the scale of the viscous ans total stresses.

The modificationos of the stresses in the annular pipe with radial aspect ratio $R_i/R_o = 0.75$ are consistent with the velocity variance observed in the previous section. In fact, the modification

appears negligible, when the particle feedback is active, for any particle mass loading considered.

Conversely, the fluid stresses are highly modulated by the particles when the mass loading is $\Phi_p = 0.3$, in the three smaller annular pipes ($R_i/R_o = 0.125$, $R_i/R_o = 0.25$ and $R_i/R_o = 0.5$). The total stress τ_T^+ is shifted downward, as compared with the unladen cases. In the central regions, where the viscous stress τ_μ^+ is negligible, the reduction is caused by the increased turbulent shear convection $\langle u_r' u_z' \rangle^+$. On the other hand, in the near-wall regions the turbulent fluctuations vanish, and the reduction of the viscous stress τ_μ^+ controls the modulation of the total stress. Therefore, the viscous wall stress increases at the external wall, but decreases at the internal wall, in absolute value. In fact, owing to the simulation setup (constant Re^*), the mean viscous wall stress $\tau_w = \frac{\tau_{w_i} R_i + \tau_{w_o} R_o}{R_i + R_o}$ is constant.

When the particle mass loading is $\Phi_p = 0.2$ (left panels) we do not observe any significant alteration in the stress profiles.

The flow rate depends on a integral, suitably weighted, of the Reynolds stress and the extra stress. The equation that regulates such dependency is derived in the appendix, in section D.1, and follows the proof of Fukagata [108], extended to the particle-laden annular pipe. Clearly the reduction of the flow rate will be solely dependent on the modification of the turbulent shear convection. In fact, the extra-stress is always negligible as compared with the Reynolds shear stress. This very important aspect will be addressed in more details in the forthcoming section.

4.2.10 The flow rate reduction due to the dispersed phase

The flow rate depends on a integral, suitably weighted, of the Reynolds stress, the extra stress and on the pressure gradient (or equivalently the mean viscous stress). The equation is derived in the appendix, in section D.1, and generalises the Fukagata's proof [108] to the particle-laden annular pipe turbulent flows. The equation is reported below

$$\frac{\pi}{4(R_o - R_i)} \left\{ R_o^4 - R_i^4 - \frac{(R_o^2 - R_i^2)^2}{ln(R_o/R_i)} \right\} \tau_w = I_\mu + I_R + I_e \tag{4.13}$$

The mean viscous wall stress $\tau_w = \frac{\tau_{w_{R_i}} R_i + \tau_{w_{R_o}} R_o}{R_o + R_i}$ is given by three contributions: the viscous I_μ, the turbulent I_R and particle (or extra-stress) contributions I_e.

$$\begin{cases} I_\mu = \mu Q \\ I_R = \pi \int_{R_i}^{R_o} \left\{ \frac{R_o^2 - R_i^2}{2ln(R_o/R_i)} - r^2 \right\} \tau_R dr \\ I_e = \pi \int_{R_i}^{R_o} \left\{ \frac{R_o^2 - R_i^2}{2ln(R_o/R_i)} - r^2 \right\} \tau_e dr \end{cases} \tag{4.14}$$

I_μ is the contribution of the wall viscous stress due to the averaged viscous diffusion. In a laminar unladen flow I_μ is entirely responsible of the wall viscous stress, since $I_R = I_e = 0$.

Under constant viscous wall drag τ_w, in a single-phase turbulent wall-bounded flow the flow rate is usually lower than in the equivalent laminar case. The reduced flow rate is associated to the existence of near wall coherent motions. These coherent structures are characterised by ejection and sweep events [109]. The ejections are fluid with low stream-wise speed moving away from the wall. The sweeps are inrushes of high stream-wise speed fluid toward the wall. The effect of such near wall motions on the averaged momentum balance is captured by the Reynolds stress τ^R. Similarly, the dispersed phase affects the fluid momentum by means of the extra-stress τ^e, as explained in the previous section. In the former section we have shown that the extra-stress is negligible, as compared with τ^R.i Therefore, according to the equations (4.13) (4.14), the alteration of the flow rate will be driven by the Reynolds shear stress. In the annular pipe the Reynolds shear stress increases on the external side, while decreases on the internal one. While the increment of the Reynolds shear stress is associated to the intensification of the near-wall sweep and ejection events, and therefore to the flow rate reduction, the decrease of the Reynolds shear stress is symptom of a

flow rate increase. Hence, the modification of the shear stress contributes to increase the flow rate at the internal side, while to reduce it at the external one. However, the Reynolds shear stress τ^R, as well as the extra-stress τ^e, affects the flow rate by means of the geometric factor $\frac{R_o^2 - R_i^2}{2ln(R_o/R_i)} - r^2$. Physically, this means that the stresses do not provide a uniform contribution, but the flow rate will depend on where, along the radial position, the stresses are modified. In the annular pipe, the modifications on the external side have greater weight than those occurring on the internal one. This is in particular true when the distance between the walls is large, i.e. when R_i/R_o is small. Therefore, basing on n the observations given in figure 4.25, we could expect that the overall effect of τ^R is to increase the viscous resistance.

All the considerations just given are captured by the flow rate equation equation (4.13) (4.14). The modification of the flow rate will depend on the integrals I_R and I_e, which are related to the Reynolds shear stress and the extra-stress, respectively. The turbulent and particle contributions of the flow rate will be now measured and reported for the two-way coupled data set.

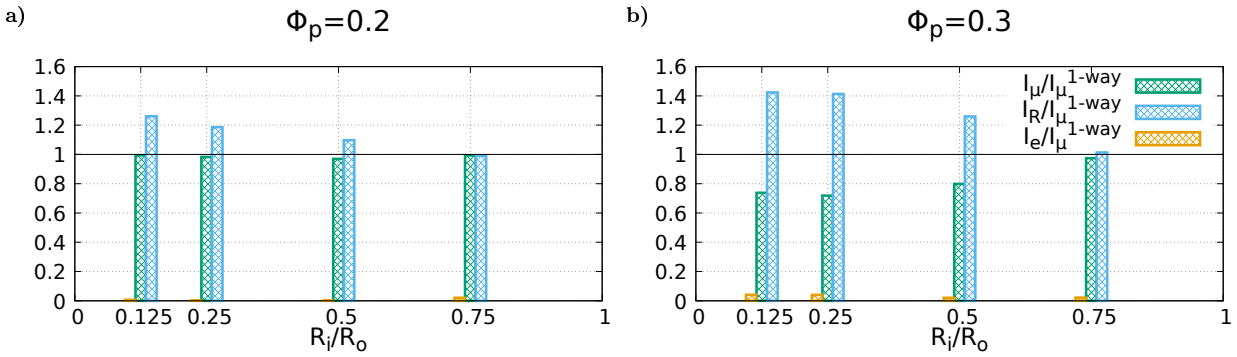

Figure 4.26: The viscous I_μ (green rectangles), turbulent I_R (blue rectangles) and extra stress I_e (orange rectangles) contributions of the mean viscous wall stress τ_w. Data are reported with respect to the viscous contribution of the unladen referred case I_μ^{1-way}. The sum of the three contributions is constant for each R_i/R_o. The reduced flow rate is observable when $\Phi_p = 0.3$. The reduction is accompanied by the increase of the turbulent contribution I_R. The extra stress contribution I_R is negligible.

In figure 4.26 the viscous I_μ (green rectangles), turbulent I_R (blue rectangles) and extra stress I_e (orange rectangles) contributions of the mean viscous wall stress τ_w are provided. Data are reported with respect to the viscous contribution of the unladen reference case I_μ^{1-way}. The sum of the three contributions is constant for each R_i/R_o, whereas it may differ when the internal wall radius is changed.

The extra stress contribution I_e is always negligible. The result is consistent with the findings presented in the previous section, where the extra-stress τ_e is shown to be insignificant as compared with the shear stress τ_R.

When the particle mass loading ratio is $\Phi_p = 0.2$ the flow rate does not decrease ($I_\mu/I_\mu^{1-way} \approx 1$). Since $I_e/I_\mu^{1-way} \approx 0$, the turbulent wall stress contribution in the 1-way I_R^{1-way} and 2-way I_R coupled cases coincide under the presented scale.

The reduced flow rate is observable when $\Phi_p = 0.3$. The exception is the case D (i.e. $R_i/R_o = 0.75$), where the confinement of the fluid is enough strong to absorb the particle-induced turbulent fluctuations (see the behaviour of τ_R and τ_e in figure 4.25).

If we compare the two histograms (panel 'a' and panel 'b') , we observe that when Q decreases the turbulent contribution I_R increases. Therefore, since I_e is negligible, the reduced flow rate is entirely attributed to the modified turbulent shear convection generated by the particles. The direct influence of the particle feedback on the flow rate is negligible.

We stress the crucial findings of this analysis. The mechanism through which the particles affect the flow rate (or the viscous wall stress) involves the modification of the turbulent shear convection

$\langle u_r' u_z' \rangle$ (or τ^R). The results suggest that, owing to the asymmetric weight of τ^R in the integral I_R, the increased viscous resistance provided by the Reynolds shear stress at the external side dominates the opposite contribution at the internal one. In addition to this, the extra-stress contribution I_e is negligible. Hence, the particle feedback significantly influences the Reynolds shear stress, but the direct effect on the flow rate, through I_e, is insignificant.

4.2.11 The two-point correlation function in the two-way coupling regime

In this section we report the two-point correlation functions of the velocity $\mathbf{u}$ and of the thermal field T, in the two-way coupling regime. The two-point correlation functions of the axial R_{zz}, radial R_{rr}, azimuthal $R_{\theta\theta}$ velocity and temperature R_{TT} fluctuations are defined in equation (4.8). The two point correlation functions $R(r, z)$ provide informations on the optimal size of the domain as well as the length-scales of the coherent structures. In figure 4.27 are reported the two-point correlation functions for annular pipe of wall radius ratio $R_i/R_o = 0.25$. The correlations are computed where the peaks of Reynolds stress occur in the one-way coupling regime. In particular, we report the correlation of the internal (left panels) and external (right panels) near-wall coherent structures.

As observed in the instantaneous snapshot in figures 4.2 4.3 4.4, the particle forcing disrupts the axially-elongated coherent structures of the wall turbulence. The phenomenon is detected by the correlations and involve both the turbulent velocity and the temperature fluctuations. In fact the convergence to zero of the correlations is accelerated. In fact, where the flow was still correlated in the one-way coupling regime, the activation of the particle feedback considerably reduces the minimum reached at the largest separation $z = L_z/2$. The effect is more pronounced when the particle mass loading is $\Phi_p = 0.3$, but is still present when $\Phi_p = 0.2$. Hence, the axial characteristic length-scale of the near-wall coherent structures decreases both at the internal and external side.

These observations are reported in all the four annular pipes (cases A, B, C, and D). However the results of the cases A, C and D are omitted, being verbosely redundant.

In conclusion, the stream-wise domain size $L_z = 2\pi$ of the domain may be unsuitable to treat the single-phase turbulent flow, as also discussed by Bagheri et al. [74]. However in the presence of a dispersed phase, the reduction of the stream-wise characteristic length-scale of the near-wall coherent structures justifies the use of periodic boundary conditions.

4.2.12 The Reynolds heat density and the heat flux in the two-way coupling regime

In the present simulations the inter-phase momentum coupling is enforced. However, the dispersed phase and the fluid can't exchange heat, since the particles are considered thermally inert. The modification of the thermal fluid field can still occur, if the turbulent mixing is altered. The turbulent thermal convection is represented by the Reynolds heat density $\langle u_r' T' \rangle$. The Reynolds heat density affects the heat exchange in the annular pipe according to the heat equation (4.7). According to the equation, the area under the curves $\langle u_r' T' \rangle$ provide the turbulent contribution of the heat exchange.

In figure 4.28 the Reynolds heat density $\langle u_r' T' \rangle^+$ is reported in wall unit. The radial distance is $\xi = (r - R_i)/(R_o - R_i)$. The one-way coupled reference (pink lines) cases are provided in comparison.

The annular pipe $R_i/R_o = 0.75$ reports no modifications of the Reynolds heat density, for any particle mass loading Φ_p considered. The other three configurations $R_i/R_o = 0.125$, $R_i/R_o = 0.25$, $R_i/R_o = 0.5$ show negligible alterations when $\Phi_p = 0.2$. When $\Phi_p = 0.3$ the curves increase on the right-hand of the annular pipe, while the position and value of the internal peak is more or less unchanged. Due to the increased area under the Reynolds heat density, we expect to find a small increase of the heat exchange when $\Phi_p = 0.3$, in the three smallest configurations ($R_i/R_o = 0.125$, $R_i/R_o = 0.25$ and $R_i/R_o = 0.5$).

The heat exchange Q_W in the two-way coupling regime is reported in figure 4.29. Data are compared with the unladen value Q_W^{1-way}. The error bar $\delta_s = 3\sigma/\sqrt{(N_s)}$, is reported, where σ is

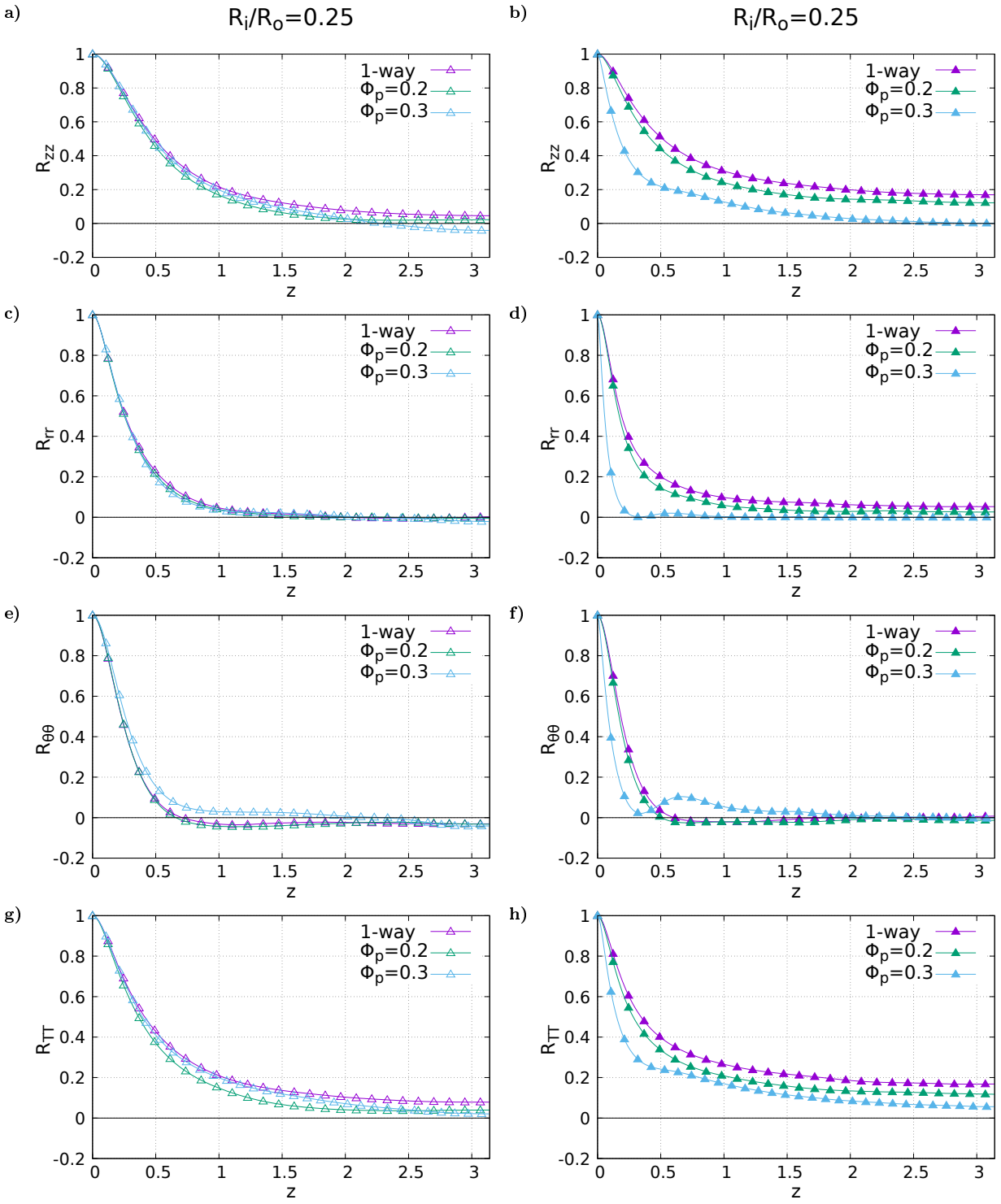

Figure 4.27: The two-point correlation functions of the axial velocity fluctuation R_{zz} (panels 'a' and 'b'), radial velocity fluctuation R_{rr} (panels 'c' and 'd'), azimuthal velocity fluctuation $R_{\theta\theta}$ (panels 'e' and 'f') and temperature fluctuation R_{TT} (panels 'g' and 'h') for the annular pipe of wall radius ratio $R_i/R_o = 0.25$. The axial distance z ranges between 0 to the half-length of the annular pipe $L_z/2 = \pi$. The correlation is computed where the peaks of the Reynolds stress occur. The left panels refer to the correlation computed at the internal side. The right panels refer to the correlation computer at the external side.

the standard deviation of the single measurement, and N_s the number of samples.

When $\Phi_p = 0.3$ the heat exchange increases in all the four configurations. The largest increment

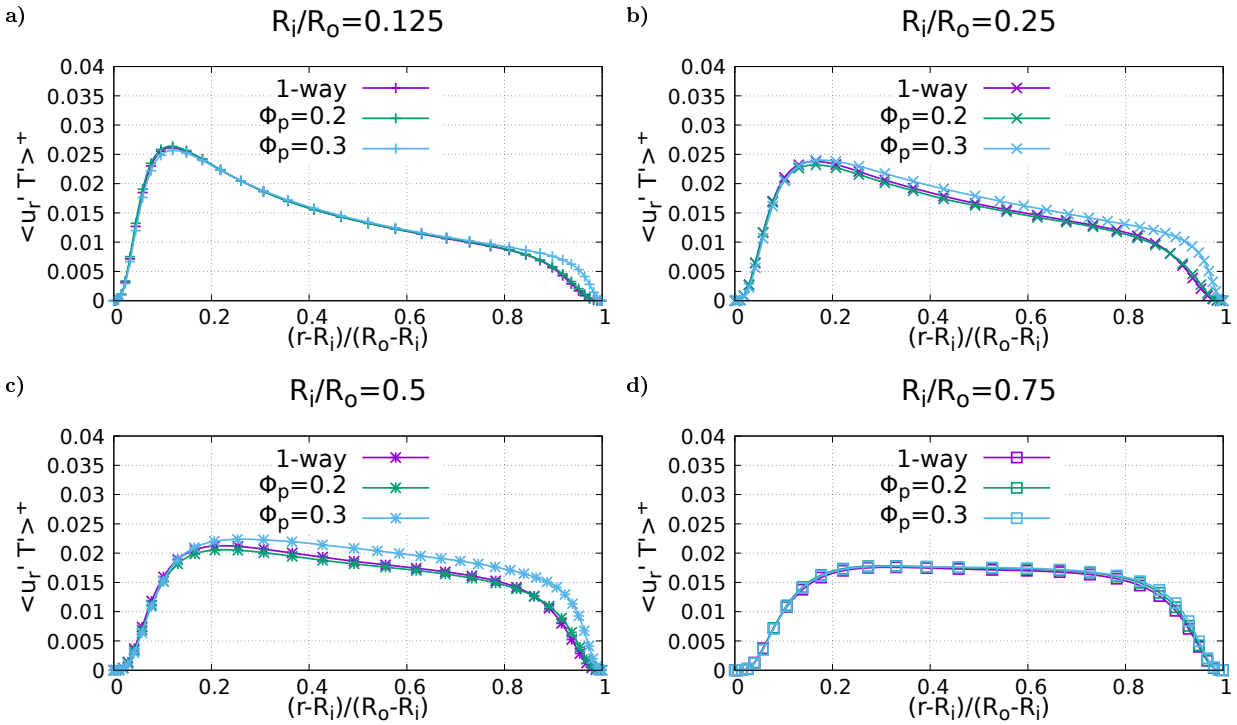

Figure 4.28: The Reynolds heat density $\langle u_r' T' \rangle^+$, wall unit, in the two-way coupling regime. The radial position is $\xi = (r - R_i)/(R_o - R_i)$.

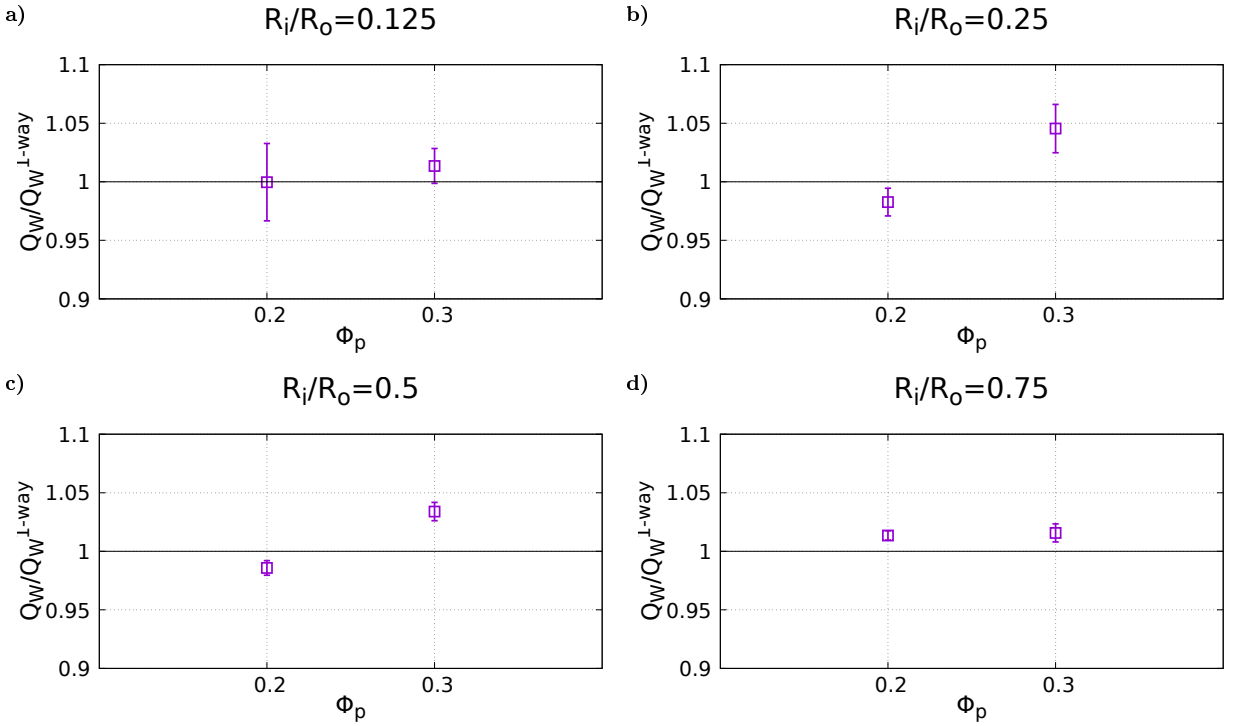

Figure 4.29: The heat exchange Q_W in the two coupling regime compared with the unladen value Q_W^{1-way}. The error bar $\delta_s = 3\sigma/\sqrt{(N_s)}$, is reported, where σ is the standard deviation of the single measurement, and N_s the number of samples.

is achieved when $R_i/R_o = 0.25$, but does not go beyond 5%. When $\Phi_p = 0.2$ the ratio $\frac{Q_W}{Q_W^{1-way}}$ oscillates very close 1. Therefore there is no specific trend with respect to the curvature of the

internal wall. The modification in this case is very small, order of 1-2%.

The small increment (few percentage points) of the heat exchange, found when $\Phi_p = 0.3$, is much lower than the reduction of the flow rate (order of 20-30%). Therefore, the two-way momentum inter-phase coupling is little effective in influencing the heat exchange, if the particles are thermally inert.

The heat exchange modification is consistent with the behaviour of the Reynolds heat density in the two-way coupling regime observed in figure 4.28.

4.2.13 The turbophoresis in the two-way coupling regime

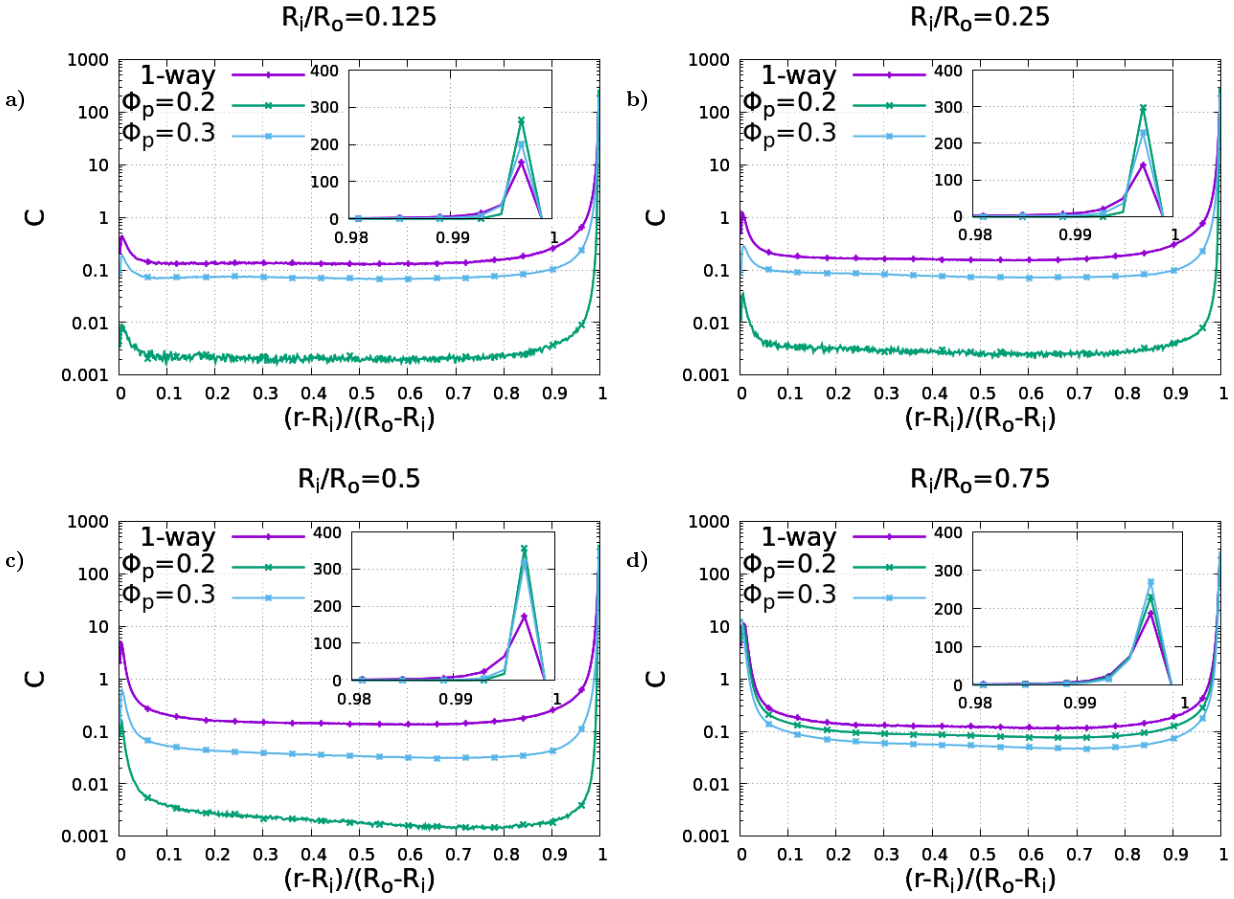

Figure 4.30: The normalised particle concentration $C(\xi)$ versus the radial position $\xi = (r - R_i)/(R_o - R_i)$. The concentration in the one-way coupled simulations are provided as well (pink lines). The enlargements of the plots close to the external wall are reported.

Owing to the modification of the turbulence structures observed in the previous sections, the particle transport can be strongly affected by the two-coupled momentum transfer. Therefore the transport of the dispersed phase, when the particle feedback is disabled, is likely far from reality.

At this aim in this section we report the analysis of the turbophoresis in the two-way coupling regime. The turbophoresis is measured by means of the normalised concentration $C(r)$, defined by the equation (4.10).

We remind to the reader that in the two-way coupled simulations, the Stokes number $St^+ = 10$ is constant. The selected Stokes number $St^+ = 10$ corresponds to the most intense turbophoresis in the one-way coupling regime. In this regime is probable to find the strongest fluid-particle interactions, once the two-way coupled momentum transfer is enabled. The influence on the particle transport, when the particle back-reaction is active, of the particle diameter (i.e. the Stokes number) is out

of the scope of the present research.

In the present simulations, the initial particle concentration is homogeneous. The turbulence activates the migration processes that lead to the turbophoresis. The characteristic time of these fluid dynamic phenomena is very long. The concentration reaches the stochastic steady state in between 800 to 1200 computational instants, depending on the specific case. If we consider a particle of axial velocity equals to the bulk velocity in the unladen case (i.e. $v_{p_z} = u_b = 1$), the particle crosses the whole length of the annular pipe between 127 to 190 times before the transient is complete. Owing to this very slow transient, it is very important that the simulations are evolved over a prolonged temporal interval. The steadiness is finally verified through the analysis of consecutive temporal chunks of the whole statistic, omitted in the present work. We now report the results at steady state.

In figure 4.30 we report the particle concentration $C(\xi)$ versus the radial dimensionless position ξ. The plots refer to the four annular pipe geometries: $R_i/R_o = 0.125$ (panel 'a'), $R_i/R_o = 0.25$ (panel 'b'), $R_i/R_o = 0.5$ (panel 'c'), $R_i/R_o = 0.75$ (panel 'd'). The findings of the one-way coupled simulations are reported (pink lines) as well.

The turbophoresis is strongly modified when the internal wall radius is $R_i/R_o = 0.125$, $R_i/R_o = 0.25$ and $R_i/R_o = 0.75$. In these three annular pipes the concentration drops in the central and internal regions, while the external peak increases. Therefore when the particle feedback is active, the particles tend to be attracted more easily to the external wall. Consequently the turbophoresis at the internal wall reduces, while at the external wall increases. The effect is greater when the particle mass loading is $\Phi_p = 0.2$. Strangely, this corresponds to the minimal turbulence modifications, in terms of velocity variances and flow rate. This tiny effects are however capable to produce large alterations in the particle transport. When the particle loading is $\Phi_p = 0.3$, a compensatory mechanism occurs. In fact, although the turbulent structures and the flow rate vary substantially, the particle concentration recovers the structure of the one-way coupled simulations.

The annular pipe with internal wall radius $R_i/R_o = 0.75$ has a complete different behaviour. In this case the increment of the turbophoresis is proportional to the particle mass loading. Moreover The effect is very small, as compared with the other three geometries.

The very important result is the enhanced turbophoresis at the external wall, occurring at particle mass loading $\Phi_p = 0.2$. In fact, standard theoretical models suggest that the largest accumulation depends on the wall-normal fluid velocity variance [102]. However, as shown in figure 4.22, this doesn not happen since we would expect a larger concentration when $\Phi_p = 0.3$. The results suggest that the mechanism of wall-accumulation is driven by some extra phenomena when the back-reaction is active. Further analyses are required in order to address the phenomena, and results are not conclusive.

4.2.14 The particle velocity in the two-way coupling regime

We will now present the particle averaged velocity $\mathbf{V_p} = \langle \mathbf{v_p} \rangle$, in comparison with the fluid $\mathbf{U} = \langle \mathbf{u} \rangle$, observed in the two-way coupling regime. As discussed in section 4.2.7, we remind that the particle and fluid velocity may differ at steady state. In fact, the unperturbed fluid velocity sampled by the particle itself, on which the particle drag depends, may differ from the fluid velocity, i.e. $\mathbf{U_{p_{(0)}}} \neq \mathbf{U}$. This is in general true even in the one-way coupling regime, where the unperturbed field coincides with the actual field, since the particle disturbance is absent (for additional details see section 2.6). In the two-way coupling regime the difference between the two fields is more pronounced, since the particle self-disturbance must be removed from the conditioned field $\mathbf{U_p}$.

In figure 4.31 we report the axial particle V_{p_z} and fluid velocity U_z in wall unit, versus the radial position $\xi = (r - R_i)/(R_o - R_i)$. The radial and azimuthal component of the velocity are omitted, since they are statistically zero.

The large flow rate reduction is observable when $\Phi_p = 0.3$ (blue curves) in all the annular pipes, except when $R_i/R_o = 0.75$. The asymmetry of the velocity profiles is conserved when the

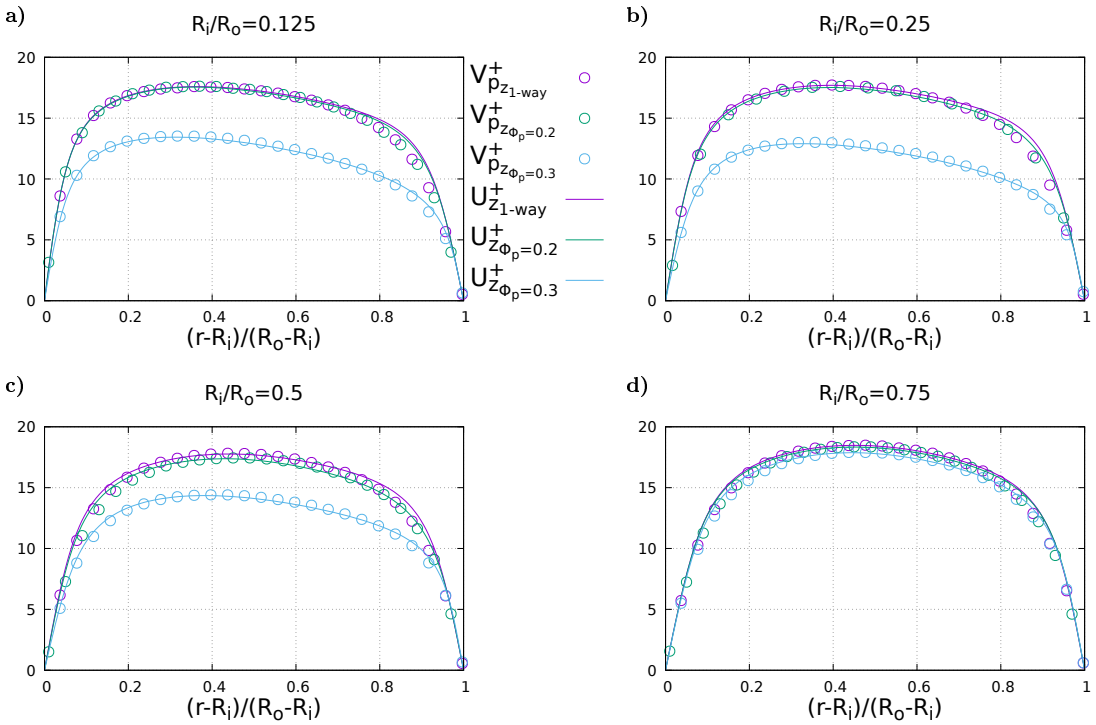

Figure 4.31: The particle averaged velocity V_p^+ (circles), in wall unit, versus the radial position $\xi = (r - R_i)/(R_o - R_i)$. The fluid velocity U_z^+ is depicted with filled lines.

back-reaction term is activated, and the profiles are evenly attenuated in all the annular pipe. When $\Phi_p = 0.2$ (green curves) the flow rate is slightly attenuated, for any R_i/R_o.

The particle and fluid velocity profiles are in analogy with the one-way coupled cases, reported in figure 4.19. In fact, the particle velocity roughly equals the fluid one everywhere, but in the vicinity of the walls, where the particle velocity is lower. This phenomenon is more emphasised at the external side, espetially for low R_i/R_o. In particular, when $R_i/R_o = 0.125$ and $R_i/R_o = 0.25$ the particle velocity matches pretty well fluid velocity internally, while it is not externally. This suggests that the particles oversample the external low-speed fluid streaks much more frequently than internally. This behaviour is independent on Φ_p, under the range of control parameters considered in this research.

4.2.15 The particle velocity variances in the two-way coupling regime

In the two-way coupling regime the particle velocity fluctuations can be affected by the particle feedback as well as the turbophoresis. The energy of the velocity fluctuations is represented by the velocity variances. The difference between the particle and fluid velocity variances describes how the dispersed phase is able to follows the fluid flow.

The particle velocity variances is reported in the present section, in the two-way coupling regime. The axial $\langle v'^2_{p_z} \rangle^+$, radial $\langle v'^2_{p_r} \rangle^+$ and azimuthal $\langle v'^2_{p_\theta} \rangle^+$ particle velocity variances are reported (circles with line) in wall unit in figures 4.32, 4.33 and 4.34. The findings of the uncoupled case are reported as well (pink curves). The corresponding fluid velocity variances (filled lines) are provided as comparison.

When the particle mass loading is $\Phi_p = 0.2$ the turbulence intensities are preserved, except small alterations close the walls. The findings show that the particle velocity fluctuations are modified accordingly. In fact, the energy of the particle axial velocity fluctuations are still larger than the fluid's one close to the external wall, as it is in the unladen case, although the peak value reduces. Moreover, the intensities of the particle radial and azimuthal fluctuations are attenuated

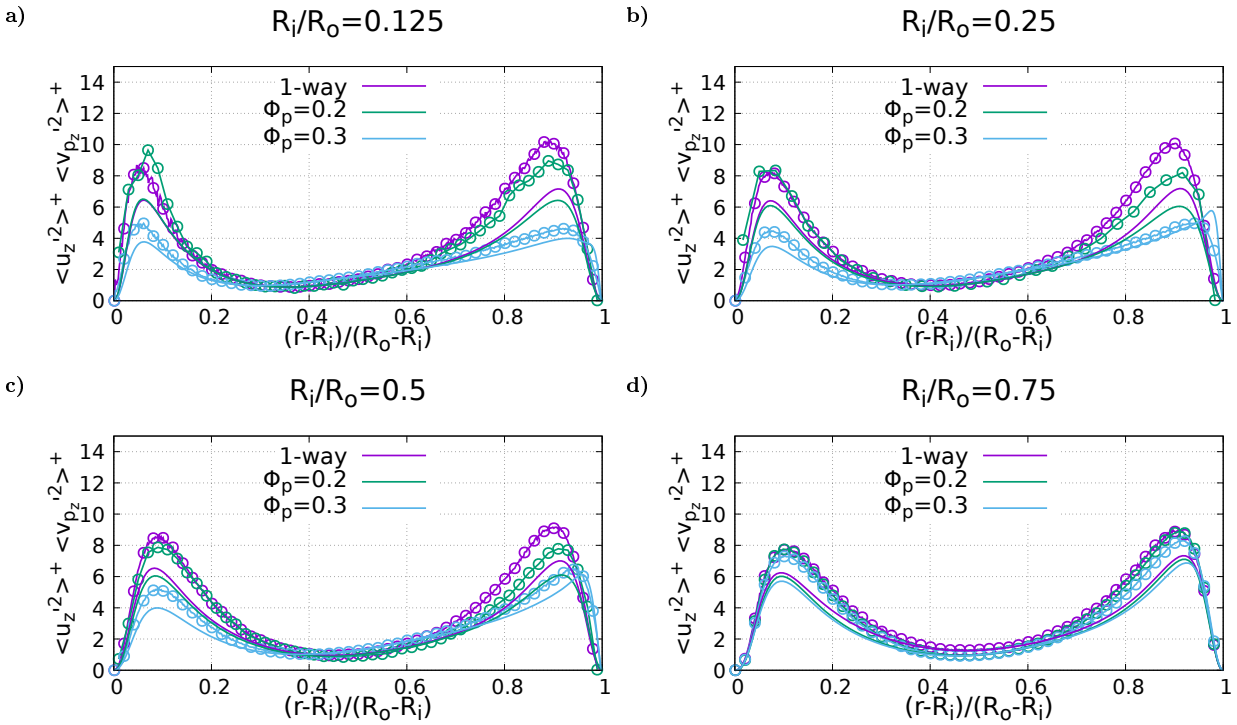

Figure 4.32: The variance of the axial component of the particle (circles with lines) and fluid (filled lines) velocity. he radial position is $\xi = (r - R_i)/(R_o - R_i)$. The findings in the one-way coupling regime are reported (pink curves).

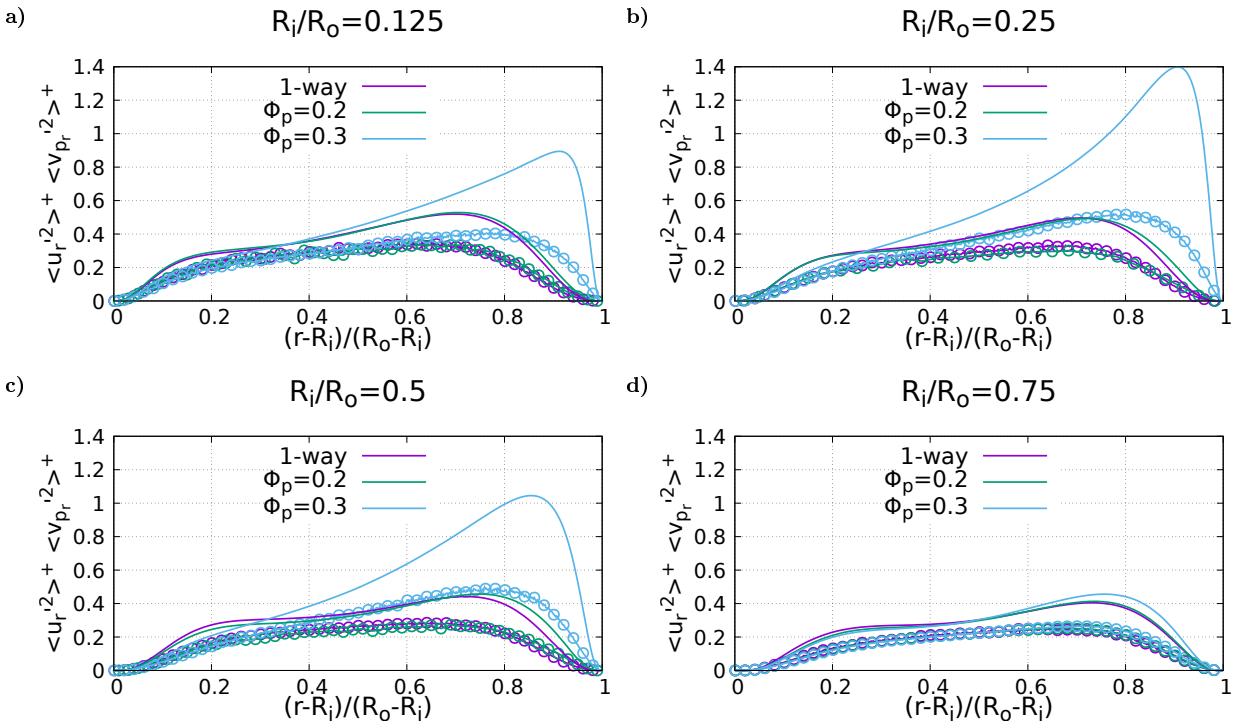

Figure 4.33: The variance of the radial component of the particle (circles with lines) and fluid (filled lines) velocity. The radial position is $\xi = (r - R_i)/(R_o - R_i)$. The findings in the one-way coupling regime are reported (pink curves).

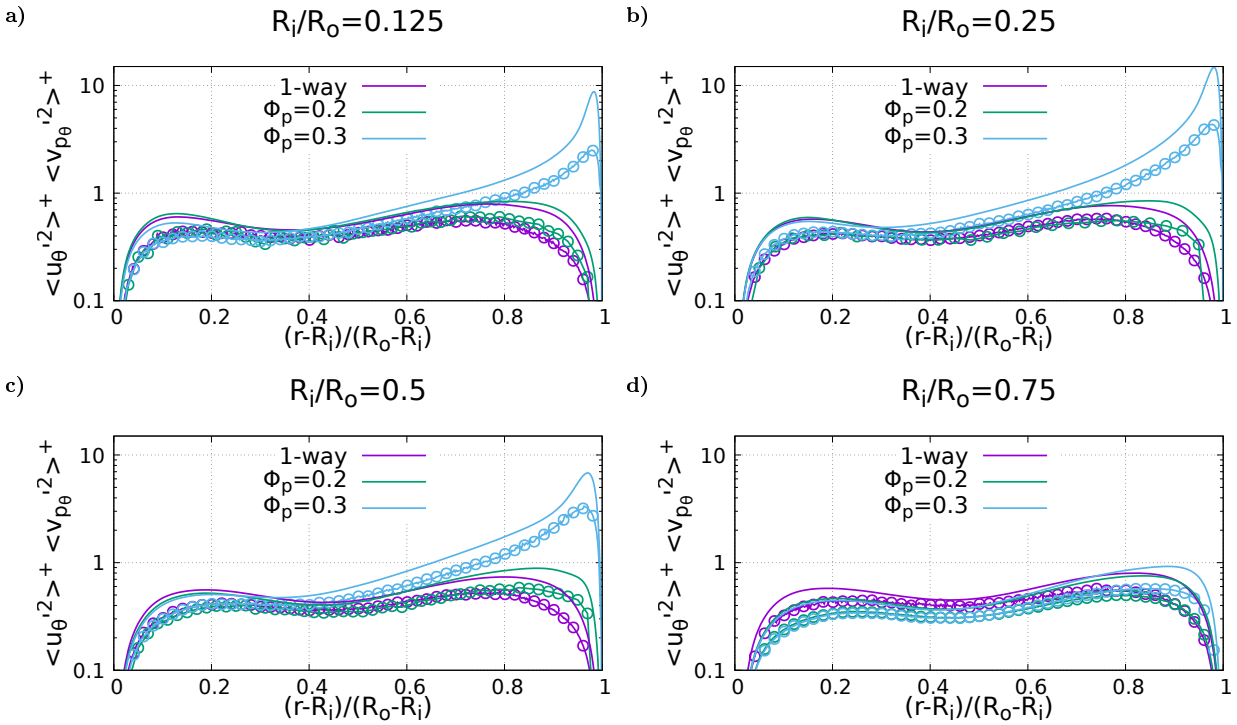

Figure 4.34: The variance of the azimuthal component of the particle (circles with lines) and fluid (filled lines) velocity. The radial position is $\xi = (r - R_i)/(R_o - R_i)$. The findings in the one-way coupling regime are reported (pink curves).

as compared with the fluid. The phenomena can be attributed to the damping effect of the Stokes force, which makes the dispersed phase unable to perfectly track the fluid unsteady motions.

When the particle mass loading is $\Phi_p = 0.3$ the turbulence structures are subjected to radical transformations. In particular, a large modification of the turbulent intensity is observable close to the external wall, where the massive particle clusters are located. The alteration involves the variances of the three fluid velocity components together. The turbulence modification is in turn transmitted to the dispersed phase. In fact, the particle velocity variances show large differences as compared with particle mass loading $\Phi_p = 0.2$. In particular the greatest changes occur when the large flow rate reduction is observed, i.e. when the wall radius ratios are $R_i/R_o = 0.125$, $R_i/R_o = 0.25$ and $R_o/R_i = 0.5$. The inclination of the particles to track the axial fluid fluctuations is improved at the external side (see panels 'a)' ,'b)' and 'c)'). In fact, the particle and fluid axial velocity variances are very close in the vicinity of the external peak. The reduction of the peaks of the fluid axial energy, which is transferred to the transverse directions, can be an explanation of such behaviour. The radial and azimuthal particle velocity variances are smaller than the fluid ones, as in the one-way coupling regime. However, in the two-way coupling regime the peaks of the energy of the transverse velocity components are significantly higher. Hence, the corresponding particle energy is similarly increased (see the blue curves in figures 4.32, 4.33 and 4.34).

When the wall radius ratio is $R_i/R_o = 0.75$ the strong fluid confinement prevents the formation of the strong particle-induced turbulence, which leads to the flow rate reduction. In fact, the turbulence intensities, as discussed in previous sections, are more or less unchanged when the distance between the walls is so short. The particle velocity variances, which are correlated to the vortical structures, are consistent to this observation. Their modification is indeed negligible when both the two particle mass loading $\Phi_p = 0.2$ and $\Phi_p = 0.3$ are considered.

Similar particle velocity variances are found in the experiments of Kulick et al. [34], who investigated a particle-laden down-flow fully developed channel flow via LDA measurements. As in our simulations, they have found that particle fluctuation intensities are larger than the unladen-

fluid velocity fluctuation in the streamwise direction but are smaller in the transverse directions.

Chapter 5

Final remarks

5.1 The bubble-laden homogeneous shear flow

The Exact Regularised Point Particle (ERPP) method has been exploited in a Direct Numerical Simulation of turbulent homogeneous shear flow laden with millions of Kolmogorov-sized rigid bubbles in the two-way coupling regime. By means of the Eulerian-Lagrangian approach, the simulations provide a study of turbulence modulation of bubble-laden shear flow exploiting a physically consistent inter-phase momentum coupling, namely the ERPP method.

The results show that bubbles are able to reduce the turbulent kinetic energy content K and dissipation rate ϵ. The modification is almost irrespective of the void fraction, but increases with St_η. Velocity variances in the three coordinate directions are equally attenuated by two-way coupling effects. Turbulent energy depletion is caused by the change of the turbulent energy production spectrum $P(k)$. In fact, the spectral distribution of the bubble-to-fluid coupling term $\Phi(k)$ is negligible. Therefore the turbulence modulation occurs through change in the spectrum of the Reynolds shear stress $\langle v_1 v_3 \rangle$. The attenuation of the energy content is small but occurs throughout the spectral scales. Significant alteration of the spectral distribution of either the turbulent kinetic energy $E(k)$ and the dissipation spectrum $D(k)$ are not observed. The results agree with those discussed in Ref.[47, 65], where gravity is considered, except for those pertaining the small scale turbulence statistics. In fact, the ERPP method predicts a small, though measurable, depletion of the energy content in the dissipative range. The effect of buoyancy, which is not considered in our simulations, on the back reaction term could affect the energy content across the spatial scales. Therefore the higher level of energy found at the smallest scales found by Mazzitelli et al. could be ascribed to the widely discussed numerical drawbacks of the PIC approach or to gravitational effects. Further investigations are required to address the phenomena described by Ref. [47, 65].

The bubble clustering, accordingly to literature, manifests in the form of thin elongated structures. The exponential behaviour of the Radial Distribution Function proves that bubbles extensively agglomerate toward smallest scales. Despite that, the clusters retain the alignment of the largest turbulence vortical structures, as documented by the SO(3) decomposition of the Angular Distribution Function. Namely, the mode $g_{21}(r)$ which samples the principal directions of the mean flow, is the most energetic revealing a preferential orientation of the clusters along the latter spatial directions. The bubble spatial distribution recovers homogeneity at increasing separation. The clustering intensity increases with St_η and is subjected to a small depletion when the back-reaction is active. This modification occurs also in the very dilute case $\varphi_v = 0.25\%$, though irrespectively of the void fraction, suggesting that the turbulence modification is more effective to the clustering process controlled by the Stokes number rather than the void fraction. This trend is well documented by cases C and D where bubbles concentrate into small scale clusters.

5.2 The particle-laden annular pipe flow

The Exact Regularised Point Particle (ERPP) method, corrected for wall-bounded flows, has been employed in Direct Numerical Simulations of turbulent annular pipe flows laden with millions of small heavy particles in the one-way and two-way coupling regime. By means of the Eulerian-Lagrangian approach, the simulations provide a study of turbulence modulation of particle-laden annular pipe flow exploiting a physically consistent inter-phase momentum coupling, namely the ERPP method.

The analysis the particle-laden annular pipe is firstly provided in the one-way coupling regime. Four different configurations, with wall radius ratio $R_i/R_o = 0.125/0.25/0.5/0.75$, are studied.

The analysis of the averaged fluid velocity shows that the profiles are asymmetric and their peaks are located into the inner half of the annular pipe. The asymmetry is inversely proportional to R_i/R_o. When $R_i/R_o = 0.75$ the solution partially recovers the structure of a turbulent channel flows.

The fluid velocity variances are asymmetric as well, and have the same trend with respect to R_i/R_o. The peaks at the internal side are smaller than they are at the external one. The dominant intensity is the stream-wise component, where the energy transfer from the mean field is provided.

The viscous $\tau_\mu = \mu\frac{\partial\langle u_z\rangle}{\partial r}$ and Reynolds shear stresses $\langle u_r' u_z'\rangle$ are reported. The zero of the stresses occurs at the same position, into the inner half of the annular pipe. Therefore, the peak of the fluid mean velocity occurs where the Reynolds shear stress is zero, for all the four geometries. In absolute values, the peak of the Reynolds stress is higher at the external side than it is internally. The viscous wall stress is larger at the convex wall, although the hydrodynamic force is larger at the concave wall.

The temperature is evolved as a passive scalar by means of the Fourier equation. The internal and external wall temperature are constant, equal to $T_i = 1$ and $T_o = 0$, respectively. The temperature is periodic along the stream-wise direction. The heat exchange is modulated by the thermal resistance of the whole system.

Owing to physical constraints, the temperature is bounded inside the boundary values, i.e. $T \in [0, 1]$. The thermal fluctuations are very close to the average at the external side, where the mean temperature is near the lower bound 0. In contrast, at the internal side the mean temperature falls rapidly down from the wall boundary value, the fluctuations are more intense.

The heat equation of the annular pipe is provided, and the heat exchange is studied as function of the radial ratio R_i/R_o. The heat exchange, with along both the thermal diffusion and turbulent contributions, shows a $1/ln(R_o/R_i)$ scaling law. In fact, the area under the Reynolds heat density is roughly constant, in the four geometry. Moreover, the heat exchange in the turbulent annular pipes is always 3 times higher than in the equivalent laminar flow.

The two point correlation functions and the one dimensional spectra show that at the external side the near wall coherent structures are longer, in the stream-wise direction, than they are internally. The spectral energy of the temperature is largest where the peak of temperature variance is observed. The spectra and the variance of a quantity are indeed strictly correlated, since the integral of the spectra is the variance itself. The asymmetry is, again, recovered when the distance between the walls decreases.

The turbophoresis is explored in the four geometries, when the particle back reaction is disabled. Eight different particle populations, each one labelled by a viscous time-scale based Stokes number St^+, are considered. The particle agglomeration close to the walls is largest when $St^+ = 10$. Moreover the peak at the external wall is between 10 to 100 times the internal value. The influence of the wall curvature is addressed. There is small influence on the turbophoresis due to the wall radii. In fact, we find only a small increment of the particle concentration close to the internal wall, when R_i/R_o increases. Although the difference between the internal and external peak is still large (1 to 10) the particle diffusion follows a similar symmetrisation process that occurs to the fluid.

The particle V_{p_z}, fluid U_z and fluid particle-conditioned U_{p_z} averaged velocities are reported.

The velocity U_{p_z} is the averaged fluid velocity experienced by the p-th particle, i.e. the velocity of the fluid constantly evaluated at particle position $x_p(t)$. At the stochastic steady state, the velocities V_p and U_{p_z} are equal, since the mean axial drag force is zero. The particle velocity variances are compared with the fluid ones. Owing to damping processes, the azimuthal and radial components of the particle kinetic energy are smaller that the fluid ones. On the contrary, the stream-wise particle velocity variance is larger than the stream-wise turbulent intensity. This phenomenon is attributed to the particle inertia. Particles can conserve the stream-wise velocity better than fluid does, while moving radially through the annular pipe. Therefore the deviation from the mean, which is conserved, increases.

The two-way coupled simulation are carried out for the particle population characterised by the Stokes number $St^+ = 10$. The turbulence modulation is explored in combination of the particle mass loading ratios $\Phi_p = 0.2/0.3$ in the four geometries presented ($R_i/R_o = 0.125$, $R_i/R_o = 0.25$, $R_i/R_o = 0.5$ and $R_i/R_o = 0.75$). The simulations are conducted under constant Reynolds friction number $Re^* = 180$ and Prandtl number $Pr = 0.79$. The nominal Reynolds number Re_N differs in the four geometries. This allows to compare the flow fields, ensuring that the bulk velocity is always $u_b = 1$ in the unladen case.

When $\Phi_p = 0.2$ there is a very small effect on the fluid velocity variances, measured in a tiny reduction of the peaks of the turbulent kinetic energy. On the contrary, when the particle mass loading is $\Phi_p = 0.3$ we observe important modifications of the turbulence intensities. In this case the stream-wise velocity variances show a large attenuation of the peaks, in particular for the case $R_i/R_o = 0.125$. The external peaks are shifted outward, close to the near wall massive particle clusters. The radial and, in particular, the azimuthal velocity variances report intense modifications as well. A large peak appears in the radial component $\langle u_r' u_r' \rangle^+$, very close the external wall. At the internal side, in contrast, the energy profiles are only slightly attenuated. The azimuthal velocity variances $\langle u_\theta' u_\theta' \rangle^+$ show even higher peaks, close the external wall. The peaks are about 10 times higher than in the uncoupled case, and they are comparable to the maxima of stream-wise component $\langle u_z' u_z' \rangle^+$. As for the radial fluctuations, the azimuthal profiles slightly reduce at the internal side.

Up to 30% reductions of the flow rate is observed, when $\Phi_p = 0.3$, in the three smallest annular pipes (i.e. $R_i/R_o = 0.125$, $R_i/R_o = 0.25$,$R_i/R_o = 0.5$). On the other hand when $R_i/R_o = 0.75$ and when $\Phi_p = 0.2$ very small or no reduction of the flow rate is observed.

The mechanism of the flow rate modification is explored by studying the Reynolds shear and extra stresses. In fact, the phenomenon can be studied by means of the equation of the flow rate of the annular pipe. The equation relates the flow rate with the mean viscous wall stress, the Reynolds stress and the extra stress. The different contributions of viscous wall stress, which in the present simulation setup is constant, are studied. When the flow rate reduces, the turbulent contribution increases. On the other hand the extra-stress contribution is always negligible. The flow rate reduction is therefore solely attributed to the modification of the turbulent shear convection. This is confirmed by the profiles of the Reynolds and extra stress. The extra stress is indeed always negligible as compared with the Reynolds stress.

The modification of the heat-exchange due to inter-phase momentum exchange is explored. The Reynolds heat density slightly increases when the flow rate occurs (i.e. $\Phi_p = 0.3$ and $R_i/R_o < 0.75$). However the increase is small, not beyond 5%. In all the other cases the heat-exchange is either attenuated or increased by the particles, but the modification is negligible, below 2%. Therefore, although the thermally-inert dispersed phase can considerably affect the fluid mechanical energy, the influence on the thermal field is small.

The analysis of the turbophoresis in the two-way coupling regime is provided. The concentration drops in the central and internal regions of the annular pipe, while the external peak increases. Therefore the turbophoresis is more intense at the external wall, when the particle feedback is active. The effect is more noticeable when $\Phi_p = 0.2$, that is when the turbulence modification is minimal. On the other hand, when $\Phi_p = 0.3$ a compensatory mechanism occurs, and the con-

centration partially recovers the behaviour of the one-way coupling regime. The important result is the enhanced turbophoresis at the external wall, occurring at particle mass loading $\Phi_p = 0.2$. Standard theoretical models suggest that the largest accumulation depends on the wall-normal fluid velocity variance [102]. However in the annular pipe this does not occur, since we would expect a larger concentration when $\Phi_p = 0.3$. The results suggest that the mechanism of wall-accumulation is driven by some extra phenomena, when the back-reaction is active. Further analyses are required in order to address these phenomena, and results are not conclusive.

The particle and fluid velocity decreases in the two-way coupling regime, owing to the flow rate reduction. However, the relation between the fluid and particle velocity is very similar to the uncoupled case. The asymmetry of the profiles is in particular preserved. While the first moment of the velocity is unchanged, the second moment is noticeably modified by the particle feedback. When the particle mass loading is $\Phi_p = 0.2$ the particle velocity fluctuations are slightly altered, in the same way as the fluid. In fact, the intensity of the particle axial fluctuations is larger than the fluid one close the walls, although the external peak is reduced. In addition, the intensities of the particle radial and azimuthal fluctuations are attenuated as compared with the fluid. When the particle mass loading is $\Phi_p = 0.3$ the particle velocity variances are subjected to radical transformations. In fact, the particle velocity variances are very different from the suspensions with $\Phi_p = 0.2$. The greatest change occurs when the large flow rate reduction is observed. The inclination of the particles to track the axial fluid fluctuations is improved at the external side. The reduction of the peaks of the fluid axial energy, which is transferred to the transverse directions, is an explanation of such behaviour. The radial and azimuthal particle velocity variances are smaller than the fluid ones, as in the one-way coupling regime. However, in the two-way coupling regime the peaks of the energy of the transverse velocity components are significantly higher. The particle velocity variances are in analogy with the experiments of Kulick et al. [34], who investigated a particle-laden down-flow fully developed channel flow via LDA measurements. As in the present simulations, they have found that particle fluctuation intensities are larger than the unladen-fluid velocity fluctuation in the streamwise direction but are smaller in the transverse directions.

5.3 Future perspectives

The behaviour of microbubble-laden homogeneous shear flow has been studied in detail in the present research. However few aspects were not considered and should be addressed in future investigations. In particular, the buoyancy introduces further level of anisotropy and may affect the back-reaction term and turbulent energy spectra. It could be relevant to study the influence of the direction of gravity with respect to the mean field. The results could suggest if the modification of the spectra found in Ref. [47] is an effect of the PIC shortcomings or of the buoyancy. Moreover, the fact that bubbles are preferentially located at the centre of the vortical structures has not statistically measured. The ADF provides informations on the bubble cluster shape. Although, it was proved that the bubble filaments are aligned as the smallest vortical structures of the shear flow, further analysis might be provided.

It is well-known that bubbles must be large and deformable in order to produce drag reduction in wall-bounded turbulence. In the point-particle model it still must be proved that such phenomenon occurs. Although it is impossible to study suspensions in the large-bubble regime , i.e. $St+ \gg 1$, with the present methodology, an effect of the bubble deformability can be recovered. In fact, the deformation of spherical microbubbles can be explored including the Rayleigh-Plesset equation in the numerical code. The oscillations of the bubble diameter due the pressure difference at the bubble interface can be addressed, and in particular their role on the drag modification investigated. It is important to remark that, even if the bubble interface can oscillate, the bubbles are still enough small to remain spherical. In other words, the simulations will be carried out always in the small-bubble regime, i.e. when $St^+ \ll 1$. This is important since this is not the regime where the drag reduction is experimentally measured. Therefore, it is not sure which effect on the turbulence could

be observed. Moreover, the microbubble deformation involve few theoretical issues that must be properly considered. The oscillation of the interface leads to a singular source or sink of flow rate at the bubble position. This singular term must be properly considered in the inter-phase momentum exchange model, i.e. ERPP. Therefore ERPP must be corrected in order to take into account the inflow/outflow at bubble position.

The results presented in the second part of the research, dealing with particle-laden annular pipe flows, are not conclusive. The mechanism of the turbophoresis still must be addressed. In fact, it is not clear why at $\Phi_p = 0.2$ we observe the largest particle accumulation at the external wall. In fact, according to the fluid velocity variances, the standard models of turbophoresis suggest that the largest accumulation is achieved when $\Phi_p = 0.3$. Moreover, the role of the particle mass loading on the large flow reduction requires further investigations. The fluid confinement has a clear influence on this phenomenon, as observed in the smallest configuration of the annular pipe. However, the important aspect is that the modification of the flow rate seems to be suddenly triggered, when a sufficient large number of particles are considered. The reasons of this fast transition are not clear, and suspensions with intermediate particle mass loading should be studied.

Finally the influence of the heat exchange can be studied for non-inert particle. The particle energy equation can be derived, similar to the Maxey-Riley-Gatignol equation, in the point-particle limit, and evolved along the particle trajectory. The temperature difference between the particle and the surrounding fluid gives rise to a singular heat flux. This 2-way coupling energy transfer can be enforced on the Fourier equation, where the singular heat must be treated with ERPP. Metal nanoparticles are sometimes injected in liquid solutions, the nanofluids, to enhance the heat transfer [110]. However, the size of nanoparticles is typically below 100nm, 1000 times smaller than the inertial particles considered in the present research (the size of small inertial particles is usually above $10\mu m$). An interesting scientific question could be to check if inertial particles with high conductivity could lead to the increased heat exchange observed with nonofluids. The influence on the heat exchange could be explored by considering different combinations of particle thermal conductivity. In particular, it could be investigated if the altered heat transfer is induced by the increased conductivity of the suspension or by the different thermal convection of the underlying flow.

Finally, owing to the intense bubble and particle concentration in the subjects of study, to consider a model for the four-way coupling interactions seems very important. In particular, in the annular pipe, the void fraction at the external wall is larger than 1, which is obviously unphysical. Therefore, the interparticle collision in the near-wall region will reduce the turbophoresis. The role of the attenuated particle accumulation on turbulence could be finally addressed.

Appendices

Appendix A

The dealiasing procedure of the non-linear terms in the spectral Navier-Stokes equations

In this section we shall discuss how to perform the dealiasing of the non-linear terms in the spectral Navier-Stokes equations (B.7). For the sake of simplicity let's consider for now a one-dimensional problem. The turbulence fluctuation $v(x)$ is periodic of period L, piecewise differentiable and summable over the interval $[0, L)$. The function $v(x)$ can be expanded into the uniformly convergent Fourier series of modes $\hat{v}_i$, namely

$$v(x) = \sum_{i=-M/2}^{M/2} \hat{v}_i e^{Jk_n x} \ , \quad \hat{v}_i = \frac{1}{L} \int_0^L v(x) e^{-Jk_n x} dx \tag{A.1}$$

The spectral domain of the modes k_n is bounded by fluid dynamic constraints. In this example only $m = M + 1$ modes are needed to reconstruct all the spatial scales of $v(x)$. If $k_\eta = \frac{2\pi}{\eta}$ is the largest relevant wavenumber of the spectrum of the turbulent kinetic energy, the number of modes required are

$$k_{MAX} = \frac{\pi M}{L} \geq k_\eta = \frac{2\pi}{\eta} \implies m \geq \frac{L}{\eta/2} + 1 \tag{A.2}$$

Therefore the minimum number of nodes are $m = \frac{L}{\eta/2} + 1$. The modes are computed through the integral in (A.1), over the periodic interval. The function $v(x)$ is represented under a discrete framework, over the computational grid immersed in the physical space. Hence, the integral in (A.1) is computed through the sum of discrete terms, rather than continuous ones. This operation may lead to a discrepancy between the exact $\hat{v}_i$ and the numerical $\bar{v}$ modes. In fact, the interval $[0, L)$ is divided into N elements of grid spacing $\Delta x = L/N$, namely $x_l = (l-1)\Delta x$, with $l = 1, N$. The velocity is exactly computed only at the N physical nodes, while approximated with the trapezoidal rule in the region between two neighbouring elements x_i. Hence, the modes $\bar{v}_i$ are computed through the sum of finite elements

$$\bar{v}_i = \frac{1}{N} \sum_{l=0}^{N} v(x_l) e^{-Jk_n x_i} \tag{A.3}$$

In order to understand the discretising error, we derive the relation between $\hat{v}_i$ and $\bar{v}_i$. We substitute the expression of $v(x)$ in the (A.1) into the equation (A.3), and we obtain

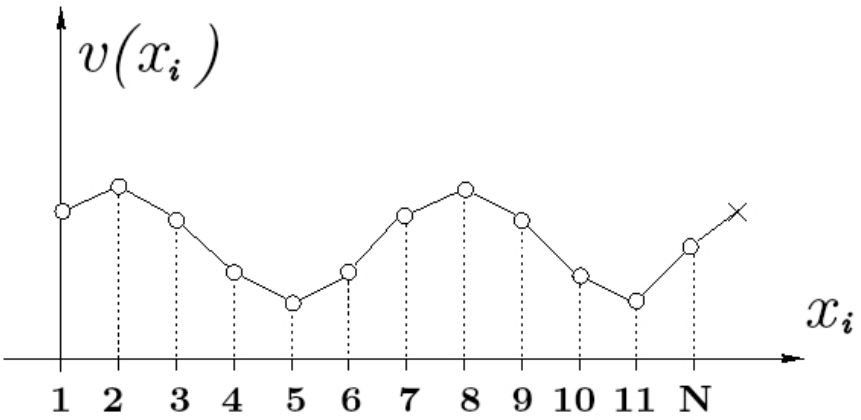

Figure A.1: The discretisation over the interval $x \in [0, L)$ of the function $v(x)$. The domain is split into the grid of N elements and spacing $\Delta x = L/N$. The function is linearly interpolated in the points within two grid elements.

$$\begin{aligned} \bar{v}_i &= \frac{1}{N} \sum_{l=0}^{N} \sum_{p=-M/2}^{M/2} \hat{v}_p e^{Jx_l(k_p - k_i)} = \\ &= \sum_{p=-M/2}^{M/2} \hat{v}_p \delta_{p,i+\alpha N} = \qquad\qquad \alpha \in \mathbb{Z} \\ &= \ldots + \hat{v}_{i-2N} + \hat{v}_{i-N} + \hat{v}_i + \hat{v}_{i+N} + \hat{v}_{i+2N} + \ldots \end{aligned} \tag{A.4}$$

Clearly the modes $\hat{v}_{i+\alpha N}$, with $\alpha \neq 0$, mustn't contaminate the solution $\bar{v}_i$. Therefore all the modes $\hat{v}_{i+\alpha N}$ that differ from the one that is actually computed must fall outside the spectral domain. The strictest conditions are at the boundary of the spectral domain, where the following inequalities must be satisfied

$$\begin{cases} -M/2 + N > M/2 \\ M/2 - N < -M/2 \end{cases} \implies N > M \tag{A.5}$$

Consequently, there exists a constraint in the discretisation of the physical space. In fact, in order to represent the $M+1$ exact Fourier modes at least $M+1$ physical nodes are required. The reasoning can be also reversed. That is, we can compute only N exact Fourier modes, through the N-discretisation of the periodic interval of $v(x)$. In conclusion, k_η determines the number of $M+1$ modes of $v(x)$ necessary to the computation. The number of physical nodes to represent $v(x)$ must consequently be $M+1$, in order not to have errors in $\bar{v}_i$.

In the Navier-Stokes equation the convective term represents a non-linearity. This quantity, on the one-dimensional ground, is expressed as the product of two functions, namely $h(x) = a(x)b(x)$. The functions $a(x)$,$b(x)$ and $h(x)$ are all periodic of period L, piecewise-differentiable and summable over the interval $x \in [0, L)$. Therefore the three functions are amenable to the Fourier decomposition, in particular $a(x)$ and $b(x)$ can be written as

$$\begin{aligned} a(x) &= \sum_{i=-M/2}^{M/2} \hat{a}_i e^{Jk_n x}, \quad \hat{a}_i = \frac{1}{L} \int_0^L a(x) e^{-Jk_n x} dx \\ b(x) &= \sum_{i=-M/2}^{M/2} \hat{b}_i e^{Jk_n x}, \quad \hat{b}_i = \frac{1}{L} \int_0^L b(x) e^{-Jk_n x} dx \end{aligned} \tag{A.6}$$

The function $h(x)$ can be expanded into the Fourier series as well. We can find the relation between the modes $\hat{h}_i$, $\hat{a}_n$, and $\hat{b}_p$ through the definition of the Fourier expansion, namely

$$h(x) = \sum_{i=-\widetilde{M}/2}^{\widetilde{M}/2} \hat{h}_i e^{Jk_n x} = \sum_{n=-M/2}^{M/2} \sum_{p=-M/2}^{M/2} \hat{a}_n \hat{b}_p e^{J(k_n+k_p)x} \tag{A.7}$$

Hence, the product between $a(x)$ and $b(x)$ is not a conservative operation with respect to the number of modes. In other words the product operator introduces additional spatial lengthscales of those included in the operands. Therefore, the number of modes $\widetilde{m} = \widetilde{M} + 1$ of $h(x)$ differs from the $M + 1$ modes of the original functions $a(x)$ and $b(x)$. The equation (A.7) provides the spectral domain of $h(x)$, which is the interval $n \in [-\widetilde{M}/2, \widetilde{M}/2]$, namely

$$\begin{cases} \widetilde{M}/2 = M/2 + M/2 \\ -\widetilde{M}/2 = -M/2 - M/2 \end{cases} \implies \widetilde{M} = 2M \tag{A.8}$$

The $2M + 1$ modes are required to describe all the spatial scales of the non-linear function $h(x)$. However, on the numerical ground, it is unfeasible to compute the entire spectrum of $h(x)$. In fact, at run time, new additional modes, resulting from the non-linear term, are supposed to be added and evolved by the Navier-Stokes equations. This path is, of course, impassable since requires infinite amount of memory. A dealiasing procedure is required, to discard some of the modes of $h(x)$. We made the choice of representing in the exact form only the modes $\hat{h}_i$ falling inside the spectra of $a(x)$ and $b(x)$. The modes $\hat{a}_i$ and $\hat{b}_i$ must satisfy the condition (A.5). With this in mind, according to equation (A.4), the number of physical nodes $\widetilde{N}$ required to correctly evaluate the computational modes $\bar{h}_i$ are prescribed by following the inequality

$$\begin{cases} -M/2 + \widetilde{N} > M \\ M/2 - \widetilde{N} = -M \end{cases} \implies \widetilde{N} > 3/2M = 3/2N - 3/2 \tag{A.9}$$

The result is better explained by a graphic analysis, provided in figure A.2, where the domain of $\hat{a}_n$ and $\hat{b}_n$ is the interval $n \in [-M/2, M/2]$, while the domain of $\hat{h}_n$ is $n \in [-M, M]$.

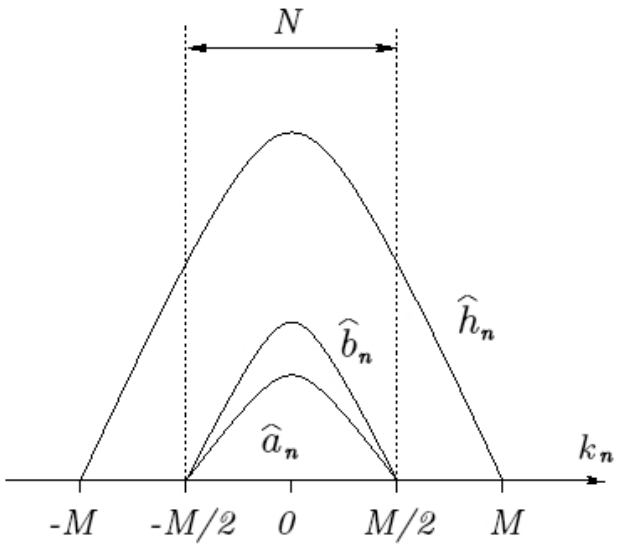

Figure A.2: Sketch of the spectra of the modes $\hat{h}_n$, $\hat{b}_n$ and $\hat{a}_n$. The domain of $\hat{a}_n$ and $\hat{b}_n$ is interval $n \in [-M/2, M/2]$. The domain of $\hat{h}_n$ ranges between $n \in [-M, M]$.

In conclusion, $h(x)$ must be resolved over the grid of $\widetilde{N} = 3/2N - 1/2$ elements to exactly describe the N modes $\hat{h}_n$ over the interval $n \in [-M/2, M/2]$. The procedure is generally referred to as the $3/2$ dealiasing rule, in which only the first $1/2$ of the low frequency modes are exactly computed, whereas the remaining $1/2$ are discarded.

The numerical treatment was discussed for the one-dimensional case, but can be extended for functions of more variables. Let's define the function $\upsilon(x_1, x_2, x_3)$, where x_i are the coordinates corresponding to the normal 3-D basis $\hat{e}_i$. The function is periodic of periods L_1,L_2,L_3, piecewise-differentiable and summable over the domain $\mathcal{B}$. Then, υ can be expanded into the Fourier series of modes $\hat{\upsilon}_{n,p,q}$

$$\begin{aligned} \upsilon(x_1, x_2, x_3) &= \sum_{n=-M_1/2}^{M_1/2} \sum_{p=-M_2/2}^{M_2/2} \sum_{q=-M_3/2}^{M_3/2} \hat{\upsilon}_{n,p,q} e^{\jmath k_{n,p,q} \cdot x} \\ \hat{\upsilon}_{n,p,q} &= \int_{\mathcal{B}} \upsilon(x_1, x_2, x_3) e^{-\jmath k_{n,p,q} \cdot x} d^3x \end{aligned} \tag{A.10}$$

$x = x_1\hat{e}_1 + x_2\hat{e}_2 + x_3\hat{e}_3$ is the displacement vector while $k_{n,p,q} = k_n^1\hat{e}_1 + k_p^2\hat{e}_2 + k_q^3\hat{e}_3$ is the wave vector. k_n^1, k_p^2, k_q^3 are the wavenumbers of the respective physical directions $\hat{e}_1$,$\hat{e}_2$,$\hat{e}_3$. Along each direction the function $\upsilon(x_1, x_2, x_3)$ is independently expanded into its one-dimensional Fourier series. The number of modes necessary to cover all the spectral space of $\hat{\upsilon}_{n,p,q}$ is $(M_1+1)(M_2+1)(M_3+1)$. For each direction, the number of modes $M_i + 1$ is prescribed by fluid dynamic conditions. In the case of homogeneous turbulence $k_\eta = \frac{2\pi}{\eta}$, where η is the Kolmogorov lengthscale, is the largest wavenumber of the turbulent kinetic energy spectrum. Therefore the spectral domain is derived by the following inequalities

$$\begin{gathered} k_{MAX}^1, k_{MAX}^2, k_{MAX}^3 > k_\eta \\ k_{MAX}^1 = \frac{\pi M_1}{L_1} \ , \quad k_{MAX}^2 = \frac{\pi M_2}{L_2} \ , \quad k_{MAX}^3 = \frac{\pi M_3}{L_3} \end{gathered} \tag{A.11}$$

The function $\upsilon(x_1, x_2, x_3)$ is discretised over the computational grid of $N_1 \times N_2 \times N_3$ elements and grid spacing $\Delta x_i = L_i/N_i$. If we denote $x_{i,l,r} = (i-1)\Delta x_1\hat{e}_1 + (l-1)\Delta x_2\hat{e}_2 + (r-1)\Delta x_3\hat{e}_3$ as the displacement vector, in analogy to the one-dimensional case, we can derive a relation between the exact modes $\hat{\upsilon}_{n,p,q}$ and the ones that are actually computed $\bar{\upsilon}_{n,p,q}$ through sum of finite elements (A.12).

$$\bar{\upsilon}_{n,p,q} = \frac{1}{N_1N_2N_3} \sum_{i=1}^{N_1} \sum_{l=1}^{N_2} \sum_{r=1}^{N_3} \upsilon(x_1, x_2, x_3) e^{-\jmath x_{i,l,r} \cdot k_{n,p,q}} \tag{A.12}$$

The equation (A.4) can be derived in the generalised form

$$\bar{\upsilon}_{n,p,q} = \frac{1}{N_1N_2N_3} \sum_{t=-M_1/2}^{M_1/2} \sum_{z=-M_2/2}^{M_2/2} \sum_{m=-M_3/2}^{M_3/2} \hat{\upsilon}_{t,z,m} \delta_{t,n+\alpha_1N_1} \delta_{z,p+\alpha_2N_2} \delta_{m,q+\alpha_3N_3} \ , \quad \alpha_1, \alpha_2, \alpha_3 \in \mathbb{Z} \tag{A.13}$$

It follows at once that the grid nodes N_i and the number of modes M_i are related as

$$N_1 > M_1 \ , \quad N_2 > M_2 \ , \quad N_3 > M_3 \ , \tag{A.14}$$

The coarsest computational grid that satisfies the requirement (A.14) has size $(M_1+1) \times (M_2+1) \times (M_3+1)$.

The non-linear term $h(x_1, x_2, x_3) = a(x_1, x_2, x_3)b(x_1, x_2, x_3)$ is treated with the 3/2 dealiasing procedure. The functions $a(x_1, x_2, x_3), b(x_1, x_2, x_3), h(x_1, x_2, x_3)$ satisfy the assumptions of derivability, integrability and periodicity made about $\upsilon(x_1, x_2, x_3)$. The treatment is then extended from the one-dimensional problem. The principle is always the same: to represent the exact Fourier modes $\hat{\upsilon}_{n,p,q}$ only within the domain of $\hat{a}_{n,p,q}$ and $\hat{b}_{n,p,q}$. The function $h(x_1, x_2, x_3)$ has to be resolved over the grid of size $\widetilde{N_1} \times \widetilde{N_2} \times \widetilde{N_3}$, where the smallest number of nodes $\widetilde{N_i}$ necessary to meet the requirement, by condition (A.13), are

$$\widetilde{N_1} = 3/2N_1 - 1/2 \ , \quad \widetilde{N_2} = 3/2N_2 - 1/2 \ , \quad \widetilde{N_3} = 3/2N_3 - 1/2 \ , \tag{A.15}$$

Therefore, for each direction, only the first $1/2$ modes of the Fourier series of the non-linear term are actually computed, while the remaining $1/2$ are discarded.

Appendix B

The Rogallo procedure

The Rogallo procedure is employed to compute the spectral Navier-Stokes equations in the homogeneous shear flow. The technique is necessary since the mean shear introduces a non-periodic term in the equations of the turbulent fluctuation $v(x,t)$. In order to understand this, we consider the turbulent shear flow, that is the object of our research. We define the first inertial reference, whose space is measured by the fixed basis $\hat{e}_1, \hat{e}_2, \hat{e}_3$. The domain $\mathcal{A}$ over such space is the box in figure B.1. Through the classical Reynolds decomposition, the instantaneous field $u(x,t)$ is decomposed into the averaged velocity $U(x_3)$ and the turbulence fluctuation $v(x,t)$, namely $u(x,t) = U(x_3) + v(x,t)$. The mean velocity is $U(x_3) = Sx_3\hat{e}_1$, where S is the mean shear. Due to the averaged shear, the turbulent field is steadily supplied with energy. This energy comes from the work of the averaged viscous and Reynolds stresses performed by the mean field over the boundary of $\mathcal{A}$, and allows that turbulence does not decays in time.

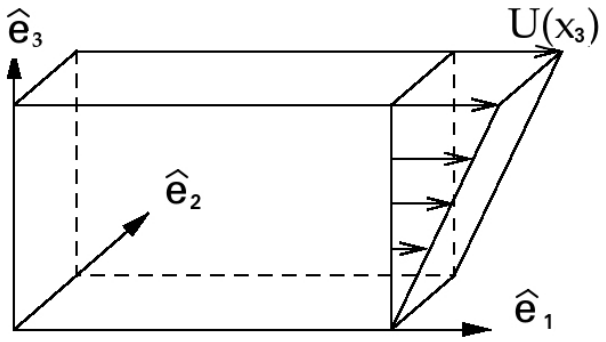

Figure B.1: The domain of the shear flow $\mathcal{A}$.

The Navier-Stokes equation of the turbulence fluctuation $v(x,t)$ are

$$\begin{cases} \rho_f \frac{\partial v}{\partial t}(x(t),t)\big|_{x=cost} + \rho_f v_3(x(t),t) S\hat{e}_1 + \rho_f S x_3 \frac{\partial v}{\partial x_1}(x(t),t) = -\nabla p(x(t),t) + \mu \nabla^2 v(x(t),t) + f_p(x(t),t) \\ \nabla \cdot v(x(t),t) = 0 \end{cases} \qquad x \in \mathcal{A} \tag{B.1}$$

The equations cannot undergo the Fourier expansion over the domain $\mathcal{A}$. The problem originates from the mean field, that is non periodic under the current reference. In particular, the equation must be somehow manipulated in order that the term $\rho_f S x_3 \frac{\partial v}{\partial x_1}$ disappears.

To deal with the problem, Rogallo proposed the following change of the parametrisation of the turbulence fluctuation

$$\begin{cases} \widetilde{v}_1 = v_1 - Sx_3 \\ \widetilde{v}_2 = v_2 \\ \widetilde{v}_3 = v_3 \\ \widetilde{t} = t \end{cases} \qquad \begin{cases} \widetilde{x}_1 = x_1 - Sx_3 t \\ \widetilde{x}_2 = x_2 \\ \widetilde{x}_3 = x_3 \\ \widetilde{t} = t \end{cases} \tag{B.2}$$

We refer to x as the coordinates of the fixed reference and to $\widetilde{x}$ as the coordinates in the moving reference. In this new reference the fluid is mapped over the space that is moving as the mean field. Hence, even if the velocities are still measured under the inertial observer, the fluid particles are tracked with respect to the moving reference. In this frame the new domain $\mathcal{B}$, that starts from the undeformed configuration $\mathcal{A}$, is progressively subjected to shear deformation, see figure B.2.

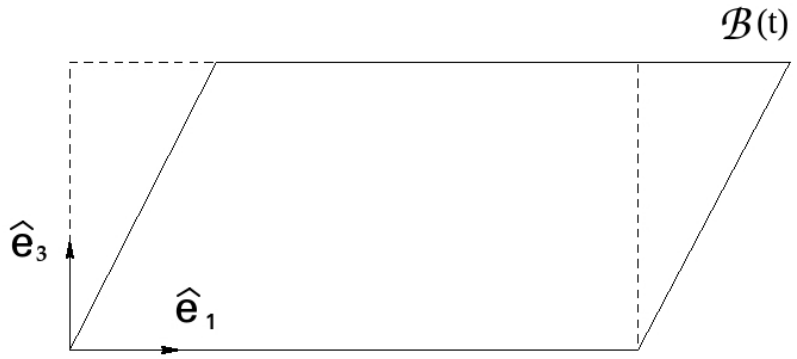

Figure B.2: The skewed $\mathcal{B}(t)$ (solid line) and fixed domain $\mathcal{A}$ (dash line) of the shear flow. Sight of the plane $\hat{e}_3, \hat{e}_1$.

The complexity of this new time-dependent topology allows to reduce the equations to a periodic problem. In fact, through the change of coordinates (B.2), there exists the following transformation of the time partial derivative of the velocity v, computed under the fixed space.

$$\left.\frac{\partial v}{\partial t}\right|_{x=cost}(x(t),t) = \left.\frac{\partial v}{\partial t}\right|_{\widetilde{x}=cost}(\widetilde{x}(t),t) - \frac{\partial v}{\partial x_1} Sx_3 \tag{B.3}$$

With such manipulation the Navier-Stokes equations (B.1) are recast into the periodic form

$$\begin{cases} \rho_f \left.\frac{\partial v}{\partial t}(\widetilde{x}(t),t)\right|_{\widetilde{x}=cost} + \rho_f v_3(\widetilde{x}(t),t) S\hat{e}_1 = -\nabla p(\widetilde{x}(t),t) + \mu\nabla^2 v(\widetilde{x}(t),t) + f_p(\widetilde{x}(t),t) \\ \nabla \cdot v(\widetilde{x}(t),t) = 0 \qquad\qquad x \in \mathcal{B} \end{cases} \tag{B.4}$$

The velocity and the pressure field are mapped in the moving reference, namely $v(\widetilde{x}(t),t)$ and $p(\widetilde{x}(t),t)$. Therefore the spatial derivatives in equations (B.4), that refer to the fixed space, must be converted into the skewing configuration as well. It easily proved that the nabla operator in the skewing space $\widetilde{\nabla}$ is related to ∇ as

$$\nabla = \widetilde{\nabla} + St\hat{e}_3 \frac{\partial}{\partial \widetilde{x}_1} \tag{B.5}$$

The fields $v(\widetilde{x}(t),t)$ and $p(\widetilde{x}(t),t)$ are periodic and continuous over the domain $\mathcal{B}(t)$, and can be expanded into the Fuorier series, with respect to the complex bases $e^{Jk_{i,m,l}\cdot\widetilde{x}}$

$$
\begin{aligned}
&\upsilon(\widetilde{x},t) = \sum_{i,m,l} \hat{\upsilon}_{i,m,l} e^{\jmath k_{i,m,l}\cdot\widetilde{x}} \ , \qquad \hat{\upsilon}_{i,m,l} = \frac{1}{V}\int_{\mathcal{B}(t)} \upsilon(\widetilde{x},t) e^{-\jmath k_{i,m,l}\cdot\widetilde{x}} d^3\widetilde{x} \\
&p(\widetilde{x},t) = \sum_{i,m,l} \hat{p}_{i,m,l} e^{\jmath k_{i,m,l}\cdot\widetilde{x}} \ , \qquad \hat{p}_{i,m,l} = \frac{1}{V}\int_{\mathcal{B}(t)} p(\widetilde{x},t) e^{-\jmath k_{i,m,l}\cdot\widetilde{x}} d^3\widetilde{x} \\
&k_{i,m,l} = \frac{2\pi i}{L_1}\hat{e}_1 + \frac{2\pi m}{L_2}\hat{e}_2 + \frac{2\pi l}{L_3}\hat{e}_3 \\
&i \in [-M_1/2, M_1/2] \ , \quad m \in [-M_2/2, M_2/2] \ , \quad l \in [-M_3/2, M_3/2] \ ,
\end{aligned}
\tag{B.6}
$$

The modes $\hat{\upsilon}_{i,m,l}$ and $\hat{p}_{i,m,l}$ measure the intensity of the fluctuation related to the scale $k_{i,m,l} = k_i^1\hat{e}_1 + k_m^2\hat{e}_2 + k_l^3\hat{e}_3$. Since the turbulent signals are band-limited, the integer indeces i, m, l span between a negative minumun to a positive maximum, as we have discussed in A. Hence, the spectral domain is chosen to describe all the turbulent lengthscale. The direction of periodicity are $\hat{e}_1, \hat{e}_2, \hat{e}_3$, of periods L_1, L_2, L_3, which are also the sides of the domain $\mathcal{A}$. V is the volume of the domain $\mathcal{B}(t)$, that corresponds to $\mathcal{A}$'s, since the change of coordinates (B.2) is isochoric. From the relation (B.5), we define the modified wave vector $k_{M_{i,m,l}} = k_{i,m,l} + Stk_i^1\hat{e}_3$ and we compute the spectral Navier-Stokes equations

$$
\begin{cases}
\rho_f \frac{\hat{\partial\upsilon}}{\partial t}_{i,m,l} + \rho_f \hat{\upsilon}_{3_{i,m,l}} S\hat{e}_1 + \jmath\rho_f k_{M_{i,m,l}} \cdot (\upsilon \hat{\otimes} \upsilon) = -\jmath k_{M_{i,m,l}} \hat{p}_{i,m,l} - \mu k_{M_{i,m,l}}^2 \hat{\upsilon}_{i,m,l} + \hat{f}_{p\,i,m,l} \\
\hat{p}_{i,m,l} = \jmath \frac{2\rho_f S k_i^1 \hat{\upsilon}_{3_{i,m,l}} - k_{M_{i,m,l}} \cdot \{\hat{f}_{p\,i,m,l} - \jmath\rho_f k_{M_{i,m,l}} \cdot (\upsilon\hat{\otimes}\upsilon)\}}{k_{M_{i,m,l}}^2}
\end{cases}
\tag{B.7}
$$

The divergence constraint is replaced by the analytic expression of the pressure $\hat{p}$, that is derived by taking the divergence of the momentum equation. The modes can be advanced in time, once known the initial conditions. The physical quantities are reconstructed over the space $\mathcal{B}$, through the Fourier decomposition (B.6).

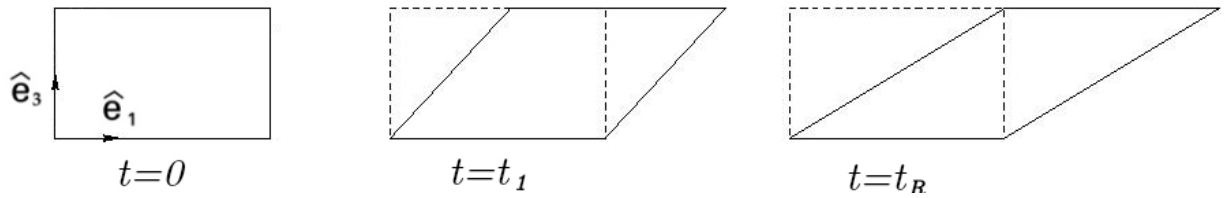

Figure B.3: Sketch of the deformation of $\mathcal{B}(t)$ (solid line). The fixed domain $\mathcal{A}$ is in dash line. View from the plane $\hat{e}_3, \hat{e}_1$. The domain $\mathcal{B}$ starts its motion at time $t = 0$, when coincides to $\mathcal{A}$. $\mathcal{B}$ is skewed by the mean shear, being deformed into a parallelogram. At time t_R, $\mathcal{B}$ can be reassembled into the original undeformed domain $\mathcal{A}$, due the periodicity.

In figure B.3 the evolution of the deformation of the computational domain $\mathcal{B}$ is presented. The temporal integration of the equations (B.7) is possible under a mathematical framework. However, while advancing in time, we would require increasing number of the modified wavenumbers, due to the relation $k_{M_{i,m,l}} = k_{i,m,l} - tk_i^1 S\hat{e}_3$. Due the limited computational resources, infinite amount of memory cannot be allocated. The solution is to remesh the computational domain $\mathcal{B}$ into the physical one $\mathcal{A}$, exploiting the periodic property of the field. In fact, the original physical space, depicted in figure B.3 ($t = 0$), is distorted into the parallelogram of increasing skewness (the domain $\mathcal{B}$). At time $t = t_R$, the top-left corner of the parallelogram intercepts the top-right corner of the original rectangular, and the field can be remeshed with no harm into the domain $\mathcal{A}$. The procedure is repeated at future time steps.

The frequency of the remeshing is controlled by the averaged shear and aspect ratio L_1/L_3

$$t_R = \frac{L_1}{L_3 S} \tag{B.8}$$

To describe the remeshing procedure we have to distinguish between the computational $\hat{\upsilon}$ and the physical $\tilde{\upsilon}$ modes.

$$\begin{aligned} \upsilon(\widetilde{x},t) &= \sum_{i,m,l} \hat{\upsilon}_{i,m,l} e^{jk_{i,m,l}\cdot\widetilde{x}} \;, \qquad \hat{\upsilon}_{i,m,l} = \frac{1}{V}\int_{\mathcal{B}(t)} \upsilon(\widetilde{x},t) e^{-jk_{i,m,l}\cdot\widetilde{x}} d^3\widetilde{x} \\ \upsilon(x,t) &= \sum_{i,m,l} \widetilde{\upsilon}_{i,m,l} e^{jk_{i,m,l}\cdot x} \;, \qquad \widetilde{\upsilon}_{i,m,l} = \frac{1}{V}\int_{\mathcal{A}(t)} \upsilon(x,t) e^{-jk_{i,m,l}\cdot x} d^3 x \end{aligned} \tag{B.9}$$

The computational modes $\hat{\upsilon}$ are computed according to (B.6) and evolved in time with the spectral Navier-Stokes equations (B.7). The domcomposition is performed over the domain $\mathcal{B}$, where the periodic conditions are enforced at run time. At remesh time, and only at remesh time, the field is periodic over both $\mathcal{A}$ and $\mathcal{B}$, as shown in figure B.3. Therefore we can compute the Fourier series od the field over the domain $\mathcal{A}$, of modes $\widetilde{\upsilon}$. During the remeshing the computational modes $\hat{\upsilon}$ must be converted back to the physical ones $\widetilde{\upsilon}$. Therefore we have to derive the relation between the two spectral variables. With this purpose we expand the wave vector $k_{i,m,l} = k_i^1\hat{e}_1 + k_m^2\hat{e}_2 + k_l^3\hat{e}_3$ and the displacement vector $\widetilde{x} = \widetilde{x}_1\hat{e}_1 + \widetilde{x}_2\hat{e}_2 + \widetilde{x}_3\hat{e}_3$ along their directions. For the sake of clarity the dependency in the spetral modes on three wavenumbers is highlighted, namely $\widetilde{\upsilon}(k_i^1, k_m^2, k_l^3)$ and $\hat{\upsilon}(k_p^1, k_q^2, k_e^3)$. By using the definitions (B.9) and exploiting the change of coordinates (B.2), we obtain

$$\begin{aligned} &\widetilde{\upsilon}(k_i^1, k_m^2, k_l^3) = \frac{1}{V}\int_{\mathcal{A}(t)} \upsilon(x,t) e^{-jk_{i,m,l}\cdot x} d^3x = \\ &= \frac{1}{V}\sum_{p,q,r} \hat{\upsilon}(k_p^1, k_q^2, k_r^3) \int_{\mathcal{B}(t)} e^{jk_{p,q,r}\cdot\widetilde{x}} e^{-j\{k_{i,m,l}\cdot\widetilde{x} + t_R S\widetilde{x}_3 k_i^1\}} d^3\widetilde{x} = \\ &= \sum_{p,q,r} \hat{\upsilon}(k_p^1, k_q^2, k_r^3) \frac{1}{V}\int_{\mathcal{B}(t)} e^{j(k_P^1 - k_i^1)\widetilde{x}_1} e^{j(k_q^2 - k_m^2)\widetilde{x}_2} e^{j(k_r^3 - k_l^3 - k_i^1 St_R)\widetilde{x}_3} d\widetilde{x}_1 d\widetilde{x}_2 d\widetilde{x}_3 = \\ &= \sum_{p,q,r} \hat{\upsilon}(k_p^1, k_q^2, k_r^3)\delta_{k_p^1,k_i^1}\delta_{k_q^2,k_m^2}\delta_{k_r^3,k_l^3+k_i^1 St_R} = \\ &= \hat{\upsilon}(k_i^1, k_m^2, k_l^3 + k_i^1 St_R) = \widetilde{\upsilon}(k_i^1, k_m^2, k_l^3) \end{aligned} \tag{B.10}$$

The equation (B.10) provides the relation between the physical $\widetilde{\upsilon}$ and computational $\hat{\upsilon}$ modes. The spectral domain of $\hat{\upsilon}$ is fixed during the computation and it is represented by $k^1 \in [-k_{MAX}^1, k_{MAX}^1]$, $k^2 \in [-k_{MAX}^2, k_{MAX}^2]$, $k^3 + k_i^1 St_R \in [-k_{MAX}^3, k_{MAX}^3]$. The modes $\hat{\upsilon}(k_i^1, k_m^2, k_l^3 + k_i^1 St_R)$ that are relevant for the turbulence are prescribed by fluidynamic contraints, in particular for homogeneous turbulence we have

$$k_{MAX}^1, k_{MAX}^2, k_{MAX}^3 \geq k_\eta = \frac{2\pi}{\eta} \tag{B.11}$$

where k_η denotes the Kolmogorov spatial scale. The domain of $\widetilde{\upsilon}(k_i^1, k_m^2, k_l^3)$ on the other hand is function of the remeshing time t_R, and requires less wavenumbers than $\hat{\upsilon}$. Since on the numerical ground the same memory is allocated for both the computational and physical modes, a dealiasing procedure is required. In particular, at remeshing time t_R, only the modes $\hat{\upsilon}(k_i^1, k_m^2, k_l^3 + k_i^1 St_R)$ such that $|k_l^3 + k_i^1 St_R| \leq k_{MAX}^3$ can be used to compute $\widetilde{\upsilon}(k_i^1, k_m^2, k_l^3)$. The remaing modes $\widetilde{\upsilon}$ inevitably come from the external region of the boundary of $\hat{\upsilon}$, and are set to zero.

The inequality $|k^3 + k^1 St_R| < k_{MAX}^3$ can be represented on the plane (k^1, k^3) to depict the modes $\widetilde{\upsilon}$ that are actually computed during the remeshing, see figure B.4. The effect of truncating such fluidynamic scales on $\widetilde{\upsilon}$ introduces an unphysical dissipation. This drag of energy is spectrally

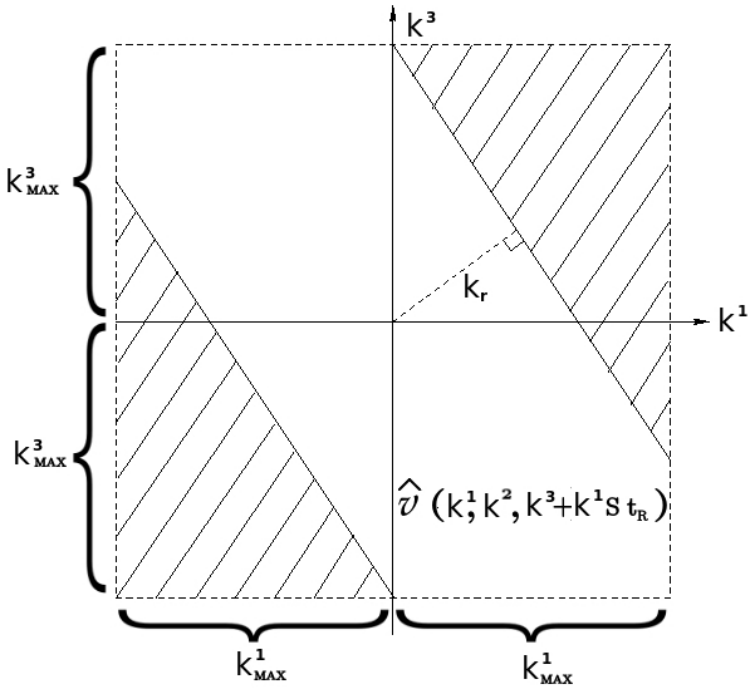

Figure B.4: Modes $\hat{v}(k^1, k^2, k^3+k^1 St_R)$, depicted over the plane (k^1, k^3), that satisfies the condition $|k^3+k^1 St_R| < k^3_{MAX}$ and are available for the remeshing procedure. The remaing modes $\widetilde{v}(k^1, k^2, k^3)$ are set to zero, since derived from the external region of the boundary of $\hat{v}$. The external rectangular of sides $2k^1_{MAX}, 2k^3_{MAX}$ is the numerical domain of $\widetilde{v}$, while the dashed zone corresponds to the truncated $\widetilde{v}$ modes. k_r is the smallest truncated wave vector of the physical modes.

located at the smallest discarded wavenumber k_r. The expression of k_r can be easly derived from the sketch B.4, and reads

$$k_r = \frac{k^3_{MAX}}{\sqrt{1+\left(\frac{L_3}{L_1}\right)^2}} \tag{B.12}$$

In order not to introduce a dealiasing bias, this unphysical forcing must fall outside the resolved spectral domain. In other words the smallest truncated scale must be placed over the dissipative range, namely $k_r > k_\eta$. Therefore the quality of the dealiasing procedure is controlled by the aspect ratio L_3/L_1 and the largest wavenumber along the shear direction $k^3_{max} = \pi(N_3 - 1)/L_3$. This explains why in our simulations the streamwise size of the domain is $L_1 = 2L_3$, while the number of nodes along the shear direction is $N_3 = 2N_1$. The reason is of course to maximise k_r in order to satisfy the constraint

$$k_r = \frac{\frac{\pi(N_3-1)}{L_3}}{\sqrt{1+\left(\frac{L_3}{L_1}\right)^2}} > \frac{2\pi}{\eta} \tag{B.13}$$

Appendix C

The numerical techniques of the annular pipe

In this section we report the numerical techinques that we employed to solve the partial differential equation of the annular pipe flow. The standard low-Mach Navier-Stokes equations for the annular pipe, in cilindrical coordinates (r, θ, z) are presented below

$$\begin{cases} \frac{\partial u_r}{\partial t} + \frac{1}{r}\frac{\partial r u_r u_r}{\partial r} + \frac{1}{r}\frac{\partial u_\theta u_r}{\partial \theta} + \frac{\partial u_z u_z}{\partial z} - \frac{u_\theta^2}{r} = -\frac{\partial p}{\partial r}\frac{1}{\rho_f} + \nu\left\{\frac{1}{r}\frac{\partial}{\partial r}\left(r\frac{\partial u_r}{\partial r}\right) + \frac{1}{r^2}\frac{\partial^2 u_r}{\partial \theta^2} + \frac{\partial^2 u_r}{\partial z^2} - \frac{2}{r^2}\frac{\partial u_\theta}{\partial \theta} - \frac{u_r}{r^2}\right\} + f_{p_r} \\ \frac{\partial u_\theta}{\partial t} + \frac{\partial u_r u_\theta}{\partial r} + \frac{1}{r}\frac{\partial u_\theta u_\theta}{\partial \theta} + \frac{\partial u_z u_\theta}{\partial z} + \frac{u_r u_\theta}{r} = -\frac{1}{r}\frac{\partial p}{\partial \theta}\frac{1}{\rho_f} + \nu\left\{\frac{1}{r}\frac{\partial}{\partial r}\left(r\frac{\partial u_\theta}{\partial r}\right) + \frac{1}{r^2}\frac{\partial^2 u_\theta}{\partial \theta^2} + \frac{\partial^2 u_\theta}{\partial z^2} + \frac{2}{r^2}\frac{\partial u_r}{\partial \theta} - \frac{u_\theta}{r^2}\right\} + f_{p_\theta} \\ \frac{\partial u_z}{\partial t} + \frac{\partial u_r u_z}{\partial r} + \frac{1}{r}\frac{\partial u_\theta u_z}{\partial \theta} + \frac{\partial u_z u_z}{\partial z} = -\frac{\partial p}{\partial z}\frac{1}{\rho_f} - \frac{dP}{dz}\frac{1}{\rho_f} + \nu\left\{\frac{1}{r}\frac{\partial}{\partial r}\left(r\frac{\partial u_z}{\partial r}\right) + \frac{1}{r^2}\frac{\partial^2 u_z}{\partial \theta^2} + \frac{\partial^2 u_z}{\partial z^2}\right\} + f_{p_z} \\ \frac{1}{r}\frac{\partial r u_r}{\partial r} + \frac{1}{r}\frac{\partial u_\theta}{\partial \theta} + \frac{\partial u_z}{\partial z} = 0 \\ \frac{\partial T}{\partial t} + \frac{1}{r}\frac{\partial r u_r T}{\partial r} + \frac{1}{r}\frac{\partial u_\theta T}{\partial \theta} + \frac{\partial u_z T}{\partial z} = \alpha\left\{\frac{1}{r}\frac{\partial}{\partial r}\left(r\frac{\partial T}{\partial r}\right) + \frac{1}{r^2}\frac{\partial^2 T}{\partial \theta^2} + \frac{\partial^2 T}{\partial z^2}\right\} \end{cases} \tag{C.1}$$

In descending order, from top to bottom, the equations are r,θ and z components of the momentum equation, the continuity equation and the Fourier equation. For simplicity, the subscript R denoting the ERPP regularised field is omitted. Hence the particle forcing f_p is here considered as a gaussian-shaped function, as prescribed by the regularising procedure. The reader is referred to section 2.8 for additional details.

The stream-wise average pressure $\frac{dP}{dz}$ is a parameter prescribed by the boundary conditions at inlet and outlet. On the other hand, the fluctuating pressure p, periodic in the stream-wise direction, must be solved through the continuity equation. At the walls, the system (C.1) is endowed with Neumann boundary conditions for the velocity $\mathbf{u}$ and the temperature T, and Dirichlet boundary condition for the pressure p, namely

$$\begin{cases} \mathbf{u}(R_i, \theta, z, t) = 0 \\ \mathbf{u}(R_o, \theta, z, t) = 0 \\ T(R_i, \theta, z, t) = 1 \\ T(R_o, \theta, z, t) = 0 \\ \frac{\partial p}{\partial r}(R_i, \theta, z, t) = 0 \\ \frac{\partial p}{\partial r}(R_o, \theta, z, t) = 0 \end{cases} \tag{C.2}$$

At the inlet and outlet the periodicity of the fields $\mathbf{u}$, T and p is enforced, namely

$$\begin{cases} \mathbf{u}(r, \theta, 0, t) = \mathbf{u}(r, \theta, L_z, t) \\ T(r, \theta, 0, t) = T(r, \theta, L_z, t) \\ p(r, \theta, 0, t) = p(r, \theta, L_z, t) \end{cases} \tag{C.3}$$

The discretision of the time derivative is performed through a low-storage four-stage Runge-Kutta algorithm. For further details the reader is referred to section E.

The spatial derivatives of the Navier-Stokes must be discretised as well, by resolving the displaced variables over the computational grid. The present section reports the algorithm used to achieve such discretisation.

C.1 The spatial discretisation of the annular-pipe Navier-Stokes equations

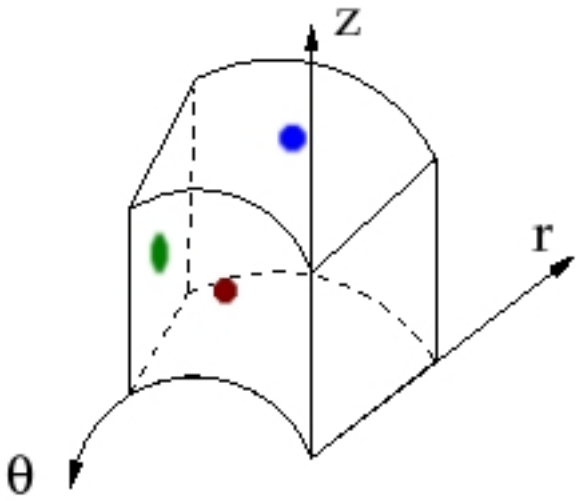

Figure C.1: The staggered arrangement in the cylindrical coordinate system (r, θ, z). The scalar variables are collocated at the center of the computational cell. The radial (red), azimuthal (green) and axial (blue) components of the vector fields are stored at cell faces.

The system of partial differential equations is resolved over a staggered mesh, by means of an energy-conserving second-order difference scheme developed by Fukagata and Kasagi [103] for incompressible flows. In the staggered mesh, see figure C.1, the scalar variables (i.e. pressure, temperature, divergence, etc...) are collocated in the centre of the computational cell, while the vectors (i.e. the velocity, momentum, forces) lie at the faces. The grid is parametrised with the vector index i, j, k, referring to the radial, azimuthal and the axial position. The integer indices correspond to the cell centres, while the fractional ones (e.g. i+1/2, j, k) to the faces . The standard second-order approximation of the arithmetic mid-sum is employed to interpolate variables that are stored in different points of the mesh. Exceptions are present in the momentum and thermal convection terms, and will be discussed later. However, many terms that require interpolation in the collocated arrangement can be computed, to this second-order approximation, without interpolation. In fact, both the pressure gradient, the viscous diffusion and the divergence of the flow are naturally computed with a central differencing scheme, with no need of interpolation. The biggest advantaged of a staggered configuration is the strong coupling between the velocity and pressure. This is helpful to avoids the formation of spurious oscillation in the pressure and velocity fields. These wiggles are typical of collocated mesh, and are generated by the inability of such numerical schemes to capture the grid-scale spatial derivatives in the projection step. In order to provide a better understanding of the problem, we would briefly focus on collocated meshes.

C.1.1 The high frequency instability in collocated arrangements

The collocated arrangement is probably the most simple configuration, since all the quantities are stored at the centre of the computational cells. The accuracy of the spatial derivatives achieved with these difference schemes is crucial to establishment of the high-frequency instability. In order to understand this concept, let's consider an one-dimensional periodic incompressible problem, over the N-discretised domain of length L and grid spacing $\Delta x = L/N$. The precision of the spatial derivatives can be determined through the Fourier, or Von Neumann, analysis. In the Von Neumann analysis the modes of the discrete spatial derivative are computed and compared with the exact ones. Hence, we should distinguish between the modes of the derivatives exactly evolved through spectral methods and their discrete formulation in difference schemes. In spectral methods the resolution of the grid is dictated by the dealiasing procedure, which allows the modes not to contaminate each other. With the N-grid resolution, $N/2$ fluid dynamic scales are captured (i.e. the Fourier modes), that we assume are the relevant ones. Accordingly, the smallest fluid dynamic scale that is detected is $\lambda_{MIN} = 2\Delta x$. While the spectral equations are evolved in time, the spatial derivatives are exactly computed, except for the error of the inverse Fourier transform. On the contrary, in a difference scheme, with identical resolution, there is always a discretisation error in the spatial derivatives. In order to increase the accuracy of the spatial derivatives, one could either increase the their order of approximation, increase the grid resolution or change the difference scheme. A finer resolution is of course possible, but the price is a greater computational effort. A higher order of approximation of the derivatives leads to the same issue, since even more nodes are required for the computation. Due to the limited computational resources, it is clear how much is important to choose the most suitable numerical scheme for the problem that must be solved.

In the present example, the central differencing second-order scheme is used over a grid with the minimum number of nodes, according to the dealiasing constraint, to resolve the smallest fluid dynamic scale λ_{MIN}. In the classical projection method, see section C.4, the velocity u is decomposed into the compressible field $\bar{u}$ and the potential correction $\frac{\partial \psi}{\partial x}$. The Poission problem and the projection step are described by the following discrete equations

$$\frac{\psi_{i+1} + \psi_{i-1} - 2\psi_i}{\Delta x^2} = -\frac{\bar{u}_{i+1} - \bar{u}_{i-1}}{2\Delta x} \ , \quad u_i = \bar{u}_i + \frac{\psi_{i+1} - \psi_{i-1}}{2\Delta x} \tag{C.4}$$

Due to periodicity, the signals ψ_i and $\bar{u}_i$ can be expanded into the Fourier series (C.5).

$$\begin{aligned} \psi_i &= \sum_{n=-N/2}^{N/2} \hat{\psi}_n e^{\jmath x_i k_n} \\ \bar{u}_i &= \sum_{n=-N/2}^{N/2} \hat{\bar{u}}_n e^{\jmath x_i k_n} \end{aligned} \qquad k_n = \frac{2\pi n}{L} \tag{C.5}$$

The wavenumber k_n describes the spatial scales of the signals ψ and $\bar{u}$, and ranges between $-k_{MAX}$ and k_{MAX}, where $k_{MAX} = \pi/\Delta x$. Through the Fourier expansion, the equations (C.4) can be expressed into the following spectral problem

$$-(k^2)_n^M \hat{\psi}_n = -\jmath k_n^M \hat{\bar{u}}_n \ , \quad \hat{u}_n = \hat{\bar{u}}_n + \jmath k_n^M \hat{\psi}_n \tag{C.6}$$

k_n^M and $(k^2)_n^M$ are the modified wavenumbers of the first and second derivatives captured by the difference scheme, respectively. Owing to the discretising error, the modified wavenumbers differ from their own analytical expressions k_n and k_n^2. The error depends on the difference scheme itself, as well as on the grid resolution and the order of approximation of the derivatives. The accuracy usually decreases at the highest frequencies, since the small-scale fluctuations are resolved with fewer nodes.

In the example, k_n^M and $(k^2)_n^M$ are computed from the Fourier transformation of the discrete derivatives. Therefore, combining equations (C.5) and (C.4), where $x_{i+1} = x_i + \Delta x$ and $x_{i-1} = x_i - \Delta x$, we obtain

$$k_n^M = \frac{sin(k_n \Delta x)}{\Delta x} \ , \quad (k^2)_n^M = \frac{2(1 - cos(k_n \Delta x))}{\Delta x^2} \tag{C.7}$$

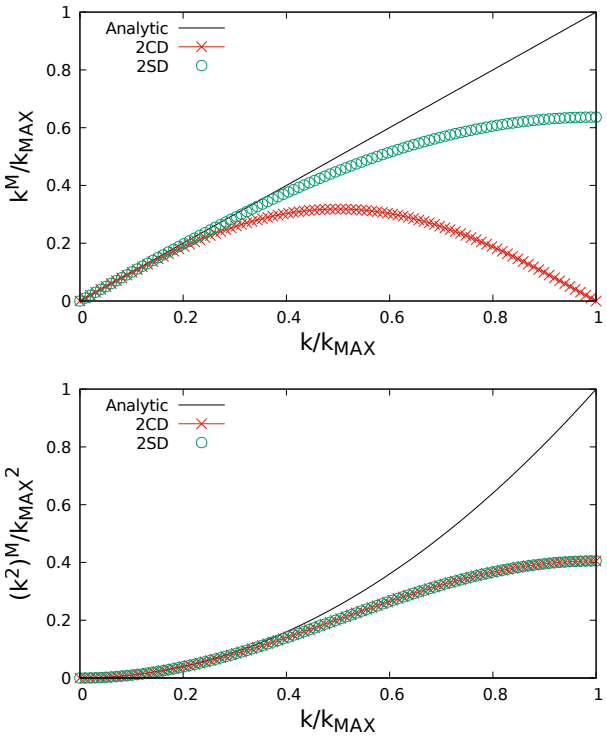

Figure C.2: The modified wavenumbers k^M and $(k^2)^M$ in a second order central (red lines) and staggered (green circles) difference scheme. Comparison with the analytical expressions (black lines) are reported.

The modified wavenumbers of the present central differencing scheme are represented in Figure C.2 (red lines) , where they are compared with the analytical expressions (black lines). While the second derivative is monotone, the first derivative has a maximum at $k/k_{MAX} = 0.5$ and then goes back to zero at the largest supported frequency k_{max}. Hence, it is clear that the numerical scheme fails to capture the spatial derivatives of the grid-scale fluctuations. This is better understood in figure C.3, where the bases $cos(k_{MAX}x)$ and $sin(k_{MAX}x)$ are depicted around the $i-th$ node. The sine function, and its derivative as well, is zero at each cell centre . The cosine function is measured with alternating values instead. Its derivative is zero since it is computed with the two outermost points of the interval of periodicity λ_{MIN}.

Thus, at the largest supported frequency of the grid, the pressure (i.e. the potential field $\frac{\partial \psi}{\partial x}$) decouples from the velocity field. The Poission equation is recast into a Laplace problem and the projection step becomes independent on the potential field, namely

$$-(k^2)_n^M \hat{\psi}_n = 0 \ , \quad \hat{u}_n = \hat{\bar{u}}_n \tag{C.8}$$

The pressure fluctuation on grid scale aren't detected and any compressible modification $\bar{u}$ of the original solenoidal field cannot be corrected by the potential field. The problem is common to any numerical scheme with $k_{MAX}^M = 0$, since shares equation (C.8). Increasing the order of approximation of the derivatives wouldn't solve the problem [111, 112]. In fact, this would increase the accuracy of the modified wavenumbers at any scale but at k_{MAX}, where still $k_{MAX}^M = 0$.

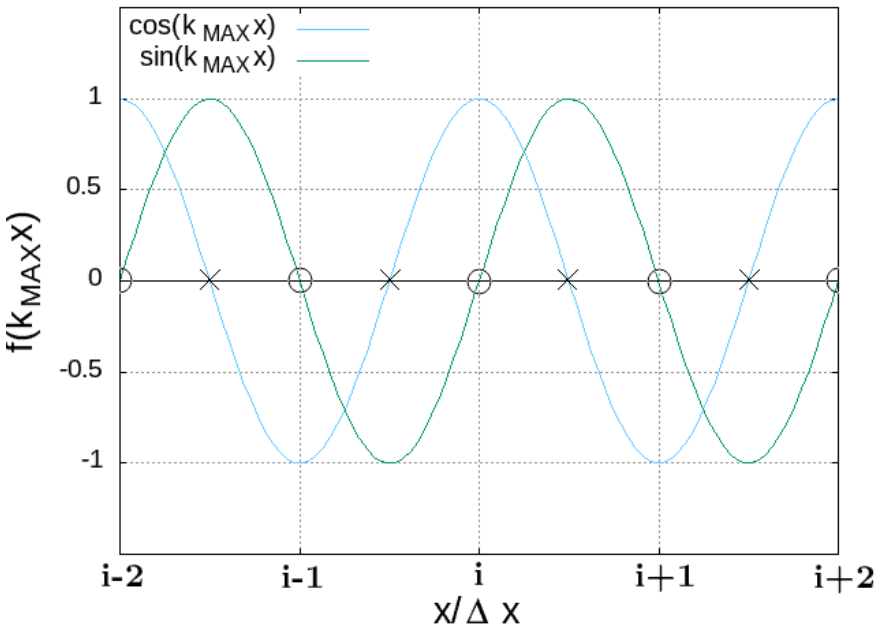

Figure C.3: The grid-scale fluctuations represented with the second-order central differencing and staggered scheme. The empty circles are the centre of the nodes while the crosses are the faces. The second-order collocated schemes are unable to detect the grid scale first derivative at the i-th node, since they require the values of f_{i+1} and f_{i-1}. The function $sin(k_{MAX}x)$ cannot be represented at all, being zero at each cell centre. The derivative of $cos(k_{MAX}x)$ is zero as well, being computed over the periodic interval. On the contrary, in the staggered arrangement the derivatives at the $i-th$ node are computed with the two neighbouring cell-face values, with no need of interpolation. Therefore the cosine basis has non-zero derivative, while the sine is still zero.

The solution of the problem is switching to a staggered grid. In the staggered configuration the Poisson problem is still computed at cell centres (ψ is a scalar), but the velocity is stored at cell faces. Hence no interpolation is required to compute the divergence of $\bar{u}$. Similarly, the potential field is naturally computed in the projection step. Therefore, the system (C.4), while represented over a staggered grid, becomes

$$\frac{\psi_{i+1}+\psi_{i-1}-2\psi_i}{\Delta x^2} = -\frac{\bar{u}_{i+1/2}-\bar{u}_{i-1/2}}{\Delta x} \quad , \quad u_{i+1/2} = \bar{u}_{i+1/2} + \frac{\psi_{i+1}-\psi_i}{\Delta x} \tag{C.9}$$

Following the Von Neumann analysis, the spectral equation is the same of the system (C.6), with the modified wavenumbers

$$k_n^M = \frac{2sin(k_n\Delta x/2)}{\Delta x} \quad , \quad (k^2)_n^M = \frac{2(1-cos(k_n\Delta x))}{\Delta x^2} \tag{C.10}$$

The wavenumber $(k^2)^M$ is still the same of the central scheme, but k^M is now monotone, with the maximum located at the highest supported frequency. The modified wavenumbers are reported in figures C.3 (green circles).

Figure C.2 shows the same concept from a different point of view. The fluctuations acting on grid-scale have non zero derivative. In fact, when the derivative is computed at the cell centre (position i), the values at two adjacent cell faces are used, with no need of interpolation. When the derivative lies at the cell face (position $i+1/2$), the values at the two neighbouring cell centre are used instead. The staggered arrangements essentially doubles the range of frequencies of the first derivatives that are resolved by central schemes. While in the collocated scheme the smallest length-scale of k^M is $\lambda_{k^M}^{CD} = 2\Delta x$, in the staggered arrangement is $\lambda_{k^M}^{SD} = \Delta x$. This can be clearly seen in figure C.2, or comparing equation (C.7) with (C.10).

Owing two this two-fold resolution, the behaviour in the range of supported frequency $[-k_{MAX}, k_{MAX}]$ in the staggered grid is the same of the collocated grid in the range $[-k_{MAX}/2, k_{MAX}/2]$. Moreover the accuracy of such derivative (i.e. the maximum of k^M) is increased.

In conclusion, the first discrete spatial derivative is never zero at each scale, with the additional advantage of the increased accuracy. Therefore, the potential (pressure) and the velocity field never decouples and the incompressible constraint is always satisfied at each scale.

C.2 The energy conservation of the finite difference scheme for the cylindrical coordinate system

One of the most important requirements of DNS incompressible flows is the energy conservation of the advection terms in the Navier-Stokes equations. If the conservation of mass and energy fluxes is not achieved within a sufficient level of accuracy, the simulation can become unstable and finally diverge. The conservation is achieved if the advection term satisfies the condition (C.11) on a discrete ground.

$$\nabla \cdot \{\rho_f \mathbf{u} \otimes \mathbf{u}\} \cdot \mathbf{u} = \nabla \cdot \left\{\rho_f \mathbf{u} \frac{\mathbf{u}^2}{2}\right\} + \frac{\mathbf{u}^2}{2} \nabla \cdot \{\rho_f \mathbf{u}\} \tag{C.11}$$

In the present incompressible case the divergence of the velocity field is zero. The fluid density ρ_f is a constant and can be factored out in equation (C.11). The conservation is not trivial when the grid is non-uniform, as in the cylindrical coordinates. The interpolation of the advected and advecting velocity must take into account the change of area of the cell faces, or the condition (C.11) won't be not achieved. In this section we present the technique adopted to achieve the energy conservation, that was developed by Fukagata and Kasagi [103]. Fukagata and Kasagi showed that the convection of the radial momentum h_r, which is stored in $(i+1/2, j, k)$ as the radial velocity, needs a special treatment. In order to ensure the energy conservation, the advecting velocity in h_r must be interpolated with the volume-flux average, while the advected velocity with the arithmetic average. The volume-flux average is denoted by $\widehat{(\cdot)}^i$ (i-direction) while the arithmetic average by $\overline{(\cdot)}^l$ (l-direction). The expression of $(h_r)_{i+1/2,j,k}$ in the discrete form consequently reads

$$\begin{aligned}
(h_r)_{i+1/2,j,k} =& \frac{1}{r_{i+1/2}\Delta r_{i+1/2}} \left[\overline{ru_r}^i_{i+1,j,k} \overline{u_r}^i_{i+1,j,k} - \overline{ru_r}^i_{i,j,k} \overline{u_r}^i_{i,j,k}\right] \\
&+ \frac{1}{r_{i+1/2}\Delta\theta} \left[\widehat{u_\theta}^i_{i+1/2,j+1/2,k} \overline{u_r}^j_{i+1/2,j+1/2,k} - \widehat{u_\theta}^i_{i+1/2,j-1/2,k} \overline{u_r}^j_{i+1/2,j-1/2,k}\right] \\
&+ \frac{1}{\Delta z} \left[\widehat{u_z}^i_{i+1/2,j,k+1/2} \overline{u_r}^k_{i+1/2,j,k+1/2} - \widehat{u_z}^i_{i+1/2,j,k-1/2} \overline{u_r}^k_{i+1/2,j,k-1/2}\right]
\end{aligned} \tag{C.12}$$

The volume flux averages are defined by

$$\begin{aligned}
\widehat{u_\theta}^i_{i+1/2,j+1/2,k} &= \frac{\Delta r_{i+1} u_{\theta_{i+1,j+1/2,k}} + \Delta r_i u_{\theta_{i,j+1/2,k}}}{2\Delta_{i+1/2}} \\
\widehat{u_z}^i_{i+1/2,k,k+1/2} &= \frac{r_{i+1}\Delta r_{i+1} u_{z_{i+1,j,k+1/2}} + r_i \Delta r_i u_{z_{i,j,k+1/2}}}{2 r_{i+1/2}\Delta r_{i+1/2}\chi_{i+1/2}}
\end{aligned} \tag{C.13}$$

while the arithmetic averages are

$$\begin{aligned}
\overline{ru_r}^i_{i+1,j,k} &= \frac{r_{i+1/2} u_{r_{i+1/2,j,k}} + r_{i+3/2} u_{r_{i+3/2,j,k}}}{2} \\
\overline{u_r}^j_{i+1/2,j+1/2,k} &= \frac{u_{r_{i+1/2,j+1,k}} + u_{r_{i+1/2,j,k}}}{2}
\end{aligned} \tag{C.14}$$

$\chi_{i+1/2}$ is a normalisation parameter, being unity if the radial spacing is uniform.

$$\chi_{i+1/2} = \frac{r_{i+1}\Delta r_{i+1} + r_i \Delta r_i}{2 r_{i+1/2}\Delta r_{i+1/2}} = 1 + \frac{\Delta r_{i+1} - \Delta r_i}{2 r_{i+1/2}} \tag{C.15}$$

Fukagata and Kasagi approximate $\chi_{i+1/2}$ as unity in general. However the author of the present work remarks that this could not be true in the vicinity of the longitudinal axis, as suggested by equation (C.15). Hence, in this thin region of space the scheme could not be energy conserving. However, the present research deals with annular pipes, where the longitudinal axis is far outside the computational domain. Therefore, for what concerning our research, the parameter can be safely considered unity.

The advection of the squared value, u_r^2, that is the radial component of the kinetic energy, is represented by the following discrete equation

$$\begin{aligned}(H_r)_{i+1/2,j,k} =& \frac{1}{r_{i+1/2}\Delta r_{i+1/2}} \left[\overline{ru_r}^{\,i}_{i+1,j,k} \frac{\widetilde{u_r^2}^{\,i}_{i+1,j,k}}{2} - \overline{ru_r}^{\,i}_{i,j,k} \frac{\widetilde{u_r^2}^{\,i}_{i,j,k}}{2} \right] \\ &+ \frac{1}{r_{i+1/2}\Delta\theta} \left[\widehat{u_\theta}^{\,i}_{i+1/2,j+1/2,k} \widetilde{u_r^2}^{\,j}_{i+1/2,j+1/2,k} - \widehat{u_\theta}^{\,i}_{i+1/2,j-1/2,k} \widetilde{u_r^2}^{\,j}_{i+1/2,j-1/2,k} \right] \\ &+ \frac{1}{\Delta z} \left[\widehat{u_z}^{\,i}_{i+1/2,j,k+1/2} \widetilde{u_r^2}^{\,k}_{i+1/2,j,k+1/2} - \widehat{u_z}^{\,i}_{i+1/2,j,k-1/2} \widetilde{u_r^2}^{\,k}_{i+1/2,j,k-1/2} \right]\end{aligned} \tag{C.16}$$

The average of the squared value of u_r , denoted by $\widetilde{(\cdot)}$, are computed according to Piacsek and Williams [113], that is

$$\begin{aligned}\widetilde{u_r^2}_{i,j,k} &= u_{r_{i+1/2,j,k}} u_{r_{i-1/2,j,k}} \\ \widetilde{u_r^2}_{i+1/2,j+1/2,k} &= u_{r_{i+1/2,j+1,k}} u_{r_{i+1/2,j,k}} \\ \widetilde{u_r^2}_{i+1/2,j,k+1/2} &= u_{r_{i+1/2,j,k+1}} u_{r_{i+1/2,j,k}}\end{aligned} \tag{C.17}$$

With the present averaging the conservation of the radial component of the kinetic energy is satisfied. In other words it can be proved the following relation

$$h_{r_{i+1/2,j,k}} u_{r_{i+1/2,j,k}} = H_{r_{i+1/2,j,k}} + \frac{r_{i+1}\Delta r_{i+1} u^2_{r_{i+1/2,j,k}}}{2 r_{i+1/2}\Delta r_{i+1/2}} (\mathbf{D}\cdot\mathbf{u})_{i+1,j,k} + \frac{r_i \Delta r_i u^2_{r_{i+1/2,j,k}}}{2 r_{i+1/2}\Delta r_{i+1/2}} (\mathbf{D}\cdot\mathbf{u})_{i,j,k} \tag{C.18}$$

where $\mathbf{D}\cdot\mathbf{u}$ represents the discrete divergence operator applied to the velocity field, namely

$$(\mathbf{D}\cdot\mathbf{u})_{i,j,k} = \frac{1}{r_i} \frac{r_{i+1/2} u_{r_{i+1/2,j,k}} - r_{i-1/2} u_{r_{i-1/2,j,k}}}{\Delta r_i} + \frac{1}{r_i} \frac{u_{\theta_{i,j+1/2,k}} - u_{\theta_{i,j-1/2,k}}}{\Delta\theta} + \frac{u_{z_{i,j,k+1/2}} - u_{z_{i,j,k-1/2}}}{\Delta z} \tag{C.19}$$

The equation (C.18) is the discretised form of the radial component of the balance (C.11), namely

$$\nabla\cdot\{\mathbf{u}u_r\}u_r = \nabla\cdot\left\{\mathbf{u}\frac{u_r^2}{2}\right\} + \frac{u_r^2}{2}\nabla\cdot\mathbf{u} \tag{C.20}$$

The divergence of $\mathbf{u}$ in equation (C.18) is evaluated at position $i+1/2, j, k$ through the averaging of $(\mathbf{D}\cdot\mathbf{u})_{i+1,j,k}$ and $(\mathbf{D}\cdot\mathbf{u})_{i,j,k}$. The fluid density ρ_f, that is present in equation (C.11), is omitted being constant. The treatment is valid only for incompressible flows. However it can be extended to a more general case, by including the density in the arithmetic averaging of the advected velocity [112].

The axial and azimuthal momentum convection h_z and h_θ, such as the as the other momentum terms, can be discretised, without harm, with the standard second order arithmetic average. Hence their discrete expressions are not presented in this section.

Finally, the metric terms of the cylindrical coordinates are discretised as proposed by Fukagata and Kasagi. Their expressions are presented below

$$\begin{aligned}\left(\frac{u_r u_\theta}{r}\right)_{i,j+1/2,k} &= \frac{1}{r_i}\overline{\overline{u_r}^i}^j_{i,j+1/2,k} u_{\theta_{i,j+1/2,k}} \\ \left(\frac{u_\theta^2}{r}\right)_{i+1/2,j,k} &= \frac{1}{r_{i+1/2}} \frac{\Delta r_{i+1}\overline{u_\theta^2}^j_{i+1,j,k} + \Delta r_i \overline{u_\theta^2}^j_{i,j,k}}{2\Delta r_{i+1/2}}\end{aligned} \tag{C.21}$$

C.3 The spatial discretisation of the scalar equations

The Fourier equation is a scalar equation for the temperature. In the present model the temperature is a passive scalar that is transported and diffused across the turbulent field. This section reports the numerical techniques adopted to discretise the domain of temperature field. The method employed is a total variation diminishing scheme, or TVD. The scheme combines two different discretisation approaches of scalar equations on a staggered grid: central and upwind differencing schemes. Before entering into details of the TVD scheme, we prefer to give a brief description of these two methods.

Both upwind and central differencing have advantages and disadvantages. In the central differencing scheme, the transported variables is subjected to false numerical oscillations, owing to the inability to detect the high frequency spatial variations [114, 115, 111]. The reason is that, although central second order schemes are accurate, they are not monotonicity preserving. Hence they can cause instability, and eventually the simulation can diverge. The simplest monotone difference scheme is the first order upwind scheme. However, the standard upwind scheme is less accurate (only first order) and introduces more numerical diffusion due to its complex modified wave number. In order to explain the feature briefly discussed, in the next sections we will provide the semi-discrete analysis of a one-dimensional problem. The temporal evolution of the error of the schemes will be helpful to understand the numerical diffusion and the accuracy of the two approaches.

C.3.1 Accuracy and stability of upwind and central differencing schemes

In this section we address the main features of the first order upwind and second order central differencing schemes. In order to provide a deep insight of the difference between the two schemes, we introduce the one-dimensional periodic problem, over the domain $\mathcal{D} = [0, L)$, of the scalar $\phi(x,t)$ transported by the advecting velocity u:

$$\begin{aligned}&\frac{\partial \phi}{\partial t} + u\frac{\partial \phi}{\partial x} = 0\ , \qquad x \in [0, L) \\ &\phi(x,0) = \phi_0(x)\end{aligned} \tag{C.22}$$

In the equation $\phi_0(x)$ is the initial condition, while u is a constant in a one-dimensional problem. The semi-discrete analysis provides the evaluation of the error $\epsilon(x,t) = \phi_D(x,t) - \phi(x,t)$, due to the spatial discretisation. To this end, we will distinguish between the exact solution $\phi(x,t)$ of the partial differential equation (C.22) and the approximated solution $\phi_D(x,t)$ of the related N-discretised equation. In the spectral space of $N+1$ modes, the difference between the two solutions is in the modified wavenumber k_n^M, namely

$$\begin{cases}\frac{\partial \hat{\phi}_n}{\partial t} + u_J k_n \hat{\phi}_n = 0, & n \in [-N/2, N/2] \\ \hat{\phi}_n(0) = \hat{\phi}_n^0\end{cases} \qquad \begin{cases}\frac{\partial \hat{\phi_D}_n}{\partial t} + u_J k_n^M \hat{\phi_D}_n = 0, & n \in [-N/2, N/2] \\ \hat{\phi}_n(0) = \hat{\phi}_n^0\end{cases} \tag{C.23}$$

The solution of the systems (C.23) can be found integrating by part, and the error $\hat{\epsilon_n}$, in the spectral space, is readily computed

$$\hat{\epsilon_n}(t) = \hat{\phi}_n^0\{e^{-Juk_n^M t} - e^{-Juk_n t}\} \tag{C.24}$$

The amplitude of the error $\epsilon_n(t)$ is computed from equation (C.24), and reads

$$|\hat{\epsilon_n}|(t) = |\hat{\phi}_n^0|\{1 + e^{2u\Im(k_n^M)t} - 2e^{u\Im(k_n^M)}cos[(\Re(k_n^M) - k_n)ut]\} \tag{C.25}$$

The modified wavenumber k_n^M depends on the scheme that is adopted, and in general may be a complex number. In equation (C.25) $\Re(k_n^M)$ denotes the real part of the modified wavenumber, whereas $\Im(k_n^M)$ the imaginary part. As clear from equations (C.24) and (C.25) , while the real part $\Re(k_n^M)$ is a source of error for the phase of $\hat{\phi_{Dn}}$, the imaginary part $\Im(k_n^M)$ generates errors in its amplitude. The modified wavenumbers of the first order upwind and second order central scheme [112, 114, 115] are reported below

$$\begin{cases} k_n^M\big|_{UPS} = \frac{sin(\Delta x k_n)}{\Delta x} - J\{\frac{1-cos(\Delta x k_n)}{\Delta x}\}\,, & u > 0 \\ k_n^M\big|_{UPS} = \frac{sin(\Delta x k_n)}{\Delta x} + J\{\frac{1-cos(\Delta x k_n)}{\Delta x}\}\,, & u < 0 \end{cases} \qquad k_n^M\big|_{CS} = \frac{sin(\Delta x k_n)}{\Delta x} \tag{C.26}$$

The modified wavenumber of central schemes has no imaginary, hence there is no error in the amplitude of the solution. The error (C.25) is doomed to perpetually oscillate, due to the phase error. The frequency of the oscillation is largest for the smallest supported spatial scale, where the modified wavenumber $k_n^M = 0$. The example illustrates the wiggles occurring in central differencing schemes, that make the code unstable. In order to reduce the oscillations one could either to increase the accuracy of the scheme or to increase the resolution. This would reduce both the discrepancy between the modified and exact wavenumber. Note that in the proposed example, this does not affect the maximum of the error $|\hat{\epsilon_n}(t)|$, that still is $2\hat{\phi}_n^0$. This is because the diffusion is not included in the problem. In a real problem to increase the resolution of the spatial derivatives would eventually increase the diffusion (i.e. the modified wavenumber $(k_n^M)^2$) captured by the scheme, damping the peaks of the error $|\hat{\epsilon_n}|$.

On the contrary in the upwind scheme k_n^M is a complex number. Its imaginary part introduces a false numerical dissipation ($u\Im(k_n^M)$ is always negative). The fictitious diffusion damps the oscillations, making the solution more stable, in particular for the smallest scales. However the error converges to a non-zero value. Therefore the numerical diffusion introduced by the imaginary part of the modified wavenumber damps the wiggles, but makes the scheme less accurate. Figure C.4 reports the differences between the central and upwind scheme in the amplitude of the error $|\hat{\epsilon_n}(t)|$, for three different spatial scales $k_{N/2} = \frac{\pi}{\Delta}$, $k_{N/4} = \frac{\pi}{2\Delta}$ and $k_{N/8} = \frac{\pi}{4\Delta}$.

In conclusion, the second order central schemes are very accurate, but can give undershoots and overshoots when the Peclet number is high (i.e. strong convection). When this high order scheme is used to solve turbulent transported quantities, this could lead to false negative values and instability. Conversely, the upwind differencing scheme is the most stable, and avoids the formation of unphysical wiggles. However the scheme introduces much diffusion due to both the low accuracy and its complex modified wavenumber.

C.3.2 The total variation diminishing schemes

The class of TVD (total variation diminishing) schemes aim at achieving oscillation-free solutions with still a high level of accuracy. Early schemes of this kind were called flux corrected transport (FCT) schemes [116, 117], and their development has led to the modern TVD schemes [118, 119, 120, 121, 122, 123].

A stable, non oscillatory scheme should be monotonicity preserving. In order to satisfy the monotonicity the scheme must not create local maxima or minima, and the value of existing local extrema must not be amplified. In other words the scheme must not create new undershoots

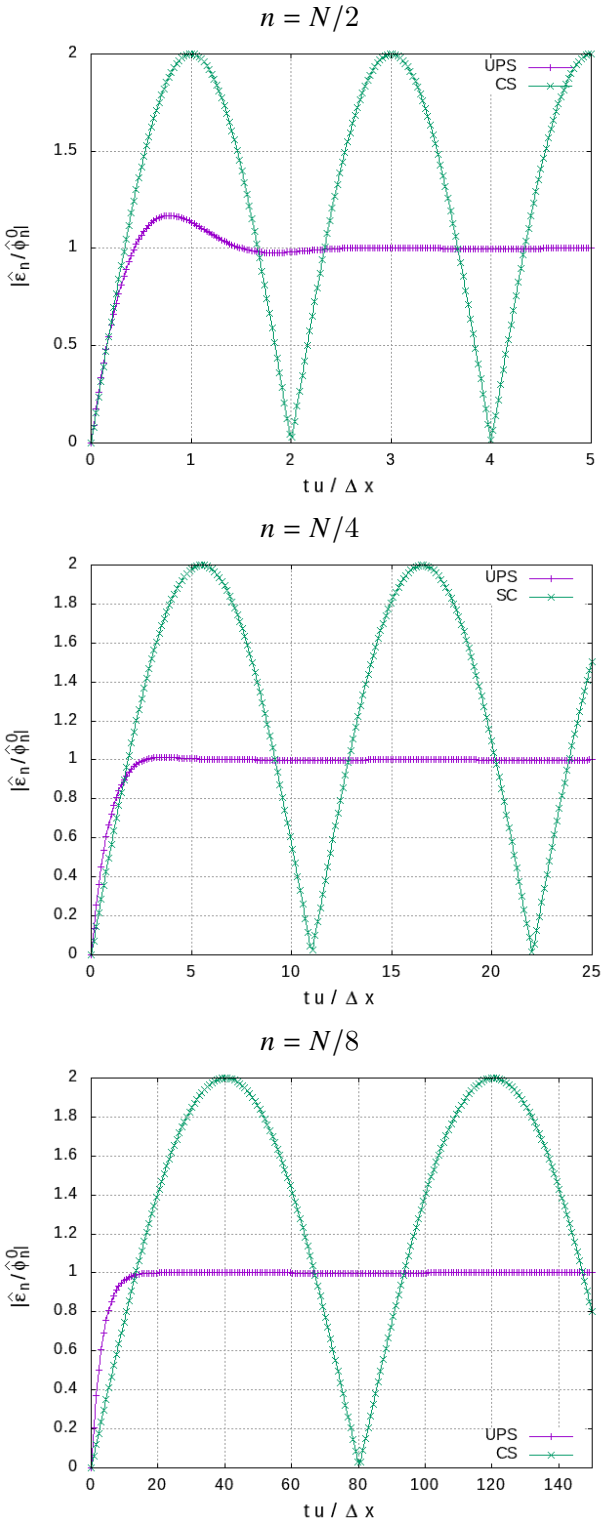

Figure C.4: The error $|\hat{\epsilon}_n/\hat{\psi}_n^0|$ versus the dimensionless time $tu/\Delta x$ for the upwind (purple) and central (green) differencing scheme. In the central schemes the error infinitely oscillates. The modes of the scales $k_{N/2}$ (top panel), $k_{N/4}$ (mid panel) and $k_{N/8}$ (bottom panel) are reported. The frequency of the oscillations in the central scheme is largest for the smallest lenght-scale $k_{N/2}$. The numerical damping from the upwind scheme causes the oscillations to reduce, although the error converges to a non-zero value.

or overshoots and must not accentuate existing extrema. The effect is that the total variation

$TV(\phi) = \sum_{i=1}^{N} |\phi_{i+1} - \phi_i|$ of the discretised solution ϕ_i should diminish with time. Therefore, the scheme is said to be total variation diminishing, or TVD, if the total variation at two consecutive time steps $n+1$ and n is always decreasing, namely

$$TV(\phi^{n+1}) \leq TV(\phi^n) \tag{C.27}$$

The reader must notice that the proof of the monotonicity preserving is always given in the one-dimensional case, while it is not for the multi-dimensional problems.

To describe the TVD scheme we consider the one-dimensional form of the convection diffusion equation (C.1). The discretisation of the diffusion equation can be done with the standard central differencing arrangement and does not require further explanation. The advection term, on the other hand, requires special care, to avoid the formation of false extrema. TVD schemes is designed to treat the convection term with the first order upwind scheme in the presence of steep gradients, while recovering the high accuracy of second order central schemes where the solution is smooth.

To illustrate the TVD scheme we consider the convection term $\left.\frac{\Delta\{\phi u\}}{\Delta x}\right|_i$ in a one-dimensional problem

$$\left.\frac{\Delta\{\phi u\}}{\Delta x}\right|_i = \frac{u_{i+1/2}\phi_{i+1/2} - u_{i-1/2}\phi_{i-1/2}}{\Delta x} \tag{C.28}$$

In this example the velocity u is assumed positive. The advection term requires no interpolation for the velocity, since it is collocated in staggered points $i+1/2$ (cell face value). On the other hand the scalar quantity ϕ is collocated in the integer index points i (cell centre value). The cell face values of ϕ must be somehow computed from the neighbouring cell centre values. In the second order central differencing the interpolation is computed according to the linear equation

$$\phi_{i+1/2} = \phi_i + \frac{\phi_{i+1} - \phi_i}{2} \tag{C.29}$$

In the first order upwind differencing the cell face quantity is obtain through the equation

$$\phi_{i+1/2} = \phi_i \tag{C.30}$$

The TVD scheme is constructed by means of the flux limiter function $\Psi(r)$, that is a non-linear function of the local variation, denoted by r, of the scalar gradient.

$$\begin{cases} \phi_{i+1/2} = \phi_i + \frac{1}{2}\Psi(r_{i+1/2})(\phi_i - \phi_{i-1}) \\ r_{i+1/2} = \frac{\phi_{i+1} - \phi_i}{\phi_i - \phi_{i-1}} \end{cases} \tag{C.31}$$

The interpolation is the sum of the diffusive first order upwind term and the anti-diffusive high-order quantity. The operatation is regulated by the flux limiter $\Psi(r)$. The upwind first order scheme is obtain when the flux limiter is $\Psi(r) = 0$, while the standard second order central differencing when $\Psi(r) = r$. The monotonicity preserving condition is achieved by the scheme if:

$$0 \leq \Psi(r) \leq 2 \tag{C.32}$$

Basing on the condition (C.32) the first order upwind scheme is clearly monotone, while the second order central differencing is not in the case of large gradient variation. By specifying a proper flux limiter function $\Psi(r)$ it is possible to achieve the monotonicity preserving property [122]. In the present research we have adopted the Chakravarthy-Osher limiter [124], reported in equation (C.33), where the constant is set to $K_1 = 2$.

$$\Psi(r) = max[0, min(r, K_1)] \tag{C.33}$$

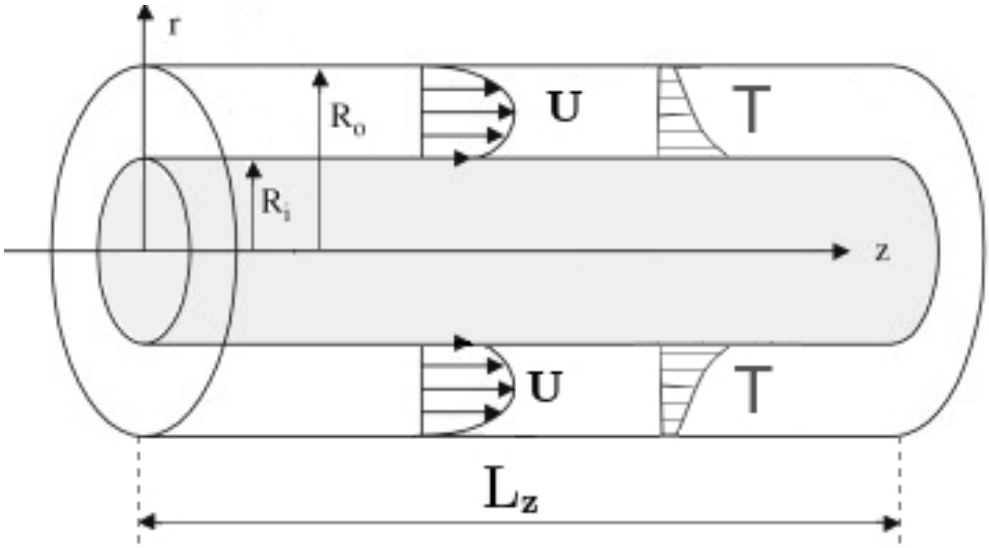

Figure C.5: Sketch of the annular domain $\mathcal{D}$. R_i and R_o are the inner and outer wall radius. The fluid flows in the gap between the cylinders.

C.4 The Chorin's projection method

The fluidynamic of the annular pipe is described by the standard-incompressible Navier-Stokes equations in the domain $\mathcal{D}$

$$\begin{cases} \nabla \cdot \mathbf{u} = 0 \\ \rho_f \left(\dfrac{\partial \mathbf{u}}{\partial t} + \mathbf{u} \cdot \nabla \mathbf{u} \right) = -\nabla p - \dfrac{dP}{dx_3} \hat{e}_3 + \mu \nabla^2 \mathbf{u} + \mathbf{f}_p \\ \mathbf{u}(\mathbf{x}, t)|_{\partial \mathcal{D}_W} = \mathbf{u}_b(\mathbf{x}, t) \\ \mathbf{u}(\mathbf{x}, t)|_{S_{in}} = \mathbf{u}(\mathbf{x}, t)|_{S_{out}} \\ \mathbf{u}(\mathbf{x}, 0) = \mathbf{u}_0(\mathbf{x}) \qquad\qquad x \in \mathcal{D} \end{cases} \tag{C.34}$$

In the equation $\mathbf{f_p}$ is the forcing from the dispersed phase and $\frac{dP}{dx_3}$ is the averaged pressure gradient in the streamwise direction. The boundary conditions are periodic at the inlet S_{in} and outlet S_{out} surface, and no-splip at the walls $\partial \mathcal{D}_W$. The initial condition, at the reference time $t = 0$, is $\mathbf{u}_0(\mathbf{x}, t)$. The problem of solving this equation is that the hyrodynamic pressure ∇p is uncoupled from the state equation, that in the present incompressible flow simply reads

$$\rho_f = constant \tag{C.35}$$

In fact, in the low-Mach limit of Navier-Stokes equation, the hydrodynamic pressure is solely determined by the flow field $\mathbf{u}$. Physically, the hydrodynamic pressure represents the constraint required to satisfies the zero-divergence condition prescribed by the continuity equation. Mathematically speaking, ∇p can be computed by the elliptic equation derived by taking the divergence of the momentum equation. This equation can replace the continuity condition in the system (C.34). By means of a backward Euler method, the over-mentioned system can be discretised in time, yielding

$$\begin{cases} \frac{\mathbf{u}^{n+1} - \mathbf{u}^n}{\Delta t} + \mathbf{u}^n \cdot \nabla \mathbf{u}^n = -\nabla p^{n+1} + \mu \nabla^2 \mathbf{u}^{n+1} \\ \nabla^2 p^{n+1} = \nabla \otimes \nabla : \{\mathbf{u}^{n+1} \otimes \mathbf{u}^{n+1}\} \end{cases} \tag{C.36}$$

The present scheme is highly inefficient since requires, at each time step, the solution $\mathbf{u}^{n+1}$. More specifically, the problem is that in the present algorithm the continuity and the momentum equation must be solved simultaneously.

To tackle the issue, Chorin [104, 125, 126] proposed a numerical technique aimed at decoupling the computation of $\mathbf{u}^{n+1}$ and p^{n+1}. The method consists in ignoring the pressure gradient and advancing an auxiliary solution $\bar{\mathbf{u}}$, which does not satisfy the divergence constraint. In a later step, the intermediate velocity field $\bar{\mathbf{u}}$ is projected back to the incompressible vector field, by mean of a potential field $\nabla\psi$. The method is repeatedly applied at each time step and ensures that the solutions $\mathbf{u}^{n+1}$ and p^{n+1} satisfy the momentum and continuity equations.

We shall discuss the procedure for a generic time-step $\Delta t = t_{n+1} - t_n$, where t_n and t_{n+1} denote the initial and advanced instant, respectively. Hence, the algorithm evolves the solution between time t_n to t_{n+1}. The reiteration of the method allows the long-term integration.

The approach consists in additively splitting the velocity field $\mathbf{u}(\mathbf{x}, t)$ into the fields $\bar{\mathbf{u}}(\mathbf{x}, t)$ and $\nabla\psi(\mathbf{x}, t)$, namely

$$\mathbf{u}(\mathbf{x}, t) = \bar{\mathbf{u}}(\mathbf{x}, t) + \nabla\psi(\mathbf{x}, t) \tag{C.37}$$

The velocity field $\bar{\mathbf{u}}(\mathbf{x}, t)$ satisfies the Navier-Stokes equation C.34 when the pressure field ∇p is ignored, namely

$$\begin{cases} \rho_f \left(\dfrac{\partial \bar{\mathbf{u}}}{\partial t} + \mathbf{u} \cdot \nabla \mathbf{u} \right) = -\dfrac{dP}{dx_3} \hat{e}_3 + \mu \nabla^2 \bar{\mathbf{u}} + \mathbf{f}_p \\ \bar{\mathbf{u}}(\mathbf{x}, t)|_{\partial \mathcal{D}} = \mathbf{u}_b(\mathbf{x}, t) \\ \bar{\mathbf{u}}(\mathbf{x}, t)|_{S_{in}} = \bar{\mathbf{u}}(\mathbf{x}, t)|_{S_{out}} \\ \bar{\mathbf{u}}(\mathbf{x}, t_n) = \mathbf{u}_0(\mathbf{x}) \qquad\qquad x \in \mathcal{D} \ , \quad t \in [t_n, t_{n+1}] \end{cases} \tag{C.38}$$

$\bar{\mathbf{u}}(\mathbf{x}, t)$ is an auxiliary solution of the Navier-Stokes equation that does not satisfy the continuity equation. After being advanced through equation (C.38), $\bar{\mathbf{u}}(\mathbf{x}, t)$ must be projected back to the divergence-free vector field. The procedure is achieved through the potential field $\nabla\psi$, that recovers the informations that are missing in the field $\bar{\mathbf{u}}$.

$$\begin{cases} \nabla \cdot (\bar{\mathbf{u}} + \nabla\psi) = 0 \\ \rho_f \dfrac{\partial \nabla\psi}{\partial t} = -\nabla p + \mu \nabla^2 \nabla\phi \\ \dfrac{\partial \psi}{\partial n}(\mathbf{x}, t)\Big|_{\partial \mathcal{D}_W} = 0 \\ \psi(\mathbf{x}, t)|_{S_{in}} = \psi(\mathbf{x}, t)|_{S_{out}} \\ \nabla\psi(\mathbf{x}, t_n) = 0 \qquad\qquad x \in \mathcal{D} \ , \quad t \in [t_n, t_{n+1}] \end{cases} \tag{C.39}$$

Starting from the reference time t_n, and evolving the solution to time $t_{n+1} = \Delta t$, the Chorin's algorithm proceeds as follows

1. to find the solution $\bar{\mathbf{u}}(x, t_{n+1})$, by integrating over the time-step Δt the equation (C.38) with initial and boundary conditions $\mathbf{u}_0$ and $\mathbf{u}_b$
2. to use the auxiliary solution $\bar{\mathbf{u}}_{ij}(r, t_{n+1})$ to solve the Laplace problem (first equation in (C.39)) with the boundary condition $\left.\frac{\partial \psi}{\partial n}\right|_{\partial \mathcal{D}_W} = 0$
3. to use the resulting potential field $\nabla\psi(\mathbf{x}, t_{n+1})$ to project $\bar{\mathbf{u}}(\mathbf{x}, t_{n+1})$ back to the space of incompressible vector fields through the relation (C.37)
4. finally the adhesion boundary condition is reapplied by hand to the resulting field $\mathbf{u}(\mathbf{x}, t_{n+1})$

The method ensures that the solution satisfies both the continuity and momentum equation of the incompressible flows. However, decomposing the solenoidal field by means of a potential flow

leads to a numerical error that is better to be addressed. In fact, the reader should notice that the system (C.39) is a second order partial differential equation for the scalar function ψ. Therefore we can apply only one boundary condition at the walls and we have to choose between impermeability and adhesion. The most common choice in the literature is to enforce the impermeability condition, that is $\left.\frac{\partial \psi}{\partial n}\right|_{\partial \mathcal{D}} = 0$. The condition is equivalent to enforce, but an error of order Δt, the pressure boundary condition of a solenoidal field, namely

$$\left.\frac{\partial p}{\partial n}\right|_{\partial \mathcal{D}_W} = 0 \tag{C.40}$$

The tangential component on the wall of the potential field is $\nabla_\pi \psi|_{\partial \mathcal{D}_W}$, where π is the local tangent plane relative to the point $\mathbf{x} \in \partial \mathcal{D}_\mathbf{W}$. Owing to the nature of the partial differential equation (C.39), the adhesion can't be enforced as well to the field $\nabla\psi$. Hence the velocity $\nabla_\pi \psi$ should appear in the boundary condition of $\bar{\mathbf{u}}$, in the system (C.38). This would ensure that the decomposition in the two system of equations, induced by the relation (C.37), is formally correct. In other words, the sum of the split systems must return the original differential equation. To this end, the wall boundary condition of the auxiliary solution should be $\bar{\mathbf{u}}(\mathbf{x},t)|_{\partial \mathcal{D}} = \mathbf{u}_b(\mathbf{x},t) - \nabla_\pi \psi|_{\partial \mathcal{D}_W}$ Unfortunately, the boundary conditions of $\bar{\mathbf{u}}$ are the same of $\mathbf{u}$. This means that the no-slip condition is enforced on the auxiliary solution instead of $\mathbf{u}$. The resulting numerical error, at the wall, is exactly the potential field $\nabla_\pi \psi|_{\partial \mathcal{D}_W}$. Fortunately, the field ψ evolves at each time step from the homogeneous configuration. Hence, the error introduced by the false adhesion is infinitesimal, and, equally important, it is not accumulated over time.

In conclusion, the resulting field $\bar{\mathbf{u}}$ does not satisfy the adhesion boundary condition, even if for an infinitesimal error. Therefore the no-splip condition of the field $\bar{\mathbf{u}}$ is reintroduced by the Navier-Stokes solver at the end of each time-step. This results in a concentrated numerical vorticity at the wall, that is later diffused by the Navier-Stokes solver [127]. If the algorithm is convergent this numerical boundary layer is bounded, with no-harm for the rest of the computation, close to the wall. A different choice of the wall boundary condition of the potential field is in principle possible, but this gives rise to different numerical boundary layers [128, 129].

C.5 The Laplace problem of the potential field

We shall now present how the Laplace equation of the potential field ψ is solved. The above-mentioned Laplace problem is derived by taking the divergence of equation (C.37), embedded with the boundary conditions in (C.39)

$$\nabla^2 \psi = -\nabla \cdot \bar{\mathbf{u}}(\mathbf{x}, t_{n+1}) \ , \quad \left.\frac{\partial \psi}{\partial n}\right|_{\partial \mathcal{D}_W} = 0 \ , \quad \psi(\mathbf{x},t)|_{S_{in}} = \psi(\mathbf{x},t)|_{S_{out}} \tag{C.41}$$

The velocity field $\bar{\mathbf{u}}(\mathbf{x}, t_{n+1})$ is the auxiliary solution, i.e. the solution of equation (C.38). At this stage of the computation, when we have to compute the potential field, $\bar{\mathbf{u}}(\mathbf{x}, t_{n+1})$ is a known function.

In cylindrical coordinates, the potential field $\psi(r,\theta,z,t)$ is periodic in both θ and z. The field is reasonably smooth and bounded, then we can expand ψ into the uniformly convergent Fourier series of modes $\hat{\psi}_{lq}(r,t)$.

$$\begin{gathered}
\hat{\psi}_{lq}(r,t) = \frac{1}{2\pi L_z} \int_0^{2\pi} \int_0^{L_z} \psi(r,\theta,z,t) e^{-J\mathbf{k}_{lq}\cdot\eta} dz d\theta \ , \quad \psi(r,\theta,z,t) = \sum_{l=-N_\theta/2}^{N_\theta/2} \sum_{q=-N_z/2}^{N_z/2} \hat{\psi}_{lq}(r,t) e^{J\mathbf{k}_{lq}\cdot\eta} \\
\mathbf{k}_{lq} = k_l^\theta \hat{\theta} + k_q^z \hat{e}_3 \ , \quad \eta = \theta\hat{\theta} + z\hat{e}_3
\end{gathered} \tag{C.42}$$

The wave vector $\mathbf{k}_{lq}$ is decomposed into the wavenumbers $k_l^\theta = l$ and $k_q^z = \frac{2\pi q}{L_z}$, of directions $\hat{\theta}$ and $\hat{e}_3$ respectively. η is the displacement vector of the periodic domain, that in the present configuration is the portion of the cartesian space $\{\theta, z\}$, such that $\theta \in [0, 2\pi)$ and $z \in [0, L_z)$. The laplacian operator can be expressed in cylindrical coordinates and by means of the Fourier transformation (C.42), the Laplace problem (C.41) is recast into the following spectral form

$$\frac{1}{r}\frac{\partial}{\partial r}\left(r\frac{\partial \hat{\psi}_{lq}}{\partial r}\right) - \left(\frac{k_l^{\theta 2}}{r^2} + k_q^{z2}\right)\hat{\psi}_{lq} = -\mathbf{k}_{lq}\cdot\hat{\bar{\mathbf{u}}}_{lq}\ , \quad \frac{\partial \hat{\psi}_{lq}}{\partial n}(R_i, t_{n+1}) = 0\ , \quad \frac{\partial \hat{\psi}_{lq}}{\partial n}(R_o, t_{n+1}) = 0 \tag{C.43}$$

The equation, once discretised along the N_r-resolved height of the annular pipe, is expressed into an algebraic equation of known term b_{lq}

$$\mathbf{A}\cdot\hat{\psi}_{lq} = b_{lq} \tag{C.44}$$

The $\mathbf{A}$ is a banded matrix, expressed as

$$\mathbf{A} = \mathbf{A}_1 + \mathbf{A}_2 + \mathbf{A}_3 \tag{C.45}$$

where $\mathbf{A}_1$ is a diagonal matrix, while all entries outside the superdiagonal of $\mathbf{A}_3$ and the subdiagonal of $\mathbf{A}_2$ are zero

$$\begin{aligned}
\mathbf{A}_1 &= \begin{pmatrix} a_{1,1} & 0 & 0 & \cdots & 0 & 0 & 0 \\ 0 & a_{1,2} & 0 & \cdots & 0 & 0 & 0 \\ 0 & 0 & \diagdown & \cdots & 0 & 0 & 0 \\ \vdots & \vdots & \vdots & \diagdown & \vdots & \vdots & \vdots \\ 0 & 0 & 0 & \cdots & \diagdown & 0 & 0 \\ 0 & 0 & 0 & \cdots & 0 & a_{1,N_r-1} & 0 \\ 0 & 0 & 0 & \cdots & 0 & 0 & a_{1,N_r} \end{pmatrix} \\
\mathbf{A}_2 &= \begin{pmatrix} 0 & 0 & 0 & \cdots & 0 & 0 & 0 \\ a_{2,1} & 0 & 0 & \cdots & 0 & 0 & 0 \\ 0 & a_{2,2} & 0 & \cdots & 0 & 0 & 0 \\ \vdots & \vdots & \diagdown & \ddots & \vdots & \vdots & \vdots \\ 0 & 0 & 0 & \diagdown & 0 & 0 & 0 \\ 0 & 0 & 0 & \cdots & a_{2,N_r-2} & 0 & 0 \\ 0 & 0 & 0 & \cdots & 0 & a_{2,N_r-1} & 0 \end{pmatrix} \\
\mathbf{A}_3 &= \begin{pmatrix} 0 & a_{3,1} & 0 & \cdots & 0 & 0 & 0 \\ 0 & 0 & a_{3,2} & \cdots & 0 & 0 & 0 \\ 0 & 0 & 0 & \diagdown & 0 & 0 & 0 \\ \vdots & \vdots & \vdots & \ddots & \diagdown & \vdots & \vdots \\ 0 & 0 & 0 & \cdots & 0 & a_{3,N_r-1} & 0 \\ 0 & 0 & 0 & \cdots & 0 & 0 & a_{3,N_r} \\ 0 & 0 & 0 & \cdots & 0 & 0 & 0 \end{pmatrix}
\end{aligned} \tag{C.46}$$

The algebraic equations is solved by the tridiagonal matrix algorithm, also known as the standard Thomas algorithm.

Once known the potential $\hat{\psi}_{lq}(r, t_{n+1})$, its gradient, in the Fourier space, can be derived as it follows

$$\widehat{\nabla\psi}_{lq}(r, t_{n+1}) = \hat{r}\frac{\partial \hat{\psi}_{lq}}{\partial r}(r, t_{n+1}) + \jmath\ \mathbf{k}_{lq}\hat{\psi}_{lq}(r, t_{n+1}) \tag{C.47}$$

The signal $\nabla\psi(\mathbf{x}, t_{n+1})$ can be now finally reconstructed, and used to project the velocity field $\bar{\mathbf{u}}(\mathbf{x}, t_{n+1})$ back to the solenoidal vector field.

Appendix D

The annular pipe averaged Navier-Stokes equations

D.1 The viscous wall drag equation of the annular pipe

In this section we report the analysis of the averaged Navier-Stokes equations of the annular pipe in presence of a discrete phase. The analysis results in a simple expression of the mean viscous wall stress τ_w. At the stochastic steady state, given the no-slip boundary conditions, the frictional drag can be decomposed into three contributions: the laminar, the turbulent and the dispersed phase contributions. The study follows the work of Fukagata et al. [108] , where a relation of the skin friction coefficient was derived for the single-phase channel, pipe and plane boundary layer flows. By adding the dispersed phase feedback to fluid averaged momentum equation we aim at addressing the contribution due to particles to the viscous wall stress.

Owing to symmetry, the Reynolds averaged Navier-Stokes equation in the streamwise direction for an incompressible annular pipe flow [130] is given by

$$\frac{dP}{dz} = \frac{1}{r}\frac{d}{dr}\left\{r\left(\mu\frac{dU_z}{dr} + \tau^R\right)\right\} + F_{p_z} \tag{D.1}$$

We denote with capital symbols the average quantities. $F_{p_z} = \langle f_{p_z} \rangle$ is the average axial particle back-reaction, $\frac{dP}{dz}$ is the averaged pressure gradient and $\mathbf{U} = U_z \hat{e_3}$ is the averaged fluid velocity. $\tau^R = -\rho_f \langle u_r' u_z' \rangle$ is the turbulent viscous stress, where the single quote marks denote the turbulent fluctuations.

The equation (D.1), once multiplied by r, can be integrated in the radial spatial direction, between R_i and r. Following the integration, the particle feedback contribution is expressed by the extra-stress $\tau^e = \frac{1}{r}\int_{R_i}^{r} F_{p_z}\eta d\eta$. The extra-stress τ^e, similar to the turbulent stress τ^R, is responsible of the increase or reduction of the viscous wall stress due to the back-reaction term. The overall stress τ^o, that is the sum of τ^e and τ^R, reads

$$\tau^o = \tau^R + \tau^e \tag{D.2}$$

After defining the wall stress over the inner wall as $\tau_w^{R_i} = \mu\frac{dU_z}{dz}\Big|_{R_i}$, the resulting equation reads

$$\frac{r^2 - R_i^2}{2}\frac{dP}{dz} = r\left\{\mu\frac{dU_z}{dr} + \tau^o\right\} - R_i\tau_w^{R_i} \tag{D.3}$$

After two consecutive integrations, the first one between R_i and r, and the second one between R_i and R_o, followed by appropriate manipulations, we get an equation that relates the average pressure gradient to the average flow rate $Q = 2\pi\int_{R_i}^{R_o} U_z r dr$, namely

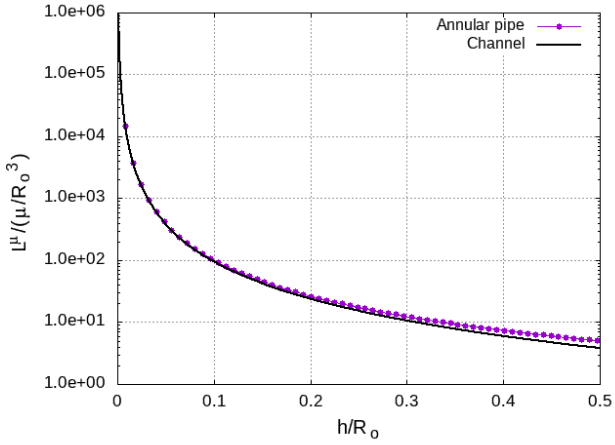

Figure D.1: The viscous contribution L^{μ}, normalised by R_o^3/μ, of the wall stress τ_w versus the height of the annular pipe $\frac{h}{R_o} = \frac{R_o - R_i}{R_o}$. At large R_o, compared with h, the viscous contribution of the annular pipe correctly approximates the channel solution $L^{\mu}_{channel}$, where $2\pi R_o L^{\mu}_{channel} = \frac{6\mu}{h^2}$.

$$-\frac{\pi}{8}\left\{R_o^4 - R_i^4 - \frac{(R_o^2 - R_i^2)^2}{ln(R_o/R_i)}\right\}\frac{dP}{dz} = \mu Q + \pi\int_{R_i}^{R_o}\left\{\frac{R_o^2 - R_i^2}{2ln(R_o/R_i)} - r^2\right\}\tau^o dr \tag{D.4}$$

The mean viscous wall stress can be defined through the mechanical balance of the averaged forces on the annular pipe. Therefore the mean viscous wall stress is $\tau_w = -\frac{dP}{dz}\frac{R_o - R_i}{2}$. This information can be included into the equation (D.4) to obtain a relation of the mean viscous wall stress, namely

$$\frac{\pi}{4(R_o - R_i)}\left\{R_o^4 - R_i^4 - \frac{(R_o^2 - R_i^2)^2}{ln(R_o/R_i)}\right\}\tau_w = \mu Q + \pi\int_{R_i}^{R_o}\left\{\frac{R_o^2 - R_i^2}{2ln(R_o/R_i)} - r^2\right\}(\tau^R + \tau^e)dr \tag{D.5}$$

Following equation (D.5), the viscous wall stress τ_w is given, by three contributions: the viscous L^{μ}, the turbulent L^R and the back-reaction contributions L^e.

$$\tau_w = QL^{\mu} + L^R + L^e \tag{D.6}$$

$$\begin{cases} L^{\mu} = \dfrac{4(R_o - R_i)\mu}{\pi\left\{R_o^4 - R_i^4 - \frac{(R_o^2 - R_i^2)^2}{ln(R_o/R_i)}\right\}} \\ L^R = \dfrac{4(R_o - R_i)\int_{R_i}^{R_o}\left\{\frac{R_o^2 - R_i^2}{2ln(R_o/R_i)} - r^2\right\}\tau^R dr}{\left\{R_o^4 - R_i^4 - \frac{(R_o^2 - R_i^2)^2}{ln(R_o/R_i)}\right\}} \\ L^e = \dfrac{4(R_o - R_i)\int_{R_i}^{R_o}\left\{\frac{R_o^2 - R_i^2}{2ln(R_o/R_i)} - r^2\right\}\tau^e dr}{\left\{R_o^4 - R_i^4 - \frac{(R_o^2 - R_i^2)^2}{ln(R_o/R_i)}\right\}} \end{cases} \tag{D.7}$$

L^{μ} solely depends on the geometry of the annular pipe, i.e. on the radial aspect ratio R_i/R_o, and on the dynamic viscosity. In a laminar flow L^{μ} is exactly the viscous wall stress per unit flow rate Q. When the radius of the cylindrical shells are very large, the curvatures of the walls are negligible. Hence the flow field of the annular pipe approximates a channel flow of width $L = 2\pi R_o$. Figure D.1 shows how L^{μ} approximates the related channel solution, i.e. $2\pi R_o L^{\mu}_{channel} = \frac{6\mu}{h^2}$, when the height of annular pipe $h = R_o - R_i$ is small as compared with R_o.

The viscous wall drag in a single-phase turbulent wall-bounded flow is usually much higher than that of a laminar one under the same flow rate. The large frictional drag is associated to the

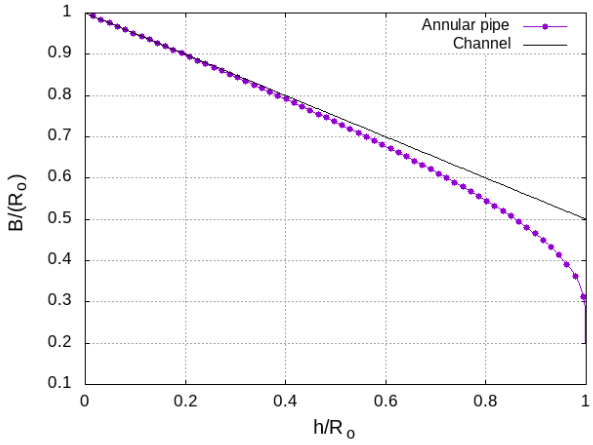

Figure D.2: The annular pipe geometric coefficient $B = \sqrt{\frac{R_o^2 - R_i^2}{2ln(R_o/R_i)}}$ versus the height of the channel $h/R_o = \frac{R_o - R_i}{R_o}$. The coefficient B approximates the channel solution $B_{channel} = \frac{R_o + R_i}{2}$ when the curvature of the walls is reduced.

existence of near-wall vortical structures [109]. The effect of such near-wall motions on the averaged momentum balance is captured by the Reynolds stress τ^R. The back-reaction term similarly affects the fluid momentum by means of the extra-stress τ^e. According to the equations (D.6) (D.7), the related increase of wall friction is represented by L^R and L^e, owing to turbulence fluctuation and particle feedback, respectively. The overall effect of the Reynolds stress τ^R and the extra-stress τ^e is averaged by means of the weight $B^2 - r^2$, where $B^2 = \frac{R_o^2 - R_i^2}{2ln(R_o/R_i)}$. When the distance from the wall is small, i.e. $R_i/R_o \to 1$, the weight of the integrals is recast into the channel expression, i.e. $B^2 - r^2 \sim \frac{R_o + R_i}{2} - r$. Hence, when increasing the size of the cylinders, the geometric coefficient B approaches the channel solution, where $B_{channel} = \frac{R_o + R_i}{2}$. Figure D.2 shows this behaviour, where the weight B/R_o is plotted against the height of the annular pipe h/R_o.

The equations (D.6) (D.7) can be used to addressed the increase of wall friction in particle-laden flow. The viscous, turbulent and particle-feedback contributions must be computed and compared at constant flow rate Q. The dispersed phase can affect the wall friction via the direct effect of its averaged feedback F_{p_z}. Such modification is described by the extra-stress τ^e and by the related wall-friction contribution L^e. Owing to turbophoresis, particles can change the near-wall vortical structures as well. The related alteration of the Reynolds stress τ^R modifies the turbulent dissipation, and therefore the viscous wall drag, in the annular pipe. Such effect is captured by the turbulent contribution of the wall friction, i.e. by L^R.

D.2 The heat equation of the annular pipe

A similar analysis can be conducted in the averaged Fourier equation. Due to the axial symmetry of the problem, at steady state the Reyolds averaged Fourier equation reads

$$0 = \frac{1}{r}\frac{d}{dr}\left\{ r\left(\kappa \frac{d\mathcal{T}}{dr} - \rho_f c_p \langle T' u_r' \rangle \right) \right\} \tag{D.8}$$

The averaged temperature is $\mathcal{T} = \langle T \rangle$, and the turbulent fluctuations is $T' = T - \mathcal{T}$. The Reynolds heat density is $q^R = -\rho_f c_p \langle T' u_r' \rangle$. The Reynolds stress τ^R is responsible for the wall drag due to the turbulent shear transport . Likewise, the Reynolds heat density affects the heat exchange owing to the turbulent thermal convection. The heat transfer Q_W will be decomposed into two contributions: the diffusive and turbulent contributions. In presence of inter-phase heat

transfer, which in the present research is discarded, an additional contribution would appear, similar to the particle feedback F_{p_z} in the momentum equation.

The heat transfer is positive when it is added to the system through the internal cylinder, or removed from the system through the external cylinder. The definition is reported below

$$Q_W = \int_{S_i} (-\kappa \nabla \mathcal{T}) \cdot \hat{r} dr = \int_{S_o} (-\kappa \nabla \mathcal{T}) \cdot \hat{r} dr \tag{D.9}$$

By means of two consecutive integration of equation (D.8), the first one between R_i and r and second one between R_i and R_o, and after appropriate manipulations, we get the equation for the heat transfer Q_W.

$$Q_W = -2\pi\kappa \frac{T_o - T_i}{ln(R_o/R_i)} - \frac{2\pi}{ln(R_o/R_i)} \int_{R_i}^{R_o} q^R dr \tag{D.10}$$

The heat exchange is generated by a diffusive effect, proportional to the thermal diffusivity κ and the difference between the external and internal temperature, and by the turbulent thermal convection, proportional by the integral of the Reynolds heat density.

$$\begin{cases} Q_W^\mu = -2\pi\kappa \frac{T_o - T_i}{ln(R_o/R_i)} \\ Q_W^R = -\frac{2\pi}{ln(R_o/R_i)} \int_{R_i}^{R_o} q^R dr \end{cases} \tag{D.11}$$

Q_W^μ is the heat transfer occurring in a laminar flow, due to solely thermal diffusion. Given the temperature difference, the heat exchange is in general higher in presence of turbulence, than it is in laminar flows. In fact, the turbulent thermal convection $\langle u_r' T' \rangle$ is usually aligned to the diffusive contribution Q_W^μ. The measure of such increase is given by the turbulent thermal convection, i.e. by Q_W^R.

The alteration of the turbulence mixing due to the dispersed phase changes the turbulent thermal convection and the heat exchange as well. The measure of such modification is given the turbulent contribution Q_W^R.

It is easily shown that, when the wall curvature is small (i.e. $h/R_o \to 0$), the equation of the heat flux returns the solution of a channel of width $2\pi R_o$, which reads

$$Q_{W_{channel}} = 2\pi R_o \left\{ -\kappa \frac{T_o - T_i}{h} - \frac{1}{h} \int_{R_i}^{R_o} q^R dr \right\} \tag{D.12}$$

Appendix E

The low-storage Runge-Kutta method

In this section we aim at providing to the reader a detailed description of the low-storage four-stage Runge-Kutta algorithm (RK4) used to advance in time the set of partial differential equations. We will present the analysis of the stability and accuracy of RK4.

E.1 The accuracy of RK4

Let's consider the following differential equation:

$$\frac{\partial u}{\partial t} = N(u) \tag{E.1}$$

where $u(k,t)$ is the variable to be integrated and $N(u)$ is in general a non linear operator. In the four-stage Runge-Kutta method the computation of u^{n+1} at the next physical time step is performed through four successive sub-steps. Each sub-step is computed through an Euler-like algorithm, whose inputs are the solutions of the two previous sub-steps. The scheme is presented in equation (E.2).

$$\begin{aligned} u^n &= u^0 \\ u^1 &= u^0 + a_1 N(u^0)\Delta t \\ u^2 &= u^1 + (a_2 N(u^1) + b_2 N(u^0))\Delta t \\ u^3 &= u^1 + (a_3 N(u^2) + b_3 N(u^1))\Delta t \\ u^4 &= u^1 + (a_4 N(u^3) + b_4 N(u^2))\Delta t \\ u^{n+1} &= u^4 \end{aligned} \tag{E.2}$$

where Δt is the physical time step, chosen by convergence criteria, see the next section E.2.

The coefficients a_i and b_i are determined with accuracy criteria. In fact, the scheme must approximate the Taylor expansion of u, up to the desired level of accuracy. For RK4 the largest accuracy that can be obtained is the fourth order. However, in the present algorithm it has been preferred to truncate the accuracy up to the third order. We will show that not all the conditions imposed by the fourth order terms of the Taylor expansion of u are satisfied, but only the one needed by the stability analysis.

The Taylor expansion of u is presented in equation (E.3).

$$u^{n+1} = u^n + \left.\frac{\partial u}{\partial t}\right|^n \Delta t + + \frac{1}{2}\left.\frac{\partial^2 u}{\partial t^2}\right|^n \Delta t^2 + \frac{1}{6}\left.\frac{\partial^3 u}{\partial t^3}\right|^n \Delta t^3 + \frac{1}{24}\left.\frac{\partial^4 u}{\partial t^4}\right|^n \Delta t^4 + o(\Delta t^4) \tag{E.3}$$

Considering the following relations

$$\begin{aligned}
\frac{\partial u}{\partial t} &= N \\
\frac{\partial^2 u}{\partial t^2} &= N\frac{\partial N}{\partial u} \\
\frac{\partial^3 u}{\partial t^3} &= N^2\frac{\partial^2 N}{\partial u^2} + N\left(\frac{\partial N}{\partial u}\right)^2 \\
\frac{\partial^4 u}{\partial t^4} &= N\left(\frac{\partial N}{\partial u}\right)^3 + N^3\frac{\partial^3 N}{\partial u^3} + 4N^2\frac{\partial N}{\partial u}\frac{\partial^2 N}{\partial u^2}
\end{aligned} \tag{E.4}$$

equation (E.3) is recast into the following expression:

$$\begin{aligned}
u^{n+1} = u^n + N|^n\,\Delta t + \frac{1}{2}\left(N\frac{\partial N}{\partial u}\right)\Big|^n \Delta t^2 + \frac{1}{6}\left(N^2\frac{\partial^2 N}{\partial u^2} + N\left(\frac{\partial N}{\partial u}\right)^2\right)\Big|^n \Delta t^3 + \\
+\frac{1}{24}\left(N\left(\frac{\partial N}{\partial u}\right)^3 + N^3\frac{\partial^3 N}{\partial u^3} + 4N^2\frac{\partial N}{\partial u}\frac{\partial^2 N}{\partial u^2}\right)\Big|^n \Delta t^4 + o(\Delta t^4)
\end{aligned} \tag{E.5}$$

For the sake of simplicity we will omit hereafter the n (or 0) superscript for variables belonging to the initial step. From the scheme represented in equations (E.2) we obtain the values of the increments Δu:

$$\begin{aligned}
\overline{\Delta u} &= u^1 - u = \Delta t a_1 N \\
\widehat{\Delta u} &= u^2 - u = \Delta t(a_1 N + a_2 N^1 + b_2 N) \\
\widetilde{\Delta u} &= u^3 - u = \Delta t(a_1 N + a_2 N^1 + b_2 N + a_3 N^2 + b_3 N^1) \\
\Delta u &= u^4 - u = \Delta t(a_1 N + a_2 N^1 + b_2 N + a_3 N^2 + b_3 N^1 + b_4 N^2 + a_4 N^3)
\end{aligned} \tag{E.6}$$

The last equation in (E.6) is the discretised Taylor expansion of u. The equation requires to express N^i as functions of the time step, to be represented in the form of (E.5), which reads

$$\begin{aligned}
N^1 &= N + \frac{\partial N}{\partial u}\overline{\Delta u} + \frac{1}{2}\frac{\partial^2 N}{\partial u^2}\overline{\Delta u}^2 + \frac{1}{6}\frac{\partial^3 N}{\partial u^3}\overline{\Delta u}^3 + o(\overline{\Delta u}^3) \\
N^2 &= N + \frac{\partial N}{\partial u}\widehat{\Delta u} + \frac{1}{2}\frac{\partial^2 N}{\partial u^2}\widehat{\Delta u}^2 + \frac{1}{6}\frac{\partial^3 N}{\partial u^3}\widehat{\Delta u}^3 + o(\widehat{\Delta u}^3) \\
N^3 &= N + \frac{\partial N}{\partial u}\widetilde{\Delta u} + \frac{1}{2}\frac{\partial^2 N}{\partial u^2}\widetilde{\Delta u}^2 + \frac{1}{6}\frac{\partial^3 N}{\partial u^3}\widetilde{\Delta u}^3 + o(\widetilde{\Delta u}^3)
\end{aligned} \tag{E.7}$$

By putting the (E.6) into the (E.7) we obtain:

$$
\begin{aligned}
N^1 &= N + N\frac{\partial N}{\partial u}a_1\Delta t + N^2\frac{\partial^2 N}{\partial u^2}a_1^2\frac{\Delta t^2}{2} + N^3\frac{\partial^3 N}{\partial u^3}a_1^3\frac{\Delta t^3}{6} + o(\Delta t^3)\\
N^2 &= N + N\frac{\partial N}{\partial u}(a_1+a_2+b_2)\Delta t + \left[a_2a_1N\left(\frac{\partial N}{\partial u}\right)^2 + \frac{N^2}{2}\frac{\partial^2 N}{\partial u^2}(a_1+b_2+a_2)^2\right]\Delta t^2 +\\
&+\left[N\frac{\partial N}{\partial u}\frac{\partial^2 N}{\partial u^2}\left(\frac{a_2a_1^2}{2}+a_2a_1(a_1+b_2+a_2)\right) + N^3\frac{\partial^3 N}{\partial u^3}\frac{(a_1+b_2+a_2)^3}{6}\right]\Delta t^3 + o(\Delta t^3)\\
N^3 &= N + N\frac{\partial N}{\partial u}(a_1+a_2+b_2+b_3+a_3)\Delta t +\\
&\Delta t^2\left[N\left(\frac{\partial N}{\partial u}\right)^2(a_3(a_1+b_2+a_2)+a_1b_3+a_2a_1) + \frac{1}{2}N^2\frac{\partial^2 N}{\partial u^2}(a_1+b_2+a_2+b_3+a_3)^2\right] +\\
&+\left\{N^2\frac{\partial N}{\partial u}\frac{\partial^2 N}{\partial u^2}\left[\frac{a_1^2}{2}(a_2+b_3)+\frac{a_3}{2}(a_1+b_2+a_2)^2+(a_1+a_2+b_2+a_3+b_3)(a_1(b_3+a_2)\right.\right. +\\
&\left.\left.+a_3(a_1+b_2+a_2))\right] + +\frac{N^3}{6}\frac{\partial^3 N}{\partial u^3}(a_1+b_2+a_2+b_3+a_3)^3 + N\left(\frac{\partial N}{\partial u}\right)^3 a_1a_2a_3\right\}\Delta t^3 + o(\Delta t^3)
\end{aligned}
\tag{E.8}
$$

Therefore Δu can be computed and after some algebra we get:

$$
\Delta u = \Delta u_1\Delta t + \Delta u_2\Delta t^2 + \Delta u_3\Delta t^3 + \Delta u_4\Delta t^4 + o(\Delta t^4) \tag{E.9}
$$

where the increments Δu_i are defined as:

$$
\begin{aligned}
\Delta u_1 &= N(a_1+a_2+b_2+a_3+b_3+a_4+b_4)\\
\Delta u_2 &= N\frac{\partial N}{\partial u}(a_1(a_2+b_3)+(a_1+b_2+a_2)(a_3+b_3)+a_4(a_1+b_2+a_2+b_3+a_3))\\
\Delta u_3 &= N^2\frac{\partial^2 N}{\partial u^2}\left[\frac{a_1^2}{2}(a_2+b_3)+(a_1+b_2+a_2)^2(a_3+b_4)/2+\frac{a_4}{2}(a_1+a_2+b_2+a_3+b_3)\right] +\\
&+N\left(\frac{\partial N}{\partial u}\right)^2[(a_3+b_4)a_2a_1+a_4(a_1(b_3+a_2)+a_3(a_1+b_2+a_2))]\\
\Delta u_4 &= \frac{N^3}{6}\frac{\partial^3 N}{\partial u^3}\left[(a_1^3(a_2+b_3)+(a_3+b_4)(a_1+b_2+a_2)^3+a_4(a_1+b_2+a_2+b_3+a_3)^3\right] +\\
&+N\left(\frac{\partial N}{\partial u}\right)^3 a_1a_2a_3a_4 + N^2\frac{\partial N}{\partial u}\frac{\partial^2 N}{\partial u^2}\left\{(a_3+b_4)[a_2a_1(a_1+b_2+a_2)+\frac{a_1^2a_2}{2}] +\right.\\
&\left.+a_4\left[\frac{a_1^2}{2}(a_2+b_3)+\frac{a_3}{2}(a_1+b_2+a_2)^2+(a_1+b_2+a_2+b_3+a_3)(a_1(a_2+b_3)+a_3(a_1+b_2+a_2)\right]\right\}
\end{aligned}
\tag{E.10}
$$

The discrete Taylor expansion of the algorithm must approximate the real Taylor expansion of the solution $u(k,t)$. Therefore, the equation (E.9) must approximate (E.5) up to the desired level of accuracy. Since N(u) is arbitrary, the comparison lead to conditions for the coefficients a_i and b_i, shown in (E.11). The conditions are expressed as a set of seven non-linear equations, one equation for each term of the Taylor expansion (E.5). In particular, we have one condition for the first-order term, one for the second-order term, two for the third-order term and three for the fourth-order term.

a_1	8/17	b_1	0
a_2	17/60	b_2	-15/68
a_3	5/12	b_3	-17/60
a_4	3/4	b_4	-5/12

Table E.1: Coefficients a_i and b_i of RK4

$$\begin{cases} a_1 + b_2 + a_2 + a_3 + b_3 + a_4 + b_4 = 1 \\ a_1(a_2 + b_3) + (a_1 + b_2 + a_2)(a_3 + b_3) + a_4(a_1 + b_2 + a_2 + b_3 + a_3 = \frac{1}{2} \\ \frac{a_1^2}{2}(a_2 + b_3) + \frac{a_3+b_4}{2}(a_1 + b_2 + a_2)^2 + \frac{a_4}{2}(a_1 + b_2 + a_2 + b_3 + a_4)^2 = \frac{1}{6} \\ a_2 a_1(a_3 + b_4) + a_4(a_1(b_3 + a_2) + a_3(a_1 + b_2 + a_2)) = \frac{1}{6} \\ a_1 a_2 a_3 a_4 = \frac{1}{24} \\ \frac{a_2+b_3}{6}a_1^3 + \frac{a_3+b_4}{6}(a_1 + b_2 + a_2)^3 + \frac{a_4}{6}(a_1 + b_2 + a_2 + b_3 + a_3)^3 = \frac{1}{24} \\ (a_3 + b_4)[a_2 a_1(a_1 + b_2 + a_2) + a_1^2 a_2/2] + a_4\{\frac{a_1^2}{2}(b_3 + a_2) + \frac{a_3}{2}(a_1 + b_2 + a_2)^2 + \\ +(a_1 + b_2 + a_2 + b_3 + a_3)[a_1(b_3 + a_2) + a_3(a_1 + b_2 + a_2)]\} = \frac{4}{24} \end{cases} \tag{E.11}$$

From this set of equations we can derive the values of the coefficients that satisfies the prescribed level of accuracy. Since we have 7 independent equations and 7 unknowns, the system is closed and a unique solution exists. The number of solutions, in the complex field, is the order of the system, namely 1152. It is worth noticing that if one of these solutions belonged to the real field, in order not to have complex sub-step solutions, it would be possible to have a 4th order algorithm. However, the last two equations in (E.11) are replaced by the relations $b_4 = -a_3$ and $b_3 = -a_2$. The selected set of parameters a_i and b_i is reported in table E.1.

In general, for a non-linear function $N(u)$, the numerical scheme is only 3th-order accurate, since the conditions coming from the 4th-order terms of the Taylor expansion are only partially satisfied. However, in the specific case where $N(u)$ is linear function, all the higher-order dervatives with respect to u are zero. In this case all fourth-order terms in equation (E.5), except for $N\left(\frac{\partial N}{\partial u}\right)^3$, are zero. The surviving term is well-approximated by the set of coefficients in E.1, which in fact satisfies the fifth equation of the set (E.11) Therefore, when $N(u)$ is a linear function, RK4 approximates the Taylor expansion up to the fourth order of accuracy.

E.2 The stability of RK4

Let us consider the equation (E.1), with $N(u)$ a non-linear function. RK4 provides a a 3th-order approximate solution, where the fourth-order term of the Taylor expansion of $N(u)$ is only partially approximated. By referring to u as the exact solution and to q as the approximated one, we can write:

$$\begin{cases} u^0 = \bar{u} \\ u^{n+1} = u^n + N|_u^n \Delta t + N\frac{\partial N}{\partial u}\Big|_u^n \frac{\Delta t^2}{2} + \left(N^2\frac{\partial^2 N}{\partial u^2} + N\left(\frac{\partial N}{\partial u}\right)^2\right)\Big|_u^n \frac{\Delta t^3}{6} + \left(N\left(\frac{\partial N}{\partial u}\right)^3\right)\Big|_u^n \frac{\Delta t^4}{24} + o(\Delta t^3) \\ \\ q^0 = \bar{u} \\ q^{n+1} = q^n + N|^n q\Delta t + N\frac{\partial N}{\partial u}\Big|_q^n \frac{\Delta t^2}{2} + \left(N^2\frac{\partial^2 N}{\partial u^2} + N\left(\frac{\partial N}{\partial u}\right)^2\right)\Big|_q^n \frac{\Delta t^3}{6} + \left(N\left(\frac{\partial N}{\partial u}\right)^3\right)\Big|_q^n \frac{\Delta t^4}{24} \end{cases} \tag{E.12}$$

If we define the error of the algorithm as $\epsilon = u - q$, T is the temporal integration interval and $n = T/\Delta t$ the number of time steps from the initial condition, the comparison of the exact and numerical equations (E.12) determines the order of magnitude of ϵ, namely

$$\epsilon^n \sim n\ o(\Delta t^3) = T\ o(\Delta t^2) \tag{E.13}$$

The error goes to zero as Δt^3, as prescribed by the choice of the coefficients a_i and b_i.We can derive the equation for ϵ^{n+1}, truncated at the second order, by subtracting the second equation of (E.12) from the first one. Thus, we write

$$\begin{aligned}\epsilon^{n+1} = \epsilon^n + (N|_u^n - N_q^n)\Delta t + \frac{\Delta t^2}{2}\left[\left(N\,\frac{\partial N}{\partial u}\right)\Big|_u^n - \left(N\frac{\partial N}{\partial u}\right)\Big|_q^n\right] + \\ + \frac{\Delta t^3}{6}\left[\left(N^2\frac{\partial^2 N}{\partial u^2} + N\left(\frac{\partial N}{\partial u}\right)^2\right)\Big|_u^n - \left(N^2\frac{\partial^2 N}{\partial u^2} + N\left(\frac{\partial N}{\partial u}\right)^2\right)\Big|_q^n\right] + \\ + \frac{\Delta t^4}{24}\left[\left(N\left(\frac{\partial N}{\partial u}\right)^3\right)\Big|_u^n - \left(N\left(\frac{\partial N}{\partial u}\right)^3\right)\Big|_q^n\right] + o(\Delta t^3)\end{aligned} \tag{E.14}$$

Now we can use the expansion of a generic function $f(u)$ centred at q, truncated at the second order, which omitting the superscript n reads

$$f(u) = f(\epsilon + q) = f(q) + \left.\frac{\partial f}{\partial u}\right|_q \epsilon + o(\epsilon^2) \tag{E.15}$$

The expansion (E.15) allows, after some algebra, to rewrite the equation (E.14) as

$$\epsilon^{n+1} = \left[1 + \frac{\partial N}{\partial u}\Delta t + \frac{\partial}{\partial u}\left(N\frac{\partial N}{\partial u}\right)\frac{\Delta t^2}{2} + \frac{\partial}{\partial u}\left(N^2\frac{\partial^2 N}{\partial u^2} + N\left(\frac{\partial N}{\partial u}\right)^2\right)\frac{\Delta t^3}{6} + \frac{\partial}{\partial u}\left(N\left(\frac{\partial N}{\partial u}\right)^3\right)\frac{\Delta t^4}{24}\right]\Bigg|_q^n \epsilon^n + o(\Delta t^3) \tag{E.16}$$

The algorithm is stable only if, for every value of n

$$\left|1 + \frac{\partial N}{\partial u}\Delta t + \frac{\partial}{\partial u}\left(N\frac{\partial N}{\partial u}\right)\frac{\Delta t^2}{2} + \frac{\partial}{\partial u}\left(N^2\frac{\partial^2 N}{\partial u^2} + N\left(\frac{\partial N}{\partial u}\right)^2\right)\frac{\Delta t^3}{6} + \frac{\partial}{\partial u}\left(N\left(\frac{\partial N}{\partial u}\right)^3\right)\frac{\Delta t^4}{24}\right| < 1 \tag{E.17}$$

By solving the above inequality, once known the function N, it is possible to find the values of Δt which guarantee the stable operation of the numerical alogorithm. Since when using spectral methods N can be in general a complex function, the solution will be bounded in a region of the complex plane, referred to as the stability region.

The inequality (E.17) has a strightforward solution when $N(u)$ is a linear differential system. In fact, under the hypothesis that $N(u)$ is expressed through a diagonalizable matrix of eigenvalues λ_i, the equation (E.17) is recast into

$$\left|I + \lambda_i\Delta t + \lambda_i^2\frac{\Delta t^2}{2} + \lambda_i^3\frac{\Delta t^3}{6} + \lambda_i^4\frac{\Delta t^4}{24}\right| < 1 \qquad \forall\ i = 1, 2, ..., M \tag{E.18}$$

where M is the number of equations of the linear system $N(u)$.

The solutions $\lambda\Delta t$ of the problem (E.18) provide the stability region of RK4. For the third-stage Runge-Kutta (RK3) we can obtain a similar relation. In this case, however, the coefficients a_i and b_i can't satisfy the approximation of the fourth-order term $N\left(\frac{\partial N}{\partial u}\right)^3$. The stability region of RK3 is therefore derived by the inequality (E.18) in the absence of the fourth-order term $\lambda_i^4\frac{\Delta t^4}{24}$.

The stability regions of RK4 and RK3 are found using the Newton-Rapson algorithm, while considering complex eigenvalues in (E.18). In figure E.2 the stability regions of RK4 and RK3 are displayed, where λ_I is the imaginary part and λ_R the real part of λ. For each eigenvalues λ_i, which are fixed by the physical problem, the code is stable when the time step is small enough that $\Delta t \lambda_i$ falls inside the stability region. In the linear analysis, RK4 has a wide stability region than RK3. In particular, for pure imaginary eigenvalues, the CFL_{max} of RK4 is $\sqrt{8}$, as compared with $\sqrt{3}$ for RK3.

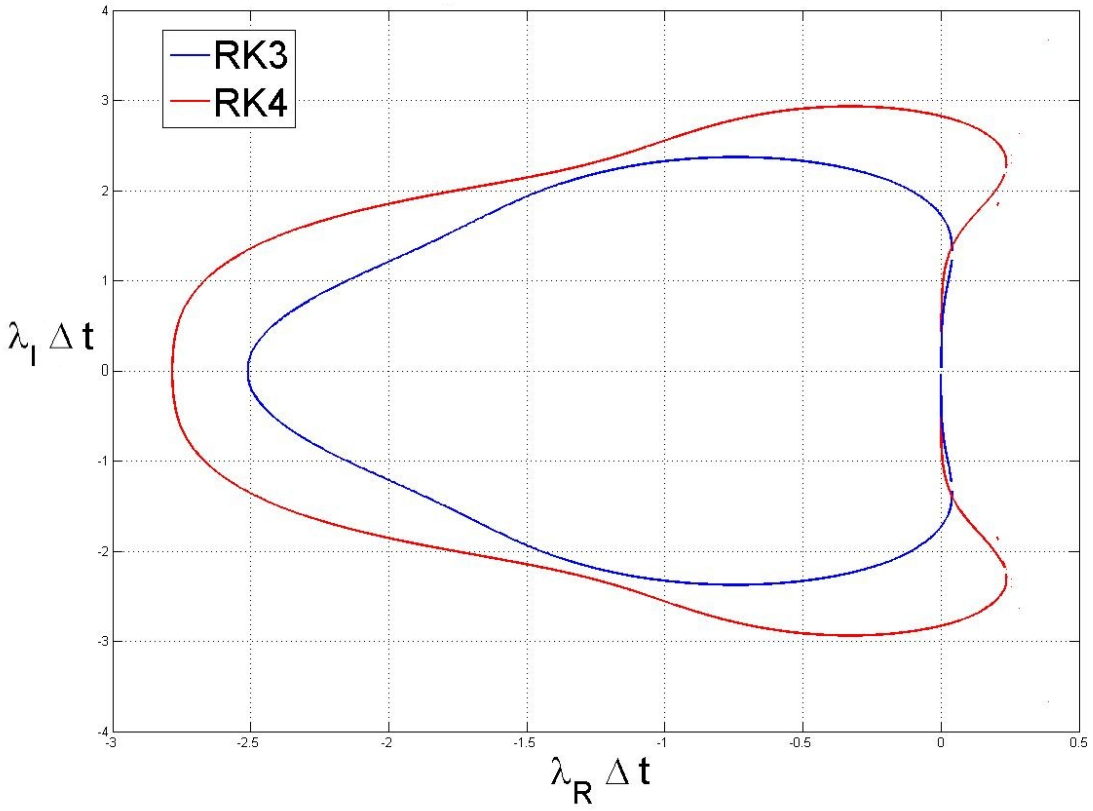

Figure E.1: The stability regions of RK3 and RK4

Appendix F

Main differential equations in ERPP derivation

F.1 Fundamental solution of the diffusion equation

The fundamental solution of the diffusion equation g(x-ψ,t-τ) in the free-space is found by solving the following singularly forced diffusion problem, coupled with the proper initial condition:

$$\begin{aligned} &\frac{\partial g}{\partial t} = \nu\nabla^2 g + \delta(x-\psi)\delta(t-\tau) \\ &\lim_{t\to\tau^-} g(x-\psi, t-\tau) = g(x-\psi, 0^-) = 0 \end{aligned} \tag{F.1}$$

By integrating the first one of (F.1) from $\tau-\epsilon$ to $\tau+\epsilon$, with ϵ going to zero, and exploiting the delta function properties and the regularity of g, equations (F.1) can be recast into an initial-value problem:

$$\begin{aligned} &\frac{\partial g}{\partial t} = \nu\nabla^2 g \qquad\qquad t > \tau, \\ &\lim_{t\to\tau^+} g(x-\psi, t-\tau) = g(x-\psi, 0^+) = \delta(x-\psi) \end{aligned} \tag{F.2}$$

and by transforming the above set of equations into the Fourier space, denoting with $\hat{g}$ the Fourier transform of g and with k the wavenumber, one immediately gets:

$$\begin{aligned} &\frac{\partial \hat{g}}{\partial t} = -\nu||k||^2\hat{g} \qquad\qquad t > \tau, \\ &\lim_{t\to\tau^+} \hat{g}(k, t-\tau) = \hat{g}(k, 0^+) = \frac{1}{(2\pi)^3} \end{aligned} \tag{F.3}$$

Equation (F.3) can be easily integrated in t from $t = \tau^+$ to t, obtaining:

$$\hat{g}(k, t-\tau) = \hat{g}(k, 0^+) exp[-\nu||k||^2(t-\tau^+)] \tag{F.4}$$

where by considering the initial condition and omitting for the sake of simplicity the superscript $+$ in τ, being a formalism not relevant here, one finally gets the solution:

$$\hat{g}(k, t-\tau) = \frac{1}{(2\pi)^3} exp[-\nu||k||^2(t-\tau)] \tag{F.5}$$

We now recognise equation (F.5) as the Gaussian distribution in the wavenumber space, with time-dependent variance $\sigma(t-\tau) = \sqrt{2\nu(t-\tau)}$, that back to the physical space becomes:

$$g(x-\psi, t-\tau) = \frac{1}{[4\pi\nu(t-\tau)]^{3/2}} exp\left[-\frac{||x-\psi||^2}{4\nu(t-\tau)}\right] \tag{F.6}$$

F.2 Fundamental solution of the free diffusion vorticity equation forced by the impulse $\zeta(x,\tau)\delta(t-\tau)$

The fundamental solution of the free diffusion vorticity equation forced by the impulse $\zeta(x,\tau)\delta(t-\tau)$ is identified by the following differential equation

$$\rho_f \frac{\partial \zeta_R}{\partial t}(x,t) = \mu\nabla^2\zeta_R(x,t) + \zeta(x,\tau)\delta(t-\tau)\ , \quad \zeta_R(x,\tau^-) = 0 \tag{F.7}$$

By applying the same procedure of F.1, one integrates equation (F.7) from time $t = \tau^-$ to time $t = \tau^+$ and gets

$$\zeta_R(x,\tau^+) = \zeta(x,\tau) \tag{F.8}$$

We now compute the Fourier transform of equation (F.7) and we obtain

$$t > \tau^+ \begin{cases} \rho_f \frac{\partial \hat{\zeta_R}}{\partial t}(k,t) = -\mu k^2 \zeta_R(k,t) \\ \hat{\zeta_R}(k,\tau^+) = \hat{\zeta}(k,\tau) \end{cases} \tag{F.9}$$

that can be integrated from $t = \tau^+$ to t obtaining

$$\hat{\zeta_R}(k,t) = (2\pi)^3\hat{\zeta}(k,\tau)\frac{1}{(2\pi)^3}e^{-\frac{k^2 2(t-\tau)\nu}{2}} = (2\pi)^3\hat{\zeta}(k,\tau)\hat{g}_\sigma(k,t-\tau) \tag{F.10}$$

By recognising the convolution product between the Gaussian $\hat{g}_\sigma(k,t-\tau)$ with variance $\sigma = \sqrt{2\nu(t-\tau)}$ and the function $\hat{\zeta}(k,\tau)$ in the (F.10), one can apply the inverse Fourier transform and find the final solution, that reads:

$$\zeta_r(x,t) = \int_{\mathbb{R}^3} \zeta(\psi,\tau)g(x-\psi,t-\tau)d^3\psi \tag{F.11}$$

F.3 Fundamental solution of the unsteady singularly forced Stokes equations

The fundamental solution of the unsteady singularly forced Stokes problem in the free-space can be found by solving the following set of equations:

$$\begin{aligned} &\rho\frac{\partial w}{\partial t} = \nabla\cdot T + \hat{e}\delta(x-\psi)\delta(t-\tau) \\ &\nabla\cdot w = 0 \\ &\lim_{t\to\tau^-} w(x-\psi,t-\tau) = w(x-\psi,0^-) = 0 \end{aligned} \tag{F.12}$$

where T is the stress tensor for incompressible Newtonian and Stokesian fluids and the singular force is applied at time τ and position ψ along the direction $\hat{e}$. By taking the curl of the first equation in (F.12) one gets the dynamic equation for the vorticity $\zeta = \nabla\times w$, shown in equation (F.13).

$$\begin{aligned} &\rho\frac{\partial \zeta}{\partial t} = \mu\nabla^2\zeta - \hat{e}\times\nabla\delta(x-\psi)\delta(t-\tau) \\ &\psi(x-\psi),0^-) = 0 \end{aligned} \tag{F.13}$$

Introducing the ansatz $\zeta = -\frac{1}{\rho}\hat{e}\times\nabla g$, equation (F.13) returns:

$$\nabla\times\left[\frac{\partial g}{\partial t}\right] = \nabla\times[\nu\nabla^2 g + \hat{e}\ \delta(x-\psi)\delta(t-\tau)] \tag{F.14}$$

that, being valid for every point of the domain, it is immediately recast into the scalar diffusion equation (F.1), and its solution $g(x-\psi, t-\tau)$ is the Gaussian function with variance $\sigma = \sqrt{2\nu(t-\tau)}$.

By substituting the expression of $g(x-\psi, t-\tau)$ into the ansatz one finds the solution for ζ. In order to derive the solution of the velocity field the free-divergence vector potential A is introduced for w, and it follows:

$$\zeta = \nabla \times w = \nabla \times \nabla \times A = -\nabla^2 A \tag{F.15}$$

We then define the operator G in such a way to have $\nabla^2 G = g$, allowing us to write an equation for A:

$$A = \frac{1}{\rho} \hat{e} \times \nabla G \tag{F.16}$$

By taking the laplacian of (F.16) and considering the definition of G it is possible to verify that the equation returns the ansatz for the vorticity. The problem is now transposed into the computation of the function $G(r, r_\tau)$, where r and r_τ are the module $||x-\psi||$ and $t-\tau$, respectively. By exploiting the isotropy of the function G, we write its definition in spherical coordinates:

$$\nabla^2 G = \frac{1}{r^2} \frac{\partial}{\partial r} \left[r^2 \frac{\partial G}{\partial r} \right] = g(r, r_\tau) = \frac{1}{(2\pi\sigma(r_\tau)^2)^{3/2}} exp \left[-\frac{r^2}{2\sigma(r_\tau)^2} \right] \tag{F.17}$$

After a successive double integration by parts, the solution of (F.17) can be found, reading:

$$G(r, r_\tau) = \frac{1}{(2\pi)^{3/2}\sigma} \left[-\frac{1}{r} \int_0^r exp \left[-\frac{r^2}{2\sigma^2} \right] dr \right] + B \tag{F.18}$$

By defining now the function $erf(\hat{\rho})$ as

$$erf(\hat{\rho}) = \frac{2}{\sqrt{\pi}} \int_0^{\hat{\rho}} e^{-\gamma} d\gamma \ , \qquad with \qquad \hat{\rho} = \frac{r}{\sqrt{2}\sigma} \tag{F.19}$$

one can rewrite the (F.18) in its final expression, where B is chosen zero

$$G(r, r_\tau) = -\frac{1}{4\pi r} erf \left(\frac{r}{\sqrt{2}\sigma} \right) = -\frac{1}{4\pi r} erf \left(\frac{r}{\sqrt{4\nu r_\tau}} \right) \ , \tag{F.20}$$

where we have considered the dependence on time of the variance σ.

The velocity field w can now be determined by substituting equation (F.20) and (F.16) into $w = \nabla \times A$, being:

$$\begin{aligned} w = \nabla \times A &= \frac{1}{\rho} \nabla \times (\hat{e} \times \nabla G) = \\ &= \frac{1}{\rho} (\nabla^2 G \hat{e} - \nabla \otimes \nabla G \cdot \hat{e}) = \\ &= \frac{1}{\rho} [(gI - \nabla \otimes \nabla G) \cdot \hat{e}] = \\ &= \mathbf{G} \cdot \hat{e} \end{aligned} \tag{F.21}$$

The expression of the Green tensor $\mathbf{G}(x-\psi, t-\tau)$ is given below.

$$\mathbf{G}(x-\psi, t-\tau) = \frac{1}{\rho} \left[\left(1 + \frac{\sigma^2}{r^2} \right) g + \frac{G}{r^2} \right] I - \frac{1}{\rho} \left[\left(1 + \frac{3\sigma^2}{r^2} \right) g + \frac{3G}{r^2} \right] \frac{r \otimes r}{r^2} \tag{F.22}$$

The pressure field associated to the problem can be found by taking the divergence of the singularly forced Stokes equation and solving the associated Laplace equation in the free-space, that reads:

$$\nabla^2 p = \hat{e} \cdot \nabla \delta(x-\psi)\delta(t-\tau) \tag{F.23}$$

The solution for (F.23) is readily found through the aim of the Green function $q = -\frac{1}{4\pi||x-y||}$, indeed we have

$$\begin{aligned} p &= -\int_{\Re^3} \hat{e} \cdot \nabla \delta(y-\psi)\delta(t-\tau)\frac{1}{4\pi||x-y||}d^3y \\ &= \delta(t-\tau)\hat{e} \cdot \nabla_\psi \int_{\Re^3} \frac{\delta(y-\psi)}{4\pi||x-y||}d^3y = \\ &= -\delta(t-\tau)\hat{e} \cdot \nabla \left[\frac{1}{4\pi||x-\psi||}\right] = \\ &= \frac{\hat{e} \cdot r}{4\pi r^3}\delta(t-\tau) \end{aligned} \tag{F.24}$$

The stress tensor T associated to the problem can be written as:

$$T = -pI + \mu(\nabla w + \nabla^\top w) \tag{F.25}$$

where the pressure p is given by the (F.24) and the velocity w by the (F.21). The stress tensor can be rewritten via a third-rank tensor $\mathbf{T}$

$$T = \mathbf{T} \cdot \hat{e} \tag{F.26}$$

being $\mathbf{T}$ the Green stress tensor defined in index notation as

$$\mathbf{T}_{ijk} = -\frac{1}{4\pi r^3}\delta(t-\tau)\delta_{ij}\ r_k + \mu(\frac{\partial \mathbf{G}_{ik}}{\partial x_j} + \frac{\partial \mathbf{G}_{jk}}{\partial x_i}) \tag{F.27}$$

By substituting the formula of $\mathbf{G}_{ij}$ into the (F.27) one can get the final expression for $\mathbf{T}_{ijk}$, that reads:

$$\begin{aligned} \mathbf{T}_{ijk} &= -\frac{r_k}{4\pi r^3}\delta(t-\tau)\delta_{ij} \\ &+ \nu\left[-2\frac{B}{r^2}\delta_{ij}r_k + \left(\frac{1}{r}\frac{dA}{dr} - \frac{B}{r^2}\right)(\delta_{jk}r_i + \delta_{ik}r_j) - 2\left(\frac{2}{r}B + \frac{dB}{dr}\right)\frac{r_i r_j r_k}{r^3}\right] \end{aligned} \tag{F.28}$$

where $A(r)$ and $B(r)$ are defined as

$$\begin{aligned} A(r) &= \left(1 + \frac{\sigma^2}{r^2}\right) + \frac{G}{r^2} \\ B(r) &= \left(1 + \frac{3\sigma^2}{r^2}\right)g + \frac{3}{r^2}G \end{aligned} \tag{F.29}$$

F.4 Fundamental solution of the unsteady Stokes equations forced by a singular time-dependent forcing

The fundamental solution of the unsteady Stokes free-space problem forced by the singular time-dependent forcing $D(t)\ \delta(x-\psi)$, can be found by solving the following set of equations:

$$\begin{aligned} &\rho\frac{\partial w^*}{\partial t} = \nabla \cdot T^* + D(t)\ \delta(x-\psi) \\ &\nabla \cdot w^* = 0 \\ &\lim_{t\to\tau^-} w^*(x-\psi, t-\tau) = w^*(x-\psi, 0^-) = 0 \end{aligned} \tag{F.30}$$

with the usual notation for the symbols used. A solution for (F.30) can be found by exploiting the linearity of the differential operator $\begin{bmatrix} \frac{\partial}{\partial t} & -\nabla\cdot \\ \nabla\cdot & 0 \end{bmatrix}$ applied to the unknowns $\begin{bmatrix} w \\ T \end{bmatrix}$.

Indeed, through the delta Dirac definition we can write the (F.30) as:

$$\begin{bmatrix} \frac{\partial}{\partial t} & -\nabla\cdot \\ \nabla\cdot & 0 \end{bmatrix} \begin{bmatrix} w^* \\ T^* \end{bmatrix} = \begin{bmatrix} \int_0^{\tau^+} \delta(x-\psi)\delta(t-\tau)D(\tau)dt \\ 0 \end{bmatrix} \qquad \text{(F.31)}$$
$$\lim_{t\to\tau^-} w^*(x-\psi,t-\tau) = w^*(x-\psi,0^-) = 0$$

and because of the linearity of this operator the solution will be a linear function of the known term. Thus, it follows:

$$\begin{aligned} w^*(x-\psi,t-\tau) &= f\left(\int_0^{t^+} \frac{D(\tau)}{\rho}\delta(x-\psi)\delta(t-\tau)d\tau\right) = \\ &= \int_0^{t^+} \frac{D_s(\tau)}{\rho} f(\hat{e}\ \delta(x-\psi)\delta(t-\tau))d\tau = \\ &= \int_0^{t^+} \frac{D_s(\tau)}{\rho} w(x-\psi,t-\tau)d\tau = \\ &= \int_0^{t^+} \frac{D_s(\tau)}{\rho} G\cdot\hat{e}d\tau = \\ &= \int_0^{t^+} G\cdot\frac{D(\tau)}{\rho}d\tau \end{aligned} \qquad \text{(F.32)}$$

where D_s is the scalar part of the vector $D(t) = D_s\hat{e}$, $\hat{e}$ is as usual the direction of the forcing, and $w(x-\psi,t-\tau)$ is the solution of (F.12), shown in (F.21). By taking the curl of $w^*(x-\psi,t-\tau)$ one can get the expression of the vorticity, that reads, after some algebra:

$$\zeta(x-\psi,t-\tau) = -\int_0^{t^+} \frac{D(\tau)}{\rho}\times\nabla g(x-\psi,t-\tau)d\tau \qquad \text{(F.33)}$$

One can repeat the same steps for pressure and viscous stresses, obtaining in index notation:

$$T^*_{ij} = \int_0^{t^+} \mathbf{T}_{ijk}\frac{D_k(\tau)}{\rho}d\tau \qquad \text{(F.34)}$$

being $\mathbf{T}_{ijk}$ the third-rank Green stress tensor expressed in (F.28).

F.5 Fundamental solution of the unsteady Stokes equation

We consider the equations for the motion of a Stokes incompressible flow resolved within the domain Ω and properly endowed with initial and boundary conditions. We write

$$\begin{cases} \rho\frac{\partial u}{\partial t} = \nabla\cdot T + f \\ \nabla\cdot u = 0 \\ u(x,0) = u_0(x) \\ u(x,t)|_{\partial\Omega} = u_b(x_b,t) \end{cases} \qquad \text{(F.35)}$$

where f is the resultant mass force, T the stress tensor for incompressible Newtonian fluids and $D(t)\delta(x-\psi)$ is the singular forcing exerted by the particle on the fluid. We want to look for solutions of equations (F.35) by means of the impulse forced unsteady Stokes problem, previously discussed in F.3, with the forcing applied at time τ and position ψ, whose equations read:

$$\begin{cases} \rho \frac{\partial w}{\partial t} = \nabla \cdot T_w + \delta(x-\psi)\delta(t-\tau)\hat{e} \\ \nabla \cdot w = 0 \\ w(x-\psi, 0^-) = 0 \end{cases} \tag{F.36}$$

The solution of equations (F.36), derived previously, are shown in the (F.21) and (F.26), for the velocity field $w(x-\psi, t-\tau)$ and the tensor stress $T_w(x-\psi, t-\tau)$, respectively. We consider the following change of coordinates for $u(x,t)$ and $w(x-\psi, t-\tau)$:

$$\begin{cases} \frac{\partial u}{\partial t} = \frac{\partial u}{\partial \tau} \quad ; \quad \frac{\partial u}{\partial x_i} = \frac{\partial u}{\partial \psi_i} \\ \frac{\partial w}{\partial t} = -\frac{\partial w}{\partial \tau} \quad ; \quad \frac{\partial w}{\partial x_i} = -\frac{\partial w}{\partial \psi_i} \end{cases} \tag{F.37}$$

and we project equation (F.35) along $w(x-\psi, t-\tau)$

$$\rho \frac{\partial u \cdot w}{\partial \tau} - \rho u \cdot \frac{\partial w}{\partial \tau} = \nabla_\psi \cdot (w \cdot T) - T : \nabla_\psi w + f \cdot w \tag{F.38}$$

By substituting the value of $\frac{\partial w}{\partial \tau}$ from the (F.36), after the above mentioned change of coordinates, one obtains:

$$\rho \frac{\partial u \cdot w}{\partial \tau} + u \cdot \hat{e}\ \delta(x-\psi)\delta(t-\tau) = \nabla_\psi \cdot (w \cdot T) - \nabla_\psi \cdot (u \cdot T_w) - T : \nabla_\psi w + T_w : \nabla_\psi u + f \cdot w \tag{F.39}$$

It is important to notice that in order to be able to say that $\nabla = \nabla_\psi$ for T_w one must change the sign of p_w, that is, then, taken negative.

Because of the incompressibility, the terms responsible of the deformation work cancel out each other, indeed we can write:

$$\begin{cases} T : \nabla_\psi w = -p \nabla_\psi \cdot w + 2\mu\ e : e_w = 2\mu\ e : e_w \\ T_w : \nabla_\psi u = p_w \nabla_\psi \cdot u + 2\mu\ e_w : e = 2\mu\ e_w : e \end{cases} \tag{F.40}$$

where e and e_w are the symmetric part of the velocity gradient of $u(\psi, \tau)$ and $w(x-\psi, t-\tau)$, respectively, always spatially derived with respect to ∇_ψ. Equation (F.39) is simplified as:

$$\rho \frac{\partial u \cdot w}{\partial \tau} + u(\psi, \tau) \cdot \hat{e}\ \delta(x-\psi)\delta(t-\tau) = \nabla_\psi \cdot (w \cdot T) - \nabla_\psi \cdot (u \cdot T_w) + f \cdot w \tag{F.41}$$

and can be integrated in ψ and τ.

$$\int_\Omega \int_0^{t^+} \rho \frac{\partial u \cdot w}{\partial \tau} d\tau d^3\psi + u(x,t) \cdot \hat{e} = \oint_{\partial\Omega} \int_0^{t^+} (w \cdot T - u \cdot T_w) \cdot n_\psi dS_\psi d\tau + \int_\Omega \int_0^{t^+} f \cdot w d^3\psi d\tau \tag{F.42}$$

The first term in the last equation can be integrated in time and, just recalling the initial condition of the impulse problem $w(x-\psi, t-t^+) = w(x-\psi, 0^-) = 0$, one obtains:

$$u(x,t) \cdot \hat{e} = -\int_\Omega \rho\ (u \cdot w)\ (x, \psi, t, 0)\ d^3\psi + \oint_{\partial\Omega} \int_0^{t^+} (w \cdot T - u \cdot T_w) \cdot n_\psi dS_\psi d\tau + \int_\Omega \int_0^{t^+} f \cdot w d^3\psi d\tau \tag{F.43}$$

Now by recalling the expression of w and T_w for the solution of the impulse Stokes equations, the (F.43) is recast into:

$$\begin{aligned} u_j(x,t)\hat{e}_j = -\int_\Omega \rho\ (u_i G_{ij} \hat{e}_j)\ (x, \psi, t, 0)\ d^3\psi + \oint_{\partial\Omega} \int_0^{t^+} G_{ij}\hat{e}_j t_i^s - u_i \mathbf{T}^w_{ikj} \hat{e}_j n_k dS_\psi d\tau + \\ + \int_\Omega \int_0^{t^+} f_i G_{ij} \hat{e}_j d^3\psi d\tau \end{aligned} \tag{F.44}$$

where t^s are the stresses exerted on the fluid, related to the stress tensor with the usual representation $t^s = T \cdot n$. Since the direction of the impulse forcing is arbitrary, from the last equation one can finally get the expression for the velocity field $u_j(x,t)$, that reads:

$$u_j(x,t) = -\int_\Omega \rho\,(u_i G_{ij})\,(x,\psi,t,0)\,d^3\psi + \oint_{\partial\Omega}\int_0^{t^+} G_{ij}t_i^s - u_i \mathbf{T}^w_{ikj} n_k dS_\psi d\tau + \int_\Omega \int_0^{t^+} f_i G_{ij} d^3\psi d\tau \quad \text{(F.45)}$$

The three terms on the right hand side represent the perturbation to the fluid due to the initial condition, the boundary conditions and the mass forcing term, respectively. If we now set the initial condition to zero and we turn off the mass forces, we obtain the following simplified expression for the velocity field:

$$u_j(x,t) = \oint_{\partial\Omega}\int_0^{t^+} G_{ij}t_i^s - u_i \mathbf{T}^w_{ikj} n_k dS_\psi d\tau \quad \text{(F.46)}$$

F.6 The background field and its derivation through ERPP

In this section we will describe how the background field is derived, in order to compute the equations (2.41) (2.43) in the 2-way coupling regime. The Maxey-Riley-Gatignol equation deals with different unperturbed fields. In the most general case, i.e. the bubbles (2.41) , these fields are the velocity $u_{(0)}$, the laplacian $\nabla^2 u_{(0)}$ the material derivative $\frac{Du_{(0)}}{Dt}$, and the vorticity $\zeta_{(0)}$. Each of these terms must be computed at the current bubble position $x_p(t)$, through the definition (2.33), namely

$$\begin{aligned}
u_{(0)}(x_p(t),t) &= u(x_p(t),t) - u_{(1)}(x_p(t),t) \\
\nabla^2 u_{(0)}(x_p(t),t) &= \nabla^2 u(x_p(t),t) - \nabla^2 u_{(1)}(x_p(t),t) \\
\zeta_{(0)}(x_p(t),t) &= \zeta(x_p(t),t) - \zeta_{(1)}(x_p(t),t) \\
\frac{Du_{(0)}}{Dt}(x_p(t),t) &= \frac{Du}{Dt}(x_p(t),t) - \frac{Du_{(1)}}{Dt}(x_p(t),t)
\end{aligned} \quad \text{(F.47)}$$

The complete fields u and ζ are the regularised fields, as prescribed by ERRP, and they obey the equations (2.32). For the sake of simplicity we have omitted the subscript R denoting the regularised condition. At run time the fields are known and resolved over the computational grid. On the contrary the self-induced fields have to be somehow calculated, for each bubble. Such computation is allowed in the context of ERPP, since the equation of the regularised disturbance field is recast into a linear Stokes equation.

The following discussion shall refer to the computation of the bubble momentum equation. Solid particles undergo the same treatment, but less terms must be computed, due to the simpler structure of their momentum equation (2.43).

If we omitted the computation of the self-disturbance, imposing the unperturbed field as the complete one, in the 2-way coupling regime we would obtain a computational error. In fact, Gualtieri et al. [64] showed that this would overestimate the terminal velocity of settling particles.

F.6.1 The velocity and vorticity self-induced field

The first terms that we are going to derive are the self-induced velocity $u_{(1)}$ and vorticity $\zeta_{(1)}$. The fields are analytically computed by solving the regularised Navier-Stokes equation

$$\begin{cases}
\frac{\partial u_{(1)}}{\partial t} = -\frac{1}{\rho_f}\nabla p_{(1)} + \nu\nabla^2 u_{(1)} - \frac{D_p(t-\epsilon_R)}{\rho_f} g(x - x_p(t-\epsilon_R), \epsilon_R) \\
\nabla \cdot u_{(1)} = 0 \\
u_{(1)}(x,t_n) = 0\,, \qquad\qquad x \in \mathbb{R}^3
\end{cases} \quad \text{(F.48)}$$

At run time t_n the equations are integrated over the time step dt, to the new configuration at time t_{n+1}.

The particle is, for this moment, considered enough far from a wall, such that the self-induced field isotropically decays in space. The integration of the equations (F.48) is split into three steps: the integration of the forcing term, the diffusive step and the projection step.

In the first stage the equation (F.48) are integrated using the homogeneous initial condition, omitting the pressure gradient and the diffusive term.

$$\tilde{u}_{(1)}(x, t+dt) = -\frac{D_p(t-\epsilon_R)}{\rho_f} g(x - x_p(t-\epsilon_R), \epsilon_R) \tag{F.49}$$

For sake of simplicity we have consider the Euler-like integration algorithm. Conceptually nothing changes if we employed different numerical schemes to advance the solution.

In the second stage the purely diffusive equation (F.50) is solved, where the initial condition is the first-step solution (F.49).

$$\begin{cases} \frac{\partial \hat{u}_{(1)}}{\partial t} = \nabla^2 \hat{u}_{(1)} \\ \hat{u}_{(1)}(x, t+dt) = \tilde{u}_{(1)}(x, t+dt) \end{cases} \tag{F.50}$$

The solution of the equation is the convolution of the initial condition with the gaussian function $g(x-\eta, dt)$, namely

$$\begin{aligned} \hat{u}_{(1)}(x, t+dt) &= \int_{\mathbb{R}^3} \tilde{u}_{(1)}(\eta, t+dt) g(x-\eta, dt) d^3\eta = \\ &= -\frac{D_p(t-\epsilon_R)dt}{\rho_f} \int_{\mathbb{R}^3} g(\eta - x_p(t-\epsilon_R), \epsilon_R) g(x-\eta, dt) d^3\eta = \\ &= -\frac{D_p(t-\epsilon_R)dt}{\rho_f} g(x - x_p(t-\epsilon_R), \epsilon_R + dt) \end{aligned} \tag{F.51}$$

The field $\hat{u}_{(1)}$ corresponds to the pseudo-velocity related to $u_{(1)}$. In fact, it is derived by integrating the Navier-Stokes equation in the absence of the pressure gradient. Hence, the self-disturbed vorticity, that is required by the lift force, is $\zeta_{(1)} = \nabla \times \hat{u}_{(1)}$

$$\zeta_{(1)} = dt \frac{D_p(t-\epsilon_R)}{\rho_f} \times \nabla g(x - x_p(t-\epsilon_R), \epsilon_R + dt) \tag{F.52}$$

The pseudo-velocity $\hat{u}_{(1)}$ must be projected back to the solenoidal vector field by means of the divergence constraint of the (F.48). The incompressible condition is achieved by introducing the divergence-free potential A, such that $u_{(1)}(x, t+dt) = \nabla \times A(x, t+dt)$. The potential A depends on the vorticity $\zeta_{(1)}$ through the differential equation

$$\zeta_{(1)} = \nabla \times \nabla \times A = -\nabla^2 A = dt \frac{D_p(t-\epsilon_R)}{\rho_f} \times \nabla g(x - x_p(t-\epsilon_R), \epsilon_R + dt) \tag{F.53}$$

Due to linearity, the solution is in the form $A = -dt \frac{D_p(t-\epsilon_R)}{\rho_f} \times \nabla G(x - x_p(t-\epsilon_R), \epsilon_R + dt)$. G is, again, the solution of the Laplace free-space problem $\nabla^2 G = g(x - x_p(t-\epsilon_R), \epsilon_R + dt)$. The resulting field $u_{(1)} = \nabla \times A$, expressed in terms of the function $G(x - x_p(t-\epsilon_R), \epsilon_R)$, reads

$$u_{(1)}(x, t+dt) = dt \frac{D_p(t-\epsilon_R)}{\rho_f} \cdot \{\nabla \otimes \nabla G(x - x_p(t-\epsilon_R), \epsilon_R + dt) - I g(x - x_p(t-\epsilon_R), \epsilon_R + dt)\} \tag{F.54}$$

where the solution of G is

$$G(r, \epsilon_R + dt) = -\frac{1}{4\pi r} erf\left(\frac{r}{\sqrt{2}\sigma(\epsilon_R + dt)}\right) \tag{F.55}$$

with $r = \sqrt{(x - x_p(t-\epsilon_R)) \cdot (x - x_p(t-\epsilon_R))}$, $\sigma(\epsilon_R + dt) = \sqrt{2\nu(\epsilon_R + dt)}$ and $erf(\eta)$the Gauss error function. By adding the solution of G into the (F.54) we compute the final expression

$$
\begin{aligned}
&u_{(1)}(x, t+dt) = dt \frac{D_p(t-\epsilon_R)}{\rho_f} \cdot \{F_{iso}(r, t+dt) I - F_{tens}(r, t+dt) \hat{r} \otimes \hat{r}\} \\
&\begin{cases}
F_{iso}(r, t+dt) = -g(r, dt+\epsilon_R) \left\{ 1 + \left(\frac{\sigma(dt+\epsilon_R)}{r} \right)^2 \right\} + \frac{1}{4\pi r^3} erf\left(\frac{r}{\sqrt{2}\sigma(\epsilon_R+dt)} \right) \\
F_{tens}(r, t+dt) = -g(r, dt+\epsilon_R) \left\{ 1 + 3\left(\frac{\sigma(dt+\epsilon_R)}{r} \right)^2 \right\} + \frac{3}{4\pi r^3} erf\left(\frac{r}{\sqrt{2}\sigma(\epsilon_R+dt)} \right)
\end{cases}
\end{aligned}
\tag{F.56}
$$

At the end of this single time step integration the fields $u_{(1)}(x, t_{n+1})$ and $\zeta_{(1)}(x, t_{n+1})$ are known, and can be used to compute $u_{(0)}(x, t_{n+1})$ and $\zeta_{(0)}(x, t_{n+1})$. This concludes the first part of our calculation.

At the beginning of the next time set, the evolved disturbance $u_{(1)}(x, t_{n+1})$ is discharged into the unperturbed velocity $u_{(0)}(x, t_{n+1})$. Therefore, the initial condition, at time t_{n+1}, of the self-disturbance is again the homogeneous condition, and the procedure can be reiterated.

F.6.2 The laplacian of the self-induced velocity field

The Faxen correction and the fluid material derivative require the evaluation of the self-disturbed laplacian $\nabla^2 u_{(1)}$, whose expression follows at once by taking the laplacian of equation (F.54).

$$
\nabla^2 u_{(1)}(x, t+dt) = dt \frac{D_p(t-\epsilon_R)}{\rho_f} \cdot \{\nabla \otimes \nabla g(x - x_p(t-\epsilon_R), \epsilon_R + dt) - I \nabla^2 g(x - x_p(t-\epsilon_R), \epsilon_R + dt)\} \tag{F.57}
$$

$g(x - x_p(t-\epsilon_R), \epsilon_R + dt)$ is the solution of $\nabla^2 G(x - x_p(t-\epsilon_R), \epsilon_R + dt)$, that is by definition the Gaussian function of variance $\sigma(\epsilon_R + dt) = \sqrt{2\nu(\epsilon_R + dt)}$. Owing to the symmetry of the Gaussian function, we can write

$$
\begin{cases}
\nabla \otimes \nabla g = \left\{ \frac{\partial^2 g}{\partial r^2} - \frac{1}{r} \frac{\partial g}{\partial r} \right\} \hat{r} \otimes \hat{r} + I \frac{1}{r} \frac{\partial g}{\partial r} \\
\nabla^2 g = \frac{\partial^2 g}{\partial r^2} + \frac{2}{r} \frac{\partial g}{\partial r}
\end{cases}
\tag{F.58}
$$

The partial derivatives with respect to r of the Gaussian function are easily computed. Then, adding the (F.58) into the (F.57), we derive the final expression we were looking for

$$
\nabla^2 u_{(1)}(x, t+dt) = dt \frac{D_p(t-\epsilon_R)}{\rho_f \sigma^2(\epsilon_R + dt)} \cdot \left\{ \frac{r^2}{\sigma^2(\epsilon_R + dt)} I + \hat{r} \otimes \hat{r} \left(\frac{r^2}{\sigma^2(\epsilon_R + dt)} - 2 \right) \right\} g(x - x_p(t-\epsilon_R), \epsilon_R + dt) \tag{F.59}
$$

F.6.3 The material derivative of the self-induced velocity field

The material velocity $\frac{Du_{(0)}}{Dt}$ is computed as it follows

$$
\frac{Du_{(0)}}{Dt} = \frac{Du}{Dt} - \frac{Du_{(1)}}{Dt} \tag{F.60}
$$

$\frac{Du}{Dt}$ and $\frac{Du_{(1)}}{Dt}$ are the material derivatives of the complete and self-induced fields, respectively. Their expressions follow from the Navier-Stokes equations (2.32) and (G.3), namely

$$
\begin{cases}
\frac{Du}{Dt} = -\frac{1}{\rho_f} \nabla p + \nu \nabla^2 u - \frac{1}{\rho_f} \sum_{n=1}^{N_p} D_n(t-\epsilon_R) g(x - x_n(t-\epsilon_R, \epsilon_R)) \\
\frac{Du_{(1)}}{Dt} = -\frac{1}{\rho_f} \nabla p_{(1)} + \nu \nabla^2 u_{(1)} - \frac{1}{\rho_f} D_p(t-\epsilon_R) g(x - x_p(t-\epsilon_R, \epsilon_R))
\end{cases}
\tag{F.61}
$$

The expression of $\frac{Du_{(0)}}{Dt}$, that is equivalent to the multipole expansion of the (G.2) for the p-th particle, reads

$$\begin{cases} \frac{Du_{(0)}}{Dt} = -\frac{1}{\rho_f}\nabla p_{(0)} + \nu\nabla^2 u_{(0)} + f - f_{(1)} \\ f(x,t) = -\frac{1}{\rho_f}\sum_{n=1}^{N_p} D_n(t-\epsilon_R)g(x - x_n(t-\epsilon_R,\epsilon_R)) \\ f_{(1)}(x,t) = \frac{1}{\rho_f} D_p(t-\epsilon_R)g(x - x_p(t-\epsilon_R,\epsilon_R)) \end{cases} \tag{F.62}$$

The material derivative requires the computation of the unperturbed pressure gradient $\nabla p_{(0)}$, the laplacian $\nabla^2 u_{(0)}$ and the unpertubed forcing term $f_{(0)}(x,t) = f(x,t) - f_{(1)}(x,t)$. The latter is derived at once since the forcing from both the whole discrete phase $f(x,t)$ and the p-th particle $f_{(1)}(x,t) = -\frac{1}{\rho_f} D_p(t-\epsilon_R)g(x-x_p(t-\epsilon_R),\epsilon_R)$ are already resolved over the computational grid. The laplacian $\nabla^2 u_{(0)}$ was presented in the previous section and the computation will not be repeated. The self-induced pressure gradient will be computed from the elliptic equation obtained by taking the divergence of the momentum equation in the (F.48). The problem is recast into the following Laplace problem

$$\nabla^2 p_{(1)} = -\frac{D_p(t-\epsilon_R)}{\rho_f}\cdot\nabla g(x - x_p(t-\epsilon_R),\epsilon_R)\ , \qquad x \in \mathbb{R}^3 \tag{F.63}$$

Due to the linearity of the equation (F.63) the solution, with usual notation, is in the form

$$p_{(1)} = -\frac{D_p(t-\epsilon_R)}{\rho_f}\cdot\nabla G(x - x_p(t-\epsilon_R,\epsilon_R)) \tag{F.64}$$

Following the expression of $\nabla\otimes\nabla G$, the self-induced pressure gradient is finally obtained

$$\begin{aligned} \nabla p_{(1)} &= -\frac{D_p(t-\epsilon_R)}{\rho_f}\cdot\nabla\otimes\nabla G(x - x_p(t-\epsilon_R,\epsilon_R)) = \\ &= \frac{D_p(t-\epsilon_R)}{\rho_f}\left\{g(r,\epsilon_R)\frac{\sigma^2(\epsilon_R)}{r^2} - \frac{1}{4\pi r^3} erf\left(\frac{r}{\sqrt{2}\sigma(\epsilon_R)}\right)\right\} - \\ &D_p(t-\epsilon_R)\cdot\hat{r}\frac{\hat{r}}{\rho_f}\left\{g(r,\epsilon_R)\left(1+3\frac{\sigma^2(\epsilon_R)}{r^2}\right) - \frac{3}{4\pi r^3} erf\left(\frac{r}{\sqrt{2}\sigma(\epsilon_R)}\right)\right\} \end{aligned} \tag{F.65}$$

Appendix G

The Maxey-Riley-Gatignol equation

In section 2.6 we have introduced the momentum equation of a pointwise particle immersed in a turbulent field, namely the Maxey-Riley-Gatignol equation. In this section we will discuss the physical and mathematical procedures employed to derive the equation. The procedure was originally introduced by Maxey & Riley and Gatignol in the papers [61][82].

Given a reference system and an orthonormal base, let's consider the dilute two-phase flow within the domain $\mathbb{R}^3$. In the low-Re_p regime the dispersed phase can be seen as the set of small spherical rigid bodies. The p-th particle of diameter d_p, positioned at $x_p(t)$, moves across a flow field whose velocity in the absence of the particle itself is $u_{(0)}(x,t)$. We remark that the field $u_{(0)}(x,t)$ is different from the field $w(x,t)$ introduced in the (2.2). In fact, $u_{(0)}(x,t)$ takes into account not only the background flow w, but also the perturbation induced by all the remaining particles. That is, the velocity $u_{(0)}(x,t)$ is the actual fluid velocity $u(x,t)$ experienced by the particle, after its self-disturbance $u_{(1)}(x,t)$ is removed. Therefore, when the p-th particle is considered, the field $u(x,t)$, obeying the system (2.1), is additively decomposed into $u_{(0)}(x,t)$ and $u_{(1)}(x,t)$, namely

$$u(x,t) = u_{(0)}(x,t) + u_{(1)}(x,t) \tag{G.1}$$

The unperturbed field $u_{(0)}$ fills the domain $\mathbb{R}^3/\widetilde{\Omega}_p$, where $\widetilde{\Omega}_p = \Omega/\Omega_p$, and obeys the Navier Stokes equations in (G.2). The control parameters of the system are the Froud number Fr and the Reynolds number $Re_\Delta = |u - v_p|_{ref}\Delta/\nu$. The field $u_{(0)}$ is observed from its smallest relevant scale $\Delta >> d_p$. For the homogeneous turbulence Δ is exactly the Kolmogorov lengthscale η. The differential equations are embedded with the neighbouring particle boundary conditions and the initial condition of the complete field $u(x,t)$. The field $u_{(0)}$ is prolonged inside the particle domain Ω_p, by means of the Taylor expansion. If $\Delta >> d_p$ the variation of $u_{(0)}$ into the p-th particle volume is indeed negligible.

$$\begin{cases} \frac{\partial u_{(0)}}{\partial t} + u_{(0)} \cdot \nabla u_{(0)} = \frac{1}{Fr^2} g + \frac{1}{Re_\Delta} \nabla \cdot T_{(0)} & x \in \mathbb{R}^3/\widetilde{\Omega}_p \\ \nabla \cdot u_{(0)} = 0 & \\ \lim_{|x| \to +\infty} u_{(0)}(x,t) = 0 & \\ u_{(0)}(x,t)|_{\partial\Omega_n} = v_n(x,t) - u_{(1)}(x,t)|_{\partial\Omega_n} \ , \quad \forall n \neq p & \\ u_{(0)}(x,0) = u_0 & \end{cases} \tag{G.2}$$

The self-disturbance field u_1 belongs to the domain $\mathbb{R}^3/\Omega_p$, and its evolution is dictated by the Navier-Stokes equations G.3, with initial homogeneous condition. The p-th particle boundary is introduced in the domain of the self-disturbance, while all the other particles disappear. The particle velocity $v_p(x,t) = \hat{v}_p(t) + \omega_p \times (x(t) - x_p(t))$ is prescribed by the kinematic law of rigid bodies, with usual notation.

The spatial derivatives of $u_{(1)}$ and $u_{(0)}$ are computed over the scales d_p and Δ, respectively. The control parameters are the particle Reynolds number Re_p and d_p/Δ.

$$\begin{cases} \frac{\partial u_{(1)}}{\partial t} + u_{(1)} \cdot \nabla u_{(1)} + u_{(0)} \cdot \nabla u_{(1)} + \frac{d_p}{\Delta} u_{(1)} \cdot \nabla u_{(0)} = + \frac{1}{Re_p} \nabla \cdot T_{(1)} & x \in \mathbb{R}^3 / \Omega_p \\ \nabla \cdot u_{(1)} = 0 \\ \lim_{|x| \to +\infty} u_{(1)}(x,t) = 0 \\ u_{(1)}(x,t)|_{\partial\Omega_p} = v_p(x,t) - u_{(0)}(x,t)|_{\partial\Omega_p} \\ u_{(1)}(x,0) = 0 \end{cases} \tag{G.3}$$

In the low-Re_p regime d_p/Δ is negligible, and the system (G.3) is recast into an unsteady Stokes equation with initial homogeneous condition. We remark that the systems (G.3) and (2.4) differ only for the domain where they are defined. In fact, in the (G.3) we include only the disturbance of the p-th particle itself, of which we are evaluating the hydrodynamic force. Therefore, after the field $u_{(1)}$ undergoes the ERPP treatment, the system (G.3) becomes exactly equal to the (2.19), where the known term is the forcing term from the p-th particle.

The particle momentum equation comes from the Cauchy equation, integrated over the domain Ω_p, namely

$$\begin{cases} \rho_p V_p \frac{dv_p}{dt} = \rho_p g V_p + D_p(t) \\ D_p(t) = \oint_{\partial\Omega_p} T \cdot \hat{n} dS \end{cases} \tag{G.4}$$

We denoted with V_p the particle volume, enclosed within the surface $\partial\Omega_p$ of outward normal unit $\hat{n}$, and with ρ_p the particle density. The only mass force considered in this formulation is the gravity force. The hydrodynamic force is derived through the surface integral over Ω_p of the stress $T \cdot \hat{n}$. The result of the integral strictly depends on the particle motion and, in particular, on the Reynolds particle number Re_p. In the low-Re_p regime it is possible to find an analytical expression of the force $D_p(t)$ as function of the field $u_{(0)}$, exploiting the analytical solution of the equations (G.3).

$$T = -pI + \mu(\nabla u + \nabla^T u) \tag{G.5}$$

The stress tensor T is related to the field u through the standard constitutive relation (G.5). Due to linearity of (G.5), the stress tensor T follows the same additively splitting of the field u, that is $T = T_{(0)} + T_{(1)}$. The hydrodynamic force is therefore decomposed as well, into the components $D_{p(0)}$ and $D_{p_{(1)}}$

$$D_p(t) = D_{p_{(0)}}(t) + D_{p_{(1)}}(t) \tag{G.6}$$

$D_{(0)}$ is the contribution of the hydrodynamic force due to the unperturbed field $u_{(0)}$, while $D_{(1)}$ derives from the particle self-disturbance $u_{(1)}$

$$\begin{cases} D_{p_{(0)}} = \oint_{\partial\Omega_p} T_{(0)} \cdot \hat{n} dS = \oint_{\partial\Omega_p} \left\{ -p_{(0)} I + \mu \left(\nabla u_{(0)} + \nabla^T u_{(0)} \right) \right\} \cdot \hat{n} dS \\ D_{p_{(1)}} = \oint_{\partial\Omega_p} T_{(1)} \cdot \hat{n} dS = \oint_{\partial\Omega_p} \left\{ -p_{(1)} I + \mu \left(\nabla u_{(1)} + \nabla^T u_{(1)} \right) \right\} \cdot \hat{n} dS \end{cases} \tag{G.7}$$

In the assumption that the particle is small, the field $u_{(0)}$ is subjected to negligible variations over the sphere. This means that we can expand the field in the neighbourhood of of the particle centroid $x_p(t)$. In particular we can think that the material derivative $\frac{Du}{Dt}(x,t)$ varies linearly in the vicinity of $x_p(t)$

$$\frac{Du}{Dt}(x,t) = \frac{Du}{Dt}(x_p(t),t) + (x - x_p(t)) \cdot \nabla \left(\frac{Du}{Dt} \right)(x_p(t),t) + o(d_p/\Delta) \tag{G.8}$$

Since $\Delta >> d_p$, $D_{p_{(0)}}$ can be computed with no further assumptions from equation (G.2). Rescaling into dimensional form, the expression of $D_{p_{(0)}}$ comes down to the volume integral that is evaluated through the condition (G.8)

$$D_{p_{(0)}} = \oint_{\partial\Omega_p} T_{(0)} \cdot n dS = \int_{V_p} (\rho_f \frac{Du_{(0)}}{Dt} - \rho_f g) dV_p = V_p \rho_p \frac{Du_{(0)}}{Dt} - V_p \rho_p g; \tag{G.9}$$

Similarly the self-disturbance force contribution $D_{(1)}$ is evaluated from the system (G.3), when Re_p and d_p/Δ are very small. In this the case non-linear convective terms are negligible with respect to the viscous forces, and the dimensional equations are recast into the following unsteady stokes equations

$$\begin{cases} \rho_f \frac{\partial u_{(1)}}{\partial t} = -\nabla p_{(1)} + \mu \nabla^2 u_{(1)} & x \in \mathbb{R}^3/\Omega_p \\ \nabla \cdot u_{(1)} = 0 \\ \lim_{|x|\to+\infty} u_{(1)}(x,t) = 0 \\ u_{(1)}(x,t)|_{\partial\Omega_p} = v_p(x,t) - u_{(0)}(x,t)|_{\partial\Omega_p} \\ u_{(1)}(x,0) = 0 \end{cases} \tag{G.10}$$

whose solution is given by the (2.5). Avoiding the detailed computation of the field $u_{(1)}$, the solution $D_{(1)}$ is evaluated in conjunction with the fundamental point force flow of Burgers [131]. The lengthy but rigorous detailed computation is out of the purpose of the present work, but the reader is referred to the work of Maxey & Riley for additional details [61]. What is important to stress is that the self-disturbance field is controlled by only the unperturbed field $u_{(0)}$, through the no-slip condition in (G.10). The resulting force $D_{(1)}$ (G.11) is restricted to the same dependency, as well as $D_{(0)}$. This might seem controversial, since the force D_p is formally derived through the surface integral of the complete fields $u(x,t)$ and $p(x,t)$. In particular the largest contribution of the self-disturbance fields is achieved at the particle surface, where the force is computed. To understand this crucial concept it is better to provide a physical interpretation of the mathematical procedure. In the hypothesis of low-Re_p the particle disturbance obeys the Stokes equations that we have presented. The scale of the motion of such flow field will be of the order of the particle size d_p. Hence, in the assumption that the diameter d_p is small, the particle disturbance will decays very fast in space. On the other hand the scale of motion of the unperturbed field $u_{(0)}$ is locked by the background hydrodynamic conditions to the scale Δ. The scale Δ does not depends on the particle Reynolds number, and in particular on the particle size. If the particle is small as compared with the (smallest) background scale Δ, the scale separation between the unperturbed and disturbance fields is achieved. When observing the motion from the particle scale d_p, the far field is dominated by only the unperturbed field. It is now clear, by analysis of the fluid integral momentum equation, how the force $D_p(t)$ is connected to only the field $u_{(0)}$, if the particle Reynold number is vanishing. However, when zooming out to the hydrodynamic scale Δ the effect of the disturbance and the background field about the particle will be concentrated in a single point. The disturbance $u_{(1)}$ is now controlled by a singular equation, and can be finite at the observed from the distance particle position $x_p(t)$. Therefore, to recover the near-field information, such self-disturbance must be removed from the complete field, when computing the hydrodynamic force $D_p(t)$.

$$\begin{aligned} D_{p_{(1)}} =& \frac{1}{2}\rho_f V_p \frac{d}{dt}\left\{u_{(0)}[x_p(t),t] - v_p(t) + \frac{1}{40}d_p^2 \nabla^2 u_{(0)}|_{x_p(t)}\right\} + 3\pi\mu d_p \left\{u_{(0)}[x_p(t),t] - v_p(t) + \frac{1}{24}d_p^2 \nabla^2 u_{(0)}|_{x_p(t)}\right\} \\ &+ 3/2\pi\mu d_p^2 \int_0^t \left(\frac{d/d\tau\left\{u_{(0)}[x_p(\tau),\tau] - v(\tau) + \frac{1}{24}d_p^2 \nabla^2 u_{(0)}|_{x_p(\tau)}\right\}}{[\pi\nu(t-\tau)]^{1/2}}\right) d\tau \end{aligned} \tag{G.11}$$

After reassembling the two contribution of the drag force, the particle momentum equation finally reads

$$\rho_p V_p \frac{dv}{dt} = (\rho_p - \rho_f) g V_p + \rho_f V_p \frac{Du_{(0)}}{Dt}(x_p(t), t) + \frac{1}{2}\rho_f V_p \frac{d}{dt}\left\{u_{(0)}[x_p(t), t] - v_p(t) + \frac{1}{40} d_p^2 \nabla^2 u_{(0)}|_{x_p(t)}\right\} +$$
$$+ 3\pi\mu d_p \left\{u_{(0)}[x_p(t), t] - v_p(t) + \frac{1}{24} d_p^2 \nabla^2 u_{(0)}|_{x_p(t)}\right\} +$$
$$+ 3/2\pi\mu d_p^2 \int_0^t \left(\frac{d/d\tau(u_{(0)}[x_p(\tau), \tau] - v(\tau) + \frac{1}{24} d_p^2 \nabla^2 u_{(0)}|_{x_p(\tau)})}{[\pi\nu(t-\tau)]^{1/2}}\right) d\tau \tag{G.12}$$

The equation is better known as the Maxey-Riley-Gatignol equation, and describes the evolution of the momentum of a tiny rigid sphere in the presence of an unsteady background flow. The notation $\frac{Du_{(0)}}{Dt}$ and $\frac{du_{(0)}}{dt}$ denotes the material derivative of the velocity $u_{(0)}$ measured following the fluid $x(t)$ and the particle $x_p(t)$, respectively. These physical quantities represent very different physical concepts and generally they can differ considerably. However the difference between the material derivatives, when compared with the drag force, is negligible if the particle is small

$$\frac{Du_{(0)}}{Dt} - \frac{du_{(0)}}{dt} = (u_{(0)} - v_p) \cdot \nabla u_{(0)} \sim o(Re_\Delta d_p^2/\Delta^2) \tag{G.13}$$

Therefore, the added mass force is approximated with the fluid material derivative with no harm, namely

$$\frac{1}{2} V_p \rho_f \left(\frac{du_{(0)}}{dt} - \frac{dv_p}{dt}\right) = \frac{1}{2} V_p \rho_f \left(\frac{Du_{(0)}}{Dt} - \frac{dv_p}{dt}\right) \tag{G.14}$$

Bibliography

[1] W. K. Melville, "The role of surface-wave breaking in air-sea interaction," *Annual Review of Fluid Mechanics*, vol. 28, no. 1, pp. 279–321, 1996.

[2] G. B. Deane and M. D. Stokes, "Scale dependence of bubble creation mechanisms in breaking waves," *Nature*, vol. 418, no. 6900, pp. 839–844, 2002.

[3] M. V. Trevorrow, S. Vagle, and D. M. Farmer, "Acoustical measurements of microbubbles within ship wakes," *The Journal of the Acoustical Society of America*, vol. 95, no. 4, pp. 1922–1930, 1994.

[4] A. M. Reed and J. H. Milgram, "Ship wakes and their radar images," *Annual Review of Fluid Mechanics*, vol. 34, no. 1, pp. 469–502, 2002.

[5] A. Prosperetti and H. N. Oguz, "The impact of drops on liquid surfaces and the underwater noise of rain," *Annual Review of Fluid Mechanics*, vol. 25, no. 1, pp. 577–602, 1993.

[6] W. H. R. Chan, S. Mirjalili, S. S. Jain, J. Urzay, A. Mani, and P. Moin, "Birth of microbubbles in turbulent breaking waves," *Physical Review Fluids*, vol. 4, no. 10, p. 100508, 2019.

[7] V. N. Prakash, J. MartÃnez Mercado, L. van Wijngaarden, E. Mancilla, Y. Tagawa, D. Lohse, and C. Sun, "Energy spectra in turbulent bubbly flows," *Journal of Fluid Mechanics*, vol. 791, pp. 174–190, 2016.

[8] B. Jacob, A. Olivieri, M. Miozzi, E. F. Campana, and R. Piva, "Drag reduction by microbubbles in a turbulent boundary layer," *Physics of Fluids*, vol. 22, no. 11, p. 115104, 2010.

[9] E. J. Terrill, W. K. Melville, and D. Stramski, "Bubble entrainment by breaking waves and their influence on optical scattering in the upper ocean," *Journal of Geophysical Research: Oceans*, vol. 106, no. C8, pp. 16815–16823, 2001.

[10] H. Pumphrey and L. Crum, "Acoustic emissions associated with drop impacts," in *Sea surface sound*, pp. 463–483, Springer, 1988.

[11] P. Jenny, D. Roekaerts, and N. Beishuizen, "Modeling of turbulent dilute spray combustion," *Progress in Energy and Combustion Science*, vol. 38, no. 6, pp. 846–887, 2012.

[12] P. Marmottant and E. Villermaux, "On spray formation," *Journal of Fluid Mechanics*, vol. 498, pp. 73–111, 2004.

[13] L. M. Pickett, J. Manin, C. L. Genzale, D. L. Siebers, M. P. Musculus, and C. A. Idicheria, "Relationship between diesel fuel spray vapor penetration/dispersion and local fuel mixture fraction," *SAE International Journal of Engines*, vol. 4, no. 1, pp. 764–799, 2011.

[14] S. Janhäll, "Review on urban vegetation and particle air pollution–deposition and dispersion," *Atmospheric environment*, vol. 105, pp. 130–137, 2015.

[15] T. Litschke and W. Kuttler, "On the reduction of urban particle concentration by vegetation-a review," *Meteorologische Zeitschrift*, vol. 17, no. 3, pp. 229–240, 2008.

[16] X. Rao, J. Zhong, R. D. Brook, and S. Rajagopalan, "Effect of particulate matter air pollution on cardiovascular oxidative stress pathways," *Antioxidants & Redox Signaling*, vol. 28, no. 9, pp. 797–818, 2018. PMID: 29084451.

[17] M. McCormick and R. Bhattacharyya, "Drag reduction of a submersible hull by electrolysis," *Naval Engineers Journal*, vol. 85, no. 2, pp. 11–16, 1973.

[18] W. Sanders, E. Winkel, D. Dowling, M. Perlin, and S. Ceccio, "Bubble friction drag reduction in a high-reynolds-number flat-plate turbulent boundary layer," *Journal of Fluid Mechanics*, vol. 552, pp. 353–380, 2006.

[19] A. Ferrante and S. Elghobashi, "On the physical mechanisms of drag reduction in a spatially developing turbulent boundary layer laden with microbubbles," *Journal of Fluid Mechanics*, vol. 503, pp. 345–355, 2004.

[20] A. Kitagawa, K. Hishida, and Y. Kodama, "Flow structure of microbubble-laden turbulent channel flow measured by piv combined with the shadow image technique," *Experiments in Fluids*, vol. 38, no. 4, pp. 466–475, 2005.

[21] C. Gabillet, C. Colin, and J. Fabre, "Experimental study of bubble injection in a turbulent boundary layer," *International Journal of Multiphase Flow*, vol. 28, no. 4, pp. 553 – 578, 2002.

[22] D. P. M. van Gils, D. Narezo Guzman, C. Sun, and D. Lohse, "The importance of bubble deformability for strong drag reduction in bubbly turbulent taylor-couette flow," *Journal of Fluid Mechanics*, vol. 722, pp. 317–47, 2013.

[23] R. Ezeta, D. Bakhuis, S. G. Huisman, C. Sun, and D. Lohse, "Drag reduction in boiling taylor-couette turbulence," *Journal of Fluid Mechanics*, vol. 881, pp. 104–118, 2019.

[24] O. Druzhinin and S. Elghobashi, "Direct numerical simulation of a three-dimensional spatially developing bubble-laden mixing layer with two-way coupling," *Journal of Fluid Mechanics*, vol. 429, pp. 23–61, 2001.

[25] S. Elghobashi, "Direct numerical simulation of turbulent flows laden with droplets or bubbles," *Annual Review of Fluid Mechanics*, vol. 51, pp. 217–244, 2019.

[26] J. Lu, A. Fernandez, and G. Tryggvason, "The effect of bubbles on the wall drag in a turbulent channel flow," *Physics of Fluids*, vol. 17, no. 9, p. 095102, 2005.

[27] G. Tryggvason, "The passage of a bubble or a drop past an obstruction in a channel," *Physics of Fluids*, vol. 32, no. 2, p. 023303, 2020.

[28] G. Tryggvason, "Numerical study of thermocapillary migration of a bubble in a channel with an obstruction," *Physics of Fluids*, vol. 31, no. 6, p. 062101, 2019.

[29] B. Weigand and H. Nemati, "Turbulence, pseudo-turbulence, and local flow topology in dispersed bubbly flow," *Physics of Fluids*, vol. 32, no. 8, p. 083310, 2020.

[30] S. Dabiri and P. Bhuvankar, "Scaling law for bubbles rising near vertical walls," *Physics of Fluids*, vol. 28, no. 6, p. 062101, 2016.

[31] S. Lin, J. Lu, G. Tryggvason, and Y. Zhang, "The effect of fluid shear on oscillating bubbly flows," *Physics of Fluids*, vol. 31, no. 4, p. 042110, 2019.

[32] B. Maneshian, K. Javadi, and M. T. Rahni, "Bubble dynamics in rotating flow under an accelerating field," *Physics of Fluids*, vol. 30, no. 8, p. 082108, 2018.

[33] A. Innocenti, A. Jaccod, S. Popinet, and S. Chibbaro, "Direct numerical simulation of bubble-induced turbulence at high reynolds numbers," 2020.

[34] J. D. Kulick, J. R. Fessler, and J. K. Eaton, "Particle response and turbulence modification in fully developed channel flow," *Journal of Fluid Mechanics*, vol. 277, pp. 109–134, 1994.

[35] J. Kuerten, "Subgrid modeling in particle-laden channel flow," *Physics of fluids*, vol. 18, no. 2, p. 025108, 2006.

[36] J. G. M. Kuerten, C. W. M. van der Geld, and B. J. Geurts, "Turbulence modification and heat transfer enhancement by inertial particles in turbulent channel flow," *Physics of Fluids*, vol. 23, no. 12, p. 123301, 2011.

[37] J. Oliveira, C. Van der Geld, and J. G. Kuerten, "Lagrangian velocity and acceleration statistics of fluid and inertial particles measured in pipe flow with 3d particle tracking velocimetry," *International journal of multiphase flow*, vol. 73, pp. 97–107, 2015.

[38] F. Battista, J. P. Mollicone, P. Gualtieri, R. Messina, and C. M. Casciola, "Exact regularised point particle (erpp) method for particle-laden wall-bounded flows in the two-way coupling regime," *Journal of Fluid Mechanics*, vol. 878, pp. 420–444, 2019.

[39] A. Vreman, "Turbulence characteristics of particle-laden pipe flow," *Journal of fluid mechanics*, vol. 584, pp. 235–279, 2007.

[40] A. Dash, A. Anantharaman, and C. Poelma, "Particle-laden taylor–couette flows: higher-order transitions and evidence for azimuthally localized wavy vortices," *Journal of Fluid Mechanics*, vol. 903, 2020.

[41] D. H. Richter and P. P. Sullivan, "Momentum transfer in a turbulent, particle-laden couette flow," *Physics of Fluids*, vol. 25, no. 5, p. 053304, 2013.

[42] D. Li, A. Wei, K. Luo, and J. Fan, "Direct numerical simulation of a particle-laden flow in a flat plate boundary layer," *International Journal of Multiphase Flow*, vol. 79, pp. 124–143, 2016.

[43] P. Costa, L. Brandt, and F. Picano, "Interface-resolved simulations of small inertial particles in turbulent channel flow," *Journal of Fluid Mechanics*, vol. 883, 2020.

[44] J. G. Kuerten and A. Vreman, "Effect of droplet interaction on droplet-laden turbulent channel flow," *Physics of fluids*, vol. 27, no. 5, p. 053304, 2015.

[45] A. Biesheuvel and P. Spelt, "Dispersion of gas bubbles in large-scale homogeneous isotropic turbulence," *Flow, turbulence and combustion*, vol. 58, no. 1-4, pp. 463–482, 1997.

[46] S. Elghobashi and G. Truesdell, "Direct simulation of particle dispersion in a decaying isotropic turbulence," *Journal of Fluid Mechanics*, vol. 242, pp. 655–700, 1992.

[47] I. Mazzitelli, D. Lohse, and F. Toschi, "On the relevance of the lift force in bubbly turbulence," *Journal of Fluid Mechanics*, vol. 488, pp. 283–313, 2003.

[48] I. Mazzitelli and D. Lohse, "Lagrangian statistics for fluid particles and bubbles in turbulence," *New Journal of Physics*, vol. 6, pp. 203–203, 2004.

[49] E. Calzavarini, T. H. van den Berg, F. Toschi, and D. Lohse, "Quantifying microbubble clustering in turbulent flow from single-point measurements," *Physics of Fluids*, vol. 20, no. 4, p. 040702, 2008.

[50] E. Calzavarini, M. Kerscher, D. Lohse, and F. Toschi, "Dimensionality and morphology of particle and bubble clusters in turbulent flow," *Journal of Fluid Mechanics*, vol. 607, pp. 13–24, 2008.

[51] Y. Tagawa, J. M. Mercado, V. N. Prakash, E. Calzavarini, C. Sun, and D. Lohse, "Three-dimensional lagrangian voronoi analysis for clustering of particles and bubbles in turbulence," *Journal of Fluid Mechanics*, vol. 693, pp. 201–215, 2012.

[52] K. D. Squires and J. K. Eaton, "Preferential concentration of particles by turbulence," *Physics of Fluids A: Fluid Dynamics*, vol. 3, no. 5, pp. 1169–1178, 1991.

[53] M. Maxey, "The gravitational settling of aerosol particles in homogeneous turbulence and random flow fields," *Journal of Fluid Mechanics*, vol. 174, pp. 441–465, 1987.

[54] J. K. Eaton and J. Fessler, "Preferential concentration of particles by turbulence," *International Journal of Multiphase Flow*, vol. 20, pp. 169–209, 1994.

[55] S. Balachandar and J. K. Eaton, "Turbulent dispersed multiphase flow," *Annual Review of Fluid Mechanics*, vol. 42, pp. 111–133, 2010.

[56] X. Zhang, J. Wang, and D. Wan, "Euler–lagrange study of bubble drag reduction in turbulent channel flow and boundary layer flow," *Physics of Fluids*, vol. 32, no. 2, p. 027101, 2020.

[57] F. Battista, P. Gualtieri, J. P. Mollicone, and C. M. Casciola, "Application of the exact regularized point particle method (erpp) to particle laden turbulent shear flows in the two-way coupling regime," *International Journal of Multiphase Flow*, vol. 101, pp. 113–124, 2018.

[58] C. Crowe, M. Sharma, and D. Stock, "The particle-source in cell method for gas droplet flow," *Journal of Fluids Engineering*, vol. 99, p. 325, 1977.

[59] M. Boivin, O. Simonin, and K. Squires, "Direct numerical simulation of turbulence modulation by particles in isotropic turbulence," *Journal of Fluid Mechanics*, vol. 375, pp. 235–263, 11 1998.

[60] P. Gualtieri, F. Picano, G. Sardina, and C. M. Casciola, "Clustering and turbulence modulation in particle-laden shear flows," *Journal of Fluid Mechanics*, vol. 715, pp. 134–162, 2013.

[61] M. Maxey and J. Riley, "Equation of motion for a small rigid sphere in a nonuniform flow," *Physics of Fluids*, vol. 26, p. 2437, 1983.

[62] J. Horwitz and A. Mani, "Accurate calculation of stokes drag for point–particle tracking in two-way coupled flows," *Journal of Computational Physics*, vol. 318, pp. 85–109, 2016.

[63] J. Horwitz and A. Mani, "Correction scheme for point-particle models applied to a nonlinear drag law in simulations of particle-fluid interaction," *International Journal of Multiphase Flow*, vol. 101, pp. 74–84, 2018.

[64] P. Gualtieri, F. Picano, G. Sardina, and C. M. Casciola, "Exact regularized point particle method for multiphase flows in the two-way coupling regime," *Journal of Fluid Mechanics*, vol. 773, pp. 520–561, 2015.

[65] I. Mazzitelli, D. Lohse, and F. Toschi, "The effect of microbubbles on developed turbulence," *Physics of Fluids*, vol. 15, no. 1, pp. L5–L8, 2003.

[66] D. P. van Gils, D. N. Guzman, C. Sun, and D. Lohse, "The importance of bubble deformability for strong drag reduction in bubbly turbulent taylor–couette flow," *Journal of Fluid Mechanics*, vol. 722, pp. 317–347, 2013.

[67] Y. Oishi, Y. Murai, Y. Tasaka, and T. Yasushi, "Frictional drag reduction by wavy advection of deformable bubbles," in *Journal of physics: conference series*, vol. 147, p. 012020, IOP Publishing, 2009.

[68] Y. Murai, "Frictional drag reduction by bubble injection," *Experiments in fluids*, vol. 55, no. 7, pp. 1–28, 2014.

[69] L. Zhao, H. I. Andersson, and J. Gillissen, "Turbulence modulation and drag reduction by spherical particles," *Physics of Fluids*, vol. 22, no. 8, p. 081702, 2010.

[70] Y. Li, J. B. McLaughlin, K. Kontomaris, and L. Portela, "Numerical simulation of particle-laden turbulent channel flow," *Physics of Fluids*, vol. 13, no. 10, pp. 2957–2967, 2001.

[71] L. Brandt and F. Coletti, "Particle-laden turbulence: Progress and perspectives," *Annual Review of Fluid Mechanics*, vol. 54, 2021.

[72] E. Bagheri and B.-C. Wang, "Direct numerical simulation of turbulent heat transfer in concentric annular pipe flows," *Physics of Fluids*, vol. 33, no. 5, p. 055131, 2021.

[73] E. Bagheri and B.-C. Wang, "Effects of radius ratio on turbulent concentric annular pipe flow and structures," *International Journal of Heat and Fluid Flow*, vol. 86, p. 108725, 2020.

[74] E. Bagheri, B.-C. Wang, and Z. Yang, "Influence of domain size on direct numerical simulation of turbulent flow in a moderately curved concentric annular pipe," *Physics of Fluids*, vol. 32, no. 6, p. 065105, 2020.

[75] M. Ould-Rouiss, L. Redjem-Saad, G. Lauriat, and A. Mazouz, "Effect of prandtl number on the turbulent thermal field in annular pipe flow," *International Communications in Heat and Mass Transfer*, vol. 37, no. 8, pp. 958–963, 2010.

[76] M. Ould-Rouiss, L. Redjem-Saad, and G. Lauriat, "Direct numerical simulation of turbulent heat transfer in annuli: Effect of heat flux ratio," *International journal of heat and fluid flow*, vol. 30, no. 4, pp. 579–589, 2009.

[77] M. M. Hernández-Cely, V. E. Baptistella, and O. M. Rodriguez, "Analysis of turbulence characteristics in two large concentric annular ducts through particle image velocimetry," *Journal of Fluids Engineering*, vol. 141, no. 6, 2019.

[78] B. J. Boersma and W.-P. Breugem, "Numerical simulation of turbulent flow in concentric annuli," *Flow, turbulence and combustion*, vol. 86, no. 1, pp. 113–127, 2011.

[79] S. Y. Chung, G. H. Rhee, and H. J. Sung, "Direct numerical simulation of turbulent concentric annular pipe flow: Part 1: Flow field," *International Journal of Heat and Fluid Flow*, vol. 23, no. 4, pp. 426–440, 2002.

[80] I. Mazzitelli, *Turbulent bubbly flow*. Twente University Press, 2003.

[81] G. Sridhar and J. Katz, "Effect of entrained bubbles on the structure of vortex rings," *Journal of Fluid Mechanics*, vol. 397, pp. 171–202, 1999.

[82] R. Gatignol, "The faxén formulas for a rigid particle in an unsteady non-uniform stokes-flow," *Journal de Mécanique théorique et appliquée*, vol. 2, no. 2, pp. 143–160, 1983.

[83] J. Magnaudet, M. Rivero, and J. Fabre, "Accelerated flows past a rigid sphere or a spherical bubble. part 1. steady straining flow," *Journal of Fluid Mechanics*, vol. 284, pp. 97–135, 1995.

[84] D. Moore, "The boundary layer on a spherical gas bubble," *Journal of Fluid Mechanics*, vol. 16, no. 2, pp. 161–176, 1963.

[85] T. R. Auton, "The lift force on a spherical body in a rotational flow," *Journal of Fluid Mechanics*, vol. 183, pp. 199–218, 1987.

[86] F. Motta, F. Battista, and P. Gualtieri, "Application of the exact regularized point particle method (erpp) to bubble laden turbulent shear flows in the two-way coupling regime," *Physics of Fluids*, vol. 32, no. 10, p. 105109, 2020.

[87] A. Pumir, "Turbulence in homogeneous shear flows," *Physics of Fluids*, vol. 8, no. 11, pp. 3112–3127, 1996.

[88] P. Gualtieri, C. Casciola, R. Benzi, G. Amati, and R. Piva, "Scaling laws and intermittency in homogeneous shear flow," *Physics of Fluids*, vol. 14, no. 2, pp. 583–596, 2002.

[89] J. Schumacher, "Relation between shear parameter and reynolds number in statistically stationary turbulent shear flows," *Physics of Fluids*, vol. 16, no. 8, pp. 3094–3102, 2004.

[90] V. Yakhot, "A simple model for self-sustained oscillations in homogeneous shear flow," *Physics of Fluids*, vol. 15, no. 2, pp. L17–L20, 2003.

[91] R. S. Rogallo, "Numerical experiments in homogeneous turbulence," *NASA TM-81315*, 1981.

[92] A. J. Griggs, A. Z. Zinchenko, and R. H. Davis, "Low-reynolds-number motion of a deformable drop between two parallel plane walls," *International Journal of Multiphase Flow*, vol. 33, no. 2, pp. 182 – 206, 2007.

[93] V. Mathai, E. Calzavarini, J. Brons, C. Sun, and D. Lohse, "Microbubbles and microparticles are not faithful tracers of turbulent acceleration," *Phys. Rev. Lett.*, vol. 117, p. 024501, 2016.

[94] M. Maxey, B. Patel, E. Chang, and L.-P. Wang, "Simulations of dispersed turbulent multiphase flow," *Fluid Dynamics Research*, vol. 20, no. 1, pp. 143 – 156, 1997.

[95] G. Eyink and K. Sreenivasan, "Onsager and the theory of hydrodynamic turbulence," *Reviews of modern physics*, vol. 78, no. 1, p. 87, 2006.

[96] U. Frisch, *Turbulence: the legacy of AN Kolmogorov*. Cambridge university press, 1995.

[97] P. Gualtieri, F. Battista, and C. M. Casciola, "Turbulence modulation in heavy-loaded suspensions of tiny particles," *Phys. Rev. Fluids*, vol. 2, p. 034304, 2017.

[98] B. Shotorban and S. Balachandar, "Particle concentration in homogeneous shear turbulence simulated via lagrangian and equilibrium eulerian approaches," *Physics of Fluids*, vol. 18, no. 6, p. 065105, 2006.

[99] P. Gualtieri, F. Picano, and C. M. Casciola, "Anisotropic clustering of inertial particles in homogeneous shear flow," *Journal of Fluid Mechanics*, vol. 629, pp. 25–39, 2009.

[100] S. Sundaram and L. R. Collins, "Collision statistics in an isotropic particle-laden turbulent suspension. part 1. direct numerical simulations," *Journal of Fluid Mechanics*, vol. 335, pp. 75–109, 1997.

[101] L. Biferale and I. Procaccia, "Anisotropy in turbulent flows and in turbulent transport," *Physics reports*, vol. 414, no. 2-3, pp. 43–164, 2005.

[102] J. Young and A. Leeming, "A theory of particle deposition in turbulent pipe flow," *Journal of Fluid Mechanics*, vol. 340, pp. 129–159, 1997.

[103] K. Fukagata and N. Kasagi, "Highly energy-conservative finite difference method for the cylindrical coordinate system," *Journal of Computational Physics*, vol. 181, no. 2, pp. 478–498, 2002.

[104] A. J. Chorin, "Numerical solution of the navier-stokes equations," *Mathematics of computation*, vol. 22, no. 104, pp. 745–762, 1968.

[105] T. Ishida, Y. Duguet, and T. Tsukahara, "Transitional structures in annular poiseuille flow depending on radius ratio," *Journal of Fluid Mechanics*, vol. 794, 2016.

[106] S. Chernyshenko and M. Baig, "The mechanism of streak formation in near-wall turbulence," *Journal of Fluid Mechanics*, vol. 544, pp. 99–131, 2005.

[107] W. Schoppa and F. Hussain, "Coherent structure dynamics in near-wall turbulence," *Fluid Dynamics Research*, vol. 26, no. 2, p. 119, 2000.

[108] K. Fukagata, K. Iwamoto, and N. Kasagi, "Contribution of reynolds stress distribution to the skin friction in wall-bounded flows," *Physics of Fluids*, vol. 14, no. 11, pp. L73–L76, 2002.

[109] S. K. Robinson, "Coherent motions in the turbulent boundary layer," *Annual Review of Fluid Mechanics*, vol. 23, no. 1, pp. 601–639, 1991.

[110] H. Mohammed, G. Bhaskaran, N. Shuaib, and R. Saidur, "Heat transfer and fluid flow characteristics in microchannels heat exchanger using nanofluids: a review," *Renewable and Sustainable Energy Reviews*, vol. 15, no. 3, pp. 1502–1512, 2011.

[111] A. F. Shchepetkin and J. C. McWilliams, "Quasi-monotone advection schemes based on explicit locally adaptive dissipation," *Monthly weather review*, vol. 126, no. 6, pp. 1541–1580, 1998.

[112] F. Picano, *Dynamics of turbulent axisymmetric jets.* PhD thesis, Università degli studi di Roma "La Sapienza", 2005.

[113] S. A. Piacsek and G. P. Williams, "Conservation properties of convection difference schemes," *Journal of Computational Physics*, vol. 6, no. 3, pp. 392–405, 1970.

[114] H. K. Versteeg and W. Malalasekera, *An introduction to computational fluid dynamics: the finite volume method.* Pearson education, 2007.

[115] J. H. Ferziger, M. Perić, and R. L. Street, *Computational methods for fluid dynamics*, vol. 3. Springer, 2002.

[116] J. P. Boris and D. L. Book, "Flux-corrected transport. i. shasta, a fluid transport algorithm that works," *Journal of Computational Physics*, vol. 11, no. 1, pp. 38–69, 1973.

[117] J. P. Boris and D. Book, "Solution of continuity equations by the method of flux-corrected transport," *Controlled Fusion*, pp. 85–129, 1976.

[118] B. Van Leer, "Towards the ultimate conservative difference scheme. ii. monotonicity and conservation combined in a second-order scheme," *Journal of Computational Physics*, vol. 14, no. 4, pp. 361–370, 1974.

[119] B. Van Leer, "Towards the ultimate conservative difference scheme iii. upstream-centered finite-difference schemes for ideal compressible flow," *Journal of Computational Physics*, vol. 23, no. 3, pp. 263–275, 1977.

[120] B. Van Leer, "Towards the ultimate conservative difference scheme. v. a second-order sequel to godunov's method," *Journal of computational Physics*, vol. 32, no. 1, pp. 101–136, 1979.

[121] A. Harten, "On a class of high resolution total-variation-stable finite-difference schemes," *SIAM Journal on Numerical Analysis*, vol. 21, no. 1, pp. 1–23, 1984.

[122] P. K. Sweby, "High resolution schemes using flux limiters for hyperbolic conservation laws," *SIAM Journal on Numerical Analysis*, vol. 21, no. 5, pp. 995–1011, 1984.

[123] P. L. Roe, "Some contributions to the modelling of discontinuous flows," *Large-scale computations in fluid mechanics*, pp. 163–193, 1985.

[124] S. Chakravarthy and S. Osher, "High resolution applications of the osher upwind scheme for the euler equations," in *6th Computational Fluid Dynamics Conference Danvers*, p. 1943, 1983.

[125] A. J. Chorin, "The numerical solution of the navier-stokes equations for an incompressible fluid," *Bulletin of the American Mathematical Society*, vol. 73, no. 6, pp. 928–931, 1967.

[126] A. J. Chorin, "On the convergence of discrete approximations to the navier-stokes equations," *Mathematics of computation*, vol. 23, no. 106, pp. 341–353, 1969.

[127] G. Benfatto and M. Pulvirenti, "Convergence of chorin-marsden product formula in the half-plane," *Communications in mathematical Physics*, vol. 106, no. 3, pp. 427–458, 1986.

[128] W. E and J.-G. Liu, "Projection method i: convergence and numerical boundary layers," *SIAM Journal on Numerical Analysis*, pp. 1017–1057, 1995.

[129] W. E and J.-G. Liu, "Projection method ii: Godunov-ryabenki analysis," *SIAM Journal on Numerical Analysis*, pp. 1597–1621, 1996.

[130] S. B. Pope, *Turbulent flows*. Cambridge university press, 2000.

[131] J. M. Burgers, "2nd report on viscosity and plasticity," *Amsterdam, Nordemann: Amsterdam Academy of Sciences*, 1938.